

Microstructure of Gas Hydrates in Sedimentary Matrices

DISSERTATION

zur Erlangung des mathematisch-naturwissenschaftlichen Doktorgrades

"Doctor rerum naturalium"

der Georg-August-Universität Göttingen

im Promotionsprogramm Geowissenschaften / Geographie

der Georg-August University School of Science (GAUSS)

vorgelegt von

Marwen Chaouachi

aus Beja, (Tunesien)

Göttingen 2015

Betreuungsausschuss:

Prof. Dr. Werner F. Kuhs

Abteilung Kristallographie, GZG, Georg-August-Universität Göttingen

Dr. Helmut Klein

Abteilung Kristallographie, GZG, Georg-August-Universität Göttingen

Mitglieder der Prüfungskommission:

Referent: Prof. Dr. Werner F. Kuhs

Abteilung Kristallographie, GZG, Georg-August-Universität Göttingen

Korreferent: Dr. Helmut Klein

Abteilung Kristallographie, GZG, Georg-August-Universität Göttingen

Weitere Mitglieder der Prüfungskommission:

Prof. Dr. Hilmar von Eynatten

Abteilung Sedimentologie und Umweltgeologie, GZG, Georg-August-Universität
Göttingen

Prof. Dr. Volker Thiel

Abteilung Geobiologie, GZG, Georg-August-Universität Göttingen

Prof. Dr. Jonas Kley

Abteilung Strukturgeologie und Geodynamik, GZG, Georg-August-
Universität Göttingen

Prof. Dr. Götz Eckold

Institut für Physikalische Chemie, Georg-August-Universität Göttingen

Tag der mündlichen Prüfung: 15. July 2015

Abstract.

Gas hydrates (GH) are found worldwide in marine sediments and permafrost regions. The detection and quantification of gas hydrates present in marine sediments is crucial for safe oil and gas extraction, seafloor stability assessments and for quantifying the impact of GH in climatic change. Therefore, there is a considerable interest in studying the microstructure of gas hydrate-bearing sediments. Although a large amount of research on gas hydrates has been carried out over the years, the micro-structural aspects of gas hydrate growth and the crystallite sizes of hydrate in sediments are still poorly known and understood.

The formation process of gas hydrates in sedimentary matrices is of crucial importance for the physical and transport properties of the resulting aggregates. This process has never been observed *in-situ* at sub-micron resolution. In this study, the nucleation and growth processes of GH were observed using synchrotron X-ray micro-computed tomography at 276 K in various sedimentary matrices such as natural quartz (with and without admixtures of clay minerals) or glass beads at varying water saturation. The process was observed on a timescale of a few minutes to many hours. Both, juvenile water as well as gas-enriched water obtained from gas hydrate decomposition was used in the experiments. Xenon gas was employed to enhance the density contrast between gas hydrate and the fluid phases involved. The nucleation sites can be easily identified and the various growth patterns are clearly established. In sediments under-saturated with juvenile water the nucleation starts at the water-gas interface resulting in an initially several micrometer thick gas hydrate film; the further growth proceeds to form chains of predominantly isometric single crystals. The growth of gas hydrate from gas-enriched water clearly follows a different pattern, via the nucleation in the bulk of liquid producing polyhedral single crystals. A striking feature in both cases is the systematic appearance of a fluid phase film of up to several μm thickness between gas hydrates and the surface of the quartz grains.

It appears that the initially different growth morphologies of gas hydrate tend to move towards more similar arrangements with coarsening of gas hydrate crystals. The initial microstructural findings obtained in laboratory experiments cannot be compared to the real situation in natural environments as the p-T conditions are different. However, the final microstructure of the system is comparable for both cases and experimental studies can permit to better understand the microstructures of GH aggregates and to tighten their physical properties required for physical detection and quantification.

Several intrinsic properties of gas hydrates e.g. low affinity between gas hydrate and sediment grains revealed by laboratory experiments can be expected to remain unchanged in natural settings.

New micro-structural models were developed based on these findings in order to explain the so-called seismic anomalies of high wave velocity and high wave attenuation characterizing GH-bearing sediments. The developed models are relevant for future efforts of quantitative rock physics modeling of effective elastic properties and electromagnetic properties of gas hydrates in sedimentary matrices.

The imaging of gas hydrate microstructures was complemented by a quantitative analysis of the *in-situ* evolution of the crystallites size distribution of synthetic xenon hydrates and of natural gas hydrate-bearing sediments retrieved from Mallik 5L-38 research well. This study revealed that the

crystal sizes of gas hydrate increase rapidly with time during the nucleation and initial growth processes. After completion of the hydrate formation process, an Ostwald ripening or normal grain growth process takes place; the number of gas hydrate crystals decreases and their intensities increase indicating the agglomeration of GH crystals into larger masses to reduce the interfacial energies of the system.

Kurzfassung.

Gashydrate sind kristalline Verbindungen aus Wasser und Gas. Gashydrate (GH) kommen weltweit in sehr großen Mengen an Kontinentalrändern, in Permafrost sowie wahrscheinlich auch in extraterrestrischen Umgebungen vor.

Der Nachweis und die Quantifizierung der in marinen Sedimenten vorhandenen GH ist entscheidend für eine sichere Öl- und Gasförderung, eine Beurteilung der Meeresbodenstabilität sowie zur Quantifizierung der Auswirkungen von GH auf den Klimawandel. Obwohl eine breit angelegte Forschung an GH im Laufe der Jahre durchgeführt wurde, waren und sind die mikrostrukturelle Aspekte des GH-Wachstums und die Kristallitgrößen von Hydraten in Sedimenten noch wenig bekannt und verstanden. Daher besteht ein erhebliches Interesse an der Untersuchung der Mikrostruktur von GH.

Der Bildungsprozess von Gashydraten in Sediment-Matrizen ist für die physikalischen und Transporteigenschaften der resultierenden Aggregate von entscheidender Bedeutung. Dieser Vorgang wurde noch nie in-situ mit Submikrometer-Auflösung beobachtet. In der vorliegenden Arbeit wurden die Keimbildungs- und Wachstumsprozesse von GH mittels Synchrotron-Röntgenmikrocomputertomographie bei 276 K in verschiedenen Sediment-Matrizen wie natürlichem Quarz (mit und ohne Zusätze von Tonmineralien) oder Glaskugeln bei unterschiedlicher Wassersättigung beobachtet. Der Vorgang wurde auf einer Zeitskala von wenigen Minuten bis zu vielen Stunden beobachtet. Sowohl juveniles Wasser wie mit Gas angereichertes Wasser wurde in den Experimenten verwendet. Xenongas wurde eingesetzt, um den Dichtekontrast zwischen Gashydrat und den beteiligten Fluidphasen zu verbessern. Die Lokation der Keimbildung kann so leicht identifiziert werden und die verschiedenen Wachstumsmuster eindeutig festgelegt werden. In Sedimenten untersättigt mit juvenilem Wasser startet die Keimbildung an der Wasser-Gas-Grenzfläche, was zu einem zunächst mehrere Mikrometer dicken Gashydrat-Film führt; das weitere Wachstum führt zu Ketten überwiegend isometrischer Einkristalle. Das Wachstum von GH in mit Gas angereichertem Wasser vollzieht sich eindeutig nach einem anderen Muster über die Keimbildung in der Flüssigkeit und dem Wachstum polyedrischer Einkristalle. Auffällig ist in beiden Fällen das systematische Auftreten eines flüssigen Films von bis zu mehreren Mikrometern Dicke zwischen Gashydraten und der Oberfläche der Quarzkörner.

Das initiale Wachstum von GH ist abhängig von den gewählten Laborverfahren und findet wahrscheinlich auch in unterschiedlicher Weise in natürlichen marinen Systemen statt. Allerdings konvergieren die Wachstumsprozesse im weiteren Verlauf der GH-Bildung in den Laborexperimenten rasch und führen zu immer ähnlichen Mikrostrukturen, sodass davon ausgegangen werden kann, dass diese durch raus auch als repräsentativ für marine Umgebungen beachtet werden können.

Mehrere intrinsische Eigenschaften von Gashydraten z.B. die geringe Affinität zwischen Gashydrat und Sedimentkörnern wie sie durch die Laborexperimente ermittelt werden, können in analoger Weise auch in natürlichen Umgebungen erwartet werden.

Neue Mikrostrukturmodelle wurden auf der Grundlage der Untersuchungen entwickelt, um die sogenannten seismischen Anomalie von hoher Wellengeschwindigkeit kombiniert mit hoher Wellendämpfung zu erklären. Die entwickelten Modelle sind für zukünftige Bemühungen für eine quantitative gesteinsphysikalische Modellierung der effektiven elastischen und elektromagnetischen

Eigenschaften von Gashydraten in Sediment-Matrizen relevant.

Die Abbildung der Gashydrat Mikrostrukturen wurde durch eine quantitative Analyse der in-situ Entwicklung der Kristallit-Größenverteilung von synthetischen Xenon-Hydraten ergänzt. Diese Studie ergab, dass die Kristallgrößen von Gashydrat sich anfangs schnell erhöhen. Es ist zu vermuten, dass nach Beendigung der Hydratbildung eine Ostwald-Reifung bzw. normales Kornwachstum stattfindet.

Acknowledgments.

After more than three years, I finally come to this last stage of my PhD. It was a tough, unforgettable and a unique experience of my life but I am happy that I managed to come through it. This is because of the support and encouragements of my family, friends and colleagues. Therefore I would like to address them my greatest gratitude.

First and foremost, I am deeply grateful to my supervisor Prof. Dr. Werner F. Kuhs for the excellent opportunity to work in his group. It has been a real pleasure to me to work with you. Thank you for being patient and for your support and encouragements especially in times of difficulties.

I would like to express my profound thanks to my second supervisor Dr. Helmut Klein for his valuable supervision and advices during my research work.

My particular thanks go to Ulf Kahmann and Heiner Bartels for their technical expertise, support, and assistance in the development of the pressure cell and in tomographic experiments.

I would like to thank Dr. Francesca Fabbiani for her support in the in-house XRD experiments and Dr. Andrzej Falenty for his help, support and the good time spent together.

I would like as well to acknowledge Klaus Häpe and Karin Offerle for their kindness and help.

I am indebted to my colleagues at the Department of Crystallography for their kindness, help and support during these years. It was a pleasure to work here with you.

I want also to acknowledge my project collaborators from the University of Mainz. Prof. Michael Kersten, Dr. Frieder Enzmann and Kathleen Sell for their cooperation to make the tomographic experiments successful.

Last but not least my deepest thanks to my family and friends who were my source of energy and emotional support. The completion of this thesis would not have been possible without your continuous encouragement.

Table of Contents.

ABSTRACT.....	3
KURZFASSUNG.....	5
ACKNOWLEDGMENTS.....	7
TABLE OF CONTENTS.....	I
LIST OF FIGURES.....	V
LIST OF TABLES.....	XVIII
1 / INTRODUCTION.....	1
1.1. BACKGROUND	1
1.2. MOTIVATION.....	2
1.3. OBJECTIVES AND APPROACHES	3
1.4. ORGANIZATION OF THE THESIS	4
2 / GAS HYDRATES	6
2.1. GAS HYDRATES PROPERTIES.....	6
2.1.1. Composition and structures	6
2.1.2. Density of gas hydrate.....	7
2.1.3. Stability and phase boundaries	8
2.1.4. Solubility of GH forming gases in water.....	10
2.1.5. Comparison between methane and xenon.....	11
2.2. FORMATION OF GAS HYDRATES	13
2.2.1. Mechanisms of GH formation	13
2.2.2. Driving forces for GH formation	15
2.2.3. Nucleation and initial growth.....	15
2.3. GAS HYDRATES-BEARING SEDIMENTS.....	21
2.3.1. Formation of GH in porous media	21
2.3.2. Factors affecting the formation	27
2.3.2.1. Salt effect:.....	28
2.3.2.2. Clay Minerals:	28
2.3.2.3. Memory effect:.....	28
2.3.3. Occurrence and seismic detection of GHs	29
2.3.4. Relationship between physical properties and GH microstructures.....	30
2.4. WAVE ATTENUATION	36
3 / METHODS AND FACILITIES	58
3.1. SCANNING ELECTRON MICROSCOPY.....	58
3.1.1. Introduction to SEM	58
3.1.2. FEI Quanta 200 FEG.....	60
3.2. X-RAYS AND SYNCHROTRON RADIATION	60

3.2.1.	<i>X-rays</i>	60
3.2.2.	<i>Synchrotron radiation</i>	61
3.2.2.1.	Introduction to synchrotron radiation.....	61
3.2.2.2.	Properties of synchrotron radiation	62
3.3.	<i>X-RAY IMAGING AND COMPUTED TOMOGRAPHY</i>	63
3.3.1.1.	<i>Interaction of X-rays with matter</i>	64
3.3.1.2.	Attenuation	64
3.3.1.3.	Phase shift	65
3.3.2.	<i>Imaging methods</i>	65
3.3.2.1.	X-ray absorption radiography	65
3.3.2.2.	Phase contrast imaging methods	66
3.3.3.	<i>Computed Tomography (CT)</i>	67
3.3.3.1.	Sample preparation	67
3.3.3.2.	Scanning configurations and data collection	68
3.3.3.3.	Image reconstruction	68
3.3.4.	<i>Resolution and image quality</i>	69
3.3.5.	<i>Artifacts</i>	70
3.3.5.1.	Beam hardening	70
3.3.5.2.	Ring artifact	70
3.3.5.3.	Partial volume effect	70
3.3.5.4.	Motion artifact	70
3.3.5.5.	Other artifacts	70
3.4.	<i>X-RAY CRYSTALLOGRAPHY AND DIFFRACTION</i>	71
3.4.1.	<i>Geometry of crystals</i>	71
3.4.2.	<i>Diffraction theory</i>	72
3.4.2.1.	Bragg's law.....	72
3.4.2.2.	Reciprocal space and Ewald construction	72
3.4.3.	<i>Structure factors</i>	73
3.4.4.	<i>Diffraction intensity</i>	74
3.4.4.1.	Multiplicity factor	74
3.4.4.2.	Absorption factor	74
3.4.4.3.	Lorentz factor	75
3.4.4.4.	Polarization factor	75
3.4.4.5.	Temperature factor	76
3.4.5.	<i>Fast X-ray crystallite size determination (FXRCS) method</i>	76
3.4.5.1.	Motivation	76
3.4.5.2.	Background.....	77
3.4.5.3.	Principle of the method	78
3.4.5.4.	Methodology	79
4 /	EXPERIMENTAL SECTION	89
4.1.	<i>FORMATION OF GAS HYDRATE IN POROUS MEDIA</i>	89

4.1.1.	<i>Starting materials</i>	89
4.1.1.1.	Porous media.....	89
4.1.1.2.	Frost.....	90
4.1.1.3.	Forming gases.....	91
4.1.2.	<i>Experimental devises</i>	91
4.1.2.1.	Laboratory low temperature/high pressure device.....	91
4.1.2.2.	Pressure cell.....	92
4.1.3.	<i>Specimen preparation</i>	95
4.1.4.	<i>Control of the reaction kinetics</i>	95
4.2.	<i>SEM INVESTIGATIONS</i>	99
4.2.1.	<i>Characterization of starting materials</i>	99
4.2.2.	<i>Microstructural observations</i>	101
4.2.3.	<i>Limits of the SEM method</i>	104
4.3.	<i>TIME-RESOLVED MICRO-COMPUTED TOMOGRAPHY OF GAS HYDRATE GROWTH IN POROUS MEDIA</i>	104
4.3.1.	<i>The TOMCAT beamline</i>	104
4.3.2.	<i>X-ray absorption radiography</i>	105
4.3.3.	<i>Samples and list of experiments</i>	107
4.3.4.	<i>Experimental setup and data collection</i>	108
4.3.5.	<i>Data quality</i>	110
4.3.6.	<i>Data analysis</i>	110
4.4.	<i>FAST X-RAY CRYSTALLITE SIZE DETERMINATION (FXRCSD) METHOD</i>	112
4.4.1.	<i>Materials</i>	112
4.4.1.1.	LaB ₆	112
4.4.1.2.	Xe hydrate	113
4.4.2.	<i>ID15B beam line setup</i>	113
4.4.2.1.	Experimental setup and data collection	114
4.4.3.	<i>Data processing</i>	117
5 /	<i>OBSERVATIONS OF GH MICROSTRUCTURES IN SEDIMENTARY MATRICES</i>	136
5.1.	<i>NUCLEATION AND GROWTH PROCESSES</i>	138
5.1.1.	<i>The memory effect</i>	147
5.1.2.	<i>Role of Qz surface</i>	150
5.1.3.	<i>Role of clay minerals</i>	150
5.2.	<i>LIQUID INTERFACE BETWEEN GH AND QZ GRAINS</i>	152
5.3.	<i>THE ROLE OF HYDROPHILIC AND HYDROPHOBIC SURFACES</i>	153
5.4.	<i>MICROSTRUCTURAL ASPECTS OF GH DISSOCIATION</i>	154
5.5.	<i>MICROSTRUCTURE OF GH ON THE PORE SCALE</i>	155
5.6.	<i>REVIEW OF THE EXISTING MODELS</i>	161
5.7.	<i>RELATIONSHIP BETWEEN HYDRATE SATURATIONS AND WAVE VELOCITY AND ATTENUATION</i>	163
5.7.1.	<i>Wave velocity</i>	163
5.7.2.	<i>Wave attenuation</i>	164

6 /	CRYSTALLITES SIZE DISTRIBUTIONS OF GHS	170
6.1.	PREVIOUS ATTEMPTS.....	170
6.2.	CALIBRATION USING LAB ₆	172
6.3.	RESULTS AND DISCUSSIONS.....	175
6.3.1.	Summary	183
7 /	CONCLUSIONS AND OUTLOOK	185
8 /	REFERENCES.....	188
9 /	APPENDICES.....	204

List of Figures.

FIGURE 1-1. DEPENDENCE OF THE WAVE VELOCITY AS A FUNCTION OF GH SATURATION ON THE MICROSTRUCTURAL MODEL CHOSEN (FROM <i>DAI ET AL.</i> [2012]).	2
FIGURE 2-1. CAGE TYPES FORMING THE THREE COMMON HYDRATE STRUCTURES. THE NUMBERS BELOW THE ARROWS DENOTE THE NUMBERS OF CAGES USED TO FORM THE HYDRATE STRUCTURE (DESIGN PROVIDED BY A. FALENTY).	7
FIGURE 2-2. SCHEMATIC OF DEPTH VERSUS TEMPERATURE FOR METHANE HYDRATE FORMATION IN MARINE SEDIMENTS [<i>HARRISON, 2010</i>].	8
FIGURE 2-3. PHASE DIAGRAM SHOWING THE BOUNDARY BETWEEN METHANE GAS (NO PATTERN) AND METHANE HYDRATE (PATTERN) FOR A PURE WATER AND PURE METHANE HYDRATE SYSTEM (FROM <i>KVENVOLDEN</i> [1993]).	9
FIGURE 2-4. PHASE DIAGRAM OF METHANE HYDRATE (A) AND XENON HYDRATE (B) AS DETERMINED USING CSMGEM PROGRAM. ..	10
FIGURE 2-5. SOLUBILITY DIAGRAMS OF CH ₄ AND Xe GASES IN WATER AS A FUNCTION OF TEMPERATURE	11
FIGURE 2-6. FORMATION CURVE OF GH FROM AQUEOUS SYSTEM. INITIAL DELAY INDICATES THE INDUCTION TIME. THE SECOND PART SHOWS A RAPID NUCLEATION AND GROWTH PROCESS. THE REACTION BECOMES SLOWER DUE TO MASS TRANSFER LIMITATION OF GAS AND WATER (MODIFIED AFTER <i>SLOAN AND KOH</i> [2008]).	14
FIGURE 2-7. ELECTRON DENSITY AND SCHEMATIC VIEW OF THE GUEST-ENRICHED SURFACE LAYER ([<i>BOEWER ET AL., 2012</i>]).	16
FIGURE 2-8. HYDRATE FILM MORPHOLOGIES FOR METHANE AND ETHANE GAS AT DIFFERENT ΔT_{SUB} (MODIFIED AFTER [<i>LI ET AL., 2014</i>])	17
FIGURE 2-9. METHANE HYDRATE COVERING THE SURFACE OF WATER DROPLETS (A,B,C) UNDER HIGH DRIVING FORCE, 10 MIN AFTER NUCLEATION. THE LOWER PICTURE IS A MAGNIFIED VIEW OF DROPLET (C).	18
FIGURE 2-10. METHANE HYDRATE COVERING TWO WATER DROPLETS UNDER LOW DRIVING FORCE, 10 H AFTER EXPERIMENT BEGAN.	18
FIGURE 2-11. NUCLEATION OF A WATER DROPLET PLACED ON A CANTILEVER AND IMMERSSED IN CYCLOPENTANE. (A) INITIAL CONTACT, (B) CYCLOPENTANE HYDRATE SHELL FORMED AROUND THE WATER DROPLET (ELAPSED TIME = 5 MIN), (C) FACETS FORMED ON THE HYDRATE SHELL (ELAPSED TIME = 0.5 H), (D) CONTINUED FACET FORMATION (ELAPSED TIME = 1.5 H), (E) CONVERSION OF INTERIOR WATER TO HYDRATE, INDICATED BY DARKENING (ELAPSED TIME = 4.5 H), (F) ALMOST COMPLETELY CONVERTED HYDRATE (ELAPSED TIME = 7 H) (FROM <i>TAYLOR ET AL.</i> [2007]).	19
FIGURE 2-12. CONFOCAL MICROSCOPE IMAGES OF THE HYDRATE FILM SHOWING PORE FILLING AS THE FILM ANNEALED (FROM <i>DAVIES ET AL.</i> [2010]).	20
FIGURE 2-13. VIDEOGRAPHS OF THE GROWTH OF METHANE-HYDRATE CRYSTALS FROM THE HYDRATE FILM INTERVENING BETWEEN METHANE AND WATER INTO LIQUID WATER PRESATURATED WITH METHANE. $P = 9.7$ MPa, $T = 273.3$ K. THE TIME LAPSE AFTER THE HYDRATE NUCLEATION AT THE METHANE-WATER INTERFACE IS INDICATED BELOW EACH VIDEOGRAPH ([<i>WATANABE ET AL., 2011</i>]).	20
FIGURE 2-14. EVOLUTION OF HYDRATE IN CLASTIC SEDIMENT. (A) HYDRATE NUCLEATES AND GROWS IN FREE PORE WATER SPACE. (B) HYDRATE GROWS AS AN ENCRUSTATION ON SEDIMENT GRAINS (FROM <i>MAX ET AL.</i> [2006]).	22
FIGURE 2-15. PORE SCALE DISTRIBUTIONS OF GH (GRAY) AND SEDIMENT GRAINS (BLACK) (FROM [<i>WAITE ET AL., 2004</i>])	22
FIGURE 2-16. DEPENDENCE OF HYDRATE HABIT ON HYDRATE FORMATION TECHNIQUE. PHYSICAL PROPERTIES OF HYDRATE-BEARING SEDIMENTS DEPEND ON THE SIZE AND DISTRIBUTION OF HYDRATE (BLACK) RELATIVE TO THE SEDIMENT GRAINS (GRAY) ([<i>WAITE ET AL., 2009</i>]).	23

FIGURE 2-17. NMR IMAGING OF (A) SAND/WATER/THF AND (B) SAND/THF HYDRATE. THE BRIGHT CHANNELS IN (B) ARE LIQUID WATER THAT HAS NOT FORMED HYDRATE (FROM [MORK ET AL., 2000]).	24
FIGURE 2-18. (A) IMAGES OF THE THF HYDRATE GROWTH HOSTED IN THE CROSS-SECTIONS OF GB RECORDED AT 10 MIN, 67 MIN, 76 MIN, 86 MIN, 97 MIN, 107 MIN, 117 MIN AND 127 MIN, (B) THE INTENSITY OF THE IMAGE AT 10 MIN AND (C) AT 86 MIN.	25
FIGURE 2-19. SCHEMATIC OF THE RELATIONSHIP BETWEEN THE NATURE OF HYDRATE AND TWO-STEP GROWTH DURING THE ATR-IR MEASUREMENT (W, LIQUID H ₂ O PHASE; G, GAS PHASE; AND H, HYDRATE PHASE): (A) BEFORE HYDRATE FORMATION, (B) IN THE FIRST STEP OF TWO-STEP GROWTH, AND (C) IN THE SECOND STEP OF THE TWO-STEP GROWTH.	26
FIGURE 2-20. A) PROCESSED TOMOGRAPHIC IMAGE SHOWING THE SPATIAL DISTRIBUTION OF HYDRATE AND ICE (GREEN COLOR) IN SAND (GREY COLOR) (FROM JIN ET AL. [2004]). B) PROCESSED X-RAY CT IMAGE. S (DARK GRAY) SAND PARTICLES, G (BLACK): FREE-GAS SPACE, W (LIGHT GRAY): WATER. H (WHITE): METHANE HYDRATE (FROM JIN ET AL. [2006]).	26
FIGURE 2-21. (A), (B), AND (C) SHOW THE OBSERVATION OF RANDOM THF HYDRATE (BLACK) GROWTH HOSTED IN GB (WHITE SPHERES) IS REPRESENTATIVE OF 2D CROSS SECTIONS (7 MM DIAMETER). THE IMAGES ARE RECORDED AT (A) 54:06 H, (B) 70:30 H, AND (C) 74:07 H. (D) AND (E) ARE 3D IMAGES RECONSTRUCTED FROM 300 SLICES.	27
FIGURE 2-22. A) FIGURE TO THE LEFT SHOWS THE EFFECT OF BENTONITE ON HYDRATE FORMATION ([ROGERS ET AL., 2004]). B) FIGURE TO THE RIGHT, SEM IMAGE OF A NGH SAMPLE FROM THE MALLIK 5L-38 RESEARCH WELL WHICH SHOWS GH AS INTERCALATE WITH CLAY MINERALS ([TECHMER ET AL., 2005]).	28
FIGURE 2-23. MAP SHOWING THE OCCURRENCE OF GH WORLDWIDE IN OCEANIC SEDIMENT OF CONTINENTAL MARGINS AND PERMAFROST REGIONS (FROM HTTP://WWW.GEOEXPRO.COM/ARTICLES/2009/02/GAS-HYDRATES-NOT-SO-UNCONVENTIONAL).	30
FIGURE 2-24. (A) LOCATION OF HYDRATE IN THE PORE SPACE FORMED USING EXCESS WATER METHOD: HYDRATE FORMS AROUND GAS BUBBLES. (B) LOCATION OF HYDRATE FORMED USING EXCESS GAS METHOD: HYDRATE FORMS WHERE WATER COLLECTS AT GRAIN CONTACTS. (C) VARIATION IN V_p AND V_s WITH HYDRATE PORE SATURATION FOR EXCESS WATER SPECIMENS (OPEN CIRCLES) AND EXCESS GAS SPECIMENS FROM AT CONFINING PRESSURE OF 500 kPa. THEORETICAL V_p AND V_s VALUES ARE ALSO SHOWN FOR PORE-FILLING MODEL (DOTTED LINE), FRAME SUPPORTING MODEL (DASHED LINE) AND CEMENTING MODEL (SOLID LINE) (FROM [PRIEST ET AL., 2009]).	32
FIGURE 2-25. (A) HYDRATE FORMATION MECHANISM OF GH PORE-FILLING MODEL. (B) MEASURED (SQUARES) V_p AND PREDICTED VALUES (FILLED CIRCLES WITH ERROR BARS) (FROM YUN ET AL. [2005]).	33
FIGURE 2-26. COMPARISON OF V_p PREDICTED BY THE FOUR HYDRATE DISTRIBUTION MODELS (A: PORE-FILLING, B: LOAD-BEARING, C: CEMENTING AT GRAIN CONTACTS, AND D: CEMENTING AT SURROUNDING GRAINS) AND EXPERIMENTAL VALUES FOR METHANE HYDRATE SAMPLE (FROM ZHANG ET AL. [2011]).	33
FIGURE 2-27. COMPARISON BETWEEN FIELD (OPEN SYMBOLS), LABORATORY (SOLID SYMBOLS), AND MODELING RESULTS (SOLID AND DASHED CURVES) FOR (A) COMPRESSIONAL AND (B) SHEAR WAVE VELOCITIES IN HYDRATE-BEARING SEDIMENTS. MODELING RESULTS ARE FROM (KLEINBERG AND DAI 2005). DOT-DASHED CURVES REPRESENT WAVE VELOCITIES FOR HYDRATE FORMING AS CEMENT AT GRAIN CONTACTS. PARTICULARLY FOR LOW HYDRATE SATURATIONS, THIS DISTRIBUTION MOST SIGNIFICANTLY INCREASES THE WAVE VELOCITY. DASHED CURVES PREDICT WAVE VELOCITIES FOR HYDRATE THAT COATS AND CEMENTS SEDIMENT GRAINS. SOLID CURVES REPRESENT LOADBEARING HYDRATE, AND DOTTED CURVES SHOW THE IMPACT OF PORE FILLING HYDRATE. PORE-FILLING DISTRIBUTIONS BEGIN BRIDGING SEDIMENT GRAINS AND BEHAVING AS LOAD-BEARING DISTRIBUTIONS (FROM [WAITE ET AL., 2009]).	34
FIGURE 2-28. DEPENDENCE OF THE HYDRAULIC CONDUCTIVITY ON THE GH MICROSTRUCTURE (FROM DAI ET AL. [2012]).	35
FIGURE 2-29. VARIATION OF THE ELECTRICAL RESISTIVITY WITH THE WATER SATURATION	35

FIGURE 2-30. THE MECHANISM OF WAVE-INDUCED FLOW. DURING THE COMPRESSION CYCLE OF A WAVE WITH PERIOD T , THERE WILL BE FLUID FLOW FROM ELASTICALLY SOFT INHOMOGENIETIES INTO THE BACKGROUND (SHOWN HERE; THE FLOW DIRECTION IS INDICATED BY ARROWS) AND FLOW FROM THE BACKGROUND INTO ELASTICALLY STIFF INHOMOGENIETIES. DURING THE EXTENSION CYCLE OF THE WAVE, THE FLUID FLOW REVERSES ([MÜLLER ET AL., 2010]).	37
FIGURE 2-31. CONCEPTUAL MODEL OF CEMENTED GRAIN CONTACTS WITH INCREASING HYDRATE SATURATION. FROM LEFT TO RIGHT: IDEALIZED VIEW OF SAND GRAIN CONTACT WITH NO HYDRATE, GRAIN CONTACTS WITH HYDRATE GROWING AT GRAIN BOUNDARIES AND CONNECTED HYDRATE CEMENTING GRAIN CONTACTS WITH COMMENCEMENT OF PORE FILLING (FROM PRIEST ET AL. [2006]).	37
FIGURE 3-1. TYPES OF INTERACTIONS BETWEEN ELECTRONS AND A SAMPLE [HENRY, 2012]	59
FIGURE 3-2. PICTURE OF THE CRYO-FE-SEM	60
FIGURE 3-3. THREE FORMS OF SYNCHROTRON RADIATION [ATTWOOD, 2007].	62
FIGURE 3-4. SCHEMATIC OF THE MODERN STORAGE RING OF THE 3 RD GENERATION FACILITIES [ATTWOOD, 2007].	62
FIGURE 3-5. X-RAY PICTURE OF THE HAND OF ROENTGEN'S WIFE BERTHA [CIERNIAK, 2011]	63
FIGURE 3-6. PHASE SHIFT AND ATTENUATION OF A WAVE IN A MEDIUM WITH REFRACTIVE INDEX $n = 1 - \delta + i\beta$. THE AMPLITUDE IS ATTENUATED AS INDICATED BY GREEN LINES AND THE PHASE IS SHIFTED WITH RESPECT TO THE WAVE PROPAGATING IN VACUUM AS INDICATED BY RED LINES (REPRODUCED FROM HTTP://EN.WIKIPEDIA.ORG/WIKI/PHASE-CONTRAST_X-RAY_IMAGING).	64
FIGURE 3-7. PRINCIPLE OF CONVENTIONAL X-RAY ABSORPTION RADIOGRAPHY [BARUCHEL, 2012]	66
FIGURE 3-8. CRYSTAL INTERFEROMETER [BECH, 2009]	66
FIGURE 3-9. ANALYZER BASED IMAGING [BECH, 2009]	66
FIGURE 3-10. PROPAGATION BASED IMAGING [BECH, 2009]	67
FIGURE 3-11. GRATING BASED IMAGING [BECH, 2009].	67
FIGURE 3-12. SCHEMATIC ILLUSTRATION OF DIFFERENT CT CONFIGURATIONS [KETCHAM, 2012]	68
FIGURE 3-13. A) GEOMETRICAL REPRESENTATION FOR OBTAINING THE SINOGRAM AS DEMONSTRATED IN B) AND WHICH IS BACK PROJECTED AS SHOWN IN C) WITHOUT APPLYING FILTERING AND D) APPLYING A RAMP FILTER (THE CUT-OUT HAS BEEN ENHANCED IN CONTRAST TO DISPLAY ARTEFACTS DUE TO RECONSTRUCTION [ZEHBE ET AL., 2010].	69
FIGURE 3-14. A POINT LATTICE AND ITS UNIT CELL.....	71
FIGURE 3-15. GEOMETRY FOR INTERFERENCE OF A WAVE SCATTERED FROM TWO PLANES SEPARATED BY SPACING, D . THE DIFFERENCE IN PATH LENGTHS IS $2d \cdot \sin(\theta)$ [FULTZ AND HOWE, 2013].	72
FIGURE 3-16. THE EWALD CONSTRUCTION (MODIFIED FROM A PRIVATE COMMUNICATION OF SYLVAIN RAVY FOUND AT HTTP://WWW-INT.IMPMC.UPMC.FR/IMPMC/ASSOCIATIONS/CGE-2008/PPT/RAVY.PPT).	73
FIGURE 3-17. SCATTERING ANGLES IN THE SURFACE REFERENCE FRAME: INCIDENT ANGLE α , IN-PLANE SCATTERING ANGLE ψ , EXIT ANGLE β , AND AZIMUTH ϕ . THESE ANGLES CO-INCIDE WITH THE RESPECTIVE DIFFRACTOMETER AXES IN THE Z-AXIS SCATTERING GEOMETRY ([SMILGIES, 2002]).	75
FIGURE 3-18. PRINCIPLE OF X-RAY DIFFRACTION OF POLYCRYSTALLINE MATERIAL	78
FIGURE 3-19. EFFECT OF THE CRYSTALLITE SIZE ON THE INTENSITIES OF REFLECTIONS IN 2D XRD PATTERN OF POLYCRYSTALLINE MATERIALS. A: LaB_6 POWDER WITH $D = 3.5 \mu\text{M}$, B: CORRUNDUM Al_2O_3 POWDER WITH $D = 90 \mu\text{M}$, AND C: CORRUNDUM Al_2O_3 POWDER WITH $D = 150 \mu\text{M}$. FROM A TO C, THE NUMBER OF REFLECTIONS DECREASES AND THE INTENSITY INCREASES WITH THE INCREASE OF THE AVERAGE CRYSTALLITE SIZE (DIAMETER (D)) AT THE SAME EXPERIMENTAL SETTINGS.	78
FIGURE 4-1. GRAIN SIZE DISTRIBUTIONS OF A) QZ SAND, B) KAOLINITE AND C) MONTMORRILLONITE {KLAPPROTH, 2006 #142}..	89

FIGURE 4-2. SCHEMATIC REPRESENTATION FOR ADDING OH GROUPS TO PARTICLES WITH SILICA SURFACE.....	90
FIGURE 4-3. SCHEMATIC REPRESENTATION OF THE SILANIZATION REACTION.	90
FIGURE 4-4. PREPARATION OF FROST: (A) PICTURE OF THE FROST MACHINE, (B) SCRATCHING FROST FROM THE SURFACE OF THE METAL DISK INTO LIQUID NITROGEN	91
FIGURE 4-5. EXPERIMENTAL SETUP FOR <i>EX-SITU</i> GH FORMATION IN LABORATORY AT THE DEPARTMENT OF CRYSTALLOGRAPHY (GEOSCIENCES CENTRE, UNIVERSITY OF GÖTTINGEN). ON THE LEFT HAND SIDE A PICTURE OF THE HIGH PRESSURE SETUP SHOWING THE THERMAL BATH AND THE PRESSURE SYSTEM USED WHICH IS EXPLAINED IN MORE DETAILS ON THE RIGHT HAND SIDE IMAGE.....	92
FIGURE 4-6. CUSTOM DESIGNED PRESSURE CELL FOR <i>IN-SITU</i> GH FORMATION. LEFT: SCHEMATIC DRAWING OF THE PRESSURE CELL, RIGHT: PICTURE OF THE PRESSURE CELL	93
FIGURE 4-7. BASE OF THE PRESSURE CELL	94
FIGURE 4-8. ALUMINUM SAMPLE HOLDER FIGURE 4-9. DOME OF THE CELL MADE OF POLYETHYLENIMINE.	94
FIGURE 4-10. GAS CONSUMPTIONS OF Xe HYDRATE FORMATION AT DIFFERENT PRESSURE DRIVING FORCE. A SAMPLE OF QZ SAND WITH 10 % WATER (276 K) WAS USED.	96
FIGURE 4-11. EXPERIMENTAL DETERMINATION OF THE PRESSURE CORRESPONDING TO THE STABILITY LIMIT OF Xe HYDRATE AT 276 K. FIRST Xe HYDRATE WAS FORMED AT 5 BAR, THEN THE PRESSURE WAS DECREASED BY STEPS OF 0.5 BAR DOWN TO 2.5 BAR (NOT SHOWN IN THIS GRAPH) AND FINALLY THE PRESSURE WAS DECREASED BY SMALLER STEPS OF 0.05 BAR UNTIL A REMARKABLE INCREASE OF PRESSURE IS OBSERVED. THE INCREASE OF PRESSURE INDICATES THE DISSOCIATION OF GH (BLACK ARROWS IN THE FIGURES INDICATE THE INITIAL PARTIAL AND THE BEGINNING OF FULL GH DISSOCIATION).	98
FIGURE 4-12. CONTROL OF GH FORMATION KINETICS. THE REACTION CAN BE INITIATED, STOPPED AND RESTARTED AGAIN IN ORDER TO STUDY THE NUCLEATION AND GROWTH PROCESSES. THE RED ARROWS SHOW THE TIME AT WHICH SCANS CAN BE EXECUTED WITHOUT INFLUENCING THE QUALITY OF DATA.	99
FIGURE 4-13. FE-SEM IMAGES OF THE NATURAL QZ SAND. A: SE IMAGE OF QZ SAND GRAINS, B: HIGH MAGNIFICATION IMAGE OF A QZ GRAIN SURFACE. C AND D ARE BSE IMAGES SHOWING THE PRESENCE OF OTHER TYPES OF MINERALS (BRIGHTER REGIONS) SUCH AS Fe, Al, OR Zr.	100
FIGURE 4-14. SEM IMAGE OF GB	100
FIGURE 4-15. SEM IMAGE OF KAOLINITE FIGURE 4-16. SEM IMAGE OF MONTMORILLONITE.....	100
FIGURE 4-17. SEM IMAGES OF FROST. A: MONOLAYER OF FROST FORMED BY CONDENSING WATER VAPOR 3 S ON A COLD PLATE. B: AGGLOMERATES OF FROST CRYSTALLITES FORMED BY CONDENSING WATER VAPOR 20 S ON A COLD PLATE.	101
FIGURE 4-18. QZ SAND ADMIXED WITH 10 WT% FROST.....	101
FIGURE 4-19. FE-SEM OBSERVATIONS OF GH DISTRIBUTED IN NATURAL SEDIMENTS. SIMILARITIES IN THE MICROSTRUCTURES BETWEEN SYNTHETIC METHANE (A) AND Xe HYDRATE (B) SAMPLES (THIS WORK), SYNTHETIC METHANE HYDRATE PREPARED BY A. KLAPPROTH (C) AND NGH SAMPLE FROM THE MALLIK 5L-38 RESEARCH WELL (D) [TECHMER ET AL., 2005]	102
FIGURE 4-20. FE-SEM OBSERVATIONS OF POROUS (A) AND DENSE (B) MORPHOLOGICAL MICROSTRUCTURES IN Xe HYDRATE SAMPLES (MEDIUM III).....	103
FIGURE 4-21. FE-SEM OBSERVATIONS OF POLYCRYSTALLINE LAYERS OF GH COVERING THE QZ SURFACE (A AND B). C: INDIVIDUAL CRYSTALS IMAGES OF Xe HYDRATE BEARING SAMPLE (17% FROST). A AND B SHOW A POLYCRYSTALLINE LAYERS OF GH PARTIALLY COVERING THE QZ GRAINS. C: A MONOCRYSTALLINE LAYER WHERE INDIVIDUAL CRYSTALS WITH SIZES IN THE ORDER OF 5-10 μM CAN BE CLEARLY DISTINGUISHED.	103

FIGURE 4-22. SEM IMAGE OF MALLIK 5L-38 SAMPLE SHOWING A POSSIBLE FROZEN WATER LAYER BETWEEN QZ GRAIN AND GH [TECHMER ET AL., 2005].	104
FIGURE 4-23. PHOTON FLUX AS A FUNCTION OF ENERGY FOR MONOCHROMATIC AND WHITE BEAM (SOURCE: HTTP://WWW.PSI.CH/SLS/TOMCAT/OPTICS)	105
FIGURE 4-24. X-RAY PATH THROUGH THE PRESSURE CELL	106
FIGURE 4-25. EXPERIMENTAL SETUP AT THE TOMCAT BEAMLINE	109
FIGURE 4-26. CLOSE-UP PICTURE OF THE PRESSURE CELL MOUNTED ON THE ROTATION STAGE	109
FIGURE 4-27. CT IMAGES SHOWING THE MOST COMMON ARTIFACTS OBSERVED DURING DATA COLLECTION: A) BEAM HARDENING: THE EDGES OF QZ GRAINS ARE BRIGHTER THAN THE INNER VOLUME, B) MOTION ARTIFACT DUE TO MOVEMENT OF THE SAMPLES DURING MEASUREMENTS, AND C) RING ARTIFACT RESULTING FROM A DETECTOR FAILURE	110
FIGURE 4-28. LEFT: AN ORIGINAL BINARY RAW 64-BIT FLOATING IMAGE INCLUDING ALL ARTIFACTS. RIGHT: A RE-SCALED 16-BIT ROI CROPPED IMAGE WITHOUT LOSS OF INFORMATION DURING RESCALING (IMAGES PROVIDED BY KATHLEEN SELL)	111
FIGURE 4-29. DIFFERENT STEPS OF DATA PROCESSING (IMAGES PROVIDED BY KATHLEEN SELL)	112
FIGURE 4-30. SEM IMAGE OF STANDARD LAB ₆ POWDER (NIST SRM 660A)	113
FIGURE 4-31. CRYSTALLITES SIZE (DIAMETER (D)) DISTRIBUTION OF 5409 PARTICLES OF LAB ₆ EXTRACTED FROM SEM IMAGES	113
FIGURE 4-32. TYPICAL SET-UP FOR HIGH ENERGY XRD AT ID15B OF THE ESRF. THE ALUMINUM PLATE ACTS TO FILTER LOW-ENERGY FLUORESCENCE X-RAYS. THE DETECTOR IMAGE SHOWN IS OF A TEXTURED ZIRCONIUM ALLOY [DANIELS AND DRAKOPOULOS, 2009]	114
FIGURE 4-33. PICTURE OF THE SAMPLE ENVIRONMENT AT THE ID15B BEAM LINE	115
FIGURE 4-34. PICTURE OF THE SETUP USED FOR <i>IN-SITU</i> INVESTIGATIONS OF THE EVOLUTION OF GH CSDS WITH TIME. THE PRESSURE CELL WAS ROCKED OVER THE ANGLE Ω	115
FIGURE 4-35. PICTURE OF THE SETUP USED FOR <i>EX-SITU</i> MEASUREMENTS OF GH CSDS IN KAPTON CAPILLARIES CO-AXIALLY COOLED USING CRYOSTREAM AT 100 K. THE SAMPLE WAS ROTATED OVER THE ANGLE Φ	116
FIGURE 4-36. SPOTTY DIFFRACTION PATTERN OF LAB ₆	117
FIGURE 4-37. IMAGES SHOWING THE SEPARATION OF PEAKS USING THRESHOLDING METHOD. A) 2D SPOTTY DIFFRACTION PATTERN OF LAB ₆ , B) SELECTION OF THE DEBYE-SCHERRER RING OF INTEREST, C) SEPARATION OF PEAKS IN THE CIRCUMFERENCE OF THE SELECTED DIFFRACTION RING (IMAGE PROVIDED BY SIGMUND NEHER)	89
FIGURE 4-38. EXAMPLE OF TREATMENT OF TWO OVERLAPPED SPOTS (IMAGE PROVIDED BY SIGMUND NEHER)	89
FIGURE 4-39. ON THE LEFT HAND SIDE, A STACK OF 2D IMAGES ANALYSED IN ORDER TO EXTRACT INTENSITY INFORMATION OF EACH PEAK FROM THE DIFFERENT IMAGES WHICH ARE SHOWN ON THE RIGHT HAND SIDE IMAGES AND MARKED BY YELLOW, RED AND GREEN BOXES (IMAGE PROVIDED BY SIGMUND NEHER)	90
FIGURE 4-40. EXAMPLE OF A ROCKING CURVE OF A CRYSTAL: INTENSITY VARIATION AS A FUNCTION OF THE ROTATION ANGLE. THE AREA UNDER THE CURVE (TEXTURED IN BLUE) CORRESPONDS TO THE INTEGRATED INTENSITY OF THE PEAK	91
FIGURE 5-1. NUCLEATION OF A THIN GH FILM AT THE GAS-WATER INTERFACE FOR GH FORMATION USING PROCEDURE I. (SAMPLE 1, W _S = 22 %): A) CT IMAGE BEFORE STARTING GH FORMATION, B) CT IMAGE TAKEN AFTER A REACTION TIME OF 70 SECONDS (T _R = 70 s). GAS HYDRATE (GH) IN WHITE, WATER (W) IN GRAY, QUARTZ SAND (Qz) IN LIGHT GRAY. GAS AND JUVENILE WATER HAVE THE SAME CONTRAST AND CAN BE DISTINGUISHED ONLY BY THE MENISCUS WHICH SEPARATES THE TWO PHASES	139
FIGURE 5-2. INITIAL GROWTH OF GH FILM PREFERENTIALLY TOWARDS THE GAS PHASE. A) FORMATION OF AN INITIAL THIN GH FILM AT THE GAS-WATER INTERFACE (T _R = 50 s), B) THICKENING OF THE GH FILM ACROSS THE GH WATER INTERFACE IN BOTH	

DIRECTIONS BUT PREFERENTIALLY TOWARDS THE GAS PHASE ($T_R = 130s$). FROM THE DASHED RED LINE REPRESENTING THE MIDDLE OF GH FILM IN (A), THE HYDRATE FILM IS MORE DEVELOPED IN THE SIDE OF THE GAS PHASE IN (B). (SAMPLE 1, $W_s = 22\%$)	140
FIGURE 5-3. SEQUENCE OF GH FILM GROWTH USING PROCEDURE I (SAMPLE 2, $W_s = 57\%$). A) INITIAL ($T_R = 4.35$ MIN), B) INTERMEDIATE ($T_R = 10.2$ MIN), AND C) FINAL ($T_R = 44.65$ MIN). POCKETS OF REST WATER TRAPPED BETWEEN GH CRYSTALS DUE TO GAS DIFFUSION LIMITATION CAN BE SEEN IN (C).	141
FIGURE 5-4. NUCLEATION OF GH CRYSTALS INSIDE THE WATER CLOSE TO THE GAS-WATER INTERFACE BY FORMATION USING PROCEDURE II (SAMPLE 3, $W_s = 49\%$). BEFORE REFORMATION, <i>IN-SITU</i> FORMED GH WAS DECOMPOSED AT 275 K AND ATMOSPHERIC PRESSURE. THE SAMPLE WAS HELD AT THESE CONDITIONS FOR ~ 1 H BEFORE THE REFORMATION. $T_R = 50$ S. ..	142
FIGURE 5-5. NUCLEATION OF GH CRYSTALS INSIDE THE WATER PHASE BY FORMATION FROM Xe-ENRICHED WATER USING PROCEDURE III (SAMPLE 4, $W_s = 34\%$). BEFORE THE FORMATION THE SAMPLE HAS BEEN LEFT FOR 1 H AT 275 K AND ATMOSPHERIC PRESSURE TO COMPLETELY DECOMPOSE Xe-HYDRATE POWDER. $T_R = 42$ S.	142
FIGURE 5-6. EVOLUTION OF GH GROWTH FROM MEMORY WATER USING PROCEDURE II (SAMPLE 3, $W_s = 49\%$). A) INITIAL ($T_R = 40$ S), B) INTERMEDIATE ($T_R = 4.2$ MIN), AND C) FINAL ($T_R = 11.3$ MIN). LARGE POLYHEDRAL CRYSTALS WERE INITIALLY FORMED INSIDE THE WATER NEAR TO THE GAS-WATER INTERFACE. THE IMAGES D, E AND F REPRESENT RESPECTIVELY THE 3D RENDERED IMAGES OF A, B AND C (PROVIDED BY KATHLEEN SELL). ROUNDED POLYHEDRAL CRYSTALS OF GH (WHITE) GROW PREFERENTIALLY TOWARDS THE CENTER OF THE PORE SPACE; THEY DO NOT ADHERE TO THE QZ (GRAY) SURFACE, WHICH IS COVERED BY A WATER LAYER OF VARIABLE THICKNESS. FOR CLARITY, THE FLUID PHASES HAVE BEEN REMOVED FROM THE RENDERED IMAGES.....	144
FIGURE 5-7. EVOLUTION OF GH GROWTH FROM MEMORY WATER, PROCEDURE III (SAMPLE 4, $W_s = 34\%$). A) INITIAL ($T_R = 32$ S), B) INTERMEDIATE ($T_R = 3.6$ MIN), AND C) FINAL ($T_R = 11.7$ MIN). THE NUCLEATION STARTS INSIDE THE LIQUID WATER.....	145
FIGURE 5-8. CONCEPTUAL MODEL OF GH FORMATION FROM JUVENILE WATER USING PROCEDURE I. A) NUCLEATION OF A POROUS GH FILM AT THE GAS-WATER INTERFACE, B) THICKENING OF THE GH FILM ACROSS THE GAS-WATER INTERFACE PREFERENTIALLY TOWARD THE GAS PHASE, AND C) FINAL MICROSTRUCTURE OF GH AFTER COMPLETION OF THE FORMATION PROCESS: A WATER LAYER REMAINS BETWEEN GH AND QZ GRAINS. THE STRUCTURE OF GH BECOMES MORE DENSE BUT CHARACTERIZED BY THE PRESENCE OF WATER POCKETS	146
FIGURE 5-9. ENRICHMENT OF WATER WITH Xe GAS WITH TIME (SAMPLE 2, $W_s = 57\%$). A) CT IMAGE BEFORE GH FORMATION ($t_R = 0$ MIN, $P = 0.22$ MPA, $T = 276$ K), B) CT IMAGE AT THE END OF GH FORMATION ($t_R = 14.65$ MIN, $P = 0.22$ MPA, $T = 276$ K). WATER AND XENON HAVE ALMOST THE SAME GRAY VALUE AT THE BEGINNING OF THE REACTION BUT WATER BECOMES BRIGHTER AT THE END OF GH FORMATION WHICH MAY INDICATES AN ENRICHMENT IN XENON GAS. THE RELATIVE GRAY VALUE OF WATER TAKING XENON AS REFERENCE INCREASES FROM 102 % TO 107 %.....	147
FIGURE 5-10. CONCEPTUAL MODEL OF GH FORMATION FROM MEMORY WATER USING PROCEDURE II OR III. A) NUCLEATION OF ISOMETRIC POLYHEDRAL GH CRYSTALS INSIDE THE LIQUID WATER, B) GROWTH OF GH CRYSTALS PREFERENTIALLY TOWARD THE PORE SPACE, AND C) THE FINAL MICROSTRUCTURE OF GH SHOW RELATIVELY LARGE GH CRYSTALS LESS INTERCONNECTED WITH LIQUID WATER REMAINING AT THEIR GRAIN BOUNDARY. A LIQUID WATER LAYER REMAINED ALSO BETWEEN GH AND SEDIMENT GRAINS AS OBSERVED IN PROCEDURE I.	149
FIGURE 5-11. GH NUCLEATION AT THE GAS-WATER INTERFACE FEW μ M AWAY FROM THE QZ SURFACE (SAMPLE 1).	150
FIGURE 5-12. DISTRIBUTION OF (A) KAOLINITE (SAMPLE 5, $W_s = 77\%$) AND (B) MONTMORILLONITE (SAMPLE 6, $W_s = 72\%$) PARTICLES IN THE WATER PHASE BEFORE THE START OF GH FORMATION.....	150

FIGURE 5-13. GH FORMATION IN NATURAL QZ WITH 8 WT % MONTMORILLONITE (SAMPLE 6, $W_s = 72\%$, $T_R = 6.2$ MIN). THE NUCLEATION OF GH (WHITE) TAKES PLACE AT THE GAS-WATER INTERFACE CLOSE TO THE MIM PARTICLES. AN INTIMATE CONTACT BETWEEN MONTMORILLONITE AND GH IS OBSERVED (RED CIRCLE).....	151
FIGURE 5-14. CT IMAGES SHOWING A THIN WATER LAYER REMAINING BETWEEN GH (WHITE) AND QZ GRAINS (GREY) IN A SYSTEMATIC MANNER AT THE END OF THE GH FORMATION PROCESS. A: USING PROCEDURE I (SAMPLE 7, $W_s = 27\%$). B: PROCEDURE II (SAMPLE 3, $W_s = 57\%$). C: THE WATER LAYER HAS AN INHOMOGENEOUS THICKNESS; IT IS THICKER AT THE GRAIN BOUNDARY (GRB) OF GH CRYSTALS (SAMPLE 8, $W_s = 41\%$). D: A REMAINING GAS PHASE NEAR GRAIN CONTACTS WAS ALSO OBSERVED (SAMPLE 9, $W_s = 37\%$).	153
FIGURE 5-15. GH FORMATION IN HYDROPHOBIC GB (GB) (SAMPLE 10, $W_s = 54\%$, $T_R = 16$ MIN). ALL WATER HAS BEEN TRANSFORMED INTO HYDRATE. FREE XE GAS FILLS SPACES BETWEEN GH AND GB GRAINS.	154
FIGURE 5-16. SEQUENCE OF GH DISSOCIATION BY DEPRESSURIZATION (SAMPLE 3, $W_s = 41\%$). A) SAMPLE FULLY TRANSFORMED, B) INITIAL DECOMPOSITION, C) PARTIAL DECOMPOSITION, D) GH REMAINS AT THE GRAIN CONTACTS. IMAGE B SHOWS THE BEGINNING OF GH DECOMPOSITION AT THE INTERFACE OF GH WITH XE GAS (RED ARROWS). IMAGE D SHOWS THE REMAINING GH AT GRAIN CONTACTS AS INDICATED BY THE BLUE ARROWS. AFTER GH DISSOCIATION, WATER IS REDISTRIBUTED IN THE SAMPLE.	155
FIGURE 5-17. THE FOUR DIFFERENT MICROSTRUCTURAL MODELS REDRAWN AFTER DVORKIN ET AL. (2000) GH (KHAKI), SEDIMENT GRAINS (DARK BLUE), AND FLUID PHASE (GREEN). (A) HYDRATE AS CEMENT AT GRAIN CONTACTS, (B) HYDRATE SURROUNDING AND CEMENTING GRAINS, (C) HYDRATE AS PART OF THE PORE FLUID, AND (D) HYDRATE AS PART OF LOAD-BEARING GRANULAR FRAME.	156
FIGURE 5-18. MICROSTRUCTURE OF GH AT LOW WATER SATURATION (SAMPLE 11, $W_s = 14.6\%$). GH FORMS AROUND QZ GRAINS AND FORMS BRIDGES BETWEEN QZ GRAINS WITHOUT CEMENTING. A FLUID PHASE REMAINED BETWEEN GH AND QZ GRAINS AND AT GRAIN CONTACTS.	157
FIGURE 5-19. MICROSTRUCTURE OF GH AT INTERMEDIATE CONCENTRATION (SAMPLE 12, $W_s = 49.5\%$). GH (WHITE) FILLS COMPLETELY SOME PART OF THE SAMPLE WHILE THE REST IS EMPTY.	157
FIGURE 5-20. MICROSTRUCTURE OF GH AT HIGH INITIAL W_s (SAMPLE 13, $W_s = 88.6\%$). GH (WHITE) OCCURS AS THE CONTINUOUS PHASE WHILE THE XE GAS FORMS BUBBLES IN THE HYDRATE STRUCTURE WITH SOME WATER POCKETS AS WELL.	158
FIGURE 5-21. EVOLUTION OF GH MICROSTRUCTURE AS A FUNCTION OF INITIAL WATER SATURATION (A: SAMPLE 11, B: SAMPLE 14, C: SAMPLE 12, D: SAMPLE 15, E: SAMPLE 13). FROM THE LEFT TO RIGHT THE W_s INCREASES. IMAGES B AND D REPRESENT TRANSITION STAGES BETWEEN LOW AND INTERMEDIATE W_s AND BETWEEN INTERMEDIATE AND HIGH W_s	159
FIGURE 5-22. COMPARISON OF GH MICROSTRUCTURES USING JUVENILE AND MEMORY WATER. GH FORMED USING PROCEDURE I (A: SAMPLE 1, $W_s = 22\%$; B: SAMPLE 4, $W_s = 34\%$; C: SAMPLE 2, $W_s = 57\%$; SAMPLE 3, $W_s = 41\%$).....	160
FIGURE 5-23. A NEW SUGGESTED NON-CEMENTING MICROSTRUCTURAL MODEL FOR LOW-GH SATURATION.....	161
FIGURE 5-24. MICROSTRUCTURAL MODEL OF HIGHER GH CONTENT IN UNDERSATURATED SEDIMENTS.....	162
FIGURE 5-25. NEW SUGGESTED MICROSTRUCTURAL MODELS FOR LOAD-BEARING GH.	162
FIGURE 5-26. CT IMAGE (LEFT) AND CONCEPTUAL MODEL (RIGHT) FOR SEISMIC WAVE ATTENUATION IN SEDIMENTS FREE OF GH. THE WATER ACCUMULATED AT GRAIN CONTACTS ATTENUATES THE PASSING ELASTIC WAVE DUE TO SQUIRT FLOW PHENOMENON.	166
FIGURE 5-27. CT IMAGE (LEFT) AND CONCEPTUAL MODEL (RIGHT) FOR SEISMIC WAVE ATTENUATION IN SEDIMENTS WITH LOW-HYDRATE SATURATION. THE HYDRATE LAYER FORMED AT THE GAS-WATER INTERFACE INCREASES THE CONTACT AREA LEADING TO AN INCREASE OF THE WAVE ATTENUATION.....	167

FIGURE 5-28. CT IMAGE (LEFT) AND CONCEPTUAL MODEL (RIGHT) FOR SEISMIC WAVE ATTENUATION IN UNDERSATURATED SEDIMENTS WHEN ALL GRAINS ARE COVERED BY GH WITH THE PRESENCE OF AN INTERFACIAL WATER LAYER. HYDRATE STARTS TO INFILL THE PORE SPACES AND TO BECOME THE CONTINUOUS PHASE.	168
FIGURE 5-29. CT IMAGE (LEFT) AND CONCEPTUAL MODEL (RIGHT) FOR SEISMIC WAVE ATTENUATION AT HIGHLY GH SATURATED SEDIMENTS. THE FURTHER INCREASE OF THE ATTENUATION WITH THE INCREASE OF HYDRATE SATURATION IS DUE TO THE MICROSCOPIC STRUCTURE OF GH. THE CONNECTED PORES OR GH GRAIN BOUNDARIES REPRESENT FLOW PATHWAYS FOR GAS OR WATER CAUSING AN ATTENUATION OF THE WAVE VELOCITIES BY SQUIRT FLOW.	169
FIGURE 6-1. EXAMPLES OF GRAIN SIZE DISTRIBUTIONS. (A) SAMPLE ODP 204 1248C 11H-5 (100,89 MBSF). THE CRYSTALLITE SIZES APPEAR TO BE NORMALLY DISTRIBUTED WITH A MEAN SIZE OF 517 MM; SAMPLE GULF OF MEXICO, BUSH HILL, TVG 10 GH 1 (SEA FLOOR). THE CRYSTALLITE SIZES APPEAR TO BE NORMALLY DISTRIBUTED WITH A MEAN SIZE OF 301 MM. (B) SYNTHETIC METHANE HYDRATE SAMPLE. THE SIZE DISTRIBUTION IS SHAPED LIKE HALF A NORMAL DISTRIBUTION, THE MEAN GRAIN SIZE WAS GIVEN AS 43 μ M ASSUMING A LOG-NORMAL DISTRIBUTION ([KLAPP ET AL., 2007]).	171
FIGURE 6-2. BAR DIAGRAM OF THE ARITHMETIC MEAN CRYSTAL SIZES GIVEN IN TABLE 1. GEOLOGICAL LOCATIONS ARE GROUPED. THE TWO SAMPLES FROM BUSH HILL/GULF OF MEXICO ARE SII GAS HYDRATES. ERROR BARS INDICATE THE STANDARD DEVIATION (FROM [KLAPP ET AL., 2010A]).	172
FIGURE 6-3. DIFFRACTION PATTERN OF LAB_6 POWDER CALCULATED USING MERCURY SOFTWARE. THE INSERT IMAGE IS A SPOTTY DIFFRACTION PATTERN OF LAB_6	173
FIGURE 6-4. DISTRIBUTION OF THE LOGARITHM OF SIZE (VOLUME (V)) DISTRIBUTION OF LAB_6	174
FIGURE 6-5. DISTRIBUTIONS OF THE LOGARITHM OF MEASURED INTENSITIES OF LAB_6 110 REFLECTION. LEFT HAND SIDE: <i>IN-SITU</i> MEASURED LAB_6 INSIDE THE PRESSURE CELL. RIGHT HAND SIDE: <i>EX-SITU</i> MEASURED LAB_6 IN KAPTON CAPILLARY.	174
FIGURE 6-6. CALCULATED DIFFRACTION PATTERN OF Xe HYDRATE USING MERCURY SOFTWARE	175
FIGURE 6-7. A MEASURED 2D SPOTTY DIFFRACTION PATTERN OF Xe HYDRATE (RUN 4DAYS).	176
FIGURE 6-8. VARIATION OF THE TOTAL NUMBER OF PEAKS AS A FUNCTION OF THE THRESHOLD MULTIPLIER OF THE HKL 211, 222 AND 400	179
FIGURE 6-9. CSDS OF Xe HYDRATES AT DIFFERENT FORMATION TIME COLLECTED FROM THE 222 AND 400 HKL REFLECTIONS.....	181
FIGURE 6-10. EVOLUTION OF GH CSDS WITH TIME	182
FIGURE 6-11. EVOLUTION OF THE MEAN DIAMETER SIZE OF GH WITH TIME	183

List of Tables

TABLE 2-1. PROPERTIES OF XENON AND METHANE GUEST MOLECULES AND THEIR HYDRATES	12
TABLE 4-1. GRANULOMETRIC COMPOSITION OF SEDIMENTS [<i>CHUVILIN AND ISTOMIN, 2012</i>]	89
TABLE 4-2. GH FORMATION RATES AT DIFFERENT PRESSURE	97
TABLE 4-3. CHARACTERISTICS OF GH SAMPLES FOR SEM INVESTIGATIONS	101
TABLE 4-4. SPECIFICATIONS OF EQUIPMENT AND ACQUISITION PARAMETERS AT TOMCAT (<i>[STAMPANONI ET AL., 2006]</i>)	105
TABLE 4-5. RATE OF X-RAY ATTENUATION BY EACH MEDIUM.....	107
TABLE 4-6. LIST OF EXPERIMENTS/TESTS DONE DURING THE TWO BEAM TIMES IN DECEMBER 2012 AND OCTOBER 2013	108
TABLE 4-7. MEASUREMENTS PARAMETERS FOR ALL <i>EX-SITU</i> AND <i>IN-SITU</i> EXPERIMENTS.....	116
TABLE 5-1. LIST OF SAMPLES PRESENTED AND DISCUSSED IN CHAPTER 5.	137
TABLE 6-1. SCALE FACTOR S_1	175
TABLE 6-2. SCALE FACTOR S_2 FOR DIFFERENT XE HYDRATE REFLECTIONS	176
TABLE 6-3. EXEMPLARY CSD CALCULATION WITH SOME RANDOM INTENSITIES VALUES OF XE HYDRATE (SAMPLE AT 2 DAYS, REFLECTION 211).....	178
TABLE 6-4. SUMMARY OF STATISTICAL PARAMETERS.....	182

1 | Introduction

The detection and quantification of gas hydrate (GH) present in marine sediments is crucial for safe oil and gas extraction, seafloor stability assessments and for quantifying the impact of GH in climatic change. Information on GH saturation in sediments can be obtained from the measurements of seismic velocities during seismic survey, drilling or well-logging data and from electric measurements. However, the analysis and interpretation of these data require information on the physical properties of the host sediments which itself depend on the microstructural characteristics of the hydrate phase such as the spatial distribution, size of crystallites and the nature of GH-sediment interaction which are not known a priori. The puzzling observation of a concomitant occurrence of high seismic velocity and high seismic attenuation in sediments containing GH called “seismic anomalies” are linked to the microstructure. Hence, there is a considerable interest in studying the microstructure of GH-bearing sediments and to constrain estimates of their physical properties.

1.1. Background

Gas hydrates (GH), called also clathrates, are crystalline inclusion compounds composed of a hydrogen-bonded water network (host) that enclose small gas molecules (guests) within cages. Hydrocarbons (e.g. methane, ethane) and noble gases (e.g. xenon, argon) are typical hydrate-forming gases *Sloan and Koh* [2008]. GHs are stable under appropriate conditions of low temperatures and/or high pressures.

Since their discovery in 1810 by the British scientist H. Davy [*Davy*, 1810], the research on GH has experienced three stages. Hydrates remained laboratory curiosities during the first stage from 1810 to the early 1930: scientists were interested in studying the different components forming GH, the stoichiometry and thermodynamic conditions. In 1930s, the discovery that hydrate formation can lead to the blockage of natural gas transmission pipelines causing big problems for the natural gas industry [*Hammerschmidt*, 1934] moved the research into a more applied direction. Studies on physical structure and the thermodynamic properties of GH were carried out in order to understand the formation process and to provide possible solutions to remove GH or inhibit hydrate formation under industrial conditions. This research was achieved with the aid of modern characterization tools such as nuclear magnetic resonance, X-ray diffraction and other microscopic methods. From the late 1960s to present, the research was more and more directed to GHs in natural environments. Various types of natural gas hydrates (NGH), their physical properties and formation conditions were studied. NGHs were localized in marine and deep lake sediments and below permafrost. As methane was found to be the most naturally occurring hydrate-forming gas, GHs are considered as a future energy resource [*Collett and Kuuskraa*, 1998; *Makogon*, 1997]. Only sandy and partially saturated GH bearing-sediments are considered to be promising for extraction. In addition, GHs could represent an option

for CO₂ sequestration (House et al., 2006; Kwon et al., 2008; Lee et al., 2002; White, 2008). There is also a link between the climate change and the stability of GH deposits. Arctic methane emissions released from GH dissociation causes an increase of climate warming [Ruppel and Noserale, 2012]. For these reasons, an understanding of the formation mechanism, microstructure and physical properties of GH-bearing sediments is required.

1.2. Motivation

The quantification of GH concentrated in sediments represents a central task for geophysical exploration. Hydrate-bearing sediments exhibit high seismic wave velocities, and therefore GH saturation can be estimated from a predictive model which relates the hydrate saturation to the seismic velocity. The ultimate goal is to establish a reliable model which relates the acoustic properties of GH and their microstructure in porous media taking into account the evolution of the microstructure as a function of the GH saturation. The difficulty of preserving the microstructure of NGH samples intact at *in-situ* conditions has been one of the key challenges in studying NGH samples. So far, the analysis of measurements from geophysical exploration methods in GH bearing-sediments was limited due to the insufficient quality of data on physical properties. It appeared that a reliable determination of the hydrate saturation, only from these measurements, is not possible without specifications of the microstructure and it is necessary to validate the elastic models with data obtained from experimental laboratory studies (see Figure 1-1).

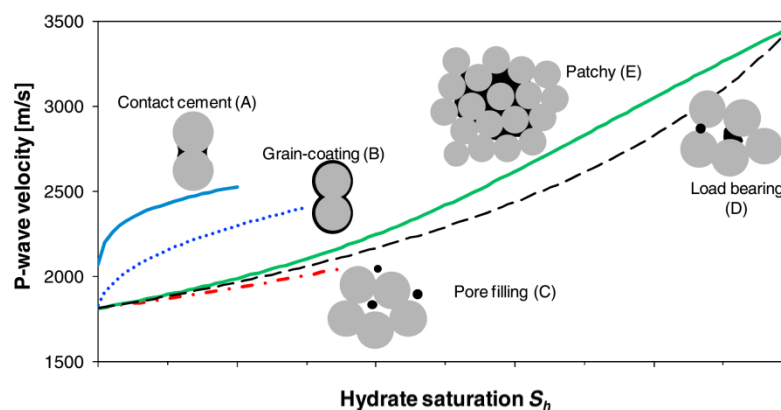


Figure 1-1. Dependence of the wave velocity as a function of GH saturation on the microstructural model chosen (from Dai et al. [2012]).

Therefore, due to these difficulties a number of researchers attempted to study the formation of GH in sedimentary matrices, in particular to reveal the physical properties of these aggregates to support geophysical exploration methods [Berge et al., 1999; Best et al., 2010; Best et al., 2013; Carcione and Gei, 2004; Dai et al., 2004; Dai et al., 2012; Dvorkin et al., 2003; Dvorkin et al., 2000; Priest et al., 2005; 2006; Yun et al., 2005; Zhang et al., 2011]. Unfortunately, all these efforts devoted primarily to study the physical properties and did not give access to the microstructure of the aggregates investigated, in any case not with sufficient resolution to look at details of the sediment-GH

contact. Accordingly, discrepancies between measured and theoretical model's values of wave velocities remain.

Experimental studies on synthetic GH in porous media were conducted in custom designed low temperature/high pressure devices with the aid of different characterization methods such as optical microscopy [Tohidi *et al.*, 2001], Nuclear Magnetic Resonance Imaging (MRI) [Bagherzadeh *et al.*, 2011; Baldwin *et al.*, 2003; Mork *et al.*, 2000; Zhao *et al.*, 2011] and micro-Computed X-ray Tomography (μ -CT) [Jin *et al.*, 2004; Jin *et al.*, 2006; Kerkar *et al.*, 2009; Kerkar *et al.*, 2014; Kneafsey *et al.*, 2007]. MRI can permit to observe the spatial distribution of the hydrate phase and to characterize the porosity but not with sufficient resolution to investigate the nature of GH-sediment interaction. In recent years, μ -CT has become a standard tool to characterize GH-bearing sediment cores. This method offers the advantage to be non-destructive and to reveal interior features of a broad kind of materials. Unfortunately, the spatial resolution of the used laboratory CT techniques was also insufficient.

At the same time, the use of tetrahydrofuran (THF) as proxy for methane, which require specific high pressure equipment and long formation time from several weeks to months, may lead to results that may not reflect the real situation in natural environments. Although, THF and methane hydrates have similar physical properties, THF is completely miscible with water and form a different structure; hence difference in the microstructure cannot be excluded.

Only a limited number of studies considered to investigate the role of clay minerals in the formation of GH in sediments and their impact on the acoustic properties of the host sediments. There are some clear indications that the presence of bentonite and montmorillonite can promote the formation of GH and that under certain conditions GH can even form intercalates with clay particles, with unknown consequences for the seismic response.

On the other hand, several visual and computer simulation studies have reported that GHs do not show a pronounced affinity to sediment grain's surface and that a liquid water layer may remain between GH and quartz grains. The understanding of the type of GH-sediment interaction may be the key to explain the observed seismic anomalies [Chand, 2008] of high seismic velocity and high seismic attenuation in GH-bearing sediments. However, a clear observation of a water layer of few μ m was not possible with the limited resolution of the methods employed so far.

1.3. Objectives and approaches

During this DFG-funded project (Ku 920/18), we are aiming to overcome the above described limitations in order to answer the following research questions:

- Where does GH in porous media start to form and how do GHs evolve during growth?
- Which growth mechanism is governing the final morphology of GH?
- What is the influence of the starting conditions such as the water saturation, porosity, etc. on the final microstructure?
- How is the contact between GH and sediment grains? Whether or not a water layer between GH and sediment grains remains?
- What is the role that may play clay minerals in the growth mechanism of GH?

- And what is the influence of the surface properties of the host sediments on the nucleation and growth processes?

To achieve the above mentioned objectives, Synchrotron micro-X-ray Computed Tomography (SMXRCT) which provides a full volumetric (three dimensional) information of the medium (quartz matrix), hydrate and the fluid (water and gas) phase distribution at sub-micron pixel size resolution was used to investigate *in-situ* the evolution of GH microstructure in various sedimentary matrices. With such resolution, we will be able to study the details of the microstructure such as the nature of GH-sediment contact.

For that, a pressure cell was designed and constructed to permit the formation in the beam of GH. In order to enhance the contrast between GH, sediment grains, and fluid phase as well as to reduce required formation pressure we replace methane with xenon gas. Xenon is likely to be a better proxy for methane than THF. Methane and xenon have both low solubility in water and form the same type of hydrate structure. A comparison of the properties of xenon and methane molecules and their hydrates is given in Chapter 2.

By controlling the kinetics of the reaction, we were able to visually follow the formation process of GH with time from the first steps of nucleation till the end of the growth process and the completion of GH formation.

During several experiments, we investigated:

- The nucleation and growth processes of GH in various sedimentary matrices
- The influence of the formation method and the starting conditions such as the water content on the microstructure.
- The effect of clay minerals (kaolinite and montmorillonite) on the formation mechanism of GH.
- The effect of the type of porous media and their surface properties on the microstructure. For that, natural quartz sand and synthetic quartz beads were used plain and with further (hydrophilic and hydrophobic) surface treatment.

The observations of the microstructure of GH in sediments were complemented by a quantitative study of the evolution of the Crystallites Size Distributions (CSDs) of GH. The CSDs carry information about the formation mechanism and coarsening process. Furthermore, a long term goal is the attempt to estimate the age of NGH by the determination of the growth constants from CSD measurements. Therefore, a new method for the determination of CSD of polycrystalline materials and powder based on Two-Dimensional X-ray Diffraction (2D-XRD) was developed. This method was applied to study *in-situ* the formation of xenon hydrate.

1.4. Organization of the thesis

The thesis is organized in 7 chapters:

Chapter 2 provides an overview of general GH properties and discusses the most relevant literature on GH formation in porous media and the relationship between the hydrate microstructure and the physical properties

Chapter 3 gives the reader the basic knowledge on the experimental methods used in this study.

In **Chapter 4** all materials, instruments and experimental setups used for the formation and characterization of gas hydrate-bearing sediments are described.

Chapter 5 presents first the results from the direct observations of the gas hydrate microstructure using X-ray tomography and discusses the influence of the observed microstructure on the physical properties. A possible explanation of the so-called "seismic anomalies" based on new developed conceptual models is given.

Chapter 6 shows the results of the evolution of the crystallite size distributions of xenon hydrate with time.

Chapter 7 summarizes the conclusions of this study and gives an outlook for future research.

The **Appendices** provide supplementary information to support the PhD thesis.

A substantial part of this PhD work has been accepted recently as publication in G-cubed (American Geophysical Union) journal in Mai 2015 (see Appendix E).

2 | Gas Hydrates

The following chapter provides an overview of GHs research with a focus on the hydrate structure, phase behavior, formation mechanisms and physical properties of hydrate bearing sediments and gives the reader the theoretical background required for better understanding the thesis. The reader may refer to the book of [Sloan and Koh, 2008] or [Makogon, 1997] for more detailed information about GHs.

2.1. Gas hydrates properties

2.1.1. Composition and structures

Gas hydrates belong to a large family of crystalline inclusion compounds known as clathrates, which are composed from a host water lattice forming relatively large cavities that includes non-polar guest gas molecules with low molecular weight (see Figure 2-1). GHs are non-stoichiometric i.e. empty cages exist in the structure. The structure of GH is similar to the hexagonal ice Ih in that water molecules are structured through hydrogen bonding. A sufficient amount of gas molecules surrounding the hydrate is essential for the formation and stability of GHs.

GHs have a crystalline structure and are divided into three predominant types: cubic structure I (sI), cubic structure II (sII), and hexagonal structure H (sH). The difference between these structures consists in the number and sizes of cages. Five types of cages are dominant [Makogon, 1997; Sloan and Koh, 2008]:

- Pentagonal dodecahedron (5^{12}) is the smallest cage formed by twelve five-sided polygons, which makes it almost spherical. It occurs in all three crystal structures (sI, sII, and sH).
- Tetrakaidecahedron ($5^{12}6^2$) is a larger cage formed by adding two hexagonal faces to the small cage. It exists in sI as a large cage and plays a main stabilization role.
- Hexakaidehedron ($5^{12}6^4$) is constructed from twelve polygons and 6 hexagonal faces. It occurs in sII as a large cage. It can encage large gas molecules such as propane.
- Irregular Dodecahedron ($4^35^66^3$) is a medium sized cavity in sH with three square, six pentagonal and three hexagonal faces.
- Irregular Icosahedron ($5^{12}6^8$) is the biggest cavity. It exists in sH and is shaped with twelve pentagons and eight hexagons as faces. With its large radius (5.17 Å), it can encase big molecules like methylocyclohexane.

Figure 2-1 depicts the five cages of all three clathrates.

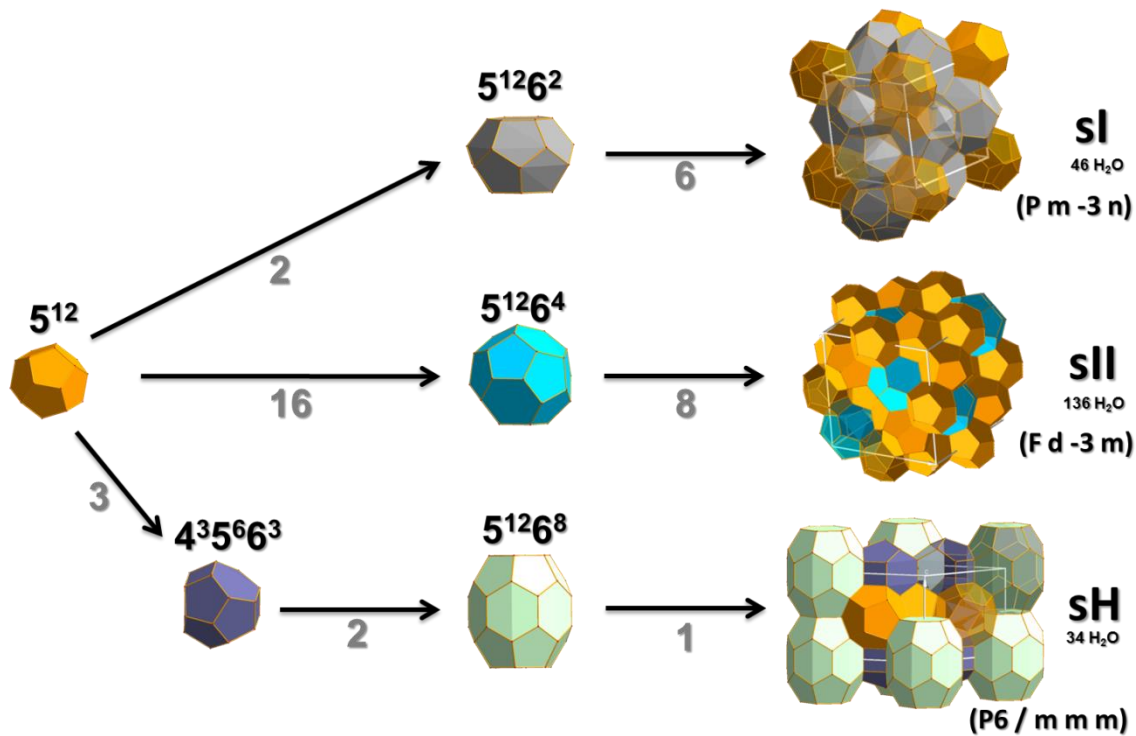


Figure 2-1. Cage types forming the three common hydrate structures. The numbers below the arrows denote the numbers of cages used to form the hydrate structure (Design provided by A. Falenty).

The sI is the most frequent structure occurring in nature. It has a cubic structure (space group Pm-3n) with a unit cell composed of 8 cages: two small (5¹²) and six large cavities (5¹²6²). Within each unit cell, 8 guest molecules are associated with 46 water molecules. The sI structure can only hold small gas molecules such as CO₂, H₂S, ethane or methane. The latter is considered as the most common guest molecule in naturally occurring GH. The sII structure has also a cubic crystal structure with different space group (Fd-3m). It can accommodate small but also larger molecules such as propane or isobutane. The unit cell of sII consists of 24 cages: 16 small cavities (5¹²) and 8 large cages (5¹²6⁴), which contain 136 water molecules. The sH clathrate is hexagonal (space group P6/mmm). Its unit cell is formed by 34 water molecules and composed of 1 large cavity (5¹²6⁸), 2 medium-sized (4³5⁶6³), and 3 small cages (5¹²) associated with 34 water molecules. The large cage can hold molecules with bigger diameters (7.1 - 9 Å).

2.1.2. Density of gas hydrate

The hydrate density depends mainly on the gas composition and the degree of filling of cavities. By knowing the dimensions of the unit cell, the number of water molecules and the number of small and large cavities per unit crystal, the GH density (ρ) may be calculated using this equation [Sloan and Koh, 2008]:

$$\rho = \frac{N_w M_w + \sum_c N_c M_c}{V_{\text{cell}}} \quad (2.1)$$

where:

N_w = number of water molecules per unit cell

M_w = molecular weight of water

M_c = molecular weight of component c

N_c = number of components in hydrate phase

N_c may be determined by this formula:

$$N_c = \sum \theta_i N_i \quad (2.2)$$

where θ_i is the fractional occupation of cavity i and N_i is the number of type i cavities in unit cell.

The densities of methane and xenon hydrate are given in Table 2-1.

2.1.3. Stability and phase boundaries

The stability of GH depends on the pressure, temperature and composition of gas and water phases. In nature, GHs occur in permafrost regions and in marine and deep lake sediments where the suitable pressure-temperature conditions naturally exist. In marine sediments, methane, produced by biogenic activity, is the most common hydrate-forming gas. Figure 2-2 shows a phase diagram of methane hydrate in geologic conditions for marine sediments. The phase diagram is a plot of depth against temperature:

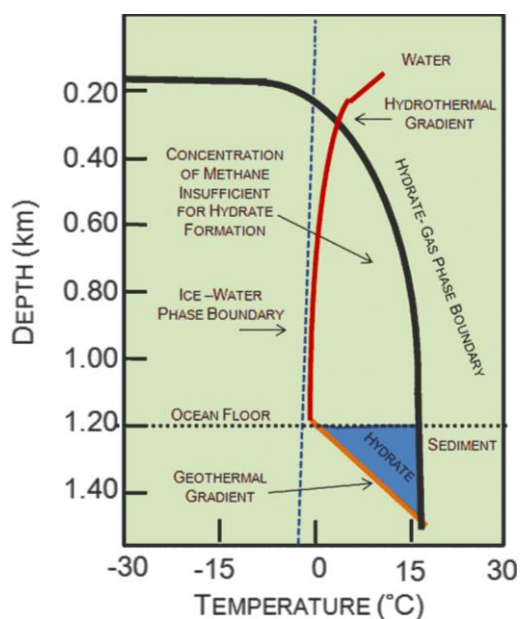


Figure 2-2. Schematic of depth versus temperature for methane hydrate formation in marine sediments [Harrison, 2010].

In permafrost regions, the GHSZ can start at 0.1 - 0.3 Km and extend for hundreds meters below the depth of permafrost.

The phase diagram of pure methane hydrate as drawn by *Kvenvolden* [1993] is illustrated in Figure 2-3. The curving solid line is a diagrammatic PT phase boundary between GH and the different phases. At this line, the different phases are in equilibrium. GH is not stable to the right of this line. To the left, the conditions are suitable to form a stable GH phase from water and enough gas.

- The red line represents the water temperature curve called hydrothermal gradient and shows the variation of temperature with increasing depth to close to 0°C at the ocean floor;

- descending deeper through the sediment, the heat emanating from the Earth's core increases the temperature (geothermal gradient - orange line);

- the black line represents the methane stability phase boundary;

- due to the hydrothermal gradient, the water close to the sediment surface is cooler by 15 °C and the methane gas which percolates up through the sediments will form spontaneously methane hydrate (zone in blue).

The region where GHs are stable – GH stability zone (GHSZ) – is defined by the intersection of the local geothermal gradient and GH phase boundary. In

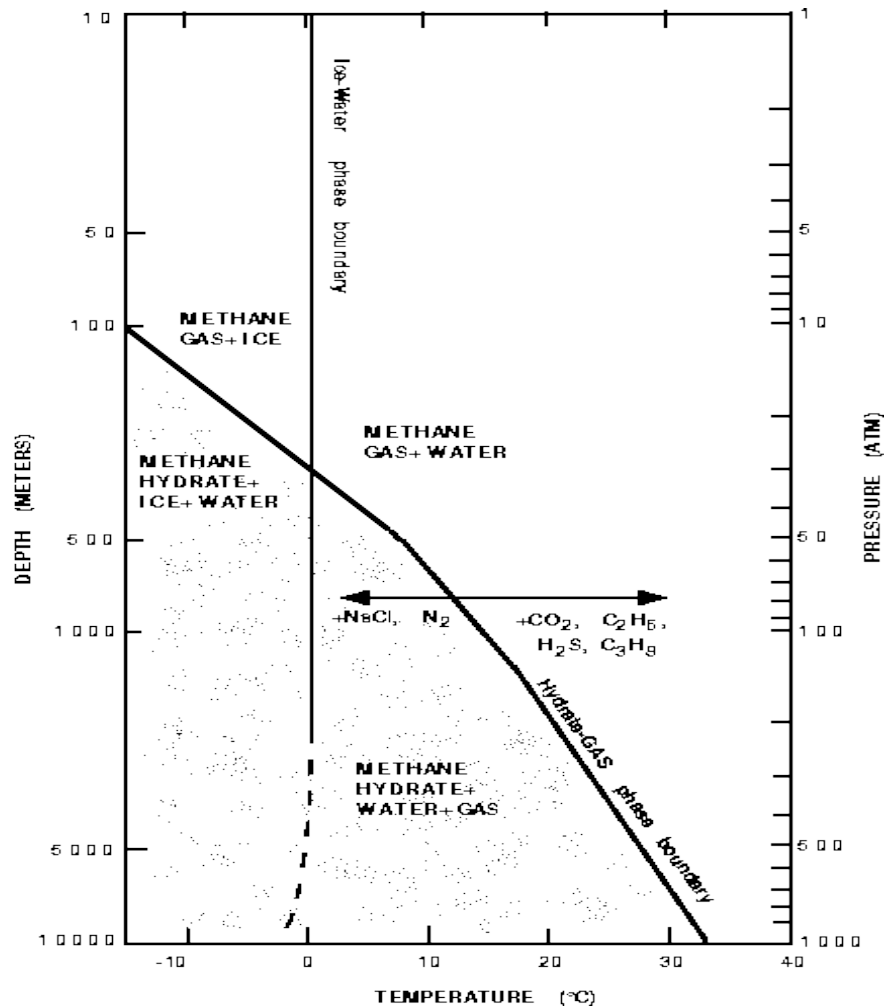
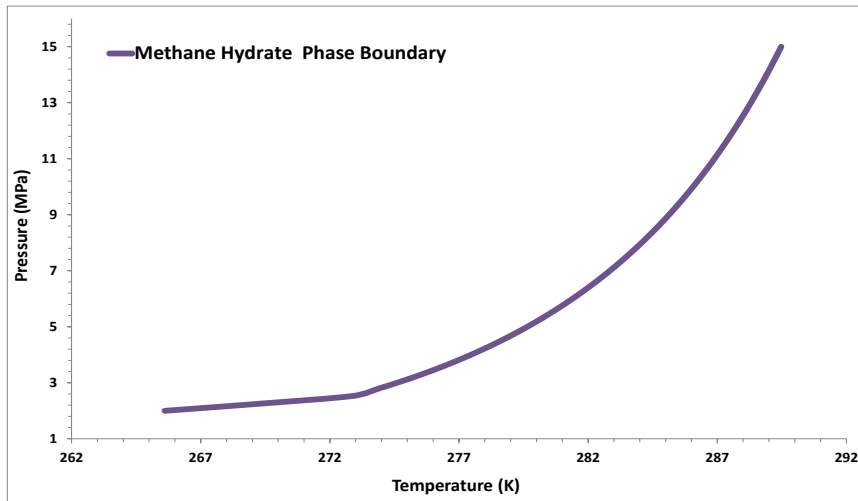
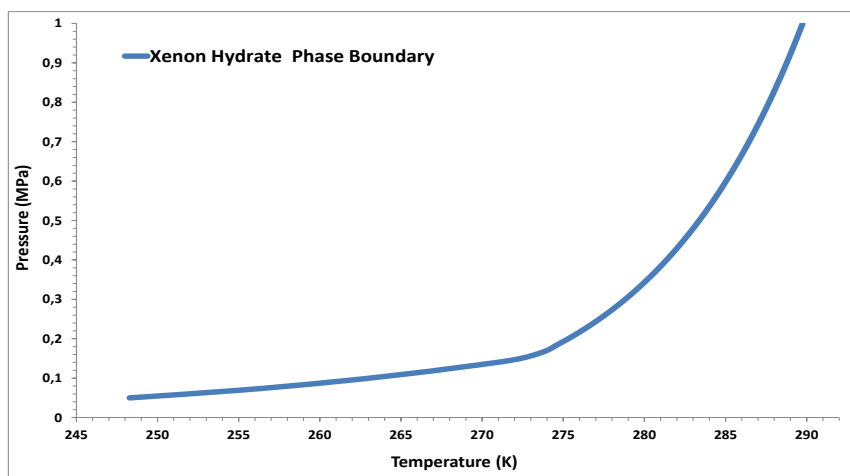


Figure 2-3. Phase diagram showing the boundary between methane gas (no pattern) and methane hydrate (pattern) for a pure water and pure methane hydrate system (from *Kvenvolden* [1993]).

The position of the stability boundary (curving solid line) of GH is determined by the gas composition [*Sloan and Koh*, 2008], the ionic strength of water [*De Roo et al.*, 1983], capillarity forces [*Clennell et al.*, 1999] and sediment mineralogy [*Cha et al.*, 1988]. At a given pressure, the stability boundary of methane hydrate can be shifted to the left (lower temperatures) in the presence of salts like NaCl. Thus the increase in salinity of water inhibits the formation and stability of GH. However, the presence of CO₂ or H₂S increases the stability of methane hydrate by shifting the boundary to higher temperatures. There are several computed-based methods for predicting the pressure-temperature conditions for GH stability. The commonly used method based on minimizing the Gibbs-free energy of the system is the CSMGem program developed by *Sloan and Koh* [2008] which allows the calculation of GH stability at different water and gas composition at a given pressure or temperature. The phase diagrams for methane and xenon hydrate determined using CSMGem are shown in Figure 2-4.



(a)



(b)

Figure 2-4. Phase diagram of methane hydrate (a) and xenon hydrate (b) as determined using CSMGem program.

At the same temperature, the formation of methane hydrate requires higher pressure than xenon hydrate. For example, at $T = 276 \text{ K}$, $P_{\text{CH}_4} = 3.5 \text{ MPa}$ and $P_{\text{Xe}} = 0.2 \text{ MPa}$.

2.1.4. Solubility of GH forming gases in water

Nonpolar gases such as methane have very low solubility in water. The formation of GH requires the presence of enough gas in the surrounding water under suitable P/T conditions. The solubility of gases in liquid water depends on pressure and temperature. The presence of GH also affects the solubility of methane in water; in the absence of a hydrate phase, the solubility increases with increase of pressure and methane has preference to exist in water rather than in the gas phase [Servio and Englezos, 2001]. The concentration of methane in water decreases as the temperature increases. High temperature allows molecules to break intermolecular bonds in water and to move in the gas phase. In the presence of GH, a small decrease in the solubility of methane is observed when the pressure rises because methane has a preference to exist in the GH phase than in the liquid water [Lu et al., 2008]. The increase in temperature boosts methane from solid hydrate to move to the water leading to an increase in the increase in water's methane concentration and therefore reduces the

solubility. Several studies have demonstrated that the presence of salts in the solution reduces the solubility of gases in water in the presence or in the absence of a hydrate phase [Davie *et al.*, 2004; Tishchenko *et al.*, 2005; Zatsepina and Buffett, 1997].

Henry's law allows the description of the quantity of gas that can be dissolved in water as a function of temperature and pressure. Henry's Law states that the amount of gas dissolved in water at a given temperature is proportional to the partial pressure of the gas (Equation 2.3):

$$M_p = k_H^{\circ} P_{app} \quad (2.3)$$

where M_p is the concentration of gas in solution (mol/L), k_H° is the Henry's Law constant at 298 K (M/atm) and P_{app} is the system pressure. The solubility of gas increases with increase of pressure, while it decreases as the temperature increases. The solubility diagrams of methane and xenon gases in water at different temperatures and for a partial pressure of the gas of 0.1 MPa are plotted in Figure 2-5. The solubility was calculated using the equations provided by *Gevantman* [2005].

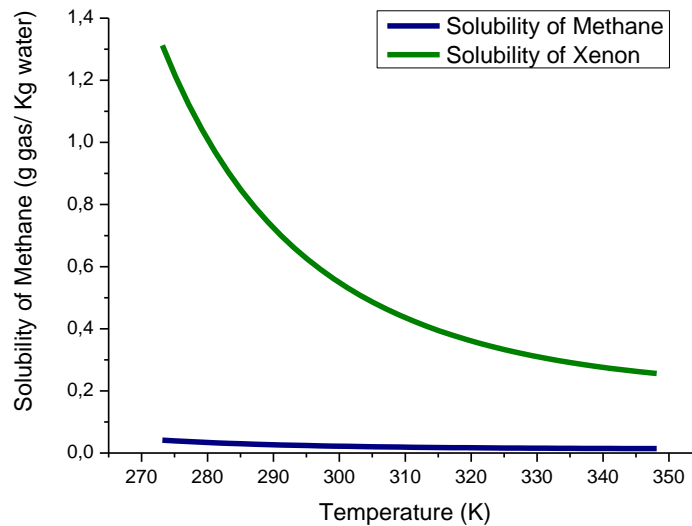


Figure 2-5. Solubility diagrams of CH_4 and Xe gases in water as a function of temperature

The solubility of xenon is higher than that of methane at the same temperature by one order of magnitude. Nonetheless, xenon gas is still a nonpolar gas and low soluble in water, hence similar growth pattern are expected for both methane and xenon hydrate.

2.1.5. Comparison between methane and xenon

Xenon is used in our experiments to replace methane gas in order to get better image contrast between water, gas and hydrate phases. Table 2-1 presents a comparison between the properties of xenon and methane guest molecules and their hydrates.

Table 2-1. Properties of xenon and methane guest molecules and their hydrates

	Methane	Xenon	Reference
Guest molecules			
Molecular size (Å)	4.36	4.58	[Sloan and Koh, 2008]
Dipole moment (D)	0.0	0.0	[Lide, 2005]
Permittivity at 293 K	1.0081	1.0017	[Lide, 2005]
Density (kg m ⁻³) at 276 K and 0.1 MPa	0.707	5.760	NIST
Viscosity (Pa.s) at 300K	11.2 × 10 ⁻⁶	23.2 × 10 ⁻⁶	[Lide, 2005]
Solubility in water (K) at 276 K (mg L ⁻¹)	4.26 × 10 ⁻⁵	16 × 10 ⁻⁵	[Lide, 2005]
Diffusion coeff. in water at 283K (cm ² s ⁻¹)	1.24 × 10 ⁻⁵	0.93 × 10 ⁻⁵	[Lide, 2005]
Thermal conductivity (W/mK) at 300 K	7.5 × 10 ⁻³	5.5 × 10 ⁻³	[Lide, 2005]
Linear attenuation coeff. (μ) at 22 keV (cm ⁻¹) at equilibrium	0.01	0.276	[Seltzer and Hubbell, 1996]
Hydrate structures			
Hydrate structure	sl	sl	[Sloan and Koh, 2008]
Lattice constant at 276K (Å)	11.970	11.984	[Hansen et al., 2015]
Cage diameter (Å)	5.09-5.86	5.1-5.85	[Sloan and Koh, 2008]
Stoichiometric ratio at 276 K	CH ₄ × 5.94 H ₂ O	Xe × 6.04 H ₂ O	[Sloan and Koh, 2008]
Stability pressure (MPa) at 276 K	3.5	0.207	[Sloan and Koh, 2008]
Density (kg m ⁻³) at equilibrium	982	1804	[Sloan and Koh, 2008]
Thermal conductivity (mW/mK)	0.45 at 213 K	0.36 at 245 K	[Handa and Cook, 1987]
Linear att. coeff. (μ) at 22 keV (cm ⁻¹) at equilibrium	0.661	22.79	[Seltzer and Hubbell, 1996]
Water			
Density (kg m ⁻³) at 276 K and 0.1 MPa	999.96		[Lide, 2005]
Linear att. coeff. (μ) of water at 22 keV (cm ⁻¹) at 276 K	0.723		[Seltzer and Hubbell, 1996]
Linear att. coeff. (μ) of water solution saturated with methane ¹ at 22 keV (cm ⁻¹)	0.723		[Seltzer and Hubbell, 1996]
Linear att. coeff. (μ) of water solution saturated with xenon ² at 22 keV (cm ⁻¹)	0.750		[Seltzer and Hubbell, 1996]

- The densities of methane, xenon and water were obtained from: <http://webbook.nist.gov/chemistry/fluid/>
- The linear attenuation coefficients (μ) were calculated from the elemental mass attenuation coefficients obtained from [Seltzer and Hubbell, 1996] using the following equation: $\mu/\rho = \sum_i w_i(\mu/\rho)_i$
- The linear attenuation coefficients for xenon and methane gases and their hydrates were calculated at the equilibrium conditions for $T = 276$ K: $P_{\text{CH}_4} = 3.5$ MPa and $P_{\text{Xe}} = 0.207$ MPa as the CT scans were done at these conditions.
- The density of GH was calculated using the equation (2.1). The cage filling and stoichiometric ratio needed to calculate the density were determined using the CSMGem program [Sloan and Koh, 2008] at equilibrium conditions.
- ¹ Water solution containing 37.8 mg L^{-1} of methane.
- ² Water solution containing $1167.04 \text{ mg L}^{-1}$ of xenon.

Table 2-1 shows that xenon and methane have in general similar properties. However there are some differences which may affect the process of formation. The solubility of xenon and methane in water differ by a factor of 4 which may have some implications on the kinetics of GH formation. While xenon is more soluble than methane in water, methane can diffuse faster than xenon. The formation process from juvenile (fresh) water may not be affected as the formation from water memory water or water obtained from GH dissociation. Both molecules form structure I hydrate and have similar crystal properties. Although there are some differences between the guest gases and their hydrates, xenon is a good substitute of methane as it has higher contrast density and comparable hydrate properties which permit to expect similar growth patterns.

2.2. Formation of gas hydrates

2.2.1. Mechanisms of GH formation

GHs can form where enough water and hydrate former species are available within the hydrate stability zone of pressure and temperature. The understanding of GH formation mechanisms is based on the thermodynamic behavior of GH systems.

The nucleation process describes the birth of new crystalline entities from the bulk fluids called nuclei. The nucleation is a stochastic process which occurs spontaneously when suitable conditions of high pressure and/or low temperature exist. The system tends to lower this energy by forming a new stable hydrate phase. This energy called driving force is important because small GH clusters are unstable toward dissolution until they reach a sufficient large size or critical size. In the classical nucleation theory, the driving force may be expressed as a supersaturation ($\Delta\mu$) which is defined as the difference in chemical potential between the old and the new phase [Kashchiev and Firoozabadi, 2002]:

$$\Delta\mu = (\mu_g + n_w\mu_w) - \mu_h \quad (2.4)$$

where n_w is the number of water molecules and μ_g , μ_w , and μ_h , are the chemical potential of gas, water and the hydrate phase respectively. The chemical potential gives an idea about the stability of a compound. The stable phase is the one which has the lowest μ value.

The nucleation can be homogenous or heterogeneous. The homogenous nucleation may occur spontaneously from clean solutions. This type of crystallization is difficult to achieve because it requires extreme conditions and high supersaturation [Kashchiev and Firoozabadi, 2003; Kashchiev and van Rosmalen, 2003]. On the other hand, the heterogeneous nucleation requires the presence of impurities to initiate the formation of the first nuclei. The foreign substrate or impurity can promote the nucleation by protecting the crystal from dissolution and therefore the required driving force is reduced. In nature, the heterogeneous nucleation of GH is the most occurring process, while the homogenous nucleation is possible only at extreme ocean depths. In contrast to primary nucleation, secondary nucleation is induced by the presence of already growing crystals in the solution [Max et al., 2006].

The crystallization process of GH is characterized by an initial incubation period. This delay called also "induction time" is the period of time which elapses between the achievement of a supersaturated solution and the appearance of first crystals. The induction period is influenced by the driving force, state of agitation, history of starting material, presence of impurities, etc.

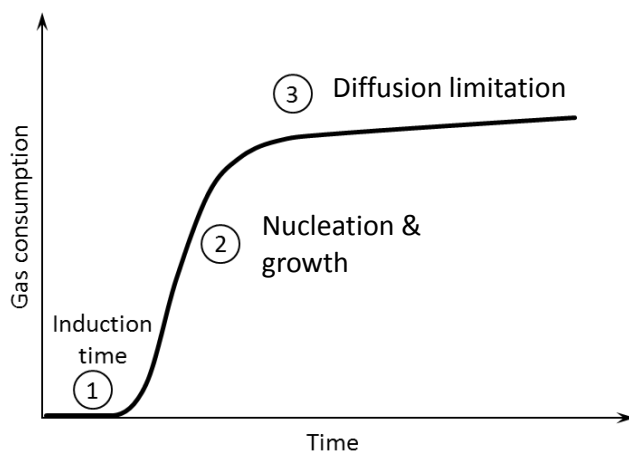


Figure 2-6. Formation curve of GH from aqueous system. Initial delay indicates the induction time. The second part shows a rapid nucleation and growth process. The reaction becomes slower due to mass transfer limitation of gas and water (modified after Sloan and Koh [2008]).

rate.

The induction time is followed by a fast initial growth. The rate of growth is depending on the transfer flux of gas and water. Therefore the formation is faster at the interface between the gas and

The growth mechanism has attracted less interest by the GH research community. The growth follows the formation of critical nuclei. As for nucleation, the growth requires also a driving force. The growth can be considered as a combination of mass transfer of water and/or gas and growth at the hydrate surface [Sloan and Koh, 2008]. It is important to understand the mechanism of growth because it can influence the final morphology (size and shape of crystals) of GH. In this work, only the growth of GH in porous media is considered (section 2.3.1). The typical curve of GH formation is shown in Figure 2-6. The rate of formation is usually expressed in terms of gas consumption

water phases [Makogon, 1997]. When the hydrate layer gets thicker, a slowdown in the formation rate is observed due to diffusion limitation [Barrer and Ruzicka, 1962].

2.2.2. Driving forces for GH formation

The formation of GH requires a driving force. Different driving forces for nucleation and growth used by the hydrate community can be found in literature [Sloan and Koh, 2008]. Mullin [2001] defines the driving force as supersaturation which may be expressed as the difference in chemical potentials between the old and new phases [Kashchiev and Firoozabadi, 2002].

The subcooling (ΔT_{sub}) was used by Vysniauskas and Bishnoi [1983] as driving force for nucleation and growth. It is defined as the difference between the temperature at equilibrium and the measured experimental temperature at the experimental pressure ($T^{\text{eq}} - T^{\text{exp}}$). By measuring the experimental temperature and knowing the hydrate equilibrium temperature, the subcooling can be easily determined.

Englezos *et al.* [1987] defined the driving force as the difference in fugacity of the gas phase at the experimental temperature and pressure and the fugacity of the guest molecule in the hydrate phase at the experimental temperature and corresponding equilibrium pressure. Similarly, Natarajan [1993] used $(f_i^{\text{exp}} / f_i^{\text{eq}} - 1)$ as driving force.

Christiansen and Sloan [1995] used the total molar change in Gibbs free energy of hydrate formation, Δg^{exp} as the driving force. It has been shown that this driving force represents the general case of all driving forces. In general, processes tend to minimize the Gibbs free energy of the system.

Skovborg *et al.* [1993] expressed the driving force as the difference in gas mole fraction at the gas-water interface and in the water phase. They reported that the formation is controlled by the mass transfer and therefore the driving force is not related to the equilibrium curve. Herri *et al.* [1999] also used the difference in the gas concentration at the gas-water interface and in the bulk water. The solubility of the hydrate former in water determines the driving force.

In our experiments, the effect of driving forces on the formation process of GH in porous media was not the goal of this study and the formation was done at constant temperature and similar pressure driving forces.

2.2.3. Nucleation and initial growth

The nucleation is the most challenging step in understanding the formation mechanism of GH. The final microstructure of GH depends on where GH starts to nucleation and on the growth pattern. Thus, studying the nucleation of GH crystals and their morphology can provide valuable information on the mechanisms of formation, decomposition and to some extent inhibition.

In general, due to the low solubility and slow diffusion rate of the most hydrate-forming gases, the nucleation starts at the interface between the water and guest fluids where the concentration of both constituents is the highest. Chaplin [2008] reported that within 250 nm of the water interface, gas molecules will bond to nano-sized clusters of water due to Van der Waals interactions. The growth requires a high amount of gas which cannot be found dissolved in water. Furthermore, results from molecular dynamic simulations support this as well; Stewart and Westacott [2008] revealed that the

structure of water at the interface is more tetrahedral and more clathrate-like making it more amenable for hydrate formation. Experimental studies have also demonstrated that the preferred nucleation site is at the hydrate former-water interface. *Boewer et al.* [2012] investigated the structure at water-guest interfaces using X-ray reflectivity and reported that the presence of a nanothick supersaturated guest layer at the interface between water and guest phases serves as a trigger for a spontaneous hydrate formation (see Figure 2-7).

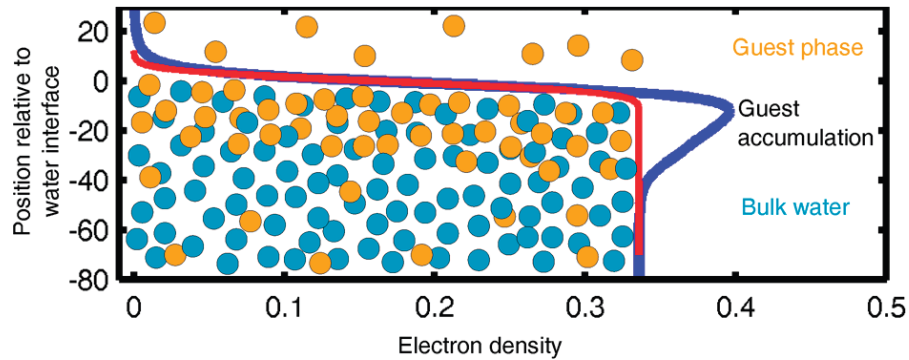


Figure 2-7. Electron density and schematic view of the guest-enriched surface layer ([*Boewer et al.*, 2012]).

The number of visual studies on the crystallization and growth of GH formation at water-hydrate former interfaces has increased in the last years due to technological advances in microscopic tools. These studies treated all possible cases of GH formation at the guest former-water interface such as water droplets exposed to a gaseous phase, bulk water phase in contact with bulk guest gas phase and gas bubbles suspended in water phase have recently appeared in the literature. Several factors affecting the hydrate formation were studied including the effect of gas composition, driving forces and “memory effect” (see section 2.3.2.3).

As most hydrate-forming gases have low solubility in water, bubbling was used in the lab as a method to disperse hydrate forming gas in liquid water in order to increase the active surface area and to promote the hydrate formation. This type of GH formation may occur in natural environment in regions where thermogenic hydrocarbon gases rise from deep subsurface to the sea floor. *Topham* [1978] observed the hydrate formation on natural gas bubbles released at sea depths 640 and 325 m in a simulated deep-sea environment. He reported that GH formed within seconds at the gas-water interfaces. The formation of GH on bubbles of fluorocarbon was studied by *Sugaya and Mori* [1996a]. They observed that tiny hydrate particles were first randomly formed on the surface of each bubble then proceeded until a fully hydrate layer covered the entire bubble.

Recently, *Li et al.* [2014] studied the kinetics and morphologies of the hydrate film growth on gas bubbles exposed to water using various hydrate-forming gases and at different degree of subcooling. They reported that the rate of the film growth and the GH crystals morphology depends on the gas composition and the driving force (see Figure 2-8).

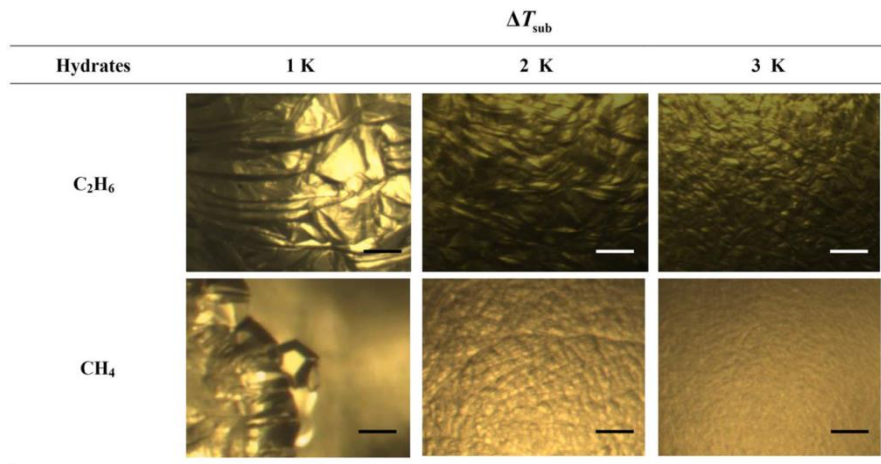


Figure 2-8. Hydrate film morphologies for methane and ethane gas at different ΔT_{sub} (modified after [Li *et al.*, 2014])

The formation at the surface of water droplets immersed in a gaseous phase was also considered by the GH research community. *Servio and Englezos* [2003] observed by optical microscopy the initial growth of GH on water droplets with two different sizes (2.5 and 5 mm) placed on a hydrophobic surface and exposed to gaseous CH_4 and CO_2 . The effects of the size of the water droplets, pressure driving force and memory effect upon the nucleation and morphology of crystals were investigated. They reported that the crystallization of GH began at the water droplet's surface for both CH_4 and CO_2 . However, the reaction started within a shorter induction time when using CO_2 than for CH_4 due to the higher solubility of CO_2 in water. The size of water droplets and the type of hydrate former had no significant influence on the morphology of GH crystals.

On the other hand, the driving force has notably influenced the crystal morphology. Under high pressure driving force, *Servio and Englezos* [2003] observed that the nucleation started at different locations and that within 5s after nucleation, the surface of the water droplet became jagged with many fine needle-like crystals extruding away from the gas-water interface (see Figure 2-9). In contrast, under low driving force, GH crystallizes in more regular manner and location. A smoother surface with no evidence of needle-like crystals was observed (see Figure 2-10). This difference in morphology observed was explained by the fact that under high driving forces, the nucleation starts simultaneously at many points on the surface leading to a rough surface. However, under low supersaturation the growth occurs preferentially along the surface from limited number of nucleation sites until the surface is covered with a smooth layer of hydrate. This explanation is consistent with the classical nucleation theory that the number of nuclei increases with the increase of the degree of supersaturation. The effect of driving forces on the hydrate film morphology was more clearly observed in the recent work of *Tanaka et al.* [2009]. They reported that the size of GH crystals decreased with increasing the degree of subcooling leading to a difference in the surface roughness or morphology. Higher driving forces give rise to more nucleation centers leading to smaller crystal sizes.

Servio and Englezos [2003] reported as well a difference in the morphology in the experiment realized with “memory” water or water that has experienced at least once a hydrate formation and decomposition. The duration of decomposition was found to influence the growth and morphology of GH. After a long decomposition time (24h) the crystallization from memory water was similar to that at

high driving forces, while after 30 min of decomposition, the nucleation started in water that most likely has hydrate templates [Servio and Englezos, 2003]. However the authors do not really define the nature of these templates or give an experimental evidence for their existence so it remains speculations by the authors. Uchida *et al.* [2000] also observed the memory effect during the reformation processes of CO₂ in water. They reported that only by cooling and without pressure increase, the reformation was faster due to the remaining amount of CO₂ in water after a cycle of formation and decomposition.

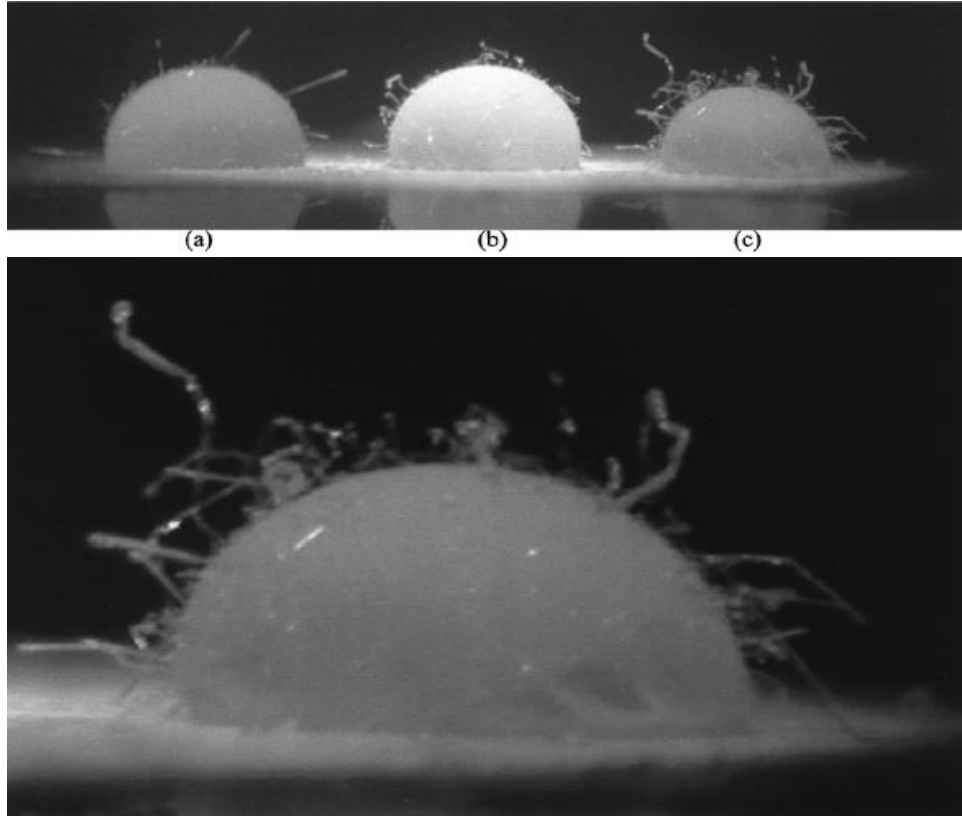


Figure 2-9. Methane hydrate covering the surface of water droplets (a,b,c) under high driving force, 10 min after nucleation. The lower picture is a magnified view of droplet (c).

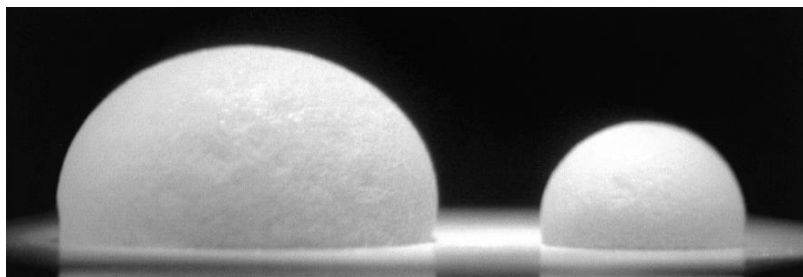


Figure 2-10. Methane hydrate covering two water droplets under low driving force, 10 h after experiment began.

The effect of gas mixture and hydrate structure on the growth and morphology of GH crystals was studied by Saito *et al.* [2010] and Smelik and King [1997] respectively. The growth from a natural gas mixture appears to be different from that of single gases as during the formation from natural gas, the composition of the vapor-phase may change continuously due to the different preferences of

gases to fill the GH cages and therefore the composition of the vapor-phase in equilibrium will be different from the feed gas. *Saito et al.* [2010] reported that the morphology of crystals from gas mixture (methane + ethane + propane) was different from that of the simple methane hydrate and that the crystal morphology changed with variation of the mole fraction of methane in the gas mixture. *Smelik and King* [1997] studied the crystal-growth behavior of the three common hydrate structures: sI, sII and sH and reported that each hydrate structure type exhibits characteristic crystal morphology. The variations in the morphology of GH crystals may have a significant relevance to the properties of the naturally occurring hydrates.

The growth mechanism of GH after formation of the initial hydrate layer is poorly understood. After the formation of a complete hydrate layer covering the surface of water droplet, *Servio and Englezos* [2003] suggested that either water might be transferred through capillaries within the porous hydrate film and reacts with the gas surrounding the water droplet as reported by *Sugaya and Mori* [1996b] and *Kobayashi et al.* [2001] or gas may diffuse through the hydrate shell for further transformation in water inside the droplet into hydrate [*Hatzikiriakos and Englezos*, 1994]. This may explain the depressions appeared on the hydrate layer on the surface of water droplets and the decrease of the volume of the water droplet due to the conversion of water into GH observed by *Taylor et al.* [2007] (see Figure 2-11).

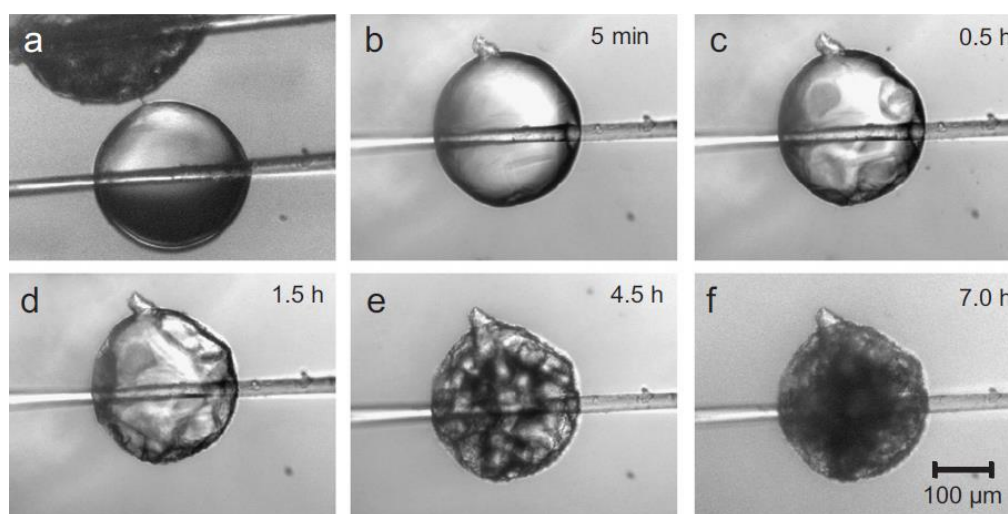


Figure 2-11. Nucleation of a water droplet placed on a cantilever and immersed in cyclopentane. (a) Initial contact, (b) cyclopentane hydrate shell formed around the water droplet (elapsed time = 5 min), (c) facets formed on the hydrate shell (elapsed time = 0.5 h), (d) continued facet formation (elapsed time = 1.5 h), (e) conversion of interior water to hydrate, indicated by darkening (elapsed time = 4.5 h), (f) almost completely converted hydrate (elapsed time = 7 h) (from *Taylor et al.* [2007]).

Staykova et al. [2003] reported that both gas and water molecules are able to diffuse through the porous hydrate layer. However, it is not known whether the further hydrate growth is controlled by transport of the guest or the water molecules through the polycrystalline film. A study by *Davies et al.* [2010] on the mass transfer mechanism across a methane hydrate layer revealed that water molecules are the most mobile species in the hydrate phase. In this work, methane hydrate layer was formed at a flat methane-water interface, and then the gas and water phases were replaced by isotopic tracers (H_2^{18}O and CHD_3).

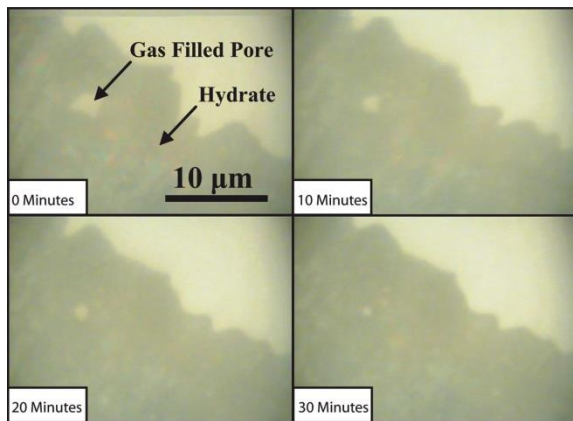


Figure 2-12. Confocal microscope images of the hydrate film showing pore filling as the film annealed (from *Davies et al.* [2010]).

The nucleation starts at a random single point when the driving force is low and from several points forming a polycrystalline film at high driving force [*Freer et al.*, 2001]. *Ohmura et al.* [2005] and *Watanabe et al.* [2011] studied the formation of GH at the gas-water interface using pure methane gas and a gas mixture (methane + ethane + propane). They reported that after formation of a polycrystalline hydrate film which intervenes between the guest and water phases, crystals will grow generally into the liquid from the hydrate film (see Figure 2-13). Two modes for the hydrate growth in water were suggested by *Watanabe et al.* [2011]: the first mode was the growth of GH crystals from the hydrate layer and the second mode was that GH crystals formed in water floated to the hydrate film, thereby growing in liquid water after attachment to the hydrate film. The morphology of GH crystals changed from polygonal or triangular flat plates to dendritic with increasing the degree of subcooling.

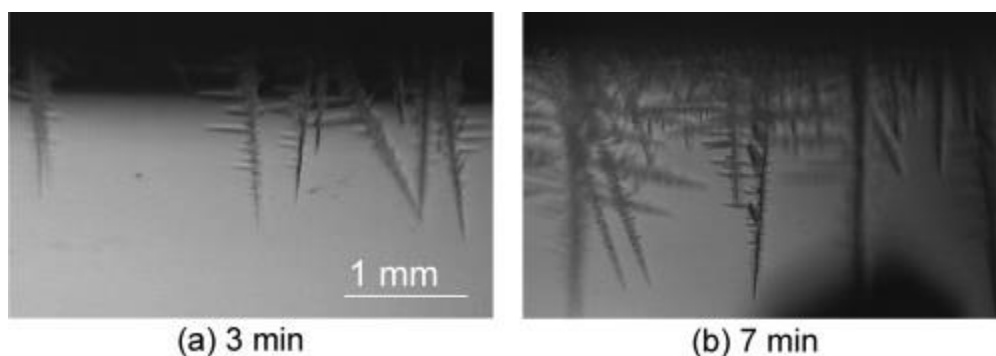


Figure 2-13. Videographs of the growth of methane-hydrate crystals from the hydrate film intervening between methane and water into liquid water presaturated with methane. $p = 9.7 \text{ MPa}$, $T = 273.3 \text{ K}$. The time lapse after the hydrate nucleation at the methane-water interface is indicated below each videograph ([*Watanabe et al.*, 2011]).

In addition to the above described studies, *Tohidi et al.* [2001] provided a first visual observation of GH formation from aqueous solution of water and dissolved CO_2 in the absence of a free-gas phase. This kind of formation may occur in upper levels of the sedimentary sections at sites where no free-gas layer exists.

The investigations of the initial hydrate film growth included the measurement of the lateral and vertical growth rate. The lateral growth is along the gas-water interface and the vertical growth is in the normal direction to the interface. The determination of the lateral growth is easier than the normal rate. The growth rate can be measured from optical images to determine the progress of the hydrate film over time. Studies on the hydrate film growth rate reported that the growth rate increased with the increase of driving force or degree of subcooling. Under the same driving forces, the type of the guest gas also affects the lateral growth rate. For example, the growth rate of CO₂ hydrate film is faster than methane hydrate because of its larger heat transfer coefficient and due to the higher solubility of CO₂ in water compared to the hydrocarbon gases. *Mori* [2001] reported that the hydrate growth rate is mainly controlled by the heat transfer. The difference between the hydrate growth rate at flat gas-water interfaces and on the surface of water droplets may be attributed as well to heat transfer issue. In contrary to the formation on water droplets, the nucleation at flat gas-water interfaces starts at multiple nucleation centers emitting by that larger heat which is difficult to remove rapidly [*Sun et al.*, 2010].

2.3. Gas hydrates-bearing sediments

2.3.1. Formation of GH in porous media

The formation of GHs in sedimentary matrices is of crucial importance for the physical and transport properties of the resulting aggregates. The mechanism by which GHs nucleate and grow in porous media is still not well understood and therefore the microstructure of GH in sedimentary matrices remains as well largely unknown. Only in a few occasions samples could be retrieved from sea-floor or sub-permafrost occurrences without major alterations due to the partial decomposition. A notable exception is the JAPEX/JNOC/GSC Mallik 5L-38 research well from which intact sediment-GH-aggregates were successfully recovered [*Techmer et al.*, 2005]. Even then, insight into the microstructure may be hampered by the fact that the recovered samples were usually stored in liquid nitrogen which freezes liquid water present in the sample – possibly altering the microstructure and obscuring details of the GH-sediment interface. Due to above difficulties a number of researchers attempted to emulate the nucleation and growth of gas hydrate in sedimentary matrices in laboratory experiments; in particular to reveal the physical properties of these aggregates to support geophysical exploration methods [*Berge et al.*, 1999; *Best et al.*, 2010; *Best et al.*, 2013; *Carcione and Gei*, 2004; *Dai et al.*, 2004; *Dai et al.*, 2012; *Dvorkin et al.*, 2003; *Dvorkin et al.*, 2000; *Priest et al.*, 2005; 2006; *Yun et al.*, 2005; *Zhang et al.*, 2011]. In this section, we review the most relevant visual studies on GH formation in porous media.

The growth mechanism governs the pore-scale distribution of GH which controls the microscale physical properties of GH-bearing sediments spatial distribution of GH in the pore spaces. Figure 2-14 illustrates how the final microstructure of GH-bearing sediments depends on where the hydrate starts to form and on the growth process followed. In the first case GH nucleates and grows in the pore spaces, while in the second case GH nucleates on the surface of the sediment grains and forms as cement around these grains.

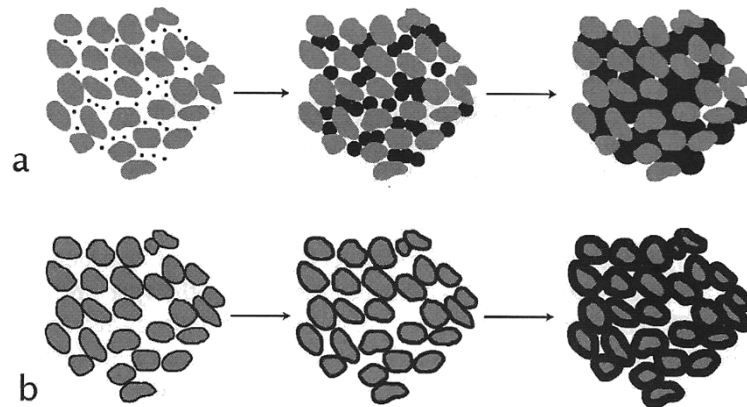


Figure 2-14. Evolution of hydrate in clastic sediment. (a) Hydrate nucleates and grows in free pore water space. (b) Hydrate grows as an encrustation on sediment grains (from *Max et al.* [2006]).

The microstructure of GH aggregates in a sedimentary matrix is frequently categorized into (a) hydrate filling-pores (b) load-bearing, (c) grain-coating and (d) hydrate cementing grain contacts based on the hydrate distribution models by [*Dvorkin et al.*, 2000; *Helgerud et al.*, 1999] (see Figure 2-15).

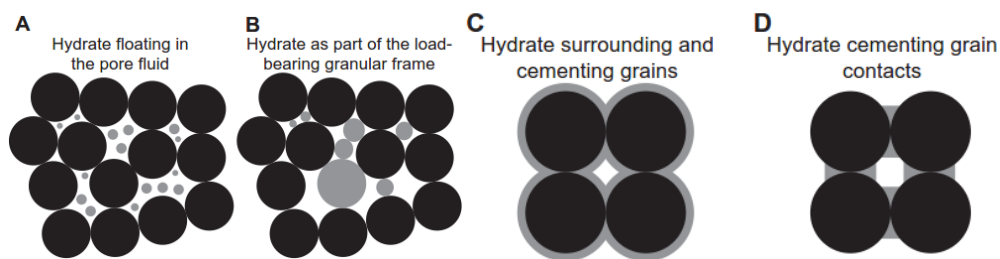


Figure 2-15. Pore scale distributions of GH (gray) and sediment grains (black) (from [*Waite et al.*, 2004])

- The first growth habit is pore filling (A) where GH nucleates and grow in the pore space without bridging the sediment grains. In this case GHs are expected to affect the stiffness of the bulk fluid [*Helgerud et al.*, 1999].

- The second microstructural model is load bearing (B). GH grows in the pore spaces as a part of the matrix and links adjacent grains together. The hydrate affects the mechanical stability of the host sediments.

The pore-filling hydrate can evolve to load-bearing model if the hydrate saturation exceeds 25- 40 % [*Berge et al.*, 1999; *Yun et al.*, 2005].

- The last GH models are cementation where GH can occur as cement surrounding sediment grains (C) or cementing grain contacts (D). A small amount of GH can increase the rigidity of the matrix by linking the grains together.

The nucleation and growth processes of GH in porous media define which pore-scale model takes place. Thus, different formation methods can result in different growth habits and pore-scale distributions [*Waite et al.*, 2009]. Researchers who studied the formation of GH in porous media

focused mainly on two formation methods: the formation of GH in low water saturated sediments in the presence of a free-gas phase [Jin *et al.*, 2006; Kneafsey *et al.*, 2007; Priest *et al.*, 2005; Priest *et al.*, 2009; Waite *et al.*, 2004]

and the hydrate formation using the dissolved gas method [Katsuki *et al.*, 2007; Lee *et al.*, 2010; Spangenberg and Kulenkampff, 2006; Tohidi *et al.*, 2001; Yun *et al.*, 2005].

The partial water saturation method consists in mixing the sediments with a limited amount of water to form partially water-saturated sediments. Then the system is pressurized with gas and cooled to enhance the formation of GH [Kneafsey *et al.*, 2007; Waite *et al.*, 2004]. The formation of fully water-saturated sediments can be achieved by injecting methane gas as bubbles before starting cooling. At low water saturation, liquid water tends to accumulate near contacts which leads to preferential GH formation at contacts ref. Undersaturated sediments can be obtained using a mixture of ice grains with cooled sediments [Stern *et al.*, 1996; 1998]. As the ice melts, water can accumulate at grain contacts prior hydrate formation [Circone *et al.*, 2004; Klapproth *et al.*, 2007]. Whereas the dissolved gas method uses a water solution enriched in gas. Generally CO₂ is used due to its high solubility in water [Katsuki *et al.*, 2006; Tohidi *et al.*, 2001]. The gas is the limiting constituent in this case. This heterogeneous nucleation of GH may occur on the mineral surface with subsequent growth in the pore spaces. Figure 2-16 shows the dependence of GH growth habit on the formation methods as suggested by [Waite *et al.*, 2009].

The experimental studies of GH formation in sedimentary matrices used various porous media such as GB, silica gels or natural quartz sand with and without clay minerals. The observations of the GH growth habit in porous media were carried out with the aid of conventional optical methods as well as modern techniques.

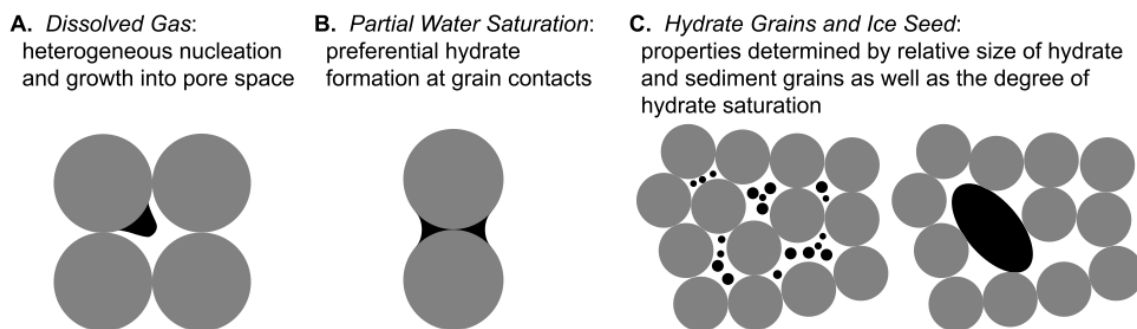


Figure 2-16. Dependence of hydrate habit on hydrate formation technique. Physical properties of hydrate-bearing sediments depend on the size and distribution of hydrate (black) relative to the sediment grains (gray) ([Waite *et al.*, 2009]).

Magnetic resonance imaging (MRI) is one of the techniques that has been largely used to characterize the growth and distribution of GH in porous media [Bagherzadeh *et al.*, 2011; Baldwin *et al.*, 2003; Kossel *et al.*, 2013; Mork *et al.*, 2000; Zhao *et al.*, 2011]. Mork *et al.* [2000] studied GH formation in synthetic sediments in a laboratory cell. They observed a lumpy structure of THF hydrates

and sand with three-dimensional channels of untransformed liquid water in between (see Figure 2-17). The GH lumps from different samples had different sizes which could be assigned to the stochastic nature of GH nucleation as suggested by the authors. The authors reported that the size of hydrate lumps varied between a few and several tens of mm.

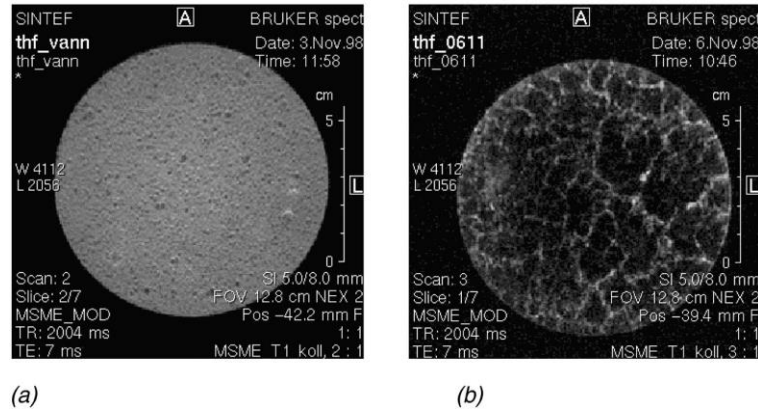


Figure 2-17. NMR imaging of (a) sand/water/THF and (b) sand/THF hydrate. The bright channels in (b) are liquid water that has not formed hydrate (from [Mork *et al.*, 2000]).

On the other hand, *Bagherzadeh et al.* [2011] investigated the growth of methane hydrate in an unconsolidated bed of silica using different sand particle sizes at different water saturations (25, 50, 75 and 100 %). They reported that the rate of formation was faster at low water concentration due to the higher porosity which provided more free pathways for mass transfer and in the case of a bed with smaller particles. Recently, *Song et al.* [2013] followed *in-situ* the growth habit of THF hydrate in quartz GB matrix. Their results suggested that GH nucleates mainly at the grain surface, then grows toward the liquid phase, fills up the pore spaces and finally cements and stiffens the sediment. They claimed that there was no wetting phase between the grain and hydrate surfaces (Figure 2-18).

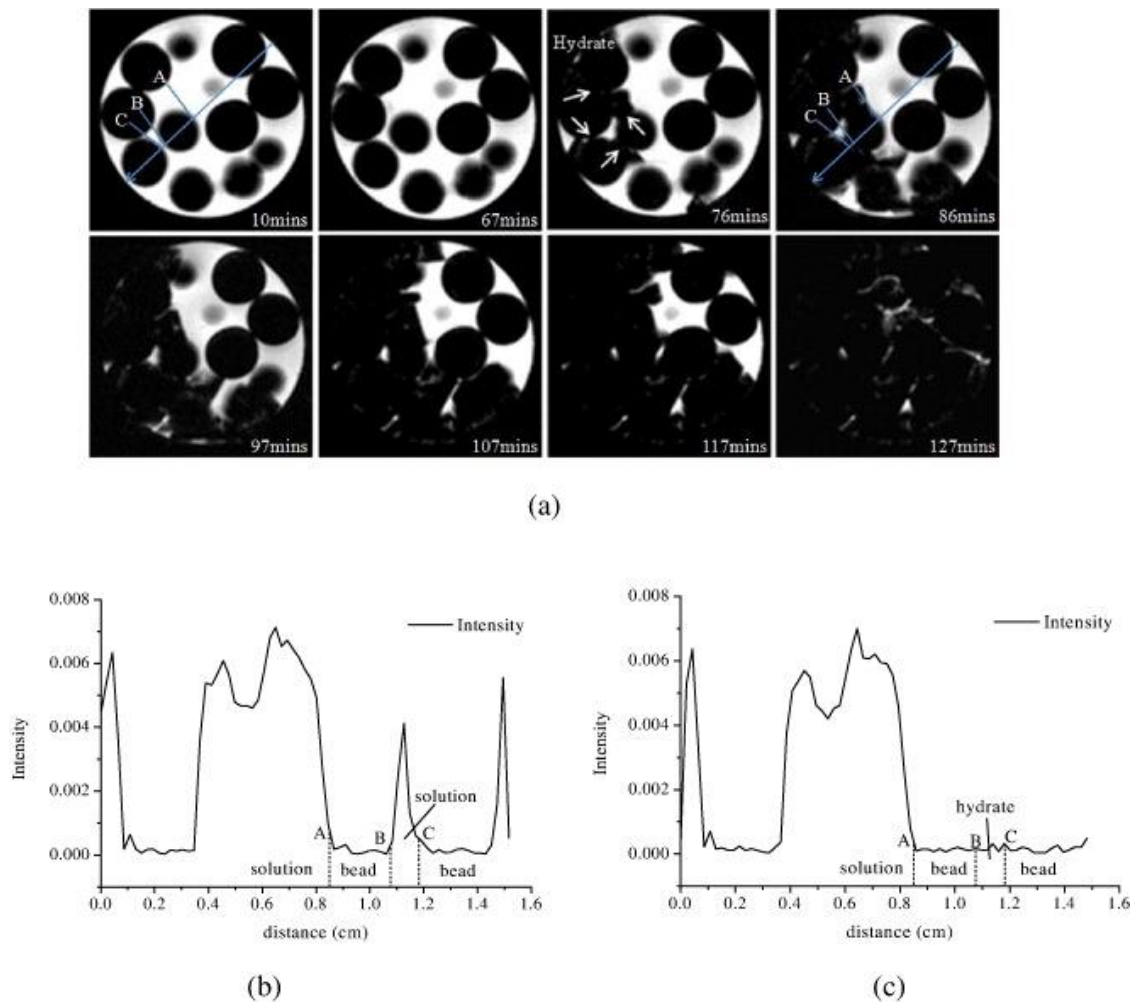


Figure 2-18. (a) Images of the THF hydrate growth hosted in the cross-sections of GB recorded at 10 min, 67 min, 76 min, 86 min, 97 min, 107 min, 117 min and 127 min, (b) the intensity of the image at 10 min and (c) at 86 min.

These results are in contradiction with the observations by *Tohidi et al.* [2001] which revealed a nucleation at the gas-water interface and a remaining water layer between GH and the surface of porous media. *Tohidi et al.* [2001] claimed that this water layer exists even at high water saturation.

Babu et al. [2013] reported two different growth habits of methane hydrate formation in silica sand and activated carbon. In silica sand, GH crystals were observed to form in the pore spaces, whereas in an activated carbon bed the nucleation started on the surface of grains. The authors suggested that particle size, pore spaces, and the low wettability of the grains may be the reason for the hydrate growth behavior in activated carbon. *Jin et al.* [2012] studied the growth of methane hydrate in porous media using attenuated total reflection infrared (ATR-IR) and proposed two steps for the growth of GH in porous media. First, a hydrate film is formed at the gas-water interface then cracks will occur in the GH films leading to further growth of water to hydrate (see Figure 2-19).

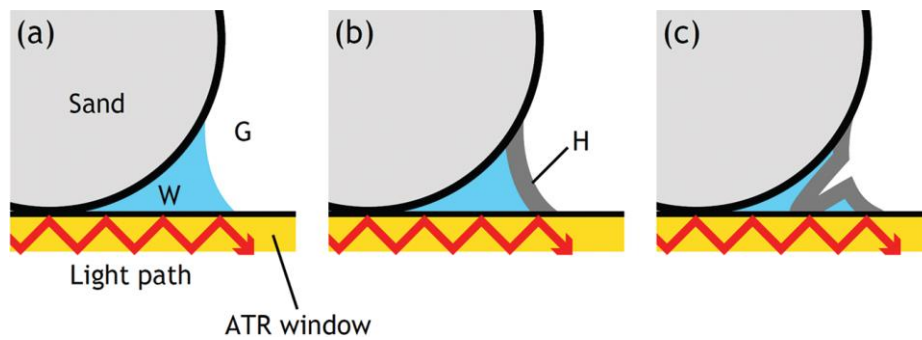


Figure 2-19. Schematic of the relationship between the nature of hydrate and two-step growth during the ATR-IR measurement (W, liquid H₂O phase; G, gas phase; and H, hydrate phase): (a) before hydrate formation, (b) in the first step of two-step growth, and (c) in the second step of the two-step growth.

A number of scientists used computed X-ray tomography to characterize GH-bearing sediment cores [Jin *et al.*, 2004; Jin *et al.*, 2006; Kerkar *et al.*, 2009; Kerkar *et al.*, 2014; Kneafsey *et al.*, 2007]

X-ray tomography offers the advantage to be a non-destructive technique and to provide insight on the interior features of samples over a wide range of size scales. The studies of [Jin *et al.*, 2004; Jin *et al.*, 2006] on artificial methane hydrates using microfocus X-ray computed tomography led to the observation of the distribution of GH in pores and the measurement of the porosity which was found to be around 40 % (see Figure 2-20).

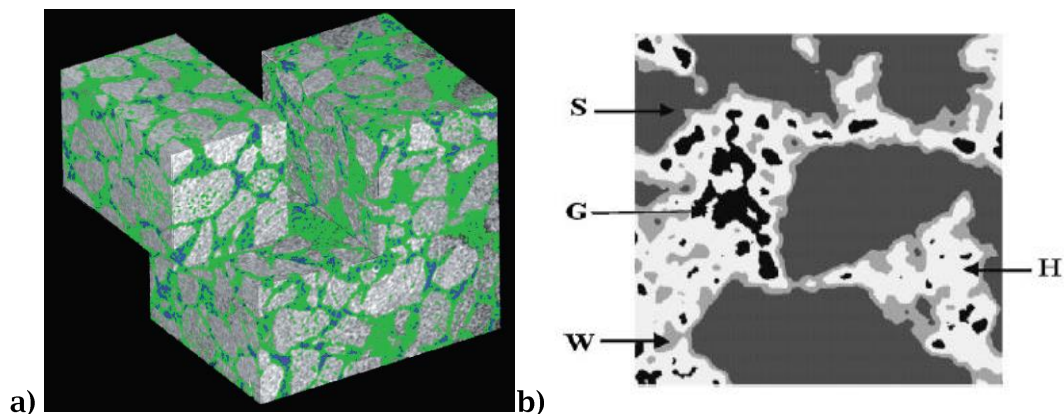


Figure 2-20. a) Processed tomographic image showing the spatial distribution of hydrate and ice (green color) in sand (grey color) (from Jin *et al.* [2004]). b) Processed X-ray CT image. S (dark gray) sand particles, G (black): free-gas space, W (light gray): water. H (white): methane hydrate (from Jin *et al.* [2006]).

The image on the right hand side of Figure 2-20 is a conceptual image which shows a water layer between GH and sediment grains which seems to be a speculation from the authors as the resolution of real images does not allow such observation. Sato *et al.* [2005] modified and used a high-speed X-ray computed tomography to measure the density and hydrate saturation of methane hydrates formed artificially in Toyoura sand. Kneafsey *et al.* [2007] explored the changes in density during methane hydrate formation in a pressure vessel using CT. They reported that as hydrate starts to form and fill the pores, water will flow to regions containing GH due to capillary forces. Kerkar *et al.*

[2009] presented a visualization of time-resolved three-dimensional growth of THF hydrates in a matrix of glass spheres matrix with better resolution using synchrotron X-ray CT at microscale (total volume $\sim 1 \text{ mm}^3$). They observed a patchy growth of GH in the pore spaces in a manner similar to the pore filling model of Dvorkin et al 2004 (see Figure 2-21). The authors reported that the inhomogeneous or patchy distribution of hydrate in porous media can alter the connection between acoustic velocities and GH saturation which always assumed a uniform distribution of hydrate in sediments.

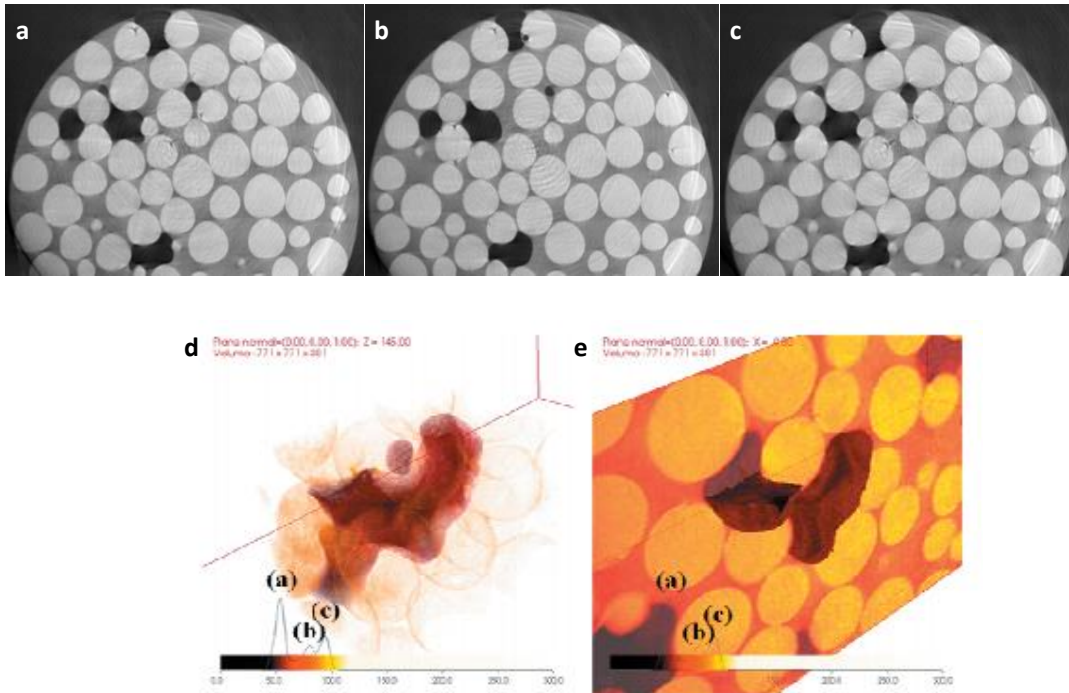


Figure 2-21. (a), (b), and (c) show the observation of random THF hydrate (black) growth hosted in GB (white spheres) is representative of 2D cross sections (7 mm diameter). The images are recorded at (a) 54:06 h, (b) 70:30 h, and (c) 74:07 h. (d) and (e) are 3D images reconstructed from 300 slices.

All studies described above were unable, due to the insufficient resolution, to reveal the details of the microstructure especially the nature of the GH-sediment interaction which may well be the key to understand the physical and acoustic characteristics of GH-bearing sediments. At the same time, not much can be learned from the use of THF as a proxy for methane in the study of GH-bearing sediments. Methane and THF have different solubility in water and form different hydrate structures. A comparison of CH_4 and THF properties and their hydrates was presented by *Lee et al.* [2007]. The interaction among water molecules and hydrate former molecules is one of the parameters that govern the nucleation and growth processes of GH in sediments. Moreover, THF is completely miscible in water, so that a complete hydrate formation in water-saturated sediments is possible. Hence, a gas phase in THF system does not occur which is different from methane case.

2.3.2. Factors affecting the formation

The formation of GH in natural environments may happen in more complicated systems than those described above due the presence of clay minerals in sediments and salts dissolved in sea water. The different factors that can affect the formation of GH in sediments are described below:

2.3.2.1. Salt effect:

The presence of dissolved salts in water in natural environment can inhibit the formation of hydrate [Sloan and Koh, 2008]: in salty water, there are less water molecules to dissolve the gas molecules because the water-ion attraction is more stable and therefore the solubility of gas in the solution is reduced. This is known as the "salting-out" effect. Salts ionized in water reduce the chemical potential of the gas/water solution making it more stable. As the GH stability zone occurs where the chemical potential of gas, water and GH are equal, the hydrate boundary is shifted to higher pressures and lower temperatures. More driving force is required for the nucleation of the first crystals to overcome the energetic barrier.

2.3.2.2. Clay Minerals:

The clay minerals can offer favorable sites for nucleation of GH by lowering the thermal agitation and spatial distribution of water molecules. The influence of these particles was investigated in several studies growth [Cha et al., 1988; Englezos and Hall, 1994; Ouar, 1992; Rogers et al., 2004]. Bentonite was found to promote the hydrate formation as reported by Rogers et al. [2004] (Figure 2-22a).

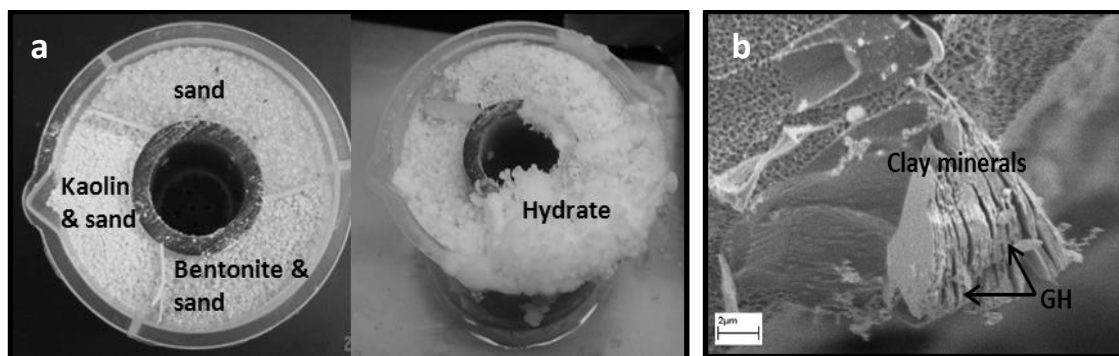


Figure 2-22. a) Figure to the left shows the effect of Bentonite on hydrate formation ([Rogers et al., 2004]). b) Figure to the right, SEM image of a NGH sample from the Mallik 5L-38 research well which shows GH as intercalate with clay minerals ([Techmer et al., 2005]).

There is also compelling evidence that under certain conditions GH can even form intercalates with a certain type of clay minerals as it was observed in a SEM image of natural GH bearing-sediments recovered from the Mallik 5L-38 research well (see Figure 2-22b) [Techmer et al., 2005].

2.3.2.3. Memory effect:

The formation of GH from water obtained from melted hydrate is faster and easier than that from fresh water. This phenomenon was defined by GH researchers as the so-called "memory effect". Enhanced formation rates of GH from "memory" water were repeatedly reported [Duchateau et al., 2010; Sefidroodi et al., 2013; Wu and Zhang, 2010; Zatsepina et al., 2004], yet the issue is still controversial [Buchanan et al., 2005; Thompson et al., 2006; Wilson and Haymet, 2010].

Two opposing hypotheses were suggested to explain this phenomenon [Sloan and Koh, 2008]:

- The residual structures (not visible by naked eye) which remain after GH dissociation act as precursors which facilitate the reformation of GH [Duchateau et al., 2010; Takeya et al., 2001]. These

structures were suggested to be either partial hydrate cages (or polyhedral crystals) or persistent hydrate crystallites [Buchanan *et al.*, 2005].

- Dissolved gas which remains in water after GH dissociation [Rodger, 2000].

Although, there is a clear evidence of the effect of memory water as enhancing factor of GH formation, the issue is still controversial [Buchanan *et al.*, 2005; Thompson *et al.*, 2006; Wilson and Haymet, 2010] and there is no conclusive molecular investigations to verify the above discussed two hypotheses. The formation of GH from memory water can affect the growth process and the final morphology of GH

2.3.3. Occurrence and seismic detection of GHs

In the 1970s, scientists discovered the existence of GH in natural environments during drilling expeditions. GH was found to occur in deep water sediments in many parts of the world beneath the seafloor. 98 % of GHs are concentrated in marine sediments while 2 % exist in permafrost regions (see Figure 2-23). The evidence for GH occurrence comes from different prospecting techniques such as seismic reflections, drilling data, well logs as well as electric methods. Seismic exploration is the most suitable technique used to identify and detect GH bearing-sediments. It has been observed that the presence of GH in the pores of sediments causing an increase in the seismic wave velocities and the free gas in adjacent sediments with low-velocity produce a high-amplitude reflection at the interface of the two sedimentary layers. This reflection is known as Bottom Simulating Reflector (BSR) [Holbrook *et al.*, 1996]. It represents generally the presence of the three-phase equilibrium: free gas, water and hydrate [Henry *et al.*, 1999]. The estimation of GH saturation in sediments is determined by performing an elastic property inversion using high-quality seismic data followed by rock physics inversion to further transform the elastic properties into gas hydrate saturation estimates. Hence, accurate data on the physical properties of the host sediment is required.

The estimation of GH saturation in sediments is determined by performing an elastic property inversion using high-quality seismic data followed by rock physics inversion to further transform the elastic properties into GH saturation estimates. Hence, accurate data on the physical properties of the host sediment is required.

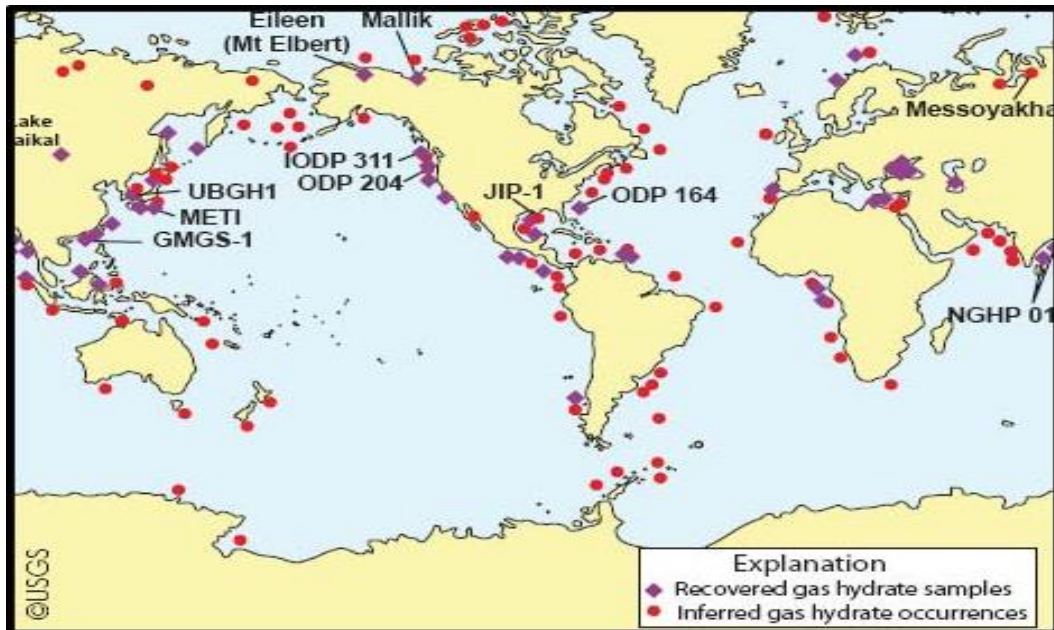


Figure 2-23. Map showing the occurrence of GH worldwide in oceanic sediment of continental margins and permafrost regions (from <http://www.geoexpro.com/articles/2009/02/gas-hydrates-not-so-unconventional>)

2.3.4. Relationship between physical properties and GH microstructures

Several physical properties of GH-bearing sediments depend on the microstructure of GH in sediments such as the spatial distribution of GH in the pore spaces and the nature of contact of GH with the sediments grains. In the first place the seismic velocities should be noted.

GH has a higher elastic modulus in comparison with pore fluid (water or gas). Thus, the formation of GH in porous media exhibits anomalously high seismic wave of the host sediments, both compressional (V_p) and shear wave (V_s) velocities. Consequently, it is possible to use seismic measurements to quantify the amount of GH present in marine sediments. For that, a predictive model which relates the hydrate saturation to seismic velocities is required. Such model has to be developed based on the microstructural information of GH in porous media.

The relationship between GH saturation and seismic velocities has been studied in laboratory by several researchers. Although the experimental results may not directly be applied to the seismic interpretation of field data, these experiments can provide some basic geophysical parameters for the exploration of the GH reservoirs.

Priest et al. [2005] used a specifically designed resonant column to determine the P and S wave velocities of synthetic methane hydrate-bearing sediments. Rich-gas samples were obtained by injecting methane gas into a mixture of sand and ice powder. The results showed that GH formed as cement at grain contacts (Figure 2-24a). In a complementary work, *Priest et al.* [2009] studied the effect of GH formed from excess of water in the pore space on the seismic behavior of the host sediments. They suggested that GHs formed in this way exhibit a frame supporting behavior similar to that observed by Yang et al. 2008 (Figure 2-24b). The wave velocity measurements on these samples showed that the increase of wave velocities with the increase of GH saturation was more significant in

the case of excess gas method (Figure 2-24c). The authors suggested that GH may form as cement in this scenario leading to a high increase of the stiffness of the host sediments. However, the experimental V_p and V_s measurements did not match exactly the predicted wave velocities from a cementing model; the rate at which the velocities increase with the increase of GH saturation is faster for the theoretical than for the measured data. This discrepancy could be due to some microstructural details omitted by the theoretical cementing model.

For GH formation using the excess water method, a significant increase in shear wave velocity was observed only when the hydrate concentration exceeded 20 %. The experimental results matched better the predicted values. This type of hydrate distribution has less effect on the acoustic velocities than the cementation model but much more than the hydrate formed in the dissolved "gas system". *Yun et al.* [2005] studied the influence of a different microstructural model where GH acts as pore-filling on the acoustic velocities. For that, THF hydrates were formed in fine-grained sand specimens. Due to its complete miscibility with water, hydrate of THF will form and grow in the pore spaces. The results show that the changes in velocities are too small for hydrate concentration below 40 %. The changes become significant when hydrates begin to contact the sediment particle at saturation higher than 40 % (see Figure 2-25).

Hu et al. [2010] used ultrasonic methods and time domain reflectometry (TDR) to measure acoustic data and hydrate saturations simultaneously during GH formation. They reported that the velocities changed very little during the first stage of GH formation (from 0 to 10 %) but they increased rapidly when the degree of saturation was higher than 10 % especially in the range of 10 % - 30 %. The authors suggested that hydrate may act as a part of the frame when the saturation is above 30 %. However, a pore model or a partly touching model may occur at low hydrate saturation.

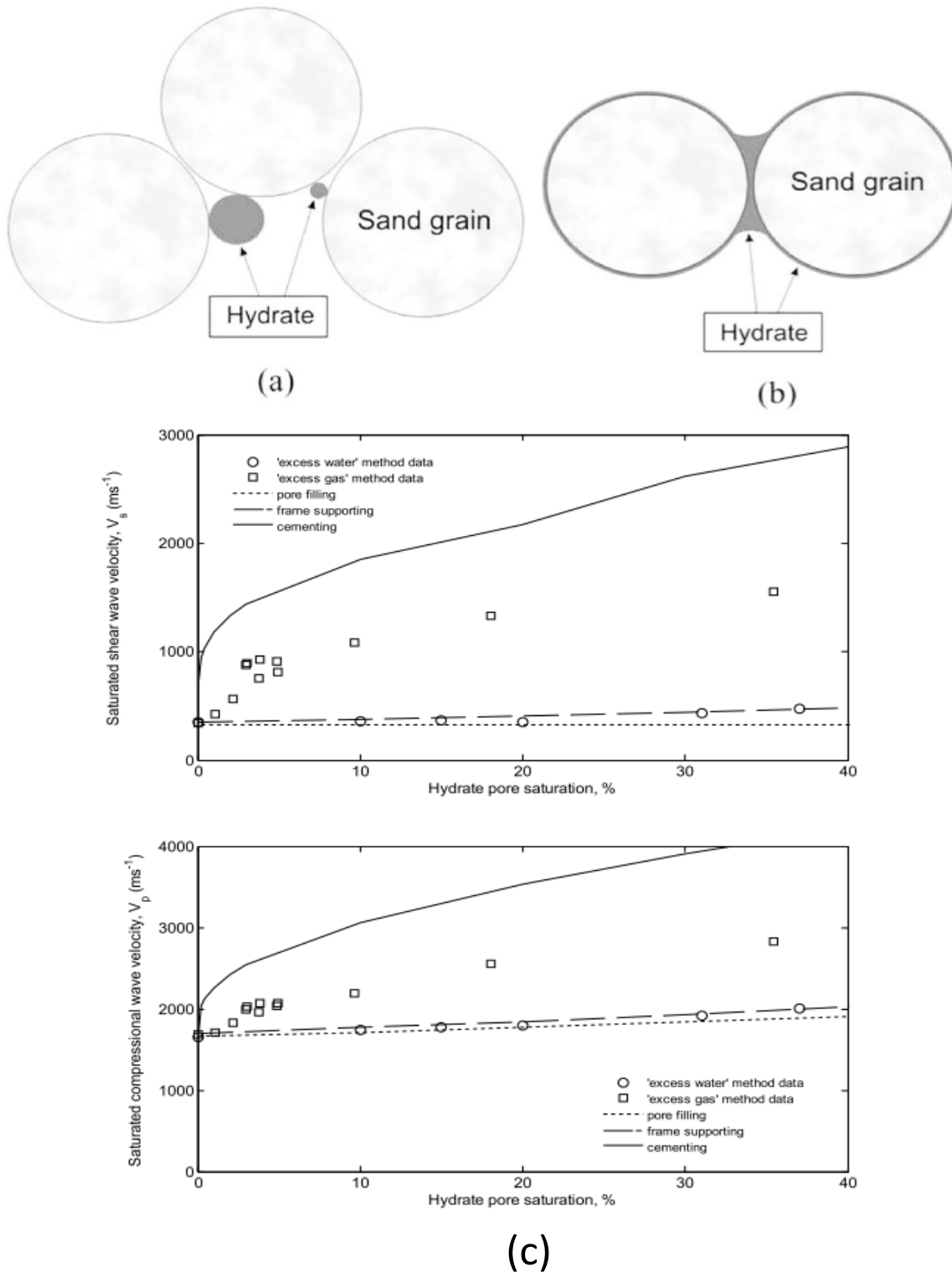


Figure 2-24. (a) Location of hydrate in the pore space formed using excess water method: Hydrate forms around gas bubbles. (b) Location of hydrate formed using excess gas method: hydrate forms where water collects at grain contacts. (c) Variation in V_p and V_s with hydrate pore saturation for excess water specimens (open circles) and excess gas specimens from at confining pressure of 500 kPa. Theoretical V_p and V_s values are also shown for pore-filling model (dotted line), frame supporting model (dashed line) and cementing model (solid line) (from [Priest *et al.*, 2009]).

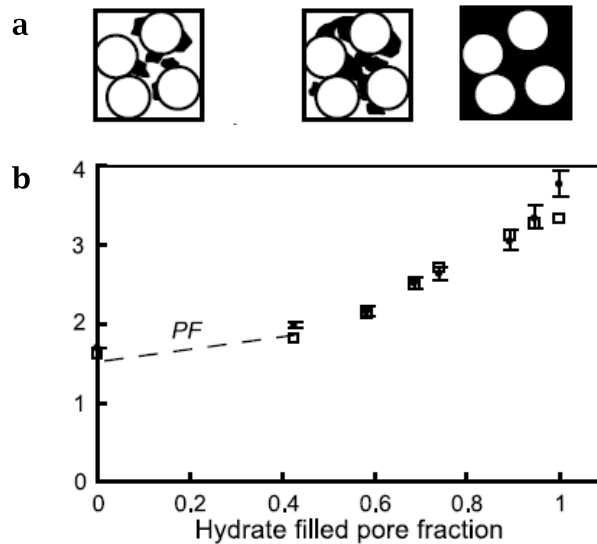


Figure 2-25. (a) Hydrate formation mechanism of GH pore-filling model. (b) Measured (squares) V_p and predicted values (filled circles with error bars) (from *Yun et al.* [2005]).

More recently, [*Zhang et al.*, 2011] measured the compressional wave velocity of sandy sediments during hydrate formation from brine and free methane gas. They reported that none of the four theoretical models can describe alone the experimental data (Figure 2-26).

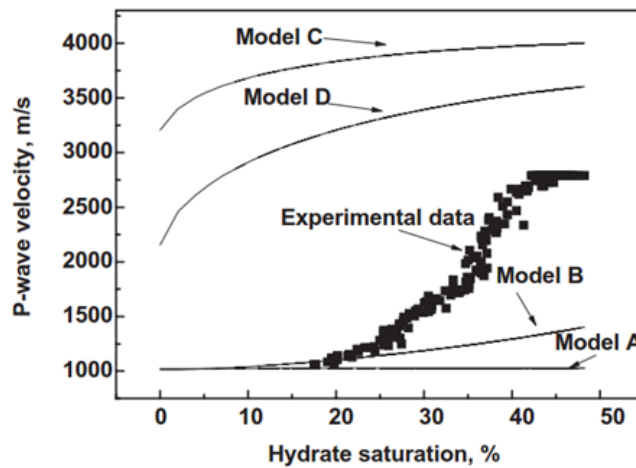


Figure 2-26. Comparison of V_p predicted by the four hydrate distribution models (A: pore-filling, B: load-bearing, C: cementing at grain contacts, and D: cementing at surrounding grains) and experimental values for methane hydrate sample (from *Zhang et al.* [2011])

Throughout these studies, the acoustic velocities appeared to be depending on the spatial distribution and morphology of GH in the pore spaces. The experimental results did not much the predicted data from the existing microstructural models. Apparently, the measured wave velocities taken by itself are not sufficient to determine the GH concentration. Furthermore, it must be assumed that the change in the microstructure with the increase of hydrate saturation as reported by *Hu et al.* [2010] can be expected. A series of measurements of the P and S-wave velocities as a function of the GH-saturation are shown in Figure 2-27.

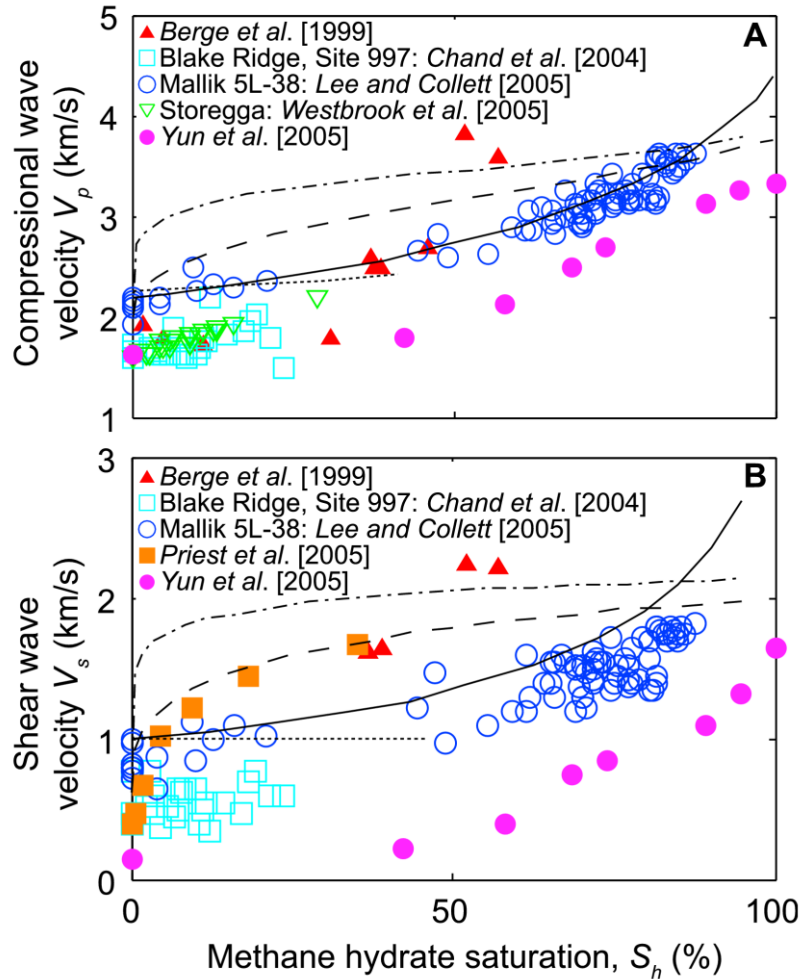


Figure 2-27. Comparison between field (open symbols), laboratory (solid symbols), and modeling results (solid and dashed curves) for (a) compressional and (b) shear wave velocities in hydrate-bearing sediments. Modeling results are from (Kleinberg and Dai 2005). Dot-dashed curves represent wave velocities for hydrate forming as cement at grain contacts. Particularly for low hydrate saturations, this distribution most significantly increases the wave velocity. Dashed curves predict wave velocities for hydrate that coats and cements sediment grains. Solid curves represent loadbearing hydrate, and dotted curves show the impact of pore filling hydrate. Pore-filling distributions begin bridging sediment grains and behaving as load-bearing distributions (from [Waite et al., 2009]).

Although many studies of elastic-wave behavior in such materials have been conducted *in-situ* in laboratory, and theoretical models have been developed the discrepancy between measured and theoretical values of wave velocities remains puzzling [Bagherzadeh et al., 2011; Chand and Minshull, 2004; Jin et al., 2004; Jin et al., 2006; Kneafsey et al., 2007]

The uncertainty of the existing models may result from the lack of direct information on the microstructure due to the inability of the actual experimental studies on the formation mechanism of GH in porous media to reveal the microstructural characteristics of GH such as the GH-sediment contacts.

In addition to seismic velocities, the electrical and hydraulic conductivity depend as well on the GH microstructure. It was found that the conductivity (electrical, hydraulic and thermal) increases with the increase of GH saturation [Cao *et al.*, 2013; Dai *et al.*, 2012]. Dai *et al.* [2012] reported that in a pore-filling model, there are thin flow pathways for water which reduces the hydraulic conductivity, whereas more conductive and larger flow paths exist in a GH cementing model. For a GH saturation of 80 %, concentrating hydrate into spherical or needle-shaped patches leaves hydrate-free sections which are less disruptive to fluid flow than homogenous hydrate distributions (see Figure 2-28).

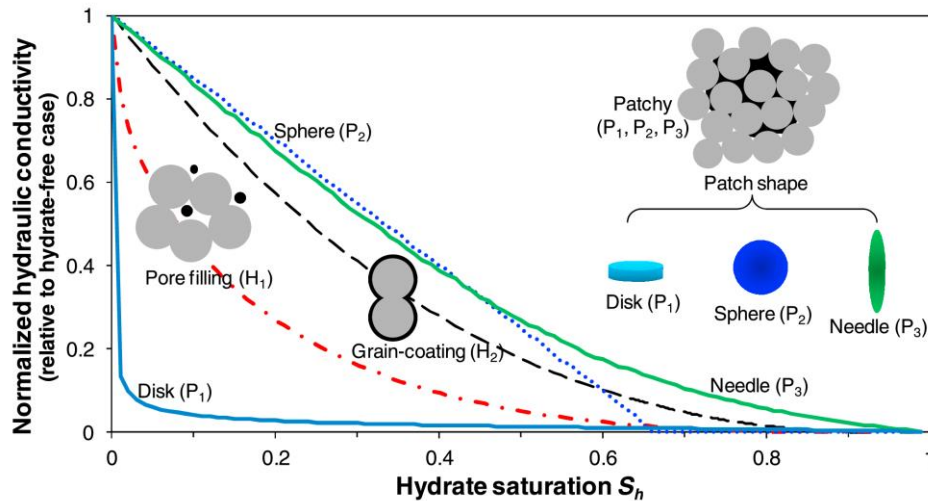


Figure 2-28. Dependence of the hydraulic conductivity on the GH microstructure (from Dai *et al.* [2012])

Spangenberg and Kulenkampff [2006] used synthetic methane hydrate in GB to measure the variation of the resistivity with GH content. They reported that the resistivity increased from 5.1 Ohm at 0 % GH saturation to 265 Ohm at 95 % GH concentration. Figure 2-29 shows how the electrical resistivity depends on the spatial distribution of GH and on the GH/water saturation.

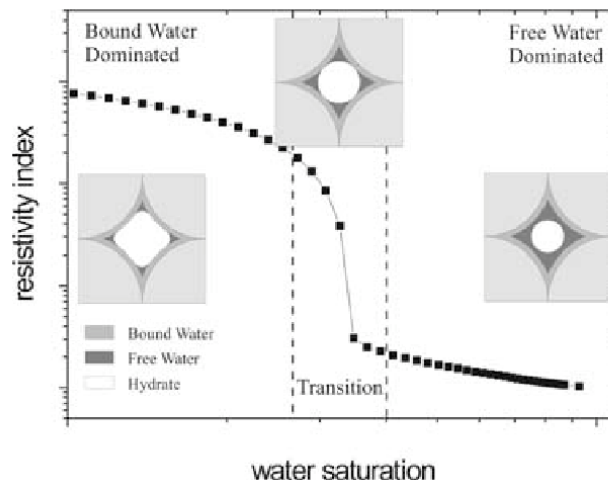


Figure 2-29. Variation of the electrical resistivity with the water saturation

The formation and distribution of GH in natural sediments influences the hydraulic conditions which affect the transport of methane gas, the temperature and salinity of water [Cao *et al.*, 2013]. The measurements of the hydraulic and electric conductivity can complement the seismic surveying and help to understand the microstructure of GH-bearing sediments

2.4. Wave attenuation

The second significant seismic characteristic of GH-bearing sediments is blanking which consists in the attenuation of seismic waves. The measurements of seismic attenuation in sediments containing GH have revealed that the wave attenuation increases with the increase of hydrate saturation. This strange behavior of GH bearing-sediments, contrary to normal rock sediments with high seismic velocity and low attenuation, is called "seismic anomalies" [Chand, 2008]. The attenuation of seismic waves observed in field data could be attributed on a macro-scale to the presence of a free-gas phase. Experimental laboratory data can provide more clear results of the attenuation of seismic waves which can be attributed to the presence of GHs on the micro-scale.

Nevertheless, the seismic anomalies were very clear in the analysis of seismic data from the Mallik 2L-38 well. Similar results obtained in Nankai Trough which revealed that low-frequency seismic waves (150-500Hz) were also attenuated but attributed the reason to the presence of free-gas, while at high frequencies (10-20 kHz) the attenuations may be linked to the microstructure and the reduce of pore spaces. There are in the literature a number of possible explanations for this puzzling observation of a concomitant occurrence of high seismic velocity and high attenuation [Chand and Minshull, 2004; Chand *et al.*, 2006; Li and Liu, 2014; Priest *et al.*, 2006; Zhang *et al.*, 2014]

Zhang *et al.* [2014] reported two mechanisms for seismic wave attenuation: intrinsic absorption and scattering loss which are associated with heterogeneities of sediments. The first type of attenuation is due to the presence of fluid within pore spaces. Under a stress generated by a passing seismic wave, fluid moves from softer portion of rock to hard portion. This movement causes friction and transfers part of energy into heat. This mechanism called wave-induced fluid flow occurs at seismic frequencies on the centimeter scale (mesoscopic) as described by Müller *et al.* [2010]. In the other hand, squirt-flow occurs at the microscopic scale. Figure 2-30 illustrates the wave induced fluid-flow at mesoscopic heterogeneities.

The thermoelasticity may represent a second absorption mechanism. During wave propagation, the spatial temperature variations will be reduced by thermal diffusion. An interaction between absorbed water-film on the solid surface by thermally induced motion is overcome by seismic energy passing through, resulting in part of attenuation.

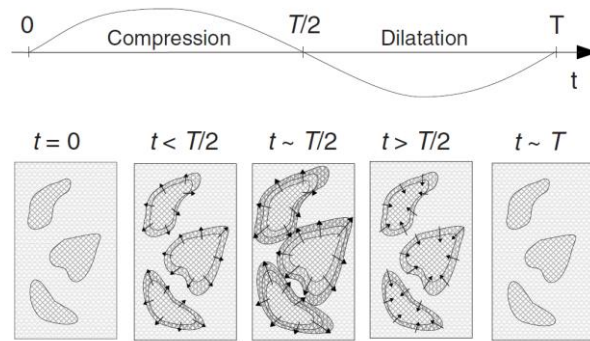


Figure 2-30. The mechanism of wave-induced flow. during the compression cycle of a wave with period T , there will be fluid flow from elastically soft inhomogenieties into the background (shown here; the flow direction is indicated by arrows) and flow from the background into elastically stiff inhomogenieties. During the extension cycle of the wave, the fluid flow reverses ([Müller *et al.*, 2010]).

The second mechanism reported by Zhang *et al.* [2014] is called scattering loss. Scattering also causes seismic attenuations with travel distance due to heterogeneities of GH-bearing sediments. During wave propagations, three waves form: scattering, reflected and transmitted wave. The energy of the reflected wave is received by the receiver, while the energy of weak reflections in different directions, forming scattering wave, loss. The scattering loss depends on the frequency and the distribution of scatters which is hydrate. Upon transmission through heterogeneity with rapidly varying velocity, high frequency waves destructively interference each other and signal of low frequency waves remain.

Alternatively, Priest *et al.* [2006] presented a qualitative conceptual model to explain the increase of seismic attenuation with the increase of hydrate saturation (see Figure 2-31). His model is based on the frictional losses that may occur from viscous fluid flow and squirt flow of absorbed fluid phase (gas or water) in cracks or small pores as suggested by Mavko and Nur [1979].

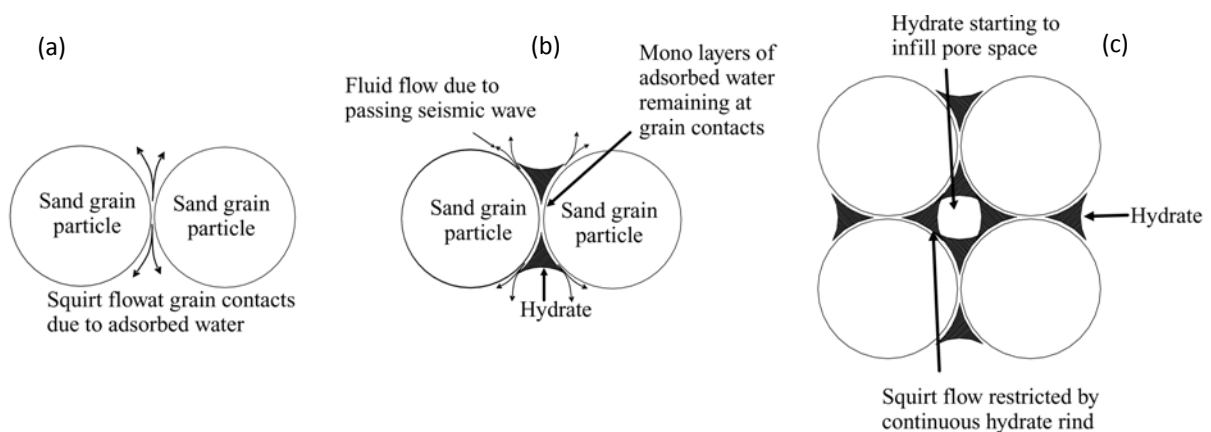


Figure 2-31. Conceptual model of cemented grain contacts with increasing hydrate saturation. From left to right: idealized view of sand grain contact with no hydrate, grain contacts with hydrate growing at grain boundaries and connected hydrate cementing grain contacts with commencement of pore filling (from Priest *et al.* [2006]).

The first stage (Figure 2-31a) is before hydrate formation. Due to capillary forces and surface tension, liquid water tends to accumulate near grain contacts. During the passing of a seismic wave these grain contacts are deformed momentarily causing dissipative fluid flow of adsorbed water (and or free gas) back and forth from this deformed zone. The attenuation in this case is minimal due to the small amount of water. Figure 2-31b shows the hydrate growth at grain boundaries where the water is located causing a cementation of grains which leads to an effective area of grain contact. The authors assume that the cementation of the sand grains is not perfect across the whole region so that the idealized crack length at the grain contact area is increased due to increased cementation.

Therefore, as the number of cemented grain contacts increase, more sites for squirt flow are created leading to an increase in the attenuation. At some point, all the grains become cemented and the attenuation will reach a maximum. Above a critical hydrate saturation range, the increasing in hydrate content leads to an encasement of the sand grains and an infilling of the pore space (Figure 2-31c) causing a reduction in the squirt flow effect and therefore a decrease in the attenuation. However, observations of seismic attenuation in sediments containing GH have demonstrated that the attenuation increase with the increase of GH saturation. The authors suggested that the porous structure of GH observed by [*Salamatın and Kuhs, 2002; Staykova et al., 2003; Stern et al., 2005*] may contribute to the attenuation. The model of *Priest et al. [2006]* provides a valuable explanation for the observed seismic anomalies with increase of hydrate content. However, it treats only the cementing GH model at low water saturation.

3 | Methods and Facilities

This chapter gives the reader the theoretical knowledge about the different methods and facilities used in this research project in order to better understand the approach followed and the methodology used to tackle the research problems.

3.1. Scanning electron microscopy

Scanning electron microscopy (SEM) was the first method used *in-house* to characterize the properties of starting materials and to observe the microstructure of *ex-situ* prepared GH-bearing samples.

3.1.1. Introduction to SEM

The SEM uses a focused electron beam of high-energy to scan the surface of a solid object and generate an image which reflects the variation of the material's surface characteristics. Information about the chemical composition, morphology or crystalline structure can be obtained from signals resulting from interactions between the incident electrons and the electrons of the atoms [Susan, 2013].

In SEM instruments a suitable source of electrons consisting in a thermionic emission (TE) gun, a cold field emission (FE) gun or a Schottky-emission (SE) electron gun is used. In a TE gun, a filament generally made of thin tungsten or Lanthanum Hexaboride (LaB₆) wire is heated to a temperature at which electrons are emitted and then gathered as an electron beam. In a FE gun, electrons are produced by applying strong electric field to a metal surface or cathode with sharpened tip. The emitter is usually a tungsten single crystal shaped to be a curvature radius of about 100 nm which allows the electric field to be concentrated to an extreme level. The electron beam generated is denser than conventional thermionic electron cathode.

The FE technology is applied for ultra-high resolution SEM. The SEM gun uses the Schottky-emission effect that takes place when a high electric field is applied to a heated metal surface. The emitter is a tungsten single crystal coated with ZrO which has a tip curvature radius of a few hundred nanometers. The SEM can produce a beam current highly stable because the emitter is kept at a high temperature and under high vacuum of about 10^{-7} . The electrons produced by the electron gun are then accelerated and focused towards the sample by passing through one or multiple electromagnetic or electrostatic lenses. When the incident beam hits the sample various signals are generated by the

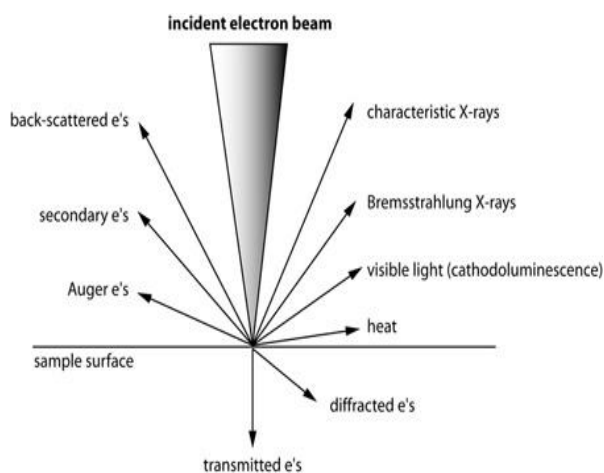


Figure 3-1. Types of interactions between electrons and a sample [Henry, 2012]

sample-electrons interaction (see Figure 3-1). These signals include secondary electrons (SE) which produce SEM images, backscattered electrons (BSE), diffracted backscattered electrons (EBSD), photons (X-rays), visible light (cathodoluminescence-CL), auger electrons and heat. Secondary electrons and backscattered electrons are the most commonly used for imaging of samples. BSE are scattered backward electrons produced due to elastic collisions of incident electrons with the sample.

BSE conserve their kinetic energy which allows obtaining information from relatively deep region. BSE depend on the composition of the sample.

Hence, BSE provide images with compositional maps of the sample where the different phases can be discriminated. For GH this effect is negligible small to the low mean atomic number of GH. BSE method was used principally to study the surface characteristic and mineral composition of the porous media used in the formation of GH.

On the other hand, secondary electrons are produced from the emission of the valence electrons (K shell mostly) of the sample by inelastic collisions. SE have a small energy and only electrons generated at the top surface layer (~ 10 nm) are emitted outside the sample and reach the detector while electrons generated at deeper region are quickly absorbed by the sample. The amount of secondary electrons emitted depends on the incidence angle of the beam. A difference in the brightness of the image is generated by the difference of the incidence angle of the beam. Therefore SE method allows studying the topography of the sample surface. Since SE have small energies, they are much influenced by electrically charged samples which produce anomalous contrast in the image. SE method was used for the pre-investigation of the microstructure of GH-bearing sediments.

3.1.2. FEI Quanta 200 FEG

The characterization of starting materials and the pre-investigation of the microstructure of GH samples were carried out using a high resolution field emission scanning electron microscope (FE-SEM), type FEI Quanta 200 FEG equipped with EDAX energy dispersive spectroscopy (EDS) and Polaron cryogenic stages (Figure 3-2) which allows measurements at low temperatures reaching -190 °C. The instrument is designed for work at low acceleration voltages (<1.5 kV) which is well adapted to study GH and ice samples in order to limit the alteration of the sample due to beam damage. It is

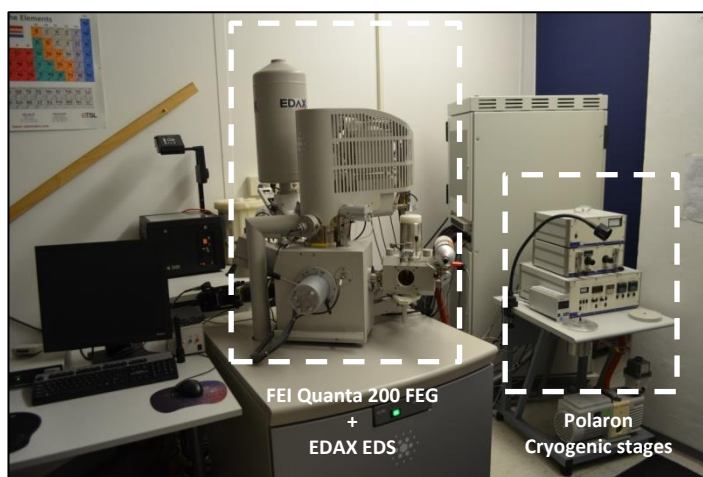


Figure 3-2. Picture of the cryo-FE-SEM

equipped with ZrO/W Schottky field emission gun for optimal spatial resolution. The additional ZrO coating on the tungsten cathode reduces the energy required for an electron to eject. Electrons are extracted and accelerated due to the applied potential difference between the cathode and the first and second anode.

The FEI Quanta 200 FEG can work under high-vacuum, low-vacuum and extended low-vacuum

(environment SEM (ESEM)) modes for imaging many types of sample. Depending on the selected mode, secondary electrons are detected by three different detectors. Under high-vacuum, an Everhardt-Thornely detector is used because of its distant position from the sample. This mode was used during the investigation of GH samples. A large field detector (LFD) and gaseous secondary electrons detector (GSED) are dedicated for low-vacuum and ESEM mode (Source: Product brochure, FEI Company, 2006).

3.2. X-rays and synchrotron radiation

3.2.1. X-rays



Wilhelm Conrad Röntgen
(1845-1923)

X-rays were first discovered by the German physicist Wilhelm Conrad Röntgen in 1895 [Röntgen, 1895]. X-rays are electromagnetic waves similar to visible light but have shorter wavelengths in the order of 1 \AA (10^{-10} m). The most important characteristic of X-rays is their ability to penetrate opaque matter. Thus, X-rays are now widely used in several non-destructive applications such as X-ray imaging, diffraction and spectroscopy. X-rays can be produced by bombarding a metal target with high speed electrons. The bombarding causes the ejection of electrons of atoms inner shells of the heavy metal leaving vacancies. These vacancies are quickly filled by electrons dropping from higher levels which emit an X-ray radiation with a wavelength characteristic of the metal target used. In addition to characteristic X-

rays, Bremsstrahlung (from German “braking radiation”) X-rays are generated due to the deceleration

of electrons fired at a metal target. The excess of kinetic energy of electrons slowed or stopped by the atoms of the metal is converted into an X-ray radiation of equal energy. The Bremsstrahlung is characterized by a continuous distribution of the radiation [Fultz and Howe, 2013]. In the last years, a new type of radiation called synchrotron radiation characterized by an extreme energy and a broad electromagnetic spectrum produced by storage rings has been developed.

3.2.2. Synchrotron radiation

3.2.2.1. Introduction to synchrotron radiation

Synchrotron radiation (SR) is an electromagnetic radiation emitted when charged particles (electrons or positrons) are accelerated in a magnetic field at relativistic speeds in circular orbits. The radiation is emitted in a narrow cone in the direction of the motion of electrons. SR is a highly collimated, extremely intense beam and has a broad energy range from infrared to hard X-rays [Attwood, 2000]. Therefore, SR has become an important tool in different research areas such as materials sciences and medical sciences. Due to these characteristics, SR was chosen as a main tool for the investigation of the microstructure of GH during this project. The description of synchrotron facilities used is presented in Chapter 4.

SR is produced in normal bending magnets or special designed magnets called wigglers and undulators (see Figure 3-3). Bending magnet radiation is generated by electrons travelling in a uniform magnetic field in circular trajectory with acceleration directed toward the center. The radiation emitted is directed tangentially outward in a narrow cone. The spectrum of bending magnet radiation is very broad, characterized by an emission angle $1/\gamma$, where γ is the Lorentz contraction factor [Attwood, 2000].

Wiggler radiation is generated from periodic magnet structures with strong magnetic field. The accelerations are stronger and the angular excursions are larger than the normal radiation cone ($1/\gamma$). The spectrum of wiggler radiation is broad, characterized by higher photon flux and shifted to harder x-rays (shorter wavelengths). On the other hands, undulators are a weaker magnetic field version of wigglers. Due to the small magnetic field, the oscillation amplitudes are weak called undulations which give rise to a narrower emission angle: $\frac{1}{\gamma\sqrt{N}}$ where N is in the order of 100. The spectral width is

very narrow and the radiation is very bright and partially coherent which can be related to the coherence properties of lasers. SR is generated in storage rings consisting of circular evacuated pipes where charged particles are forced to follow circular trajectories under the action of magnets placed along the circumference. The charged particles are pre-accelerated to high speed and energy in linear accelerator or "linac" prior entering in the storage ring. This operation is known as injection. Electrons may be further accelerated by the radio frequency electric fields. During each turn in the storage ring, electrons lose a part of their energy emitting synchrotron light. The energy lost may be recovered by passing through the radio frequency electric fields.

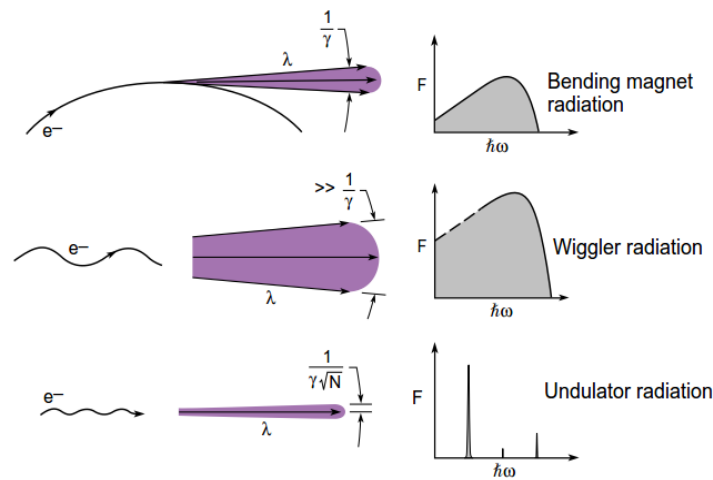


Figure 3-3. Three forms of synchrotron radiation [Attwood, 2007].

The first generation synchrotron radiation facilities were simple parasitic facilities built and operated for

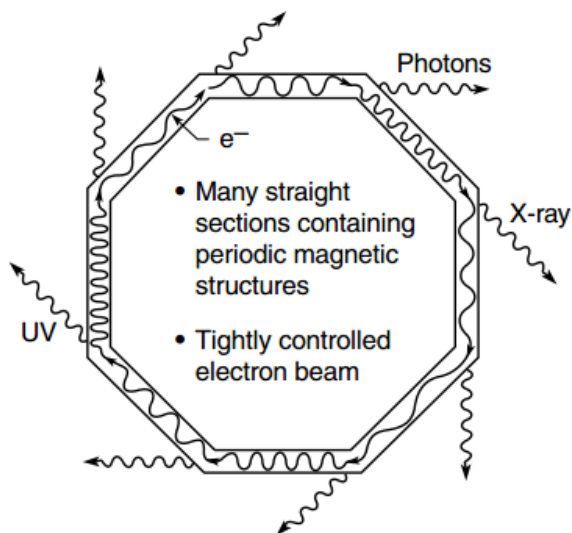


Figure 3-4. Schematic of the modern storage ring of the 3rd generation facilities [Attwood, 2007].

high-energy or nuclear physics, using the lost radiation at existing storage rings. Over time, in the mid-70's, sources totally dedicated to synchrotron light using bending magnets representing the second generation sources have been constructed. The third generation of synchrotron facilities is characterized by new magnetic structures like wigglers and undulators placed in many straight sections to produce high brightness radiation. Figure 3-4 illustrates the storage ring of the third generation facilities.

3.2.2.2. Properties of synchrotron radiation

The essential features of SR of interest for a user depend on the characteristics of the storage ring. Therefore, the user always chose the SR facility or beam line which satisfies his

requirements for the experiment. A SR facility can be characterized by the following properties:

- **Broad spectrum:** SR facilities have very broad and continuous spectral range from infrared to hard X-rays. Users can select the wavelength suitable for their experiments [Baruchel et al., 1993].
- **High photon flux:** the photon flux at a given wavelength is an important parameter of interest for a user. It is defined as the number of photons emitted per second in a spectral bandwidth. The high intensity of the beam permits to do fast experiments and to detect weakly scattering particles [Baruchel et al., 1993].

- Total flux: number of photons emitted per unit time

$$\text{Total flux} = \frac{\text{Photons}}{s} \quad [\text{Roehlsberger, 2005}] \quad (3.1)$$

- Spectral flux: number of photons emitted per unit time in a small bandwidth usually taken to be 0.1%

$$\text{Spectral flux} = \frac{\text{photons/s}}{0.1\% \text{bandwidth}} \quad [\text{Roehlsberger, 2005}] \quad (3.2)$$

- **Brightness:** the user is more interested in the photon flux impinging on the sample which depends on the flux per solid angle called the brightness. It is defined as the number of photons per unit time in a 0.1 % bandwidth normalized to the phase space volume.

$$\text{Brightness} = \frac{\text{photons/s}}{\text{mrad}^2 \cdot 0.1\% \text{bandwidth}} \quad [\text{Roehlsberger, 2005}] \quad (3.3)$$

- **Brilliance:** SR has high brilliance due to the high degree of collimation and the small cross section of the beam. The brilliance became the parameter which characterizes the performance of a SR facility. It is defined as the photon density in the image spot per solid angle in a 0.1 % bandwidth.

$$\text{Brilliance} = \frac{\text{photons/s}}{\text{mrad}^2 \cdot \text{mm}^2 \cdot 0.1\% \text{bandwidth}} \quad [\text{Roehlsberger, 2005}] \quad (3.4)$$

Actually the brilliance is the most relevant feature of the most experiments and considered as an important figure of merit for the development of new synchrotron radiation sources. Further properties of SR can be summarized into: high beam stability, good spatial coherence, high degree of polarization, and pulsed time structure.

3.3. X-ray imaging and computed tomography

X-ray imaging is known since the discovery of X-rays by W.C. Roentgen in 1895 characterized by their ability to penetrate opaque matter. The famous radiograph of W. C. Roentgen's wife illustrated in Figure 3-5 was the first X-ray picture [Cierniak, 2011]. X-ray imaging is based on the contrast



Figure 3-5. X-ray picture of the hand of Roentgen's wife Bertha [Cierniak, 2011]

resulting from the inhomogeneous response of the object to X-rays [Baruchel, 2004]. X-ray radiography introduced by W. C. Roentgen uses the phenomenon of X-ray attenuation by matter as a source of contrast. For many years, X-ray absorption radiography was the only form of X-ray imaging. Lately, new imaging methods using the phase shift as a source of contrast have appeared. Computed tomography (CT) became feasible with the development of computer software and mathematical algorithms which permit to reconstruct a three-dimensional (3D) image from multiple adjacent projections of the object collected during rotation at different angles. CT imaging was first established in medicine but later extended to

applications in chemistry, physics, materials sciences and recently geosciences.

3.3.1.1. Interaction of X-rays with matter

The fundamental aspects of the theory of X-ray interaction with matter and how this interaction can be used in imaging is presented in this section. The interaction between X-rays and a specimen depend on both characteristics of the radiation (i.e. wavelength) and the object (i.e. composition, density). In addition to their ability to penetrate matter, X-rays can also refract in a similar way as light. Due to refraction, when X-rays travel through matter, the amplitude and the phase of the electromagnetic wave are both affected: the amplitude gets attenuated and the phase gets shifted. The interactions of X-rays with an object can be described using the complex refractive index:

$$n = 1 - \delta + i\beta \quad (3.6)$$

where δ describes the absorption of X-rays and β the phase change with respect to a path in free space [Baruchel, 2004].

Figure 3-6 illustrates the phase shift and attenuation of a wave by an object.

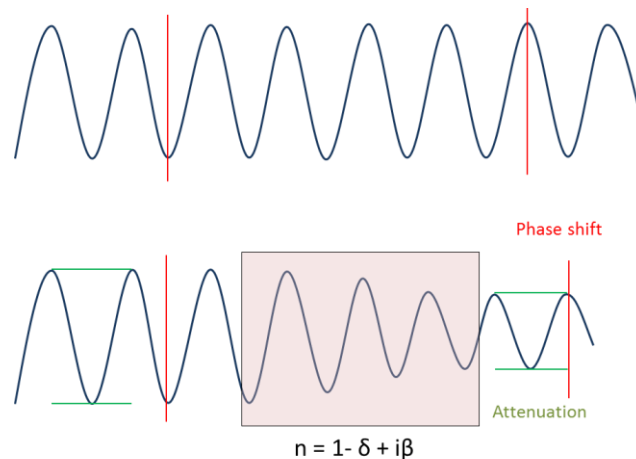


Figure 3-6. Phase shift and attenuation of a wave in a medium with refractive index $n = 1 - \delta + i\beta$. The amplitude is attenuated as indicated by green lines and the phase is shifted with respect to the wave propagating in vacuum as indicated by red lines (reproduced from http://en.wikipedia.org/wiki/Phase-contrast_X-ray_imaging).

3.3.1.2. Attenuation

X-ray absorption occurs when an X-ray photon is absorbed by an atom and the excess of energy serves to eject an electron from the atom leaving it ionized; this process is known as the photoelectric absorption [Als-Nielsen and McMorrow, 2001]. The attenuation of X-rays is related to the loss of the amplitude of the X-ray wave. At a given X-ray energy, the attenuation of X-rays depends on the density, thickness and the elemental composition of the imaged object. The absorption is expressed by the linear absorption coefficient μ which is a function of the photon energy. The attenuation is expressed by the relationship between the incident (I_0) and the transmitted intensity (I) emerging from a specimen with thickness x as follow:

$$\frac{I}{I_0} = \exp\left[-\int \mu(x,y,z)dx\right] \quad (3.7)$$

The linear absorption coefficient μ is related to β through the expression:

$$\beta = \frac{\lambda\mu}{4\pi} \quad (3.8)$$

where λ is the X-ray wavelength.

3.3.1.3. Phase shift

The phase shift is an alternative source of contrast in X-ray imaging. X-ray absorption is an excellent tool in distinguishing between heavier elements and low-absorbing materials such as soft tissues. In some cases (e.g. tumors in breast), there is a need to differentiate between different types of soft tissues. Due to the low absorption of such materials and the small differences in density and chemical composition, X-ray absorption radiography is not suitable in this case. The phase shift cross section of soft tissue is much larger than the absorption cross section.

The refractive index deviates slightly from unity through a decrement δ which is in the order of 10^{-5} - 10^{-6} . δ is proportional to the electronic density (mass density) of the material. It can be expressed as:

$$\delta = \frac{\lambda^2 r_0}{2V\pi} \sum_j N_j Z_j \quad (3.9)$$

where r_0 is the classical electron radius ($2.82 \cdot 10^{-5} \text{ \AA}$), and N_j is the number of atoms of atomic number Z_j present in the volume V .

When X-rays pass through an object, the phase gets shifted. The phase shift can be written as:

$$\varphi(x,y) = \frac{2\pi}{\lambda} \int_{\text{path}} \delta(x,y,z) dz \quad (3.10)$$

This method is very sensitive to small changes in density and composition within the material. This phase change is measured using more complex systems than X-ray absorption [Baruchel, 2004].

3.3.2. Imaging methods

3.3.2.1. X-ray absorption radiography

X-ray absorption is a simple method of X-ray imaging which does not require complex optics. It consists in measuring the transmitted intensities through the sample using an area detector and to obtain a distribution of the integral of μ along the X-ray path. The contrast in the images results from the variation of the transmitted due to the differences in the absorption cross-section of the constituents of the object (Figure 3-7).

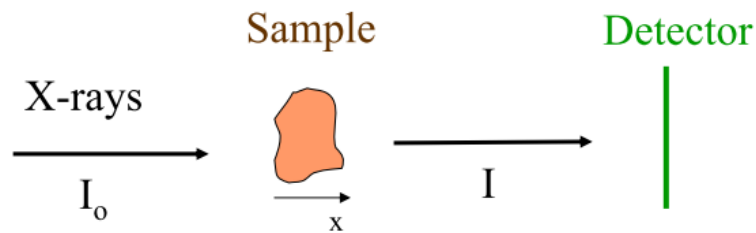


Figure 3-7. Principle of conventional X-ray absorption radiography [Baruchel, 2012]

3.3.2.2. Phase contrast imaging methods

In the last years, several imaging techniques based on phase contrast have been developed. A brief summary of these methods is given in the following.

Crystal interferometer:

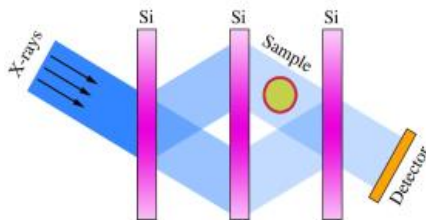


Figure 3-8. Crystal interferometer [Bech, 2009]

This method was first used by [Bonse and Hart, 1965]. It consists of using three crystals aligned parallel to each other to split the X-ray beam. Figure 3-8 shows a sketch of a crystal interferometer setup. The first crystal splits the beam in two; one beam remains undisturbed and the second beam passes through the sample before the two beams are recombined at the third crystal due to the action of the second crystal. The phase shift induced by the sample creates an interference pattern which is measured by a detector placed behind the last crystal. The method requires high spatial coherence [Bonse and Hart, 1965; Momose, 1995].

Analyzer based imaging:

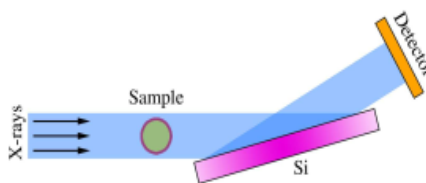


Figure 3-9. Analyzer based imaging [Bech, 2009]

This method is known as well as diffraction enhanced imaging method and was introduced by [Goetz *et al.*, 1979; Ingal, 1995]. In this method, a collimated beam passes through the sample and then an analyzer crystal placed in Bragg geometry reflects the beam onto the detector (see Figure 3.9). When X-rays hit the analyzer, only the signals of a part of the beam which satisfies the Bragg condition will be measured by

the detector. The crystal is slightly rotated in θ (rocked) in order to analyze different refraction angles [Wernick *et al.*, 2003]. Data set of images from different positions on the rocking curve is recorded. The contrast of the image is based on different refraction angles in the sample.

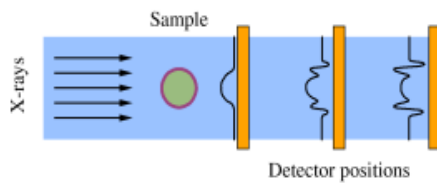
Propagation based imaging:

Figure 3-10. Propagation based imaging [Bech, 2009]

It is a simple method of phase contrast as it requires only an X-ray source, sample and an X-ray detector placed at different distances behind the sample [Cloetens *et al.*, 1997; Snigirev *et al.*, 1995; Wilkins *et al.*, 1996]. The method consists of measuring the interference pattern of Fresnel fringes arising in the free space propagation in the Fresnel regime. For the distance between the detector and the sample, the Fresnel diffraction equation is valid for the near field. The measured intensity fringes are proportional to the second derivative (the Laplacian) and not a direct measure of the phase of the wave front. High spatial coherence and high resolution detector are required [Cloetens *et al.*, 1997; Wilkins *et al.*, 1996].

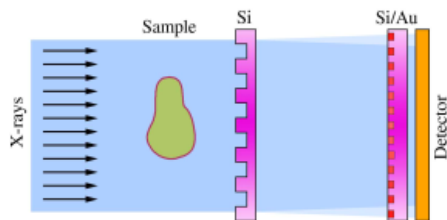
Grating interferometry:

Figure 3-11. Grating based imaging [Bech, 2009]

This technique was recently developed and it consists of two phase gratings and an analyzer crystal placed between the sample and the detector. The method is based on the "Talbot effect" or the called self-imaging phenomenon which is a near-field diffraction effect (Fresnel effect) that produces repetitive periodic wave front at regular distances called the Talbot length. The periodic wave front generated by a spatial coherent beam of a diffraction grating generates a wave intensity pattern at the Talbot length which resembles to the structure of the grating called self-image [Talbot, 1836]. The refraction in a sample is measured by detecting the transverse shift of the interference pattern with a high resolution detector [Takeda *et al.*, 2007].

3.3.3. Computed Tomography (CT)

Computed tomography is a nondestructive technique which uses computer software to visualize the interior characteristics of an object and to generate a digital 3D image from multiple adjacent 2D images taken around the axis of rotation of the object. The CT scanner was developed by G. Hounsfield and his co-worker A. Cormack in the beginning of 1970ies in England. They were awarded the Nobel Prize in medicine in 1979 for their invention [Cormack, 1973; Hounsfield, 1973].

3.3.3.1. Sample preparation

The most efficient geometry of the investigated sample is a cylinder because the full scan field of a CT is a stack of circular fields of view (cylinder) [Ketcham, 2001]. Therefore, it is recommended to have the object in a cylindrical form or by packing the sample in a cylindrical container. The cylindrical geometry permits as well a good centering of the object and a constant X-ray attenuation at different angles. Furthermore, the object should fit inside the field of view and remain fixed or motionless during the scan.

3.3.3.2. Scanning configurations and data collection

There are different configurations of CT measurements which depend on the geometry of the X-ray source and detectors with respect to the sample. For our experiments we use the parallel beam

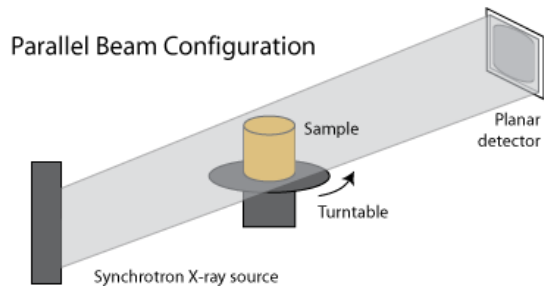


Figure 3-12. Schematic illustration of different CT configurations [Ketcham, 2012]

scanning configuration based on synchrotron radiation which provides a parallel and high intense X-ray beam allowing for fast data acquisition and greater penetration as our sample is embedded in a pressure cell. In this configuration, a small size of the sample is required [Ketcham, 2012]. Figure 3-12 illustrates the parallel beam configuration.

The data collection consists of rotating the sample with small steps over 180° (or 360°) and taking 2D cross-section images. The most important parameters which should be taken into account during the scan are the number of views and the acquisition time per view.

3.3.3.3. Image reconstruction

Image reconstruction is a mathematical process which consists in creating 2D images from measured projections data acquired at different angles around the object. The reconstruction method has a considerable impact on the quality of images generated. For X-ray absorption imaging, the parameter that has to be reconstructed is the linear attenuation coefficient μ which is proportional to the density of the object. In the following, the basic concepts of the reconstruction in parallel-beam geometry are presented.

There are two general methods: filtered back-projection (FBP) and iterative reconstruction.

FBP is the most commonly used method to reconstruct data. X-rays passing through the object produce a particular density profile on the detector. It is possible from many projections to back project individual detector distributions into image space that produces the 2D image. The projection is a set of measurements of the integrated values of μ (in case of absorption radiography) along straight lines called line integral. A line integral can represent the total attenuation of X-rays as they pass through the object in a straight line. The measured projection along the X-ray path l at angle θ is expressed as follow:

$$p(l, \theta) = \exp \left[- \int \mu(l) dl \right] \quad (3.11)$$

This equation can be written in more practical way:

$$p(l, \theta) = \exp \left[- \sum_{ij} l_{ij} \mu_{ij} \right] \quad (3.12)$$

where j is a pixel index, I_i is the set of image pixels through which X-ray beam i passes, l_{ij} is the intersection length of beam i with pixel j , and μ_j is the attenuation coefficient for pixel j [Paulus *et al.*, 2000].

If $f(x,y)$ represents the image to be reconstructed, the line integral projection through $f(x,y)$ is called the Radon transform. The transform was suggested by John Radon in 1917 and he provided as well a formula for the inverse transform. The inverse of the Radon transform allows reconstructing the original density from the projection data. The radon transform data is commonly referred to as a sinogram because the Radon transform of Dirac delta function describes a sinusoid [Paulus *et al.*, 2000]. Backprojection consists in converting the data in the sinogram to CT numbers or CT values in order to produce a backprojected image. However, simple back projection generates a somewhat blurred image. Therefore, the concept of filtered back projection provides a better image fidelity (see Figure 3-13).

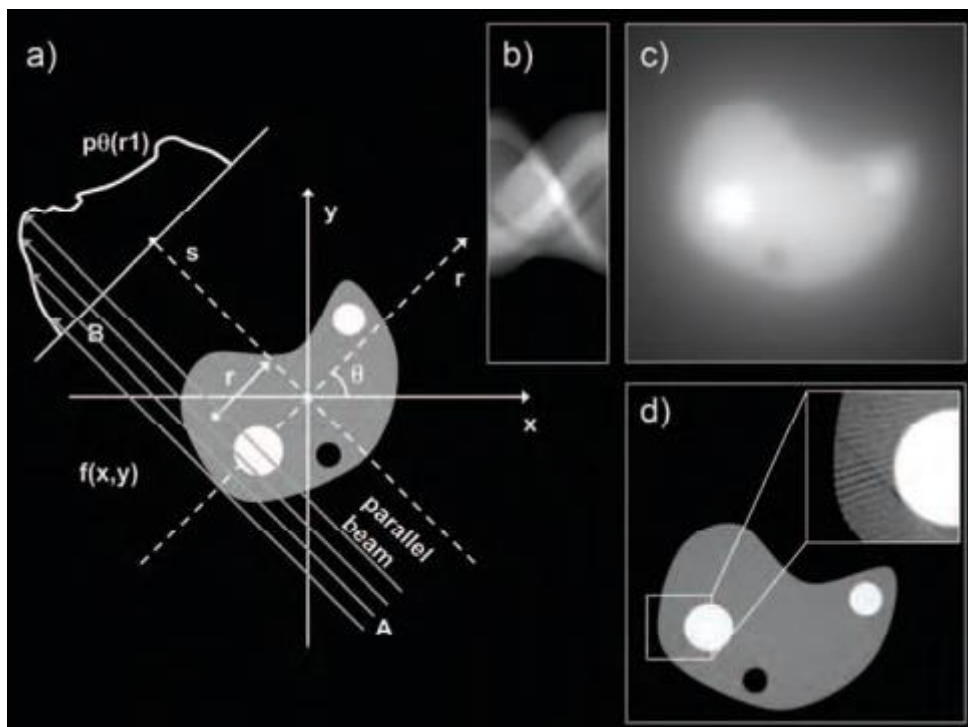


Figure 3-13. a) Geometrical representation for obtaining the sinogram as demonstrated in b) and which is back projected as shown in c) without applying filtering and d) applying a ramp filter (the cut-out has been enhanced in contrast to display artefacts due to reconstruction [Zehbe *et al.*, 2010].

3.3.4. Resolution and image quality

The spatial resolution is an important characteristic of any imaging system. The spatial resolution depends on the physical parameters such as the size of detector elements, size of the focal-spot and the source-object-detector distances and on the image-reconstruction methods as well. The spatial resolution refers to the ability to distinguish two objects in an image.

The ability to distinguish the different phases of the scanned object is an essential task in X-ray tomography. This depends on the density and chemical composition of the specimen as well as on the experimental settings such as the X-ray energy, sample to detector distance and signal-to-noise

ratio. For materials with similar properties, only large scale and big particles can be imaged while if they are different high spatial resolution can be achieved and very fine details can be seen.

The sample size can represent a constraint; therefore the choice of the size of the object depending on the characteristics of the CT machine is very important. If the sample is too thick, X-ray attenuation will be high and only small X-ray flux will reach the detector which results in a poor image quality. Small sample size is required to achieve micron or sub-micron resolution. Larger samples can be scanned using synchrotron radiation which has greater penetration and a choice of wavelength [Ketcham, 2001].

3.3.5. Artifacts

CT imaging methods can be biased by scanning artifacts such as beam hardening or ring artifacts. These artifacts can obscure information of interest or simulate pathology. Here the most common artifacts and the approaches to solve them are discussed.

3.3.5.1. Beam hardening

This artifact leads to brighter edges of an object than the center which may give a wrong impression that objects are coated with high absorbing materials. The artifact occurs because when a polychromatic beam passes through an object, lower-energy photons are more absorbed than higher-energy photons which cause an increase in mean X-ray energy or "hardening" of the X-ray beam. Therefore, an artificial darkening of the center of long ray paths and a corresponding brightening near the edges occur [Ketcham, 2001].

Several solutions were suggested to solve this problem which can be summarized in: removing the outer edges of the images or using high-energy beams to reduce the effect of beam hardening.

3.3.5.2. Ring artifact

This type of artifact appears in reconstructed images as full or partial centering circles centered on the rotational axis. Ring artifacts occur due to miscalibration or defection of one or multiple detector elements. These artifacts can be visible in many 2D sections at the same location. Flat-field correction or recalibration is commonly used to fix this problem [Wei *et al.*, 2013].

3.3.5.3. Partial volume effect

It is produced when the absorption of different substances is encompassed on the same voxel which has an average value of all substances. It appears as bands and streaks and could complicate the task of segmentation and volume or surface rendering. The solution proposed to reduce this type of artifact consists in using thinner slice and some computer algorithm [Souza *et al.*, 2005].

3.3.5.4. Motion artifact

The motion artifact is generated by sample movement during the scan. It causes blurring, double images and long range streaks in CT images. In medical CT, motion can be caused by body motion of the patient. Fast scans can reduce this artifact [Boas, 2012].

3.3.5.5. Other artifacts

Other artifacts in CT images can be summarized into metal artifact, noise (photon starvation), and out of field artifact [Boas, 2012].

3.4. X-ray Crystallography and diffraction

The phenomenon of X-ray diffraction (XRD) by crystalline materials was discovered by Max von Laue in 1912. Each specimen has a typical arrangement of atoms within its crystal structure; hence a specific diffraction pattern can be ascribed to each structure. Thus, XRD has become an important tool for the characterization of materials as well as for fundamental studies on the atomic scale which increased the understanding of their properties. XRD is a non-destructive method and it is suitable for *in-situ* studies of materials not stable at ambient conditions such as gas hydrates. XRD was used during this project as a quantitative tool for GH characterization. A new method for determining the crystallites size distribution (CSD) of polycrystalline materials based on two-dimensional (2D) XRD was developed.

3.4.1. Geometry of crystals

The concept of the unit cell is a fundamental concept in crystallography. The unit cell is the volume of the lattice which builds up the whole crystal structure by repeated translations along the three spatial directions. The shape and size of the unit cell is characterized by three lattice constants a , b , c which are the lengths of the basis vectors and by three angles α , β , γ which separate the vectors from another: α between the vectors b and c , β between a and c , and γ between a and b [Hammond, 2009] (see Figure 3-14)

In a unit cell, there are a number of equivalent parallel planes. The family of equivalent parallel planes is defined by Miller indices: h , k , and l (three integers). The “ hkl ” indices of each family of lattice planes are determined by the nearest plane to the origin which does not pass through it. The plane hkl intersects the a , b and c axes of the unit cell at $1/h$, $1/k$ and $1/l$ respectively [Massa, 2004].

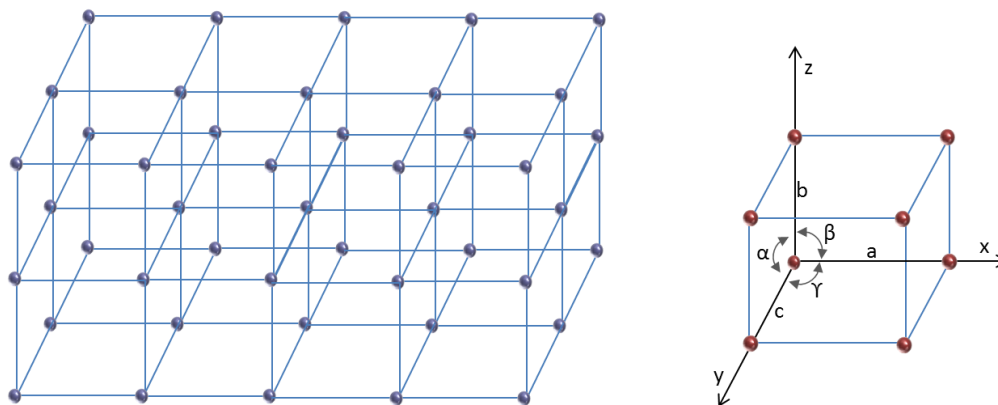


Figure 3-14. A point lattice and its unit cell

The most important characteristic of crystals, in addition to the three dimensional periodicity, is their symmetry (inversion, or rotation). The classification of crystals is based on their symmetry. All crystals can be classified into not more than 14 unit cell types known as the Bravais lattices (see Figure 3-15) [Massa, 2004].

3.4.2. Diffraction theory

3.4.2.1. Bragg's law

X-rays are scattered by matter in all directions. Diffraction occurs when X-ray waves are scattered in phase by ordered crystal atoms. The Bragg's law determines the conditions required for constructive interference between interfering diffracted waves in an easy way through one simple equation:

$$n\lambda = 2d \cdot \sin(\theta) \quad (3.13)$$

where λ is the wavelength, d is the distance between each adjacent crystal planes, θ is the Bragg angle at which one observes a diffraction peak, and n is an integer number called order of reflection.

Bragg diffraction occurs when the angle of incidence is equal to the angle of reflection. This angle must have such a value that the path difference between two rays reflected ($2d \sin \theta$) between neighboring planes is an integral number of the wavelength λ (see Figure 3-15).

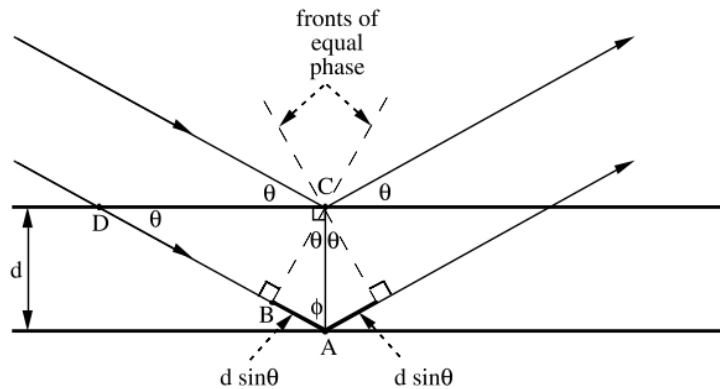


Figure 3-15. Geometry for interference of a wave scattered from two planes separated by spacing, d . The difference in path lengths is $2d \cdot \sin(\theta)$ [Fultz and Howe, 2013].

3.4.2.2. Reciprocal space and Ewald construction

The concept of the reciprocal lattice is used in crystallography in a combination with the Ewald sphere to explain visually the rules for when diffraction occurs. The reciprocal lattice is obtained by Fourier transform of the direct lattice. The dimensions and angles of the reciprocal cell are inversely proportional to the real unit cell and each family of planes in the real space is represented by a lattice point in the reciprocal space.

The Ewald sphere or Ewald construction was introduced by P.P. Ewald. The sphere is constructed such as the crystal is positioned in the center of a sphere with a radius of $2\pi/\lambda$ (where λ is the X-ray wavelength). The incident beam can be visualized by the wave vector k_i , and the diffracted beam is the wave vector k_d . Both vectors are at an angle θ from the crystal planes (hkl) with d -spacing. The vector Q is the reciprocal lattice and scattering vector and is perpendicular to the crystal planes for any value of θ .

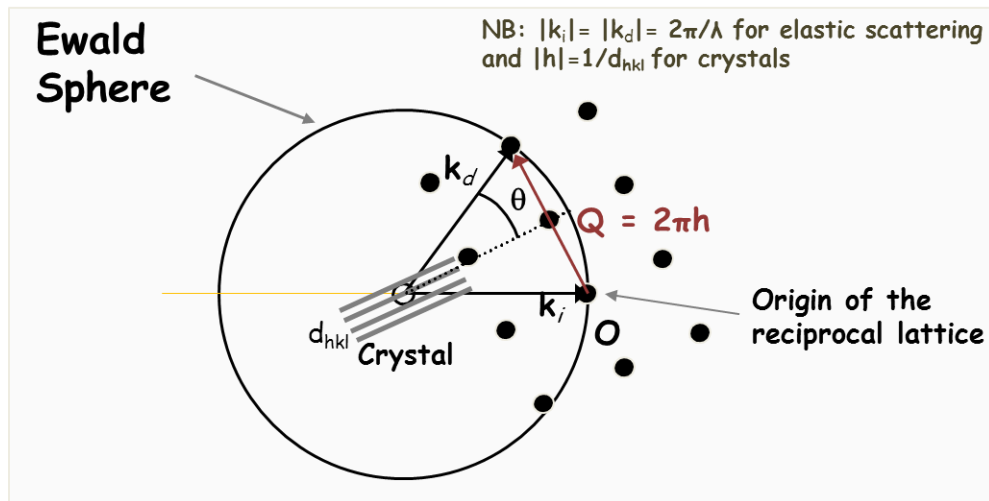


Figure 3-16. The Ewald construction (modified from a private communication of Sylvain Ravy found at <http://www-int.impmc.upmc.fr/impmc/Associations/CGE-2008/PPT/Ravy.ppt>).

This vector has a length of $(2|k|\sin\lambda)$ and as the sphere has a radius of $1/\lambda$ we obtain: $|Q|=4\pi\sin\lambda/\lambda$. The vector Q itself corresponds to $2\pi/d_{hkl}$ in diffraction theory, hence $1/d_{hkl} = 2\sin\theta/\lambda$ which is comparable to the Bragg's law ($\lambda = 2d\sin\theta$). This means that wherever a reciprocal point falls on the Ewald sphere (scattering vector Q intersects with the Ewald sphere), Bragg's law is obeyed and a diffracted beam is observed. For a fixed λ one needs to move the reciprocal lattice (and thus the crystal) in order to bring the different hkl planes or lattice points in diffraction condition i.e. onto the Ewald sphere [He, 2009]. The Ewald sphere is in fact for any real experiment a shell with a finite thickness due to the fact that perfectly monochromatic radiation does not exist. During the rotation of a crystal, the lattice points stay in the diffraction condition from the point they touch the Ewald sphere shell until they move out of it. During this movement, the intensity of the reflection increases until it reaches a maximum at the center of the Ewald shell then starts to decrease. The variation of the diffracted intensity during the rotation of the crystal is described by the rocking curve plot: intensity versus angle of rotation.

3.4.3. Structure factors

The scattering of X-rays is generated by electrons surrounding the atom. The amplitude of the wave scattered by an atom is essentially the sum of all Z electrons around the nucleus. The scattering amplitude is expressed by the number f , called the "atomic scattering factor", which is the ratio of the scattering amplitude of the atom divided by that of a single electron [Hammond, 2009].

$$\text{atomic scattering factor } f = \frac{\text{amplitude scattered by atom}}{\text{amplitude scattered by electron}} \quad (3.14)$$

The electrons around an atom scatter radiation in the manner described by Thomson. Due to the coherence of the wave hitting the atom, the summation must take into account the phase differences between the different scattered waves. This leads to a strong angular dependence of the scattering. At θ angle equal to zero, f is equal to Z . The scattering amplitude decreases as the

scattering angle θ increases because of the increase of the number of destructive scattered waves. In an X-ray diffraction pattern, the peak intensities drop off at high θ values because of the decrease of the form factor.

The scattering amplitude of a unit cell is the sum of contributions from all atoms in the unit cell. It is called the structure factor and it is expressed by F_{hkl} . The structure factor is the Fourier transform of the electron density of the unit cell:

$$\rho_{uvw} = \sum_n \rho_n(r - r_n) \quad (3.15)$$

$$F(q) = \rho_{uvw}(r) e^{-iqx} = \sum_n f_n e^{-iqx_n} \quad (3.16)$$

$$F_{hkl} = \sum_1^n \sum_j f_n e^{2i\pi(hu_n + kv_n + lw_n)} \quad (3.17)$$

where f_n is the form factor of the n^{th} atom in the unit cell, and (u_n, v_n, w_n) are its fractional coordinates. The structure factor defines and the amplitude and the phase of the scattering wave resulting from the scattering of all atoms in the unit cell [He, 2009].

3.4.4. Diffracted intensity

The diffracted intensity is proportional to the structure factor squared but there are as well several physical and geometrical factors which must be taken into account such as the multiplicity, the absorption and the Lorentz-polarization factor. The integrated intensity for a powder can be written as follow:

$$I \approx k M_{hkl} A LP(\theta) |F_{hkl}|^2 \quad (3.18)$$

where k is an instrument constant that is the scaling factor between experimental observed and calculated intensity, A is the absorption factor, M_{hkl} is the multiplicity factor of the crystal plane (hkl) , LP is the Lorentz and Polarization factors. This equation does not include the possible effects of the preferred orientation and extinction.

3.4.4.1. Multiplicity factor

Equivalent parallel planes in a crystal give rise to the same reflection. The intensity of the reflection is proportional to the number of planes. The diffraction from each plane produces a reflection with the same intensity; therefore the total diffracted intensity from this family of planes corresponds to the intensity from one of the equivalent planes times the number of equivalent planes or the multiplicity. The multiplicity depends on the crystal structure [He, 2009].

3.4.4.2. Absorption factor

When an X-ray beam passes through the material, an X-ray photon is absorbed by the atom and the excess of energy serves to expel an electron from the atom. Hence, the intensity is reduced due to the process of photoelectric absorption. The attenuation of X-rays depends on the density and thickness of the specimen. It follows an exponential decay and it is given by the linear absorption coefficient μ . The intensity attenuated by the sample can be expressed by the Beer-Lambert's law:

$$I = I_0 e^{-\mu t} \quad (3.19)$$

where I , is the intensity through the material, I_0 the incident intensity, μ the linear absorption coefficient and t the thickness of the material [Als-Nielsen and McMorrow, 2001].

3.4.4.3. Lorentz factor

For a fixed λ , the various reciprocal lattice points will pass through the Ewald sphere at different speeds during the rotation of the sample. Consequently, they don't spend equal times in the diffraction condition. The diffracted intensity depends on the time opportunity to reflect. As a small crystal may stay for a long time in diffraction and give unexpected high intensity so it is necessary to correct the intensities for the so called Lorentz factor. The Lorentz factor is inversely proportional to the velocity of the hkl reflection [Buerger, 1940]. Hence, it depends on both the diffraction geometry and the diffraction Bragg angle. The Lorentz factor corresponds to the Jacobian (mathematical concept of a derivative of a coordinate transformation) of the transformation from angular space to q space [Smilgies, 2002]. For in-plane diffraction and rod scans other than the specular rod, it can be expressed as:

$$L = 1 / [\cos(\alpha) \sin(\psi) \cos(\beta)] \quad [\text{Smilgies, 2002}] \quad (3.20)$$

with the azimuth rotation ϕ as the rocking angle.

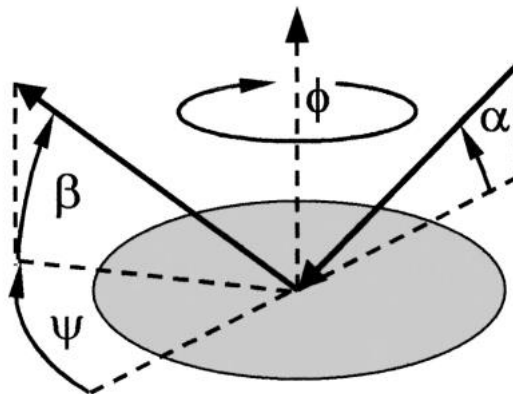


Figure 3-17. Scattering angles in the surface reference frame: incident angle α , in-plane scattering angle ψ , exit angle β , and azimuth ϕ . These angles co-incide with the respective diffractometer axes in the z-axis scattering geometry ([Smilgies, 2002]).

3.4.4.4. Polarization factor

Synchrotron radiation is polarized in the horizontal plane and perpendicular to the beam direction k . The general expression for the polarization factor is:

$$P = \sin^2 [\angle(p, k_s)] = \|\mathbf{p} \times \mathbf{k}_s\|^2 \quad (3.21)$$

where p and k_s are unity vectors in the direction of the polarization of the incident beam and the wave vector of the scattered photon, respectively, whereas $\angle(p, k_s)$ denotes the angle between p and k_s [Smilgies, 2002].

3.4.4.5. Temperature factor

The diffracted intensity is influenced by the thermal vibrational amplitude of the atoms in the unit cell. The vibration of atoms around their equilibrium position increases as the temperature increases which leads to a change in the lattice spacing and an overall decrease of the intensity. The effective scattering can be described by the following relationship:

$$f = f_0 - B \sin^2 \theta / \lambda^2 \quad (3.21)$$

where B is the Debye-Waller temperature factor which is defined as $B = 8\pi^2 U^2$. U^2 represents the mean-square amplitude of vibration of an atom and is directly related to the thermal energy (kT). The increase in temperature leads to a linear increase of B for a harmonic crystal and as B increases, the scattering amplitude will be reduced in particular at high scattering angles θ .

3.4.5. Fast X-ray crystallite size determination (FXRCS) method

3.4.5.1. Motivation

There is currently considerable scientific interest in crystallite size analysis. The properties of polycrystalline materials are considerably dependent on their microstructure characteristics such as the average crystallite size, and crystallite size distributions (CSD's). The size of grains has significant effect on the mechanical properties e.g. the dependency of yield strength of metals and alloys on the grain diameter via the Hall-Petch relationship [Hall, 1951; Petch, 1953]. Material with finer particles has more boundaries to impede dislocations movement and, therefore, has higher mechanical strength. Furthermore, particle size and size distribution can be related to the physical, chemical and pharmacological properties of drugs such as the dissolution rate, activity and stability. Smaller particles will have big surface area which allows an intimate contact of the drug with the dissolution fluids in-vivo and increases the drug solubility and dissolution. Hence faster and greater drug action is obtained. CSD's are also of particular importance because they carry information about the formation process (natural samples) and enable better understanding of the manufacturing process. Thus the determination and control of crystallite size and CSD's is of considerable importance in both geosciences and materials science.

Current techniques for the analysis of crystallite size can be categorized into optical methods such as Laser light scattering and Laser diffraction, physico-chemical techniques such as sedimentation and sieving and electron microscopy techniques such as scanning electron microscopy and transmission electron microscopy. These methods offer advantages but they have certain limitations (e.g. time-consuming, applicability range) and in certain cases are unsuitable, in particular for unstable samples or *in-situ* investigations.

X-ray diffraction is one of the most direct ways of analyzing and extracting crystallite size information of polycrystalline materials over a wide range of sizes and there is a large literature concerned with methods of data processing in this context: The conventional method based on diffraction peak broadening developed by Scherrer in 1918 [Scherrer, 1918]. When the crystallites of powder specimen are sufficiently small, a broadening in the peak profiles of the diffraction pattern occurs. The peak width varies inversely with the grain size. The average crystallite size D can be calculated using the Scherrer's equation:

$$D = K \lambda / B \cos (\theta) \quad (3.22)$$

where B is the full width at half maximum intensity of the peak corrected for instrument resolution effects, λ is the X-ray wavelength, θ is the diffraction angle and K is the Scherrer constant. However, this method cannot be used to evaluate crystallite size larger than several micrometers. Ninety years later, T. Ida proposed a new method to overcome the above-described problems of the conventional analysis technique [Ida and Jiang, 2011]. He suggested a new method for calculating the average crystallite size based on statistical analysis of the intensities data. With this method, it becomes possible to evaluate grain size of polycrystalline material measuring several micrometers or greater using one dimensional diffractometers.

In the last years, the advances in detector technology made possible the collection of X-ray powder diffraction data in two-dimension (2D) using area detectors. This advent has enabled the development of new methods for particle size determination: The method of A. B. Rodriguez Navarro [Rodriguez Navarro *et al.*, 2006] determines the average crystallite size from the mean intensity of reflection peaks. This method has the advantage to be independent of the aggregation state and also adequate for material with different mineral phases. However, this method relies on a calibrant of the same material with known crystallite size which can limit its range of applicability. A few years later, [He, 2011] obtained a patent for his method called “quantitative γ -profile analysis”. The averaged crystal sizes are estimated by counting the number of Bragg peaks in the circumference of a Debye-Scherrer ring along the azimuthal angle γ . This method has an insufficient accuracy and it requires extreme care in sample preparation.

All methods described above are only dedicated to determine the average crystallites size. However, this parameter carries only limited information about the nucleation and growth processes of materials. Moreover, in statistics it is possible to have different distributions with the same mean value so wrong interpretation based only on the mean value can be made. Therefore, in order to fully understand the microstructural characteristics and the formation process of materials, an access to the CSD is highly desirable. From the shape of the distribution, information about some specific processes occurring during the formation such as recrystallization or Oswald coarsening can be obtained.

Here, a new method, based on 2D-XRD, derived from the former method is proposed for determining the CSD of polycrystalline materials (or powder) from peak intensities after calibration with material with known CSD is presented.

3.4.5.2. Background

The 2D diffraction pattern of polycrystalline sample or powder is composed of concentric Debye-Scherrer rings resulting from the intersection of a series of diffraction cones with an area detector. Each ring consists of reflections from many crystallites satisfying Bragg's law. A spotty diffraction pattern is obtained when few crystallites are illuminated (Figure 3-18). The number of diffraction spots in the Debye-Scherrer ring depends on several parameters such as the sample volume, crystallite size, beam size, and sample to detector distance. Such patterns offer the advantage to extract crystallite characteristics such as the volume.

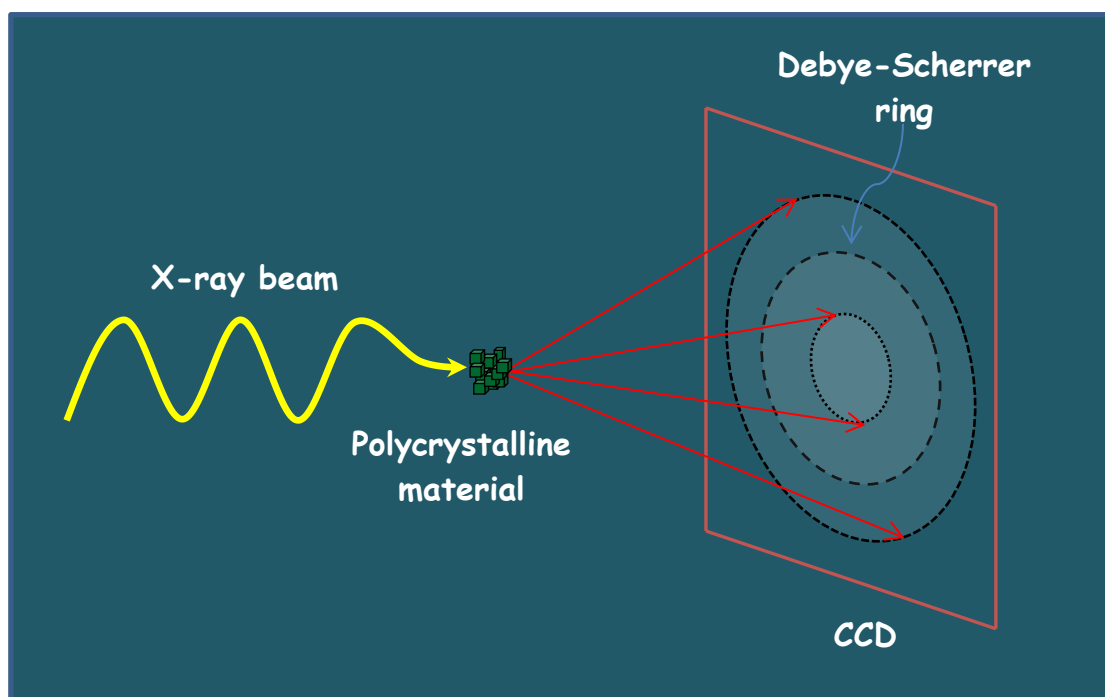


Figure 3-18. Principle of X-ray diffraction of Polycrystalline material

Crystallite sizes can be determined from the diffracted intensity of reflection spots. If the investigated crystal is far from being perfect, the diffracted intensity grows linearly with the crystal size [Als-Nielsen and McMorro, 2001]. For a given volume, the number of spots increases and their intensity decreases as the crystallite size decreases. Figure 3-19 illustrates the effect of the crystal sizes on the intensities.

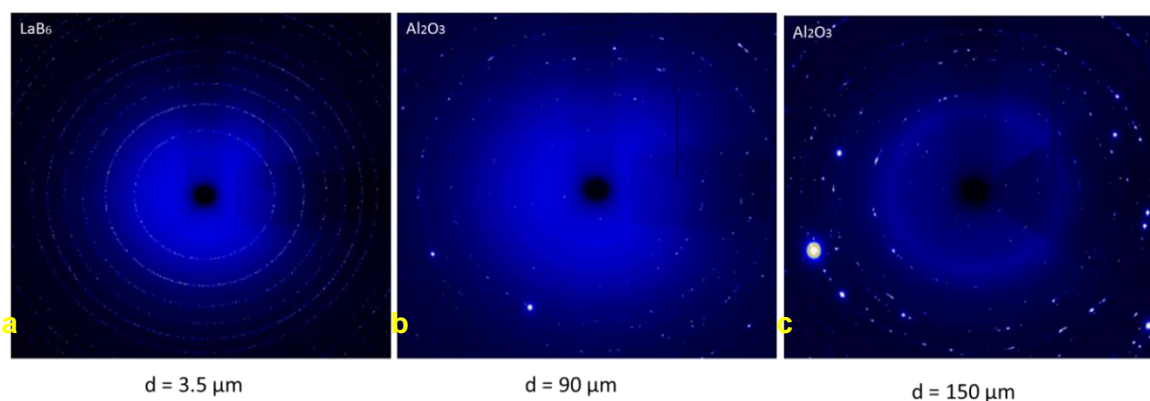


Figure 3-19. Effect of the crystallite size on the intensities of reflections in 2D XRD pattern of polycrystalline materials. a: LaB₆ powder with $d = 3.5 \mu\text{m}$, b: Corundum Al₂O₃ powder with $d = 90 \mu\text{m}$, and c: Corundum Al₂O₃ powder with $d = 150 \mu\text{m}$. From a to c, the number of reflections decreases and the intensity increases with the increase of the average crystallite size (diameter (d)) at the same experimental settings.

3.4.5.3. Principle of the method

The novel approach of the present method is that, rather than using the same material with known crystallite size for calibration as it is the case in the method of (A. Rodriguez Navarro), the

calibrant can be a different material with known CSD. However, the method requires that the crystallographic structures of the calibrant and the investigated material are known in advance. If the latter has an unknown structure, a phase analysis can be achieved using XRD in order to determine the crystallographic structure before starting the CSD measurements. The material used as calibrant must have the following characteristics: single crystal particles, and no preferred orientation.

The calibration of intensities is done in two steps via two scale factors:

- First scale factor S_1 :

The intensity is proportional to the number of unit cells within a crystal. Therefore a large crystal produces a high intensity spot because it contains more unit cells than a small crystal.

The first scale factor relates the measured intensity to the known crystallite size volume of the calibrant:

$$V = S_1 \times I \quad (3.23)$$

- Second scale factor S_2 :

The diffracted intensity depends on the structure factor squared which itself depends on the unit cell volume. Thus, the intensity is inversely proportional to the cell volume because the number of unit cells per unit volume in a crystal decreases when the unit cell volume increases.

Hence we can write: $I \sim |F^2|/V_c$

As the calibrant and the materials investigated have different crystal structure, intensities must be normalized to unit cell volume via the scale factor S_2 determined by the ratio of the structure factor of the corresponding hkl reflections:

$$S_2 = \frac{I[i]_{\text{calibrant}}}{I[i]_{\text{material}}} = \frac{(|F^2|/V_c)_{\text{calibrant}}}{(|F^2|/V_c)_{\text{material}}} \quad (3.24)$$

In case of a calibrant of the same material, only the first scale factor is needed.

3.4.5.4. Methodology

The method comprises the steps of:

- (1) determining the CSD of the calibrant material e.g. by a electron optical method like SEM,
- (2) mounting the sample on a 2D-XRD machine and adjusting the beam size and/or the sample volume to get a spotty diffraction pattern of few tens of spots per ring,
- (3) measuring the calibrant by stepping in omega or by an omega rotation of a few degrees,
- (4) analyzing the 2D diffraction frames and extracting peak intensities of the corresponding hkl reflections to obtain intensities distribution (ID) of the calibrant material (see section Acquisition and data processing),
- (5) fitting the probability density function of a log-normal distribution to both, the CSD and the ID of the standard, to establish the scale factor " S_1 " between the two mean values of the two fits,
- (6) measuring the investigated material under the same conditions (same geometry, exposure time, sample to detector distance),
- (7) extracting peak intensities of the corresponding hkl reflections of the investigated material,

- (8) calculating the structure factors ratio of the standard and the investigated material to be used as a second scale factor " S_2 ",
- (9) using S_1 and S_2 for calculating the crystal sizes of the investigated material,
- (10) applying some other geometric correction factors which could be problematic such as the Lorentz correction.

4 | Experimental section

In the following Chapter, a detailed description of the starting materials, experimental devices and methods used are presented.

4.1. Formation of gas hydrate in porous media

4.1.1. Starting materials

4.1.1.1. Porous media

All natural sediments used in the preparation of synthetic GH samples were the same as the ones used in the work of *Klapproth et al.* [2007], which were provided by Dr. Chuvilin (Moscow State University). Natural quartz (Qz) sand, consisting of rounded shaped grains with grain sizes of 200-300 μm were obtained from Lyubertsy/Moscow region/Russia and kaolinite and montmorillonite from Dzhebel/Turkmenistan [*Chuvilin et al.*, 2011]. The main grain sizes of kaolinite are around 7 μm and 15 μm for montmorillonite. The granulometric composition of the sediments provided by Chuvilin (2012) is given in Table 4-1 and the grain size distribution measured using Laser granulometer type LS 230, Beckman Coulter Inc. by A. Klapproth (2006) is presented in Figure 4-1.

Table 4-1. Granulometric composition of sediments [*Chuvilin and Istomin*, 2012]

Sediment	Grain size distribution %		
	1000-50 μm	50 - 1 μm	< 1 μm
Qz sand	94.8	3.1	2.1
Kaolinite	4.5	70.9	24.6
Montmorillonite	0.3	46.2	53.5

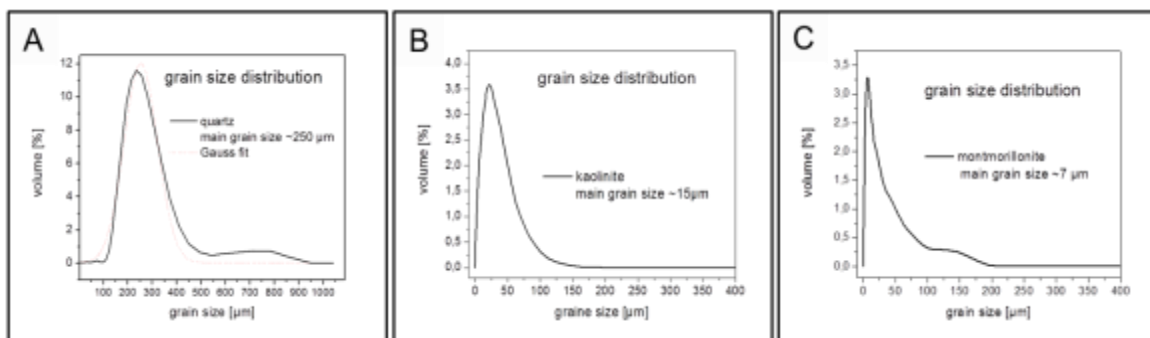


Figure 4-1. Grain size distributions of A) Qz sand, B) kaolinite and C) montmorillonite [*Klapproth*, 2006].

In addition to natural samples, synthetic glass beads (GB) were purchased from Sigma-Aldrich Germany. The particles have a spherical shape with a diameter of 150-212 μm . Qz sand and GB were used plain without further treatment and in some experiments a special treatment to obtain hydrophilic and hydrophobic properties of the surface was applied. The hydrophilic treatment consists of cleaning the porous media for one hour using a freshly prepared Piranha solution [3:1 H_2SO_4 (98%)/ H_2O_2 (30%)] at 90°C. Subsequently the media were rinsed with deionized water and dried in an oven at 120°C for 1 h. The resulting cleaned surface is hydrophilic due to the added reactive Si-OH groups (see Figure 4-2).

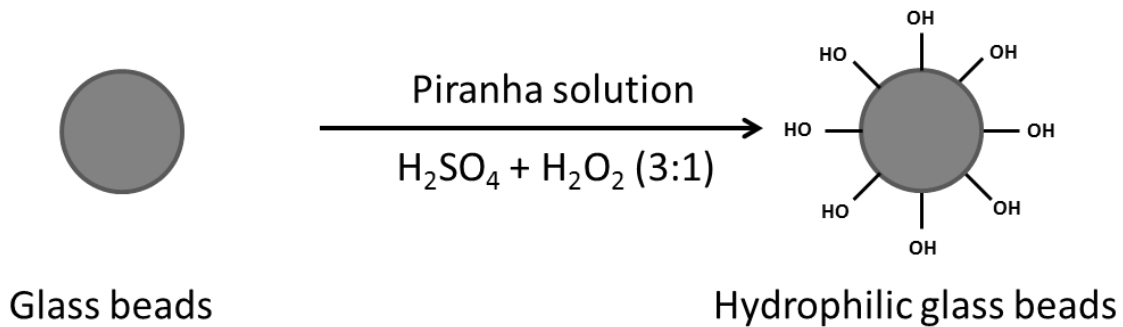


Figure 4-2. Schematic representation for adding OH groups to particles with silica surface

Clean porous media were treated in a silanization process to obtain a hydrophobic surface, the particles of Qz sand and GB were immersed in a solution of trimethylethoxysilane at 90°C for 1 h, then rinsed with deionized water and dried in a clean oven at 120°C [Jradi et al., 2011] (see Figure 4-3).

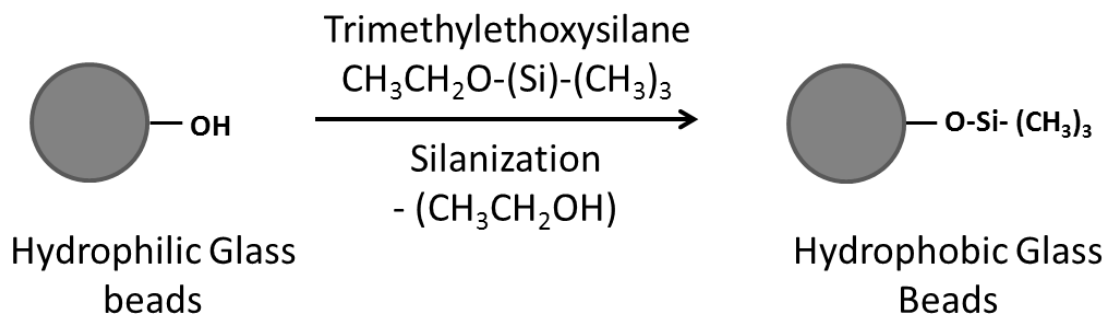


Figure 4-3. Schematic representation of the silanization reaction.

4.1.1.2. Frost

Frost was produced by condensation of water vapor using a heat gun on a pre-cooled rotating metal disk partially emerged into liquid nitrogen. The frost formed on the surface of the disk was scraped into liquid nitrogen, dried and then stored in a cold room to be ready for use (see

Figure 4-4).

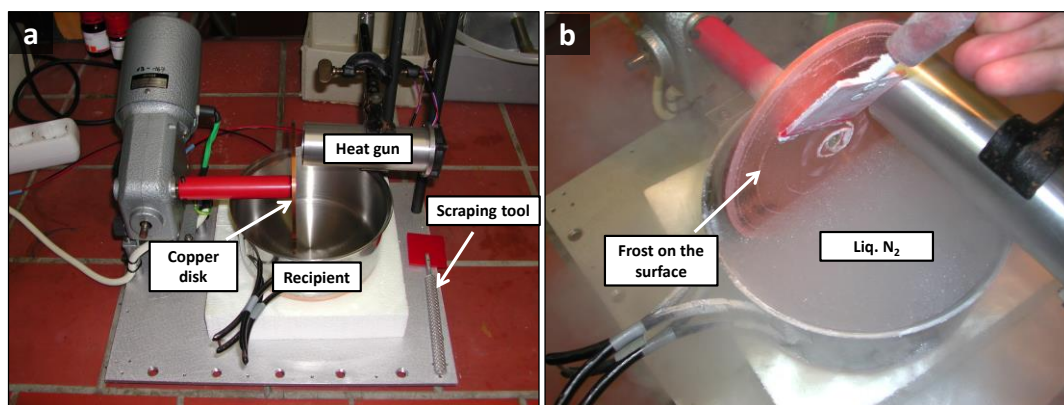


Figure 4-4. Preparation of frost: (A) picture of the frost machine, (B) scratching frost from the surface of the metal disk into liquid nitrogen

4.1.1.3. Forming gases

Methane (CH₄) and xenon (Xe) gases with purity higher than 99.99 % were purchased from AIR LIQUIDE Germany.

4.1.2. Experimental devises

4.1.2.1. Laboratory low temperature/high pressure device

Ex-situ GH samples were synthesized in our laboratory using a low temperature/high pressure system (up to 300 MPa). A detailed description of the devise can be found in [Genov *et al.*, 2004]. Briefly, the apparatus consists of a thermo bath type Neslab Instruments, RTE -140 filled with a cooling liquid (ethylenglycol-water mixture or d-limonene) able to operate down to 250 K, a gas pressure stick with high pressure cell hosting the aluminum sample holder, high pressure line with inlet and outlet valves for pressurizing and depressurizing the cell connected to a gas bottle, and readout systems of pressures and temperatures connected to a computer for recording data (see Figure 4-5).

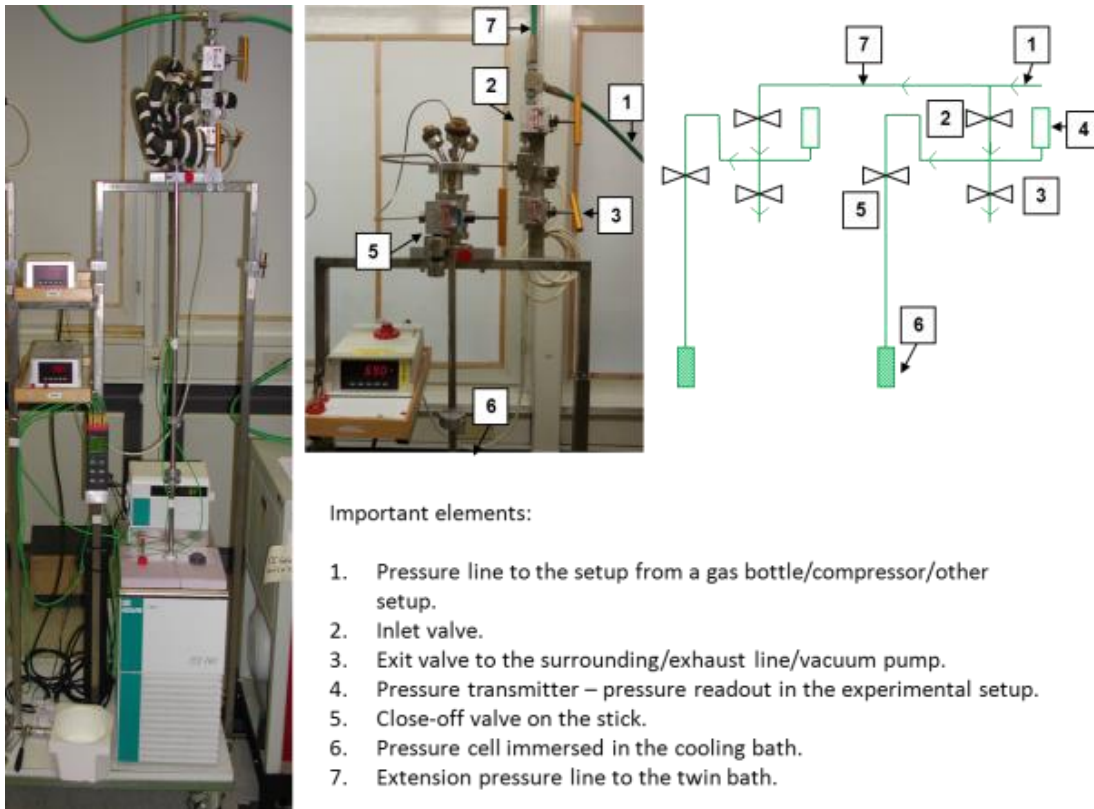


Figure 4-5. Experimental setup for *ex-situ* GH formation in laboratory at the Department of Crystallography (Geosciences Centre, University of Göttingen). On the left hand side a picture of the high pressure setup showing the thermal bath and the pressure system used which is explained in more details on the right hand side image.

4.1.2.2. Pressure cell

In-situ time resolved micro-computed tomography and CSD analysis experiments at synchrotron facilities were carried out on GH samples formed inside a small transportable pressure cell. The first prototype of the cell was designed and constructed by our technicians Mr. Ulf Kahmann and Mr. Heiner Bartels. During the design and construction of the pressure cell, several criteria have to be fulfilled and compromises had to be made in order for such a cell to function properly:

- The cell must be able to contain a gas pressure of 10 MPa to ensure the formation of GH.
- The cooling process must permit a uniform and constant temperature of the sample as we want to control the formation by pressure driving force.
- The sample size should be small enough to reach μm resolution but not too small in order to be able to see changes in pressure and to follow more precisely the progression of the formation process.
- The rotation and the cooling of the cell must not generate any vibrations during the scan to avoid image artefacts.
- The attenuation of X-rays must be as uniform as possible.

In order to meet the above requirements, a cylindrical pressure cell was designed. The cylindrical shape offers the advantage that X-rays have a constant attenuation at different azimuthal angle. A Peltier element was used for cooling the cell because it is more convenient for our setup.

Cooling devices based on the Peltier-effect are now widely used in different areas of applications requiring well controlled temperature and compact transfer of heat: e.g. in protein crystallography [Machin *et al.*, 1984], single crystal research [Agron and Levy, 1972] and X-ray or neutron powder diffraction [Oksansen *et al.*, 2010; Wood *et al.*, 2012] (Figure 4-6).

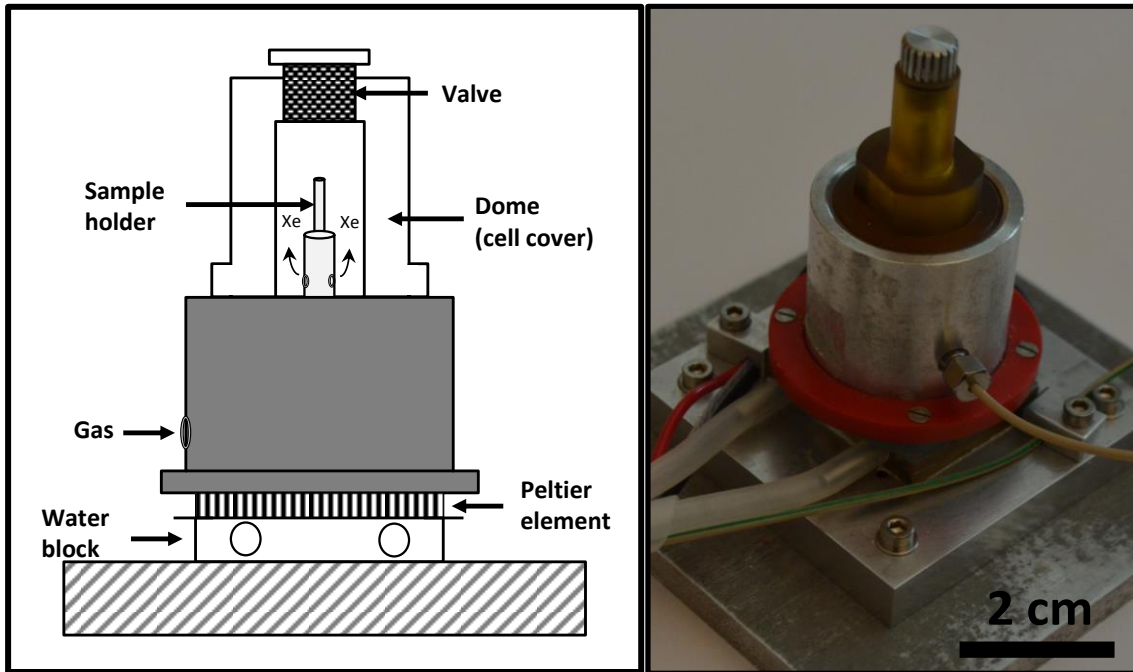


Figure 4-6. Custom designed pressure cell for *in-situ* GH formation. Left: schematic drawing of the pressure cell, right: picture of the pressure cell

A thermo-electric module type CP 1.4-71-06, MELCOR is mounted with its cold side in thermal contact with a central aluminum cylinder (or the base of the cell) and its hot side in contact with a rectangular water jacket. The latter is simply built by drilling U-shaped channels in our workshop. The supply of cooling water is taken from a tank of 31 L. The water is cooled by gravitation-flow (laminar flow, 2.4 L/h to avoid vibration) to the inlet of the water jacket and travels back and forth through the chambers of the water block thereby absorbing the heat. The warmer water exiting the water exchanger is pumped back to the water tank (Figure 4-7).

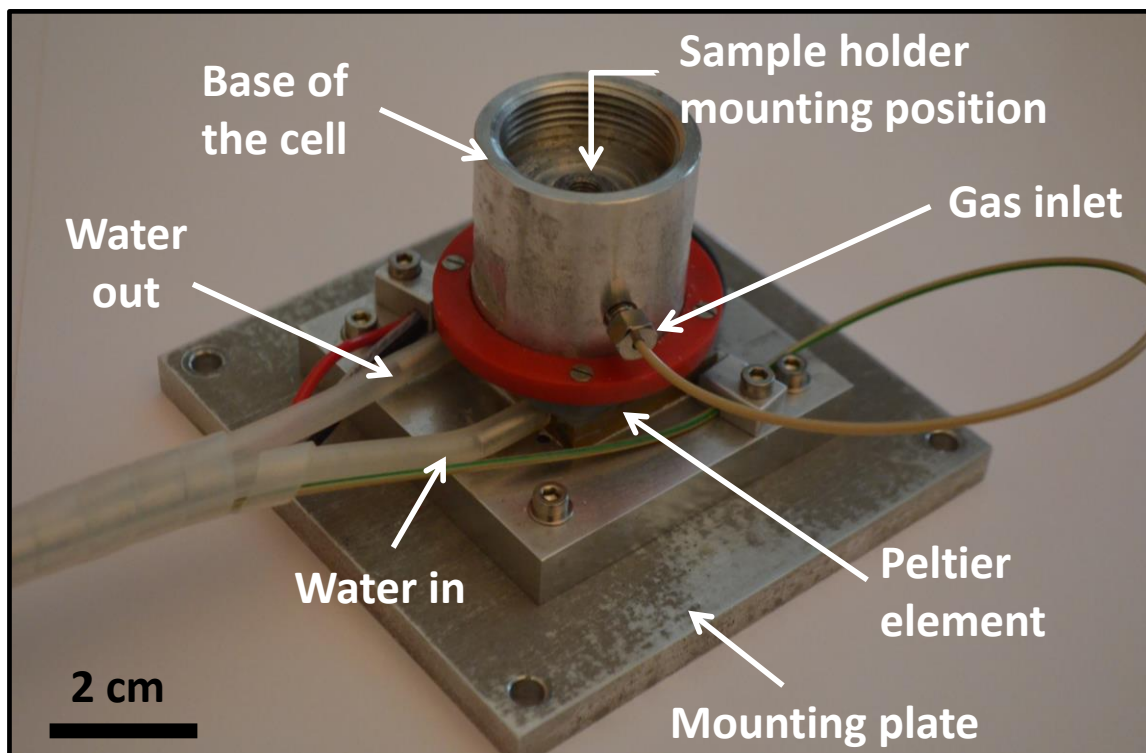


Figure 4-7. Base of the pressure cell

The sample holder is a thin-walled aluminum cylinder and it is fixed with a screw mount terminal on the base (Figure 4-8). Aluminum was used because it is a good conductor of heat, it has a low density and high strength, and it can be easily shaped. The junctions between these elements are achieved using screws and the thermal contact is improved by using thermal conducting paste. The device is closed by a polyethyleneimine cover (dome) clamped to the base of the cell (Figure 4-9). Polyethyleneimine was chosen for its low X-ray absorption and adequate mechanical properties. The dome is connected to the central aluminum cylinder through a screw mount terminal. On the top of the dome a pressure valve is mounted and it is used to evacuate air.

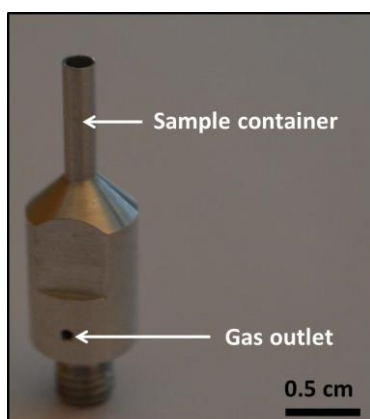


Figure 4-8. Aluminum sample holder

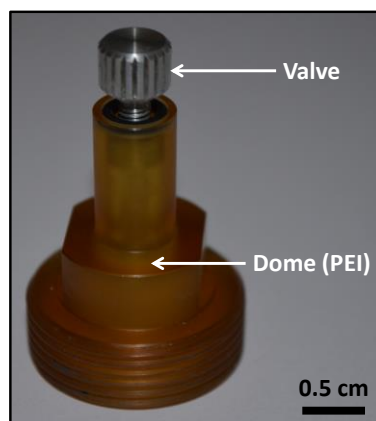


Figure 4-9. Dome of the cell made of polyethyleneimine.

The cooling of the sample is achieved by powering the Peltier module with 8.6 V DC at 5A. A PT 100 temperature sensor is mounted at the bottom of the base of the cell close to the Peltier element. The temperature measured by the sensor is fed to a temperature regulator (type Peltron

PRG H 100) which will compare it to the set temperature (276 K) and control the cooling process. The thermal equilibrium is reached after a few minutes (~ 5 min) and remains stable to within ± 0.1 °C over periods of many hours.

The sample temperature was measured at different positions using another PT 100 sensor controlled with a Lakeshore regulator. Two materials with different thermal conductivity: thermal grease and honey were used for this purpose to estimate the temperature gradient along the sample. The measured results revealed the existence of a temperature gradient of about 0.85 °C degree over a length of 10 mm. A uniform sample temperature is preferred but the actual temperature gradient does not represent a major problem for the experiments. A first prototype of the cell was constructed then several modifications were made to improve its working performance and to meet some specific requirements depending on the planned experiment. The pressure cell was first designed to work with Xe gas so at pressure below 1 MPa. Recently the cell was modified to be able to hold a pressure exceeding 10 MPa in order to be used for future experiments (not this project) on methane hydrate.

4.1.3. Specimen preparation

The synthesis of GH in unconsolidated sediments starts by preparing different mixtures with the appropriate amount of each component. Various mixtures with different water content were prepared and different kinds of formation processes were tested:

- procedure (I): formation from juvenile water,
- procedure (II): formation from Xe-enriched water obtained from *in-situ* formed and subsequently decomposed Xe-hydrate (“memory water”), and
- procedure (III): reformation from *ex-situ* formed and *in-situ* decomposed Xe-hydrate.

The first procedure is the general method followed to prepare GH-bearing sediments' samples as described by Klapproth *et al.* [2007]. It consists of admixing sediments with the appropriate amount of frost powder in a mortar under liquid nitrogen in a cold room (263 K). A small portion of the homogenized sediment is then filled under liquid nitrogen into the sample holder and subsequently manually compacted to avoid big gaps in unconsolidated sediments. The sample holder is then loaded in the pressure cell at constant temperature of 276 K. After 25 min of thermal equilibration and melting of the ice phase, the cell chamber is flushed three times with gas to evacuate air and a gas pressure is applied. This method was used for *ex-situ* and *in-situ* preparation of GH samples. In procedure II, the experiment was performed *in-situ* in three stages on the same sample: the first stage consists of forming Xe hydrate following method I, then hydrates were decomposed by reducing the pressure to a value below the three-phase equilibrium pressure, and finally in stage 3, GH was reformed by restoring the pressure to the condition of formation. For method III, porous media were mixed with *ex-situ* formed Xe hydrates grown from ice spheres [Kuks *et al.*, 2006; Staykova *et al.*, 2003]. The mixture was filled into the pressure cell and hydrates were completely dissociated for 25 min at 276 K under ambient pressure. Xe hydrates were then reformed from this “memory” water.

4.1.4. Control of the reaction kinetics

The scope of this work includes the study of the nucleation and growth mechanisms of GH in sediments. This goal can be achieved by performing several measurements at different stages of

formation. Hence, the understanding of GH formation kinetics is very important for the success of *in-situ* time resolved experiments. As the formation rate depends on the pressure driving force, the pressure to be applied to simulate the formation of Xe hydrate is a critical parameter which must be chosen carefully in order to obtain a moderate time of nucleation.

The beam times granted at synchrotron facilities are only a few days. Therefore, reasonable duration of GH formation was preferred to achieve all planned experiments. On the other hand, a fast reaction of formation does not allow us to follow the progress of the formation process by means of pressure drop. For these reasons, several tests have been made in order to choose the safe onset working pressure. The tests were done using the same mixture composed of Qz sand with 10 wt.% frost at constant temperature of 276 K and various pressures of 2.5, 3.0, 3.5, 4.0 and 4.5 bar. Figure 4-10 shows how the induction time and the formation rate vary with the driving force. The results are summarized in Table 2-1. At 2.5 bar, the reaction did not start after 2 hours so it was abandoned.

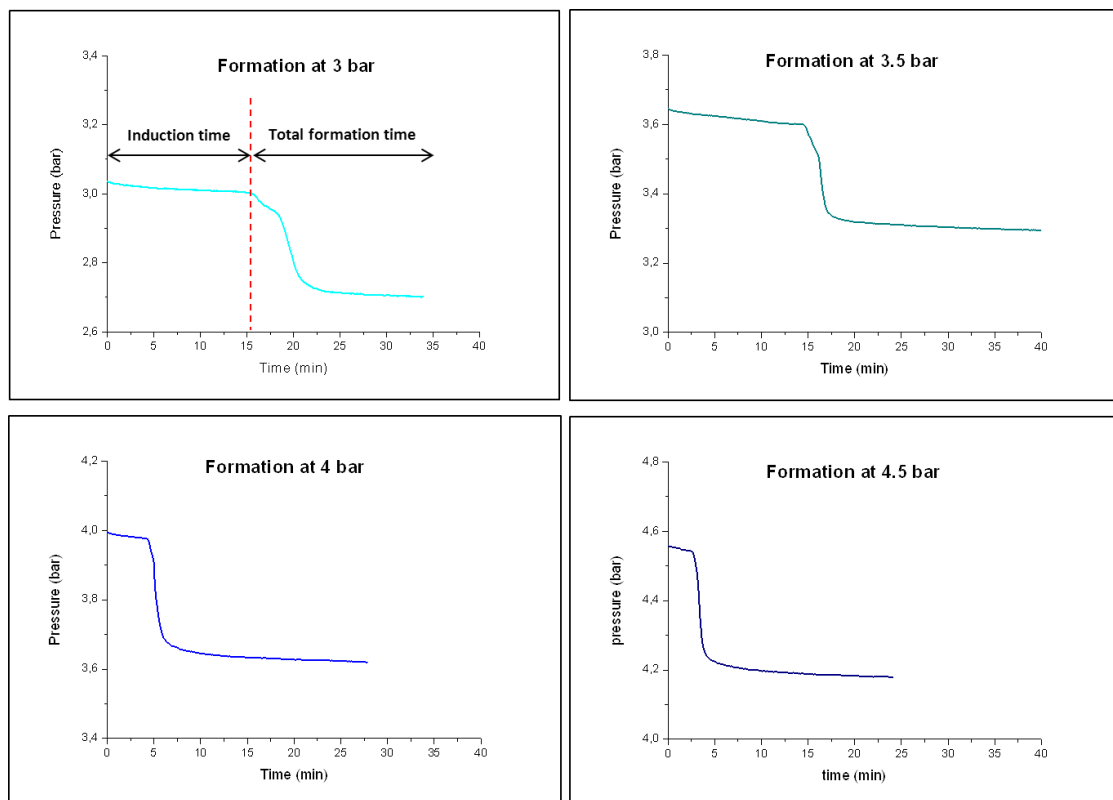


Figure 4-10. Gas consumptions of Xe hydrate formation at different pressure driving force. A sample of Qz sand with 10 % water (276 K) was used.

The pressure driving force is defined as $\ln(f_{\text{exp}}/f_{\text{eq}})$, where f_{exp} and f_{eq} are the fugacities at the experimental pressure and at equilibrium respectively. The pressure of Xe hydrate stability at 276 K was determined using the CSMGem program [Sloan and Koh, 2008] and the Xe fugacities were calculated from isothermal fluid data of Xe gas obtained from NIST webbook (available at <http://webbook.nist.gov/chemistry/fluid/> using the following state equation):

$$f = P \exp\left(\frac{1}{RT} \int_0^P \frac{RT}{P} dP\right) \quad (4.1)$$

Table 4-2. GH formation rates at different pressure

Pressure (bar)	$\ln(f_{\text{exp}}/f_{\text{eq}})$	Induction time (min)	Reaction time (min)
2.5	0.180	> 2 hours	-
3.0	0.359	16	25
3.5	0.510	15	24
4.0	0.640	5	21
4.5	0.754	3	19

At T= 276 K, $f_{\text{eq}} = 2.055$ bar ($P_{\text{eq}} = 2.07$)

From the above results, the pressure can be set at a value between 4 and 5 bar in order to obtain a reasonable reaction time.

The acquisition of tomographic and CSD data requires that all phases within the sample are in equilibrium. Both methods are sensitive to any small movement of the sample. Therefore, measurements at different stages of formation must be done when all phases within the sample are in equilibrium. For that, we developed a way to stop the reaction before each scan: “stop and go”. Our approach consists of decreasing the pressure to a value slightly higher than the stability limit of Xe hydrate at 276 K. At this pressure, the driving force is too small so that hydrate remains stable and the formation process is slowed down until it is stopped after few minutes. The scans were taken when the pressure is stabilized. The pressure corresponding to the stability limit of Xe hydrate was determined experimentally due to the existing temperature gradient as the sample is cooled from one side. The procedure consists of forming GH and then decreasing the pressure slowly until an increase of pressure characterizing the dissociation of GH is clearly observed (Figure 4-11).

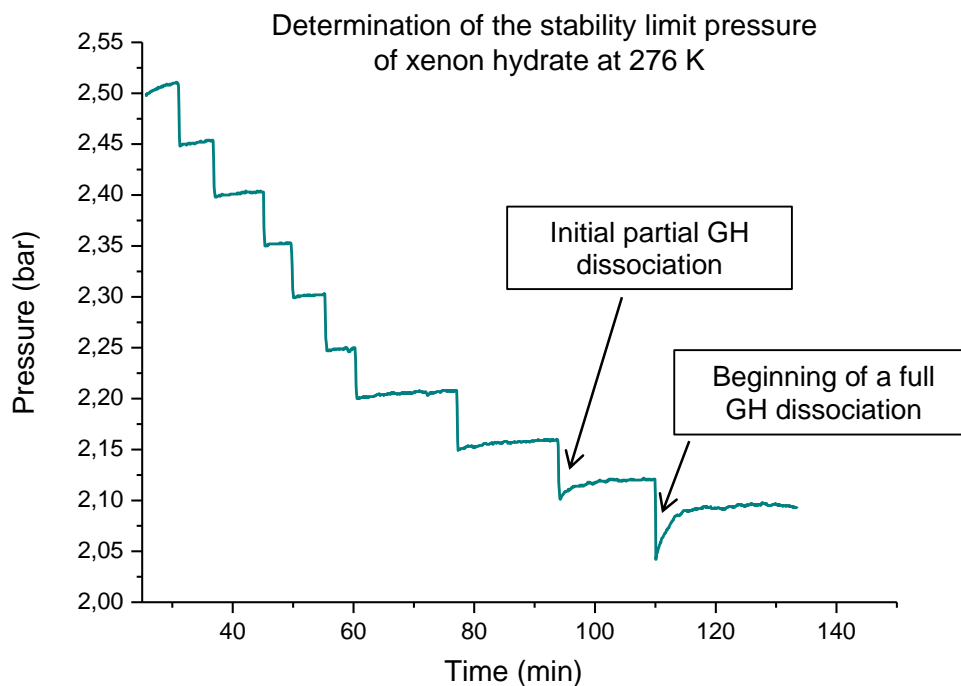


Figure 4-11. Experimental determination of the pressure corresponding to the stability limit of Xe hydrate at 276 K. First Xe hydrate was formed at 5 bar, then the pressure was decreased by steps of 0.5 bar down to 2.5 bar (not shown in this graph) and finally the pressure was decreased by smaller steps of 0.05 bar until a remarkable increase of pressure is observed. The increase of pressure indicates the dissociation of GH (black arrows in the figures indicate the initial partial and the beginning of full GH dissociation).

Due to the temperature gradient along the sample, the dissociation of GH is not homogeneous. Figure 4-11 shows that the dissociation starts first at 2.1 bar which may corresponds to a part of the sample at higher temperature which corresponds

When the pressure was further decreased to 2.05 bar, a fast increase in the pressure is observed which indicates that all the sample started to decompose. Hence, in order to stop the pressure and avoid any partial GH dissociation the pressure must be dropped to a value above 2.1 bar, 2.2 bar. At this pressure the driving force is negligible ~ 0.05 , so after few minutes all phases are in equilibrium. Figure 4-12 illustrates how the reaction can be initiated successfully, stopped and restarted again. Using this approach, scans at different stage of formation can be achieved allowing studying the nucleation and growth processes within the reaction time without affecting the quality of data recorded.

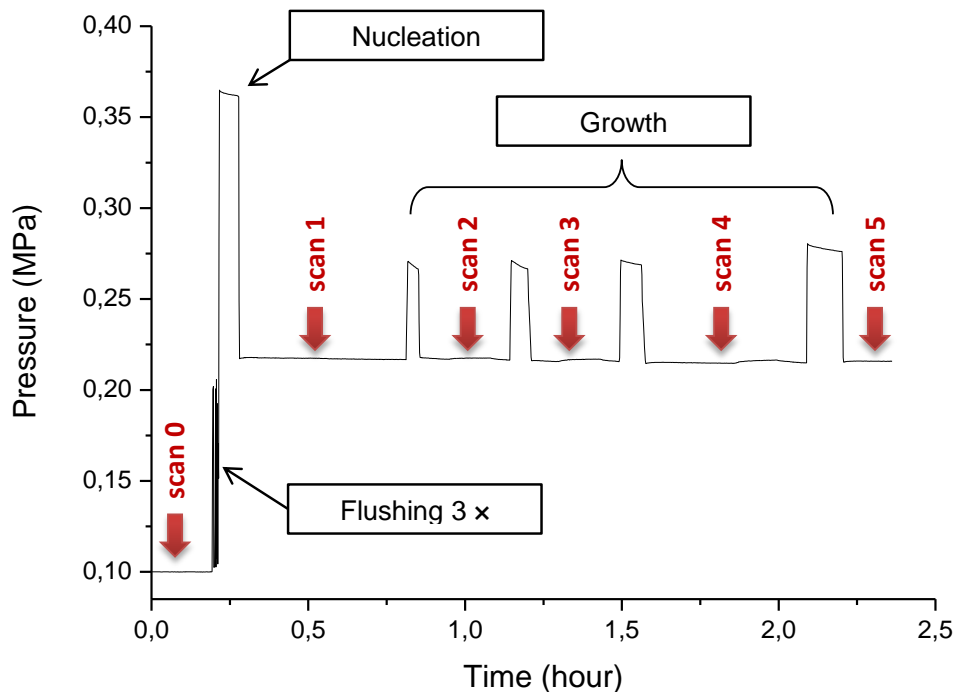


Figure 4-12. Control of GH formation kinetics. The reaction can be initiated, stopped and restarted again in order to study the nucleation and growth processes. The red arrows show the time at which scans can be executed without influencing the quality of data.

4.2. SEM investigations

4.2.1. Characterization of starting materials

The different starting materials were investigated using FE-SEM. Both secondary electrons and backscattered electrons modes were used. Ice and GH samples were studied under high vacuum and low temperature using the Polaron cryogenic system cooled with liquid nitrogen.

FE-SEM images show that the natural Qz sand consists of rounded grains characterized by a rough surface. The steps and corners of the surface of Qz could represent sites to accumulate water. *Chuvilin and Istomin* [2012] reported that Qz sand are composed of more than 90% of SiO_2 . The SEM analysis shows that some Al, Fe, Ca, Zr oxide/carbonate thin-layer coatings are covering the surface (see Figure 4-13).

On the other hand, purchased synthetic GB consist of SiO_2 spherical particles with a smooth surface. Some imperfections are observed which might be related to the formation process and to mechanical shocks during preparation (Figure 4-14).

Kaolinite and montmorillonite were characterized as well by FE-SEM. Both clay minerals are small plate-like particles which form aggregates of bigger sizes. Kaolinite sample is composed of: 92 % kaolinite, 6 % Qz and 2 % muscovite (see Figure 4-15). While montmorillonite sample is composed of 93.4 % montmorillonite, 2.9 % andesite, 2.9 % biotite, and 0.8 % calcite (see Figure 4-16) [*Chuvilin and Istomin*, 2012].

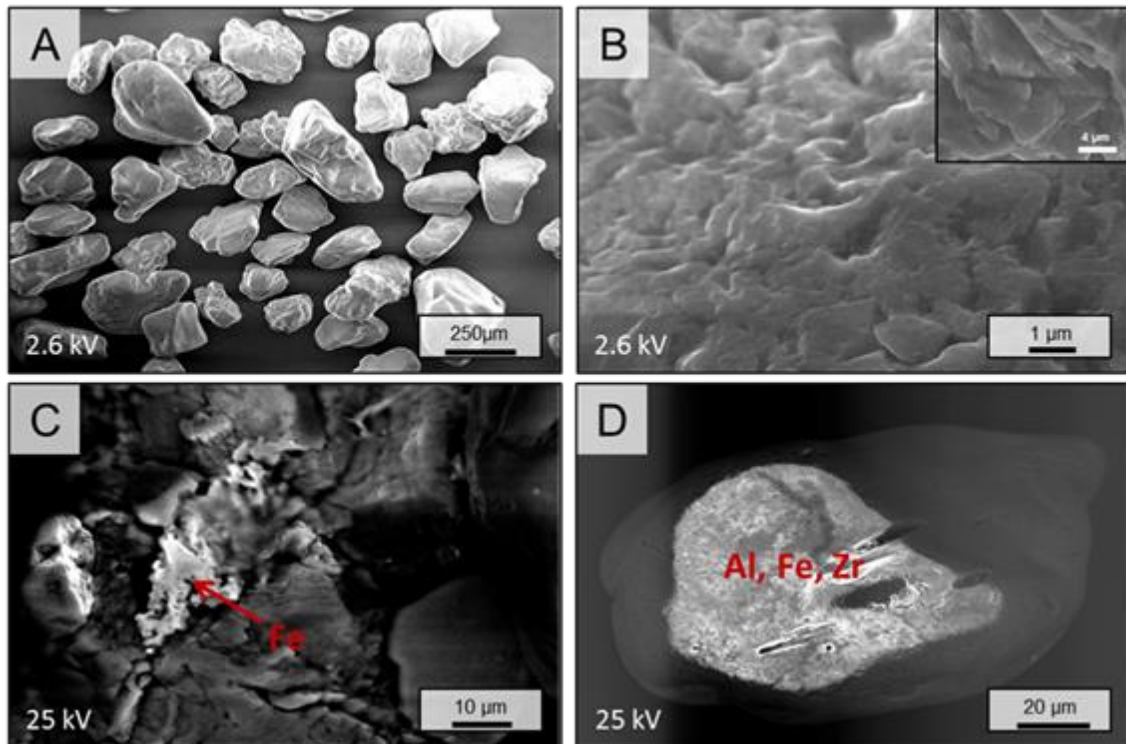


Figure 4-13. FE-SEM images of the natural Qz sand. A: SE image of Qz sand grains, B: high magnification image of a Qz grain surface. C and D are BSE images showing the presence of other types of minerals (brighter regions) such as Fe, Al, or Zr.

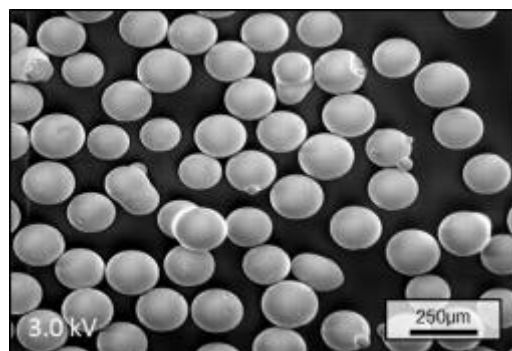


Figure 4-14. SEM image of GB

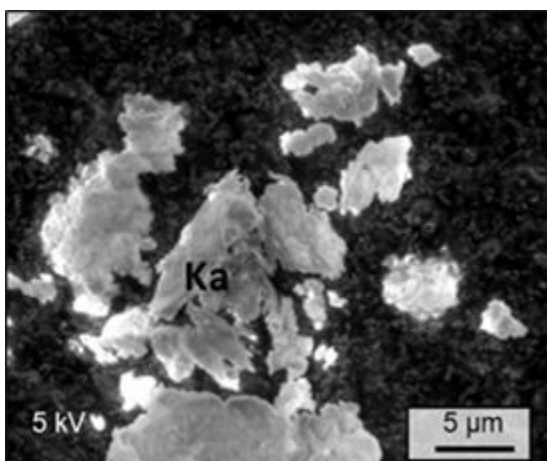


Figure 4-15. SEM image of Kaolinite

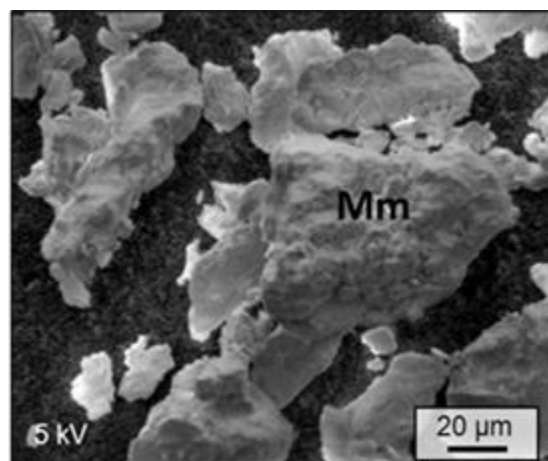


Figure 4-16. SEM image of montmorillonite

FE-SEM measurements of frost powder show that it consists of small individual grains or crystallites of frost have a small size below 200 nm. These particles form agglomerates of about 10 μm in size (see Figure 4.14). Diffraction experiments on frost produced indicate that is crystallographically stacking faulty cubic ice “Ic_h” [Hansen *et al.*, 2008; Kuhs *et al.*, 2012].

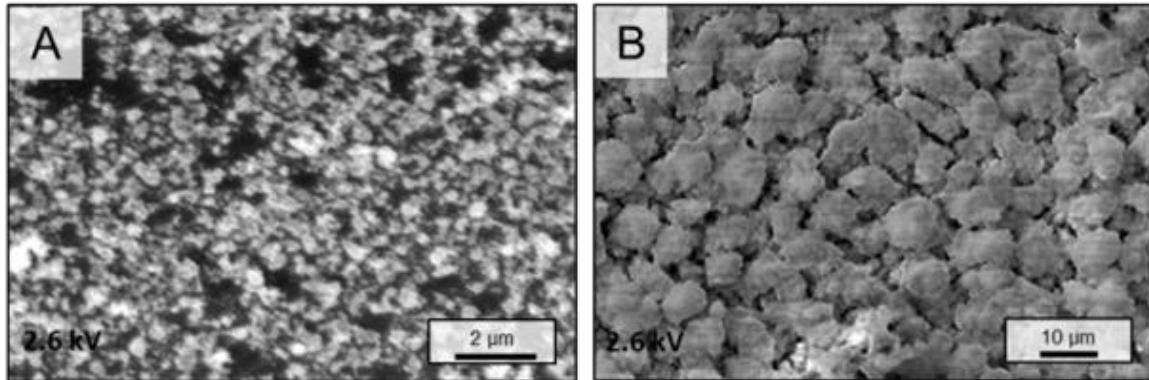


Figure 4-17. SEM images of frost. A: monolayer of frost formed by condensing water vapor 3 s on a cold plate. B: agglomerates of frost crystallites formed by condensing water vapor 20 s on a cold plate.

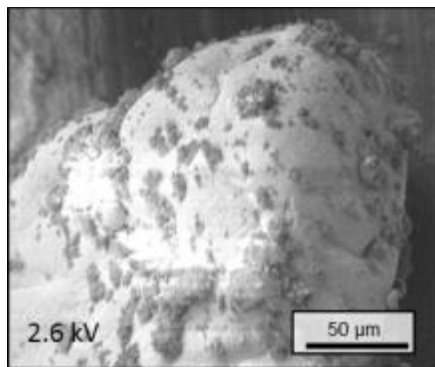


Figure 4-18. Qz sand admixed with 10 wt% frost

The initial mixture of Qz sand and frost was as well characterized by FE-SEM. The SEM image in Figure 4-18 shows that small frost particles are agglutinated on the surface of Qz grains. This method uses ice powder instead of liquid water in order to avoid migration of water through pores to the bottom of the sample before starting the formation of GH. Furthermore, it is easier to weight the appropriate amount of frost powder than to micropipette water in the sample [Klapproth *et al.*, 2007]. The distribution of water in the Qz sand matrix was always checked for each sample by μ -CT before starting the reaction (see Chapter 5).

4.2.2. Microstructural observations

FE-SEM observations of the microstructure of GH were carried on 3 synthetic GH samples prepared *ex-situ* using procedure I. The characteristics of these samples are summarized in the Table 4-3.

Table 4-3. Characteristics of GH samples for SEM investigations

Specimen	Matrix	Frost (wt.%)	Gas	Porosity (%)	P (MPa)	Formation time
Sample 1	Nat. Qz	10	CH ₄	39	10	36 h
Sample 2	Nat. Qz	10	Xe	39	0.6	36h
Sample 3	Nat. Qz	20	Xe	30	0.6	48 h

FE-SEM observations showed similarities between the microstructure of methane hydrate (MH) and Xe hydrate (XeH) samples. Both hydrates appear from SEM images to form as cement between the Qz grains (Figure 4-19). Qz grains look to be linked together by hydrate which can increase the stiffness and rigidity of the specimen. Qz grains fully surrounded by GH were not observed. This is probably due to the fact that samples were crushed into small pieces before the analysis. These results are similar to the observations of *Klapproth et al.* [2007] on synthetic methane hydrate samples and from NGH samples from Mallik 5L-38 research well [*Techmer et al.*, 2005].

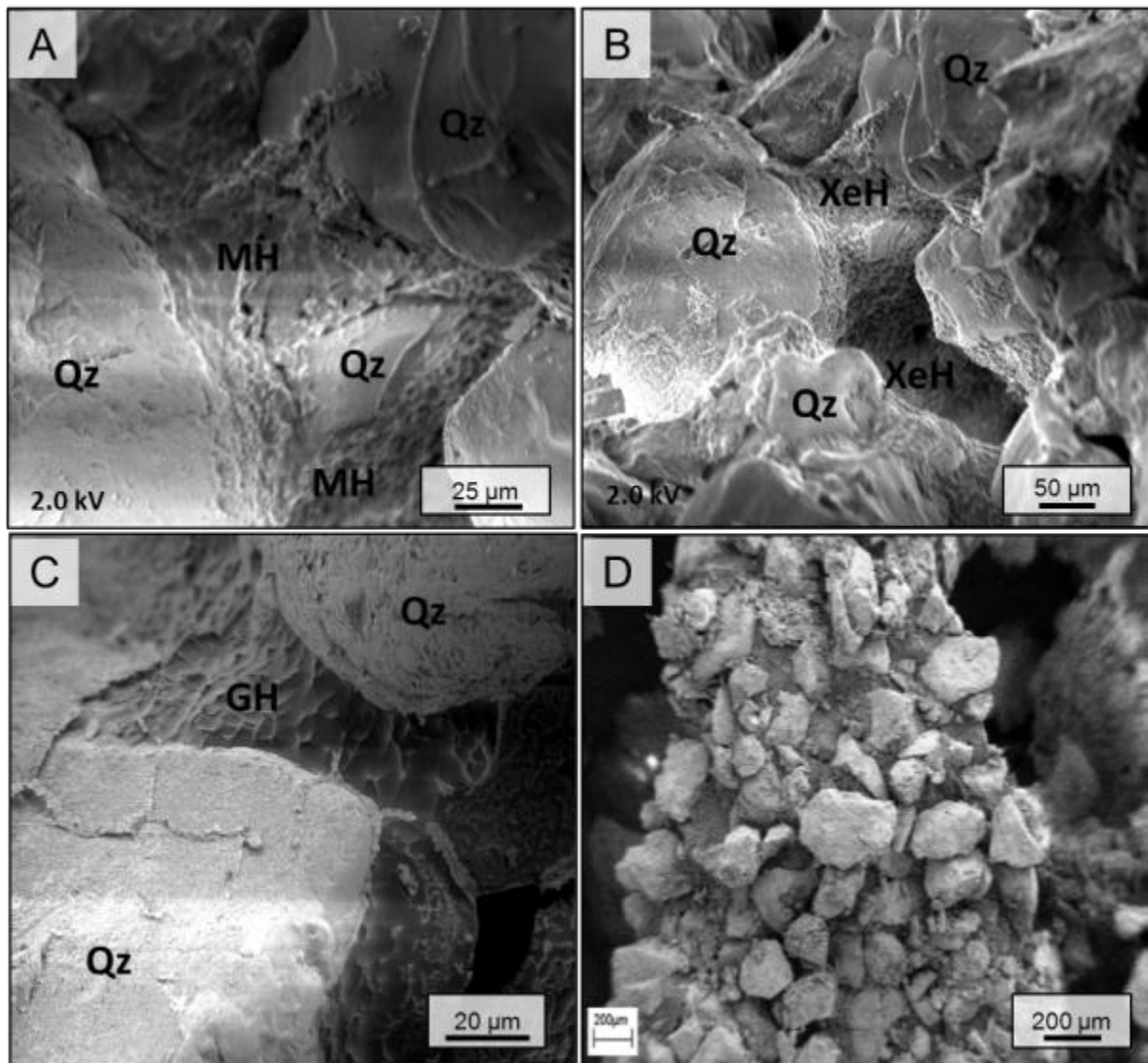


Figure 4-19. FE-SEM observations of GH distributed in natural sediments. Similarities in the microstructures between synthetic methane (A) and Xe hydrate (B) samples (this work), synthetic methane hydrate prepared by A. Klapproth (C) and NGH sample from the Mallik 5L-38 research well (D) [*Techmer et al.*, 2005].

GH formed between sediment grains displays either porous or dense morphological structures (Figure 4-20). The size of pores is in the order of 1 µm and sometimes smaller. Both observed microstructures have been reported by *Klapproth et al.* [2007] and *Klapp et al.* [2010b].

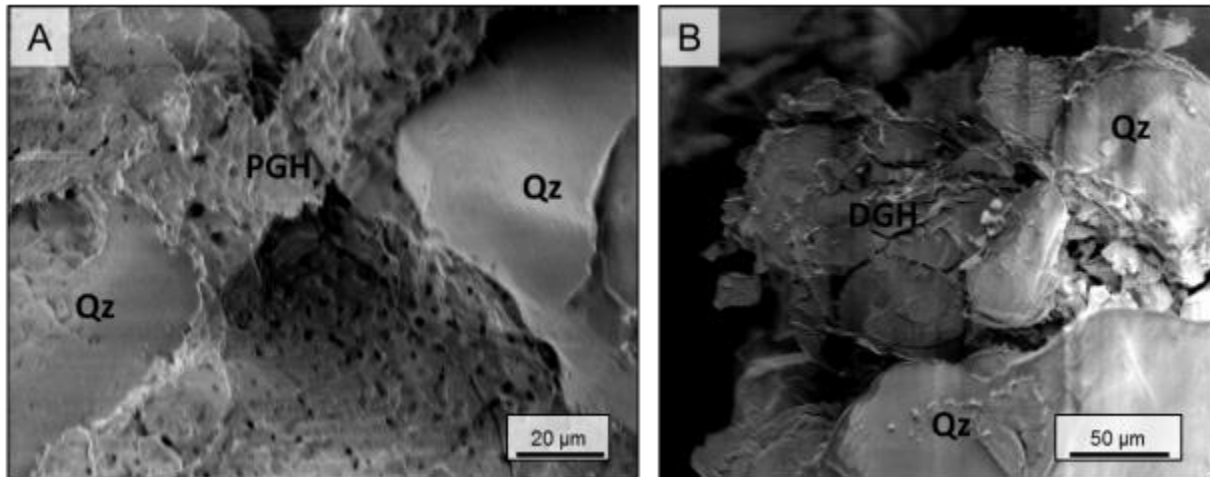


Figure 4-20. FE-SEM observations of porous (A) and dense (B) morphological microstructures in Xe hydrate samples (medium III).

Some SEM images show polycrystalline layers of GH covering partially the sediments grains (see Figure 4-21). Individual crystallites can be clearly seen on the right hand side image (C) where only a monolayer of GH crystals is agglutinated to the Qz surface. These images are from a fully transformed GH samples. Nevertheless, it appears that the nucleation started at different sites and that GH crystals have a specific crystallographic orientation. The average size of GH crystals is around 10-15 μm . Quantitative information on the crystallites size distribution cannot be precisely extracted from SEM images. Therefore, a new method based on X-ray diffraction has been developed for this purpose in order to extract such information which is crucial for understanding the formation process of GH in sediments.

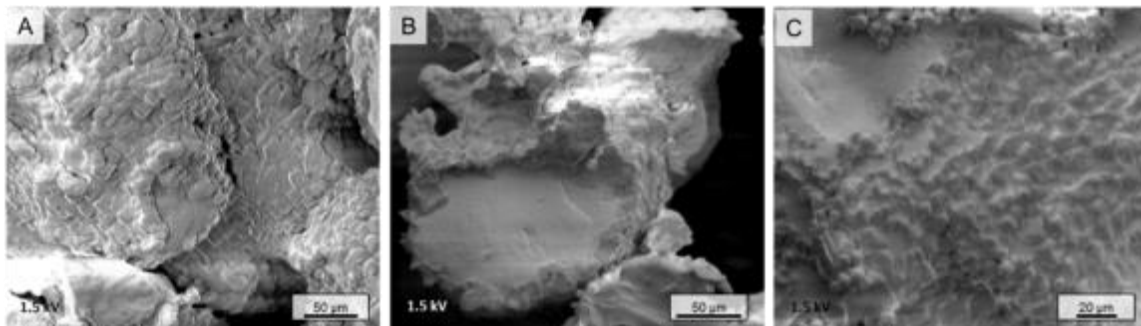


Figure 4-21. FE-SEM observations of polycrystalline layers of GH covering the Qz surface (A and B). C: individual crystals images of Xe hydrate bearing sample (17% frost). A and B show a polycrystalline layers of GH partially covering the Qz grains. C: a monocrystalline layer where individual crystals with sizes in the order of 5-10 μm can be clearly distinguished.

4.2.3. Limits of the SEM method

The SEM method offers several advantages but it has as well some limitations (see section 3.1, Chapter 3). Possible sublimation of GH may occur at high vacuum conditions and due to the electron beam at low vacuum conditions. The SEM method is not suitable for *in-situ* investigation of GH at high pressure; hence measurements were done at low temperature on *ex-situ* prepared GH samples recovered and stored in liquid nitrogen which freezes the liquid water. It becomes therefore difficult to distinguish between frozen water and dense GH or to observe a remained water layer between GH and sediment grains as illustrated in Figure 4-22.

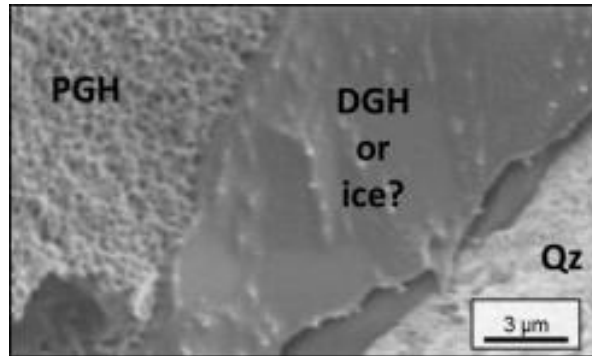


Figure 4-22. SEM image of Mallik 5L-38 sample showing a possible frozen water layer between Qz grain and GH [Techmer et al., 2005].

4.3. Time-resolved micro-computed tomography of gas hydrate growth in porous media

Synchrotron Radiation X-ray Computed Tomography (SRXCT) was used to observe, for the first time, the evolution of the GH microstructure in various porous media at a pixel resolution below 1 μm . The investigations were carried out during two experimental campaigns; the first beam time was in December 2012 and the second in October 2013.

4.3.1. The TOMCAT beamline

The TOMCAT (TOMographic Microscopy and Coherent rAdiology experimenTs) beamline for X-ray tomography at the Swiss Light Source (SLS) of the Paul Scherrer Institut (PSI) was chosen to observe *in-situ* the microstructure of GH in porous media due to its high resolution and the adequate range of energy (8- 45 keV) that can offer. The synchrotron light is delivered to the beamline by a 2.9 T superbend. The expected performance of the multilayer monochromator (bandwidth between 2-3 %) is illustrated in Figure 4-23 **Error! Reference source not found.** Further characteristics of the OMCAT beamline are summarized in Table 4-4.

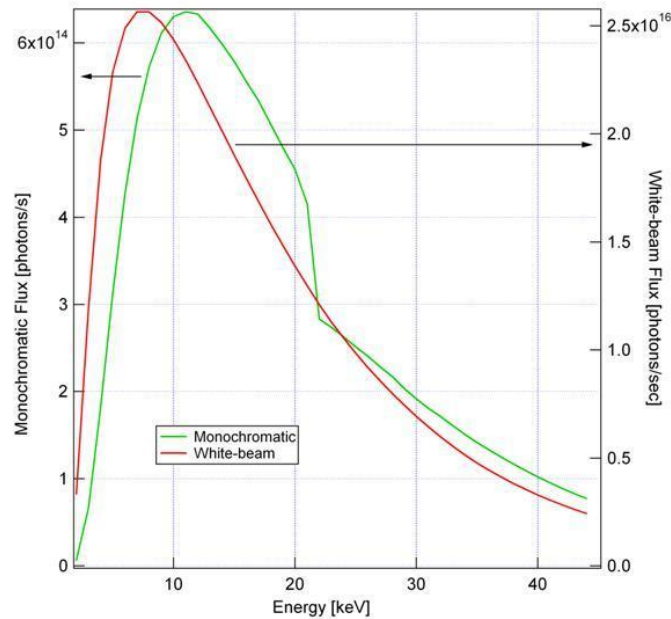


Figure 4-23. Photon flux as a function of energy for monochromatic and white beam (source: <http://www.psi.ch/sls/tomcat/optics>)

Table 4-4. Specifications of equipment and acquisition parameters at TOMCAT ([*Stampanoni et al.*, 2006])

X-ray source	Super bend magnet 2.9 T Ring current 400 mA Ring energy 2.4 GeV	
Photon source size (Σ_x, Σ_y)	53 μm \times 16 μm	
Beam size at sample (Σ_x, Σ_y)	40 μm \times 4 μm	
Beam flux	6.8×10^5 photons s^{-1} μm^{-2}	
Monochromator type	Double-crystal multilayer, bandwidth 2–3%	
Monochromator to source distance	7 m	
Sample to source distance	25 m	
Scintillator type	Single-crystal lutetium aluminum garnet doped with cerium (LuAG:Ce) ($\lambda = 535$ nm), 20 μm	
Detector type	CCD: PCO2000	
Detector resolution	2048 \times 2048 pixels (14-bit)	
Objective type	Field of view	Pixel resolution
Olympus Uplapo 4 \times	3.7 \times 3.7 mm^2	1.85 \times 1.85 μm^2
Olympus Uplapo 10 \times	1.5 \times 1.5 mm^2	0.74 \times 0.74 μm^2
Olympus Uplapo 20 \times	0.75 \times 0.75 mm^2	0.37 \times 0.37 μm^2

4.3.2. X-ray absorption radiography

The microstructure of GH was imaged using X-ray absorption radiography method because of the characteristics of the investigated specimen. The samples have an inhomogeneous chemical composition and contain high and low absorbing elements so contrast between the different phases is

expected. Furthermore, Xe was used to increase the contrast between the low-absorbing phases including water, gas and GH. Hence, it is not necessary to use phase contrast imaging in this case.

The rate of transmitted X-rays was calculated for each medium and for the total sample at the initial and final state of GH formation for a standard sample composed of Qz sand and 10 % water. As we have a newly developed pressure cell and the experiments were carried out for the first time, it was important to do these calculations in advance to have the time to do any modification on the cell before the beam time. Figure 4-24 depicts the X-ray path through the different media of the pressure cell. The intensity of X-rays is attenuated as it passes through each medium as described by the Beer-Lambert's law (Equation 3.19). Table 4-5 shows the attenuation of X-rays by each medium and the total X-ray absorption for the initial and final state of GH formation. For X-ray absorption imaging, the total attenuation should be in general about 90 %. The details of X-ray absorption calculations are given in Appendix A.

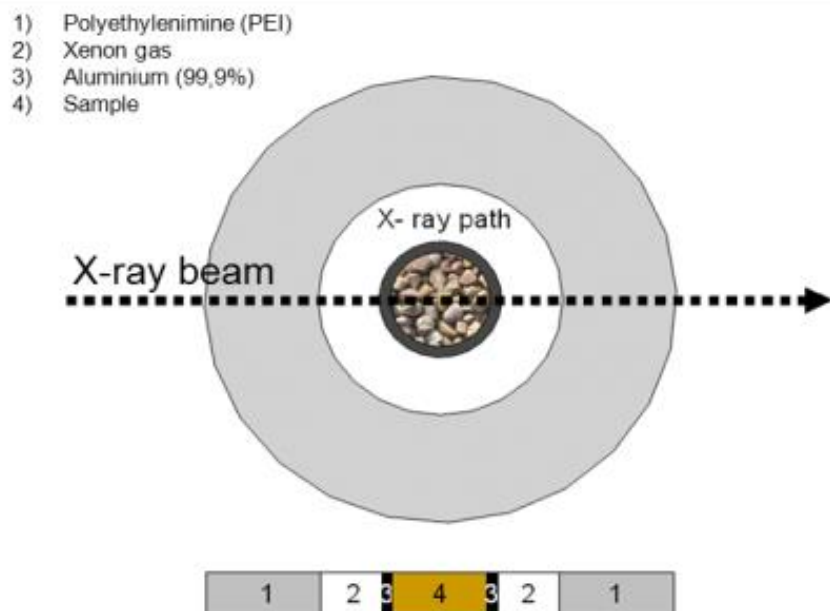


Figure 4-24. X-ray path through the pressure cell.

Table 4-5. Rate of X-ray attenuation by each medium

Initial state of the reaction				
nr	medium	Abs. Coef.	Trans. Coef.	% Trans.
1	Polyethylenimine (0.3 cm)	0.129	0.871	87.08
2	Xe outer space, 0.2 MPa (0.08 cm)	0.021	0.979	85.27
3	Al (0.02 cm)	0.195	0.805	68.63
4	60 % Qz (0.2 cm)	0.411	0.589	40.44
4	30% Xe in sample at 0.2 MPa	0.023	0.977	39.49
4	10 % Water	0,014	0.987	38.96
3	Al (0.02 cm)	0.195	0.805	31.36
2	Xe outer space, 2 bar (0.08 cm)	0.021	0.979	30.71
1	Polyethylenimine (0.3 cm)	0.129	0.871	26.74
Total Transmission				26.74
Total Absorption				73.26
Final state of the reaction				
nr	medium	Abs. Coef.	Trans. Coef.	% Trans.
1	Polyethylenimine (0.3 cm)	0.129	0.871	87.08
2	Xe outer space, 0.2 MPa (0.08 cm)	0.021	0.979	85.27
3	Al (0.02 cm)	0.195	0.805	68.63
4	60 % Qz (0.2 cm)	0.411	0.589	40.44
4	30% Xe in sample at 0.2 MPa	0,023	0.977	39.49
4	10% Xe hydrates	0.351	0.649	25.62
3	Al (0,02 cm)	0.195	0.805	20.62
2	Xe outer space, 2 bar (0.08 cm)	0.021	0.979	20.19
1	Polyethylenimine (0.3 cm)	0.129	0.871	17.58
Total Transmission				17.58
Total Absorption				82.42

4.3.3. Samples and list of experiments

Several samples with different compositions were measured during two experimental campaigns at the TOMCAT beamline in December 2012 and October 2013. During the first beam time, samples of natural Qz sand with various amount of water were measured in order to study the nucleation and growth processes of Xe hydrate in sedimentary matrices. This beam time was the first occasion to test the performance of the pressure cell and to explore the quality of data produced. As the experiments were successful and we could achieve our goals, a second beam time was planned with more experiments in order to corroborate the first observations and to investigate new parameters which may play a role in the formation mechanism of GH in porous media. The complete list of experiments and tests done during the two experiments is presented in Table 4-6.

Table 4-6. List of experiments/tests done during the two beam times in December 2012 and October 2013

Experiment/test	Proc.	Type of Sediment (wt.%)	Frost (wt.%)	Nb of samples
December 2012				
Nucleation/Growth	I	Nat. Qz sand	10.3	6
Nucleation/Growth	I	Nat. Qz sand	14.3	5
Nucleation/Growth	I	Nat. Qz sand	17.4	4
Dissociation/reformation	II	Nat. Qz sand	17.4	1
Annealing test	I	Nat. Qz sand	17.4	1
October 2013				
Nucleation/Growth	I	Nat. Qz sand	10.2	2
	I	Glass beads	10.3	2
Clay Minerals	I	Nat. Qz + 8% Kaolinite	15.3	2
	I	Nat. Qz + 8% Montmorillonite	15.4	2
Surface effect	I	Hydrophobic Qz Sand	15.5	2
	I	Hydrophilic Qz Sand	15.4	1
	I	Hydrophobic GB	15.3	2
	I	Hydrophilic GB	15.4	1
	I	Acid Washed Qz Sand	15.3	2
High water saturation	I	Nat. Qz Sand	25.7	3
Reformation	II	Nat. Qz Sand	15.2	1
Reformation	III	Natural Qz Sand	20% Xe hyd	2
	III	Glass beads	20% Xe hyd	2
Salt effect	I	Nat. Qz Sand	15.2 (2% NaCl)	1

Not all results from the experiments listed here will be discussed in Chapter 5. Some tests were unsuccessful such as the test with salty water or there was a problem with the data collection (i.e. annealing experiment).

4.3.4. Experimental setup and data collection

The pressure cell was mounted on a precision rotation stage which allows translation along the x,y,z directions with a resolution better than 1 μm and the centering of the sample can be achieved within 0.1 μm reproducibility. The experimental setup is shown in Figure 4-25 and 4-26.

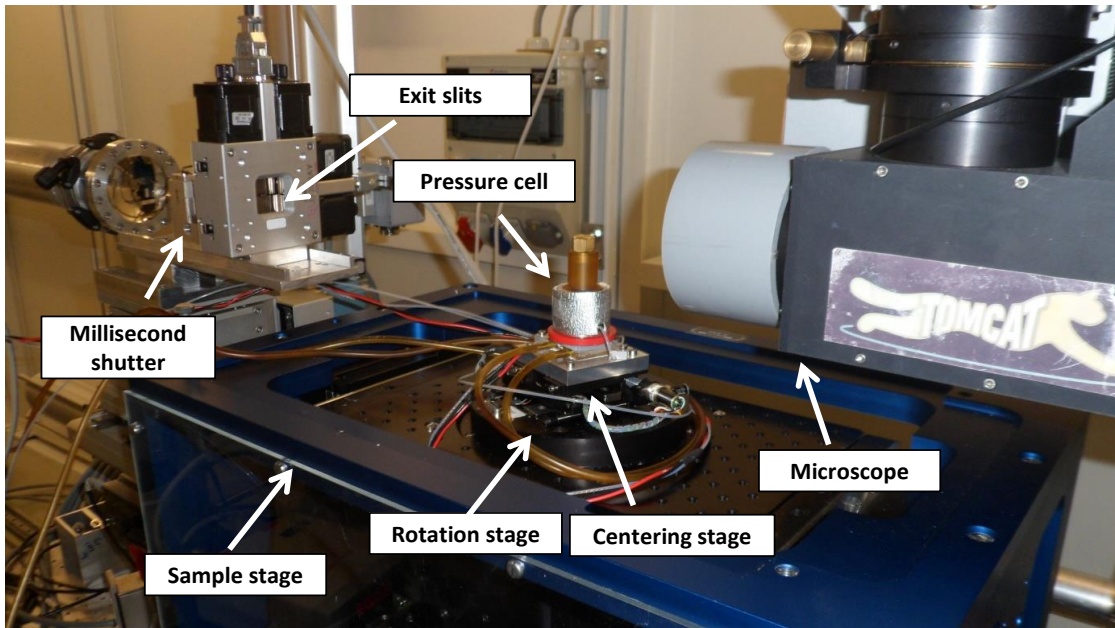


Figure 4-25. Experimental setup at the TOMCAT beamline

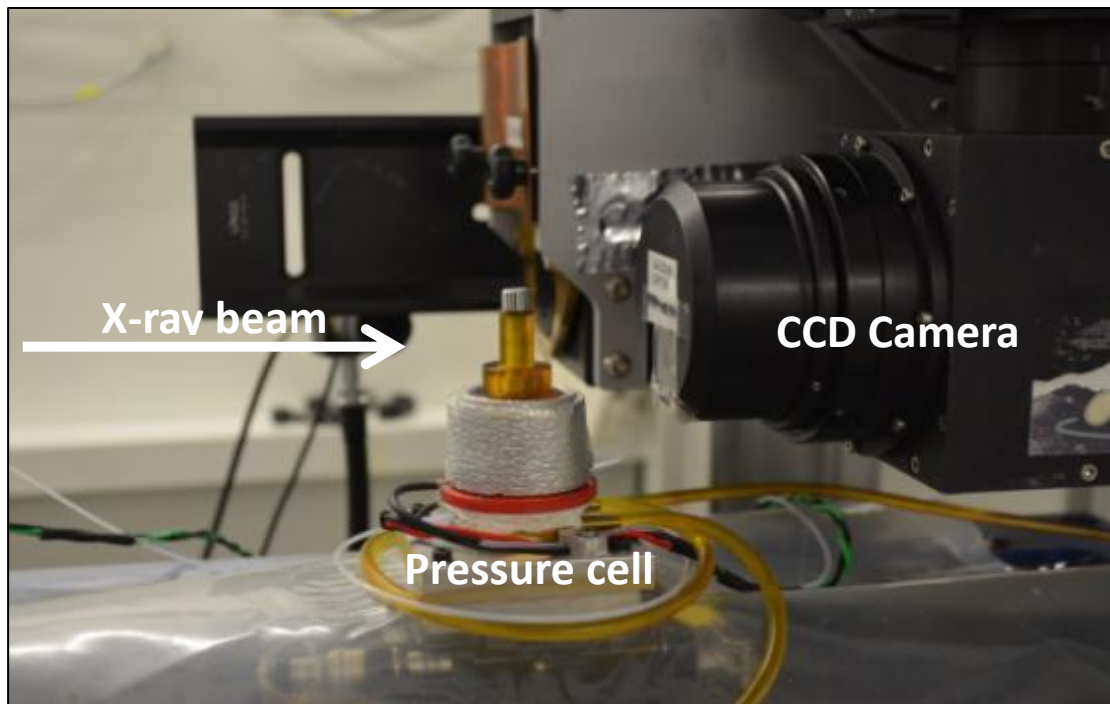


Figure 4-26. Close-up picture of the pressure cell mounted on the rotation stage

A large amount of high quality data (> 24 TB) was collected during two experimental campaigns of 12 shifts (96 hours) each. The first beam time was in December 2012 and the second in October 2013. A total of 240 tomograms of the 16 different hydrate-bearing sediment samples were measured. For each tomogram, 3201 (1501 second beamtime) projections at an integration time of 150 ms (350 ms) each were acquired over a sample rotation of 180° with a monochromatic X-ray beam energy of 21.9 keV. Two objectives (UPLAPO10x and UPLAPO20x) were mainly used with optical magnifications 10x and 20x. Nevertheless, some CT images with a low magnification 4x were taken in order to get an overview of the whole sample. After penetrating the sample, transmitted X-

rays were converted into visible light by a 20 μm -thick single-crystal lutetium aluminum garnet doped with cerium scintillator LuAG:Ce and captured by a high-resolution CCD camera type (2048 \times 2048 pixels). Subsequently the data was reconstructed by a gridded Fourier transform-based reconstruction algorithm [Hintermüller *et al.*, 2010; Marone and Stampanoni, 2012]. This results in datasets with an isometric voxel size of 740 and 380 nm (for the 10 \times and 20 \times magnifications respectively), which enables to distinguish between gas, water, sediment grains and hydrate also in interfacial areas of the sample.

4.3.5. Data quality

The data collected has in general very good quality; however CT images are not free of artifacts more or less apparent. As described in section 3.3.5 in Chapter 3, these artifacts may complicate the quantitative analysis or simulate pathology which leads to misinterpretation of the results. Figure 4-27 shows some images affected by different types of artifacts.

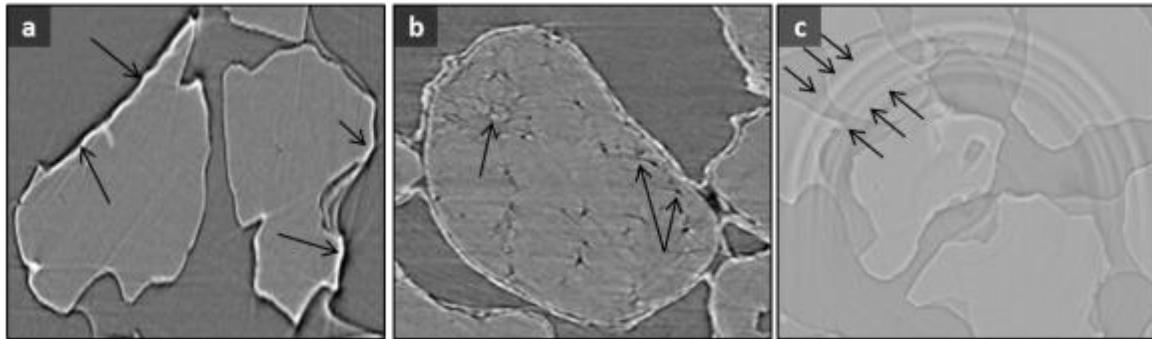


Figure 4-27. CT images showing the most common artifacts observed during data collection: a) beam hardening: the edges of Qz grains are brighter than the inner volume, b) motion artifact due to movement of the samples during measurements, and c) ring artifact resulting from a detector failure.

Beam hardening is a known problem in X-ray tomography. All Qz grains show on their edges a lighter gray value in the same range of GH, so it is important to consider this pathology during the interpretation of results. On the other hand, the motion artifact resulting either from the movement of the sample during scanning or from a partial decomposition of hydrates due to beam heating was less apparent in the CT images and the most affected scans were re-measured immediately when it was possible. Ring artefacts are less apparent and occurred occasionally due to detector failure.

4.3.6. Data analysis

The post-processing of the reconstructed data is carried out by our collaborator from the University of Mainz. In this section, only a brief overview of the steps of data processing is given. For a detailed description of the whole working flow of data analysis the reader may refer to the PhD thesis of Kathleen Sell.

For a quantitative analysis, the data has to be segmented. The segmentation is a process which consists of partitioning the image in sets of pixels called segments and assigning label to every pixel image or phases with a certain gray value. This operation has for goal to simplify the representation of images by identifying each phase within the sample and to make the image analysis easier. There are several methods of image segmentation in literature [Issonov *et al.*, 2009].

The first step of data processing consisted of rescaling the original data using Matlab script from “64-bit floating rek.dmp” files to “16-bit Unsigned RAW” data with file dimension of $2560 \times 2560 \times 2160$ pixels³. Due to less complete data related to the rotation symmetry inherent in tomography, the corners of images contain artifacts so data were cropped to use only the inner volume with the highest quality as shown in Figure 4-28.

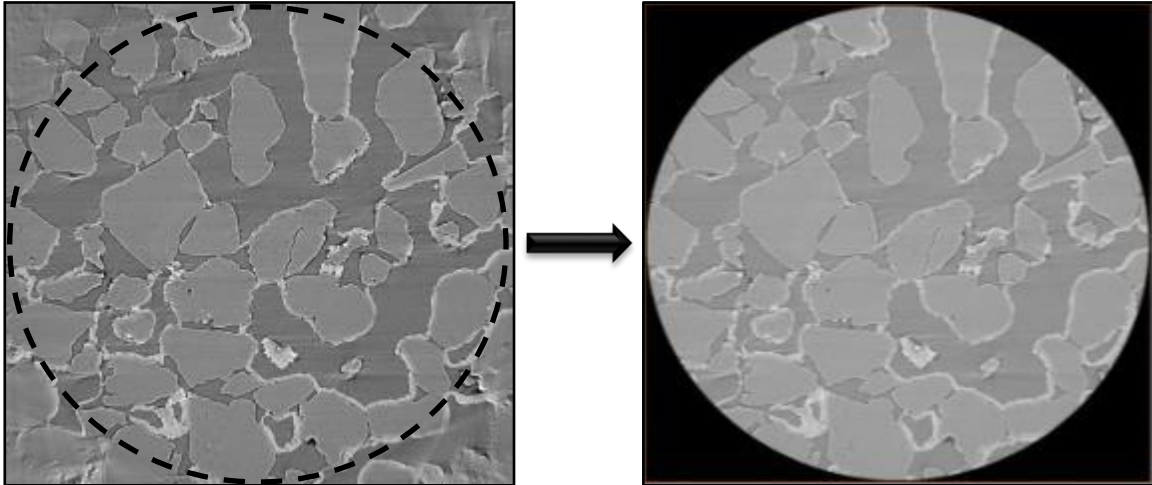


Figure 4-28. Left: an original binary raw 64-bit floating image including all artifacts. Right: a re-scaled 16-bit ROI cropped image without loss of information during rescaling (images provided by Kathleen Sell).

The post-processing of data was carried out with Avizo Fire 7.0 software from VSG (Mérignac, France). The second step was to apply different image enhancement filters such as the Non-Local Means (NLM), the Edge Preserve Smoothing (EPS) and the Anisotropic Diffusion (AD) filter.

The third step consisted of using a combination of global threshold, watershed algorithm and region growing technique to segment the data into sediment grains, hydrates and fluid phase (see Figure 4-29). Unfortunately, the attempts to segment the gas and water were not successful so far due to the low-density contrast between the two phases as you can see in Figure 4-28. More effort has to be invested on this task in the future and may be different reconstruction algorithms should be used.

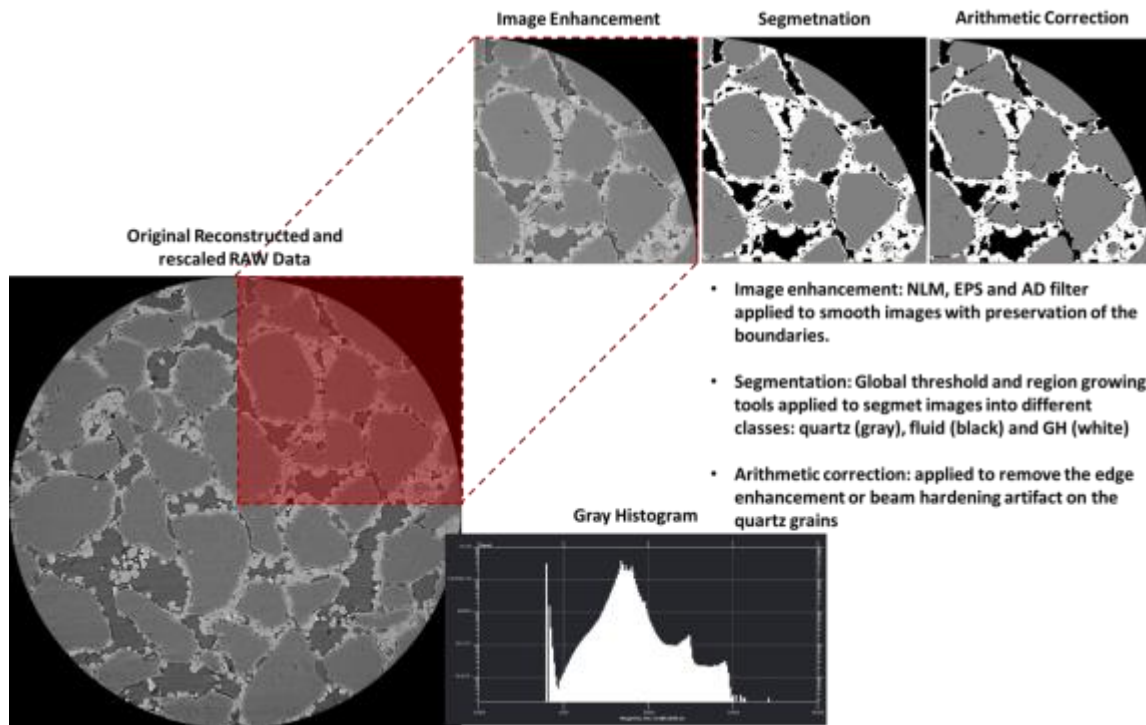


Figure 4-29. Different steps of data processing (images provided by Kathleen Sell)

Once the data are segmented and each phase in the sample is identified, the data can be rendered using Avizo software and a 3D image of the distribution of GH in porous media can be generated. As conclusions could be drawn from 2D images, the 3D rendering was not done systematically for all samples.

4.4. Fast X-ray crystallite size determination (FXRCS) method

4.4.1. Materials

4.4.1.1. LaB₆

Standard LaB₆ powder (NIST SRM 660a) was used without further treatment as calibrant of the method. Each particle of LaB₆ represents one crystallite. Several SEM images of different batches of LaB₆ mounted on a scotch film were taken with different magnifications. Figure 4-30 illustrates an example of SEM image of LaB₆. The CSD of LaB₆ obtained by SEM image analysis is plotted in Figure 4-31. The size of particles was extracted from SEM images with the aid of "Photoshop CS3" computer software for image analysis. The size of each crystallite was specified as the diameter of a circle with equivalent projected area as the particle.

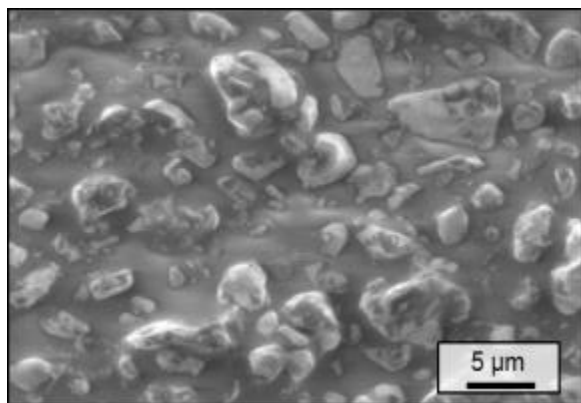


Figure 4-30. SEM image of standard LaB_6 powder (NIST SRM 660a)

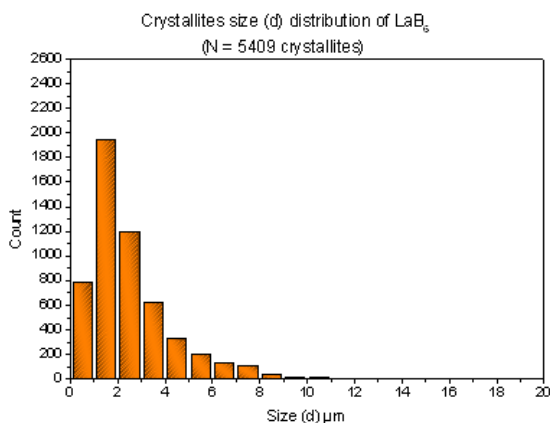


Figure 4-31. Crystallites size (diameter (d)) distribution of 5409 particles of LaB_6 extracted from SEM images.

The diameter of particles estimated by this method may be overestimated because as the particles are not spherical, they tend to adhere to the surface of Scotch by their large surface (shorter diameter normal to the surface of Scotch). Small particles of LaB_6 were determined from SEM images at high magnification. The calculated average diameter of LaB_6 from 5409 particles is 2.5 μm (standard deviation (SD) = 1.84).

LaB_6 was diluted with starch powder [1:6] (commercialized Mondamin Stärke). For the ex-situ calibration, a kapton capillary (0.8 mm) was filled while for in-situ calibration the LaB_6 powder mixture was filled into the aluminum sample holder (0.8 mm) of the pressure cell then mounted on the cell and a Xe gas pressure of 0.2 MPa was applied to meet similar conditions as for Xe hydrate samples.

4.4.1.2. Xe hydrate

Several Xe hydrate-bearing sediment samples with 20 wt.% frost were investigated. *In-situ* measurements inside the pressure cell were achieved at different formation times of 2 min, 30 min, 2 days, and 4 days. Longer formation runs were done *ex-situ* in 2 mm kapton capillaries for 1 week and 4 weeks using the same starting mixture. For all samples, the formation was started by applying a pressure of 0.5 MPa under constant temperature of 276 K. For *in-situ* measurements, we used the stop-pause procedure as for tomographic experiments to stop the reaction and to take a scan.

4.4.2. ID15B beam line setup

The ID15B beam line of the European Synchrotron Radiation Facility (ESRF) in Grenoble (France) was used for the investigation of the crystallite sizes of GH-bearing sediments. The ID15B beam line is dedicated to diffraction studies of powders, amorphous materials and single crystals, and to high-resolution Compton studies. The beam line is suitable for *in-situ* and high-pressure works. It provides high-energy between 60 and 90 keV. The beam line is equipped with a Pixium 4700 flat-panel detector which has a useful pixel array of 1910 \times 2480 pixels with a pixel size of 154 \times 154 μm . The detector has a good efficiency at high X-ray energy; hence it is capable of acquiring high quality data in a short time [Daniels and Drakopoulos, 2009].

Due to these characteristics, this beam line was chosen for *in-situ* studies of the microstructure of GH. The beam line satisfies the requirement needed for successful experiments such as suitable sample environment for *in-situ* work, high-intensity beam for good penetration through the pressure cell and for fast measurements. The typical set-up for high-energy X-ray diffraction at ID15B is shown in Figure 4-32.

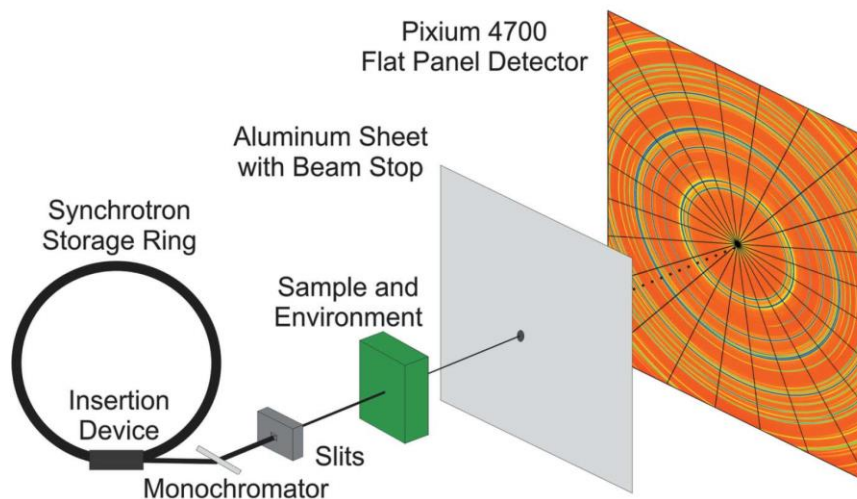


Figure 4-32. Typical set-up for high energy XRD at ID15B of the ESRF. The aluminum plate acts to filter low-energy fluorescence X-rays. The detector image shown is of a textured zirconium alloy [Daniels and Drakopoulos, 2009].

4.4.2.1. Experimental setup and data collection

The pressure cell was mounted on a precision rotation stage. Figure 4-33 and Figure 4-34 show the sample environment and the experimental setup for *in-situ* CSD investigations of Xe hydrate with time. Figure 4-35 depicts the experimental setup for ex-situ measurements of GH CSDs in kapton capillaries using cryogenic stream cooling ($T = 100$ K) to main the samples stable. A monochromatic beam with a variable rectangular cross section was collimated on the sample. The 2D Pixium detector was placed at a distance of 1100 mm from the sample.

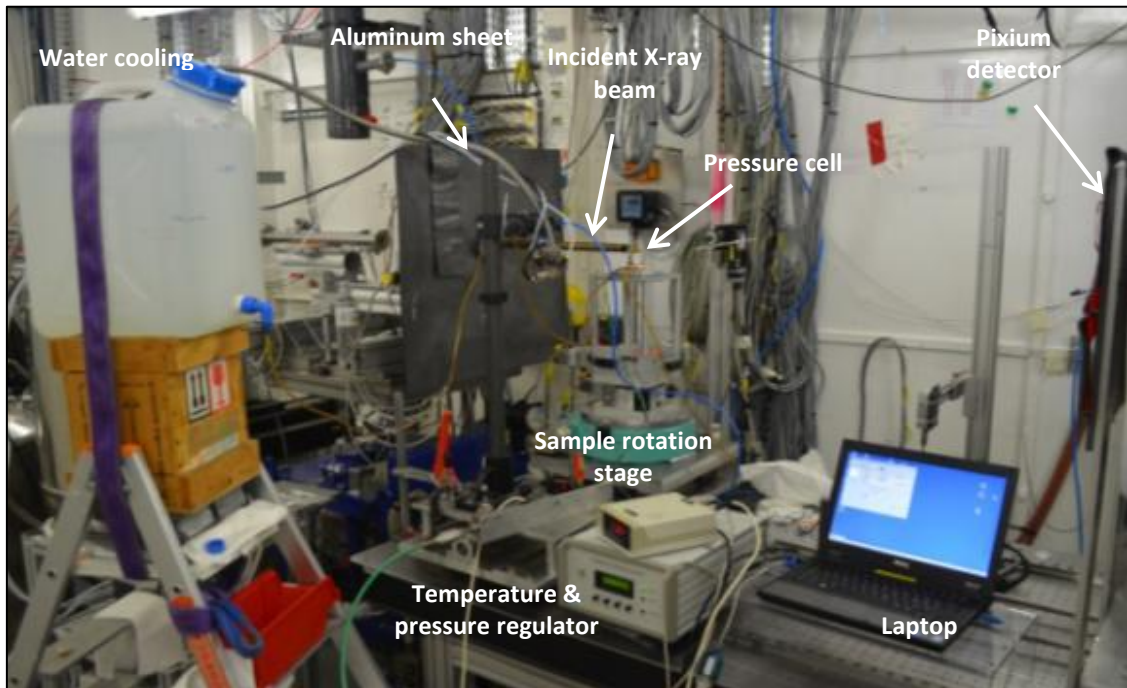


Figure 4-33. Picture of the sample environment at the ID15B beam line

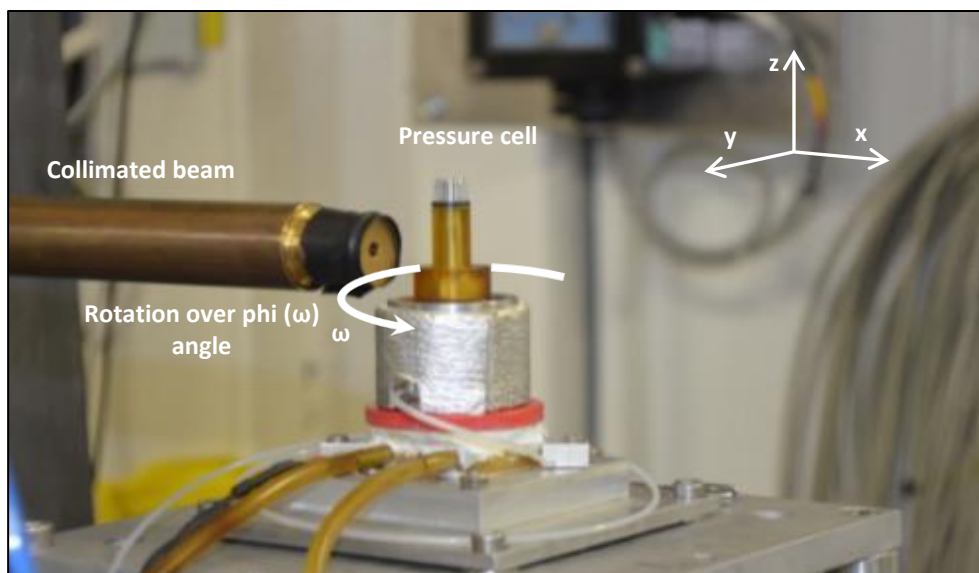


Figure 4-34. Picture of the setup used for *in-situ* investigations of the evolution of GH CSDs with time. The pressure cell was rocked over the angle ω .

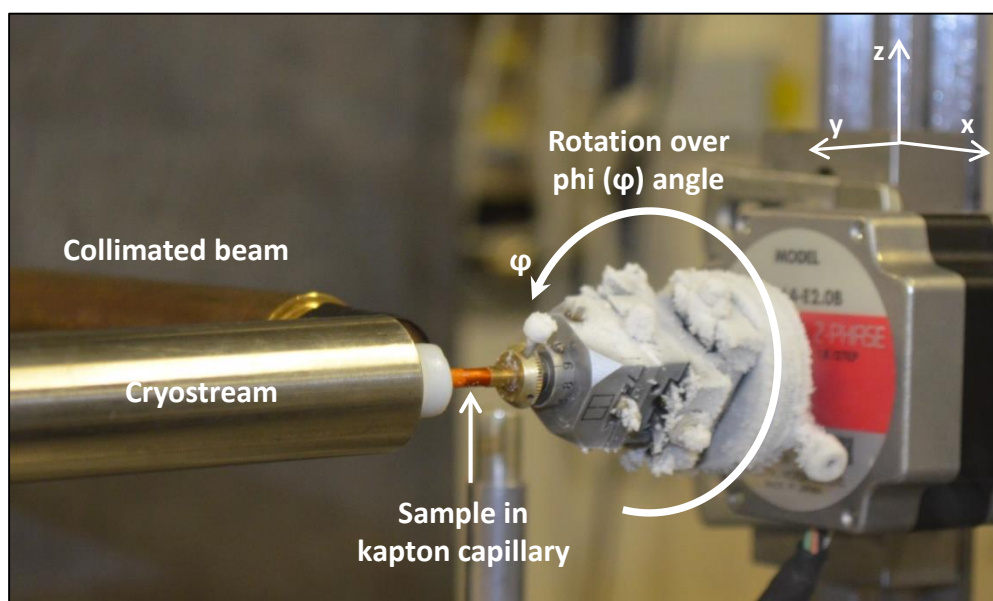


Figure 4-35. Picture of the setup used for *ex-situ* measurements of GH CSDs in kapton capillaries co-axially cooled using cryostream at 100 K. The sample was rotated over the angle φ .

Before starting the data acquisition, the beam size was adjusted in order to get a spotty diffraction pattern of Xe hydrate and of LaB_6 . The spotty diffraction pattern should contain a few tens of spots with small number of overlapped peaks. Afterwards, several snapshots were taken with different exposure times to choose the optimum exposure time which provides a high intensity to background ratio and which permits a fast measurements as well. Finally the step size was chosen depending on the morphological characteristic (e.g. mosaicity) of the crystal of each material. The sample/pressure cell was rocked for few degrees over the rotation angle ω and between 300 and 500 frames were collected per scan. All measurements parameters are summarized in Table 4-7.

Table 4-7. Measurements parameters for all *ex-situ* and *in-situ* experiments

	Sample	Beam size (mm)	Step size (deg)	Sweep (deg)	Exposure time (s)
<i>Ex-situ</i>	LaB_6 + starch (1:6)	0.1 × 0.1	0.005	2	5
	Xe hydrate (1 week)	0.1 × 0.1	0.005	2.5	5
	Xe hydrate (4 weeks)	0.1 × 0.1	0.005	2.5	5
<i>In-situ</i>	LaB_6 + starch (1:6)	0.3 × 0.3	0.005	1	5
	Xe-hyd: t = 2 min	0.3 × 0.3	0.005	2	5
	Xe-hyd: t = 30 min	0.3 × 0.3	0.005	2	5
	Xe-hyd: t = 2 days	0.3 × 0.3	0.005	2	5
	Xe-hyd: t = 4 days	0.3 × 0.3	0.005	2	5

4.4.3. Data processing

The measured 2DXRD diffraction patterns are simply 2D images saved as uncompressed TIFF images. shows an exemplary 2D spotty diffraction pattern of LaB_6 .

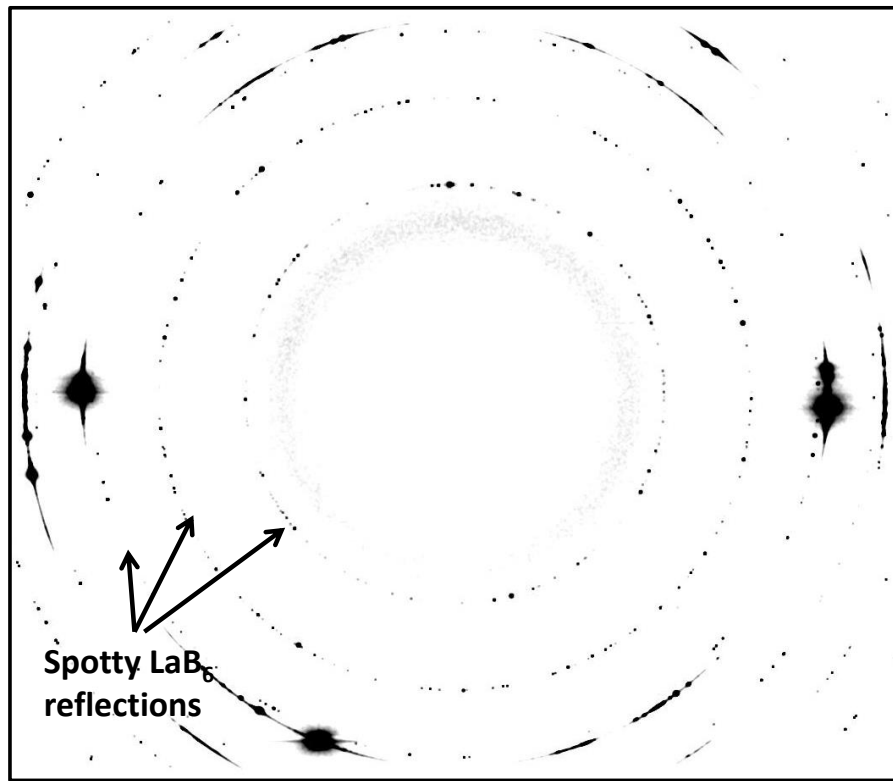


Figure 4-36. Spotty diffraction pattern of LaB_6 .

The main goal of data processing consists of extracting the intensity of each spot from a specific “hkl” diffraction ring in order to use this information to determine the crystallite size. For this purpose, an image analysis program has been developed in order to analyze 2D diffraction patterns and extract necessary information. The program was written on the programming language Python (available at www.python.org) by the PhD student Sigmund Neher. The program will be discussed in more details in his PhD thesis. Here only an overview of the steps of data processing is given.

The data analysis is done in following steps:

- (1) the user has to select the Debye-Scherrer ring of interest
- (2) a thresholding operation is used to separate peaks with respect to background. The thresholding is a very well-known method used to separate regions of an image corresponding to objects of interest which we would like to analyse. The separation is based on the difference of intensity between the pixels of the object of interest and the background pixels. The threshold in our case corresponds to the mean values of adjacent ring section areas are used which can be multiplied by the user (set-multiplier) in order to increase (or reduce) the limit of detection of spots. All peaks which have intensities above this threshold will be detected and taking into account (see Figure 4-37).

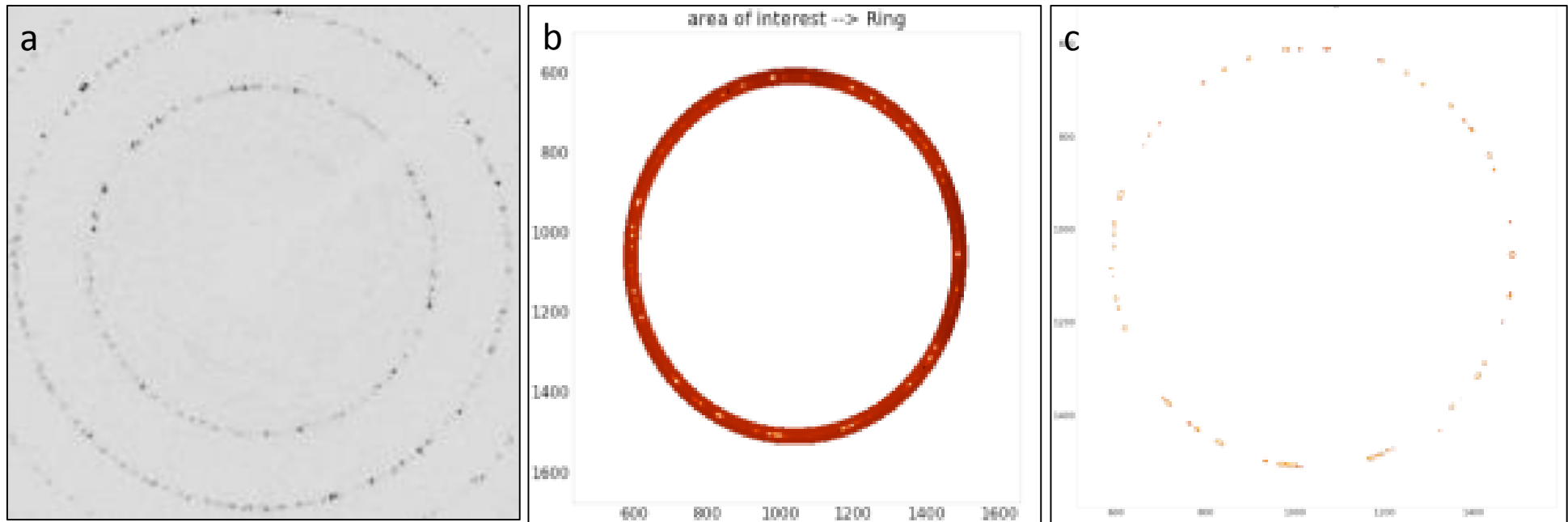


Figure 4-37. Images showing the separation of peaks using thresholding method. a) 2D spotty diffraction pattern of LaB_6 , b) selection of the Debye-Scherrer ring of interest, c) separation of peaks in the circumference of the selected diffraction ring (image provided by Sigmund Neher).

- (3) in case of partly overlapping peaks a seeded watershed algorithm is used¹ [P. J. Soille, 1990] (Figure 4-38).

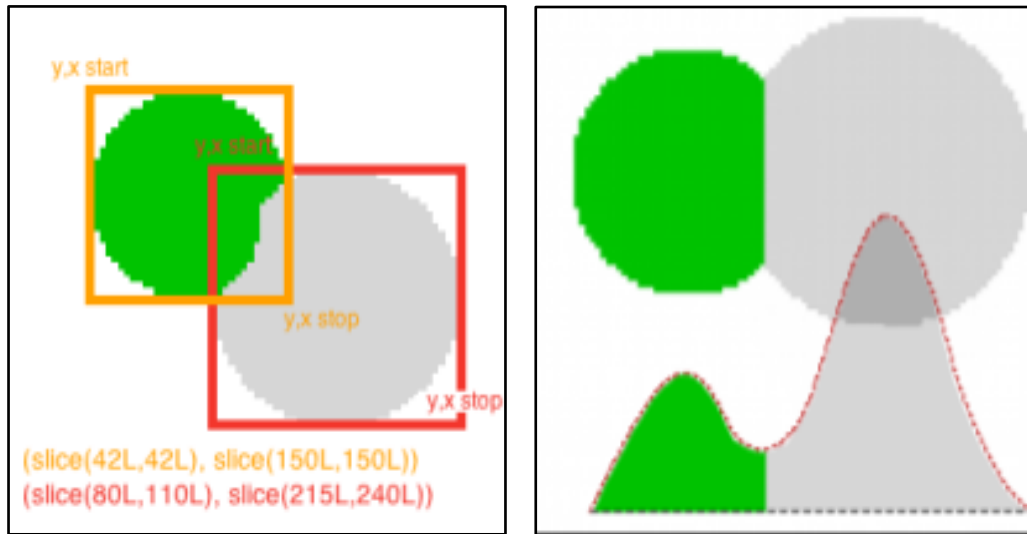


Figure 4-38. Example of treatment of two overlapped spots (image provided by Sigmund Neher)

- (4) the subsequent step is the allocation of peaks found in adjacent images. The allocation combines the 2D area information of each peak in each image to 3D volume information of every reflection (see Figure 4-39).

With this information the program is able to return the rocking curve of each reflection. The integrated intensity corresponds to the area under the curve (see Figure 4-40). It is determined either by fitting the curve by a Pseudo-Voigt function or by integrating over θ using the trapezoidal rule.

¹ Watershed separation is no longer applicable in the new version of the python program.

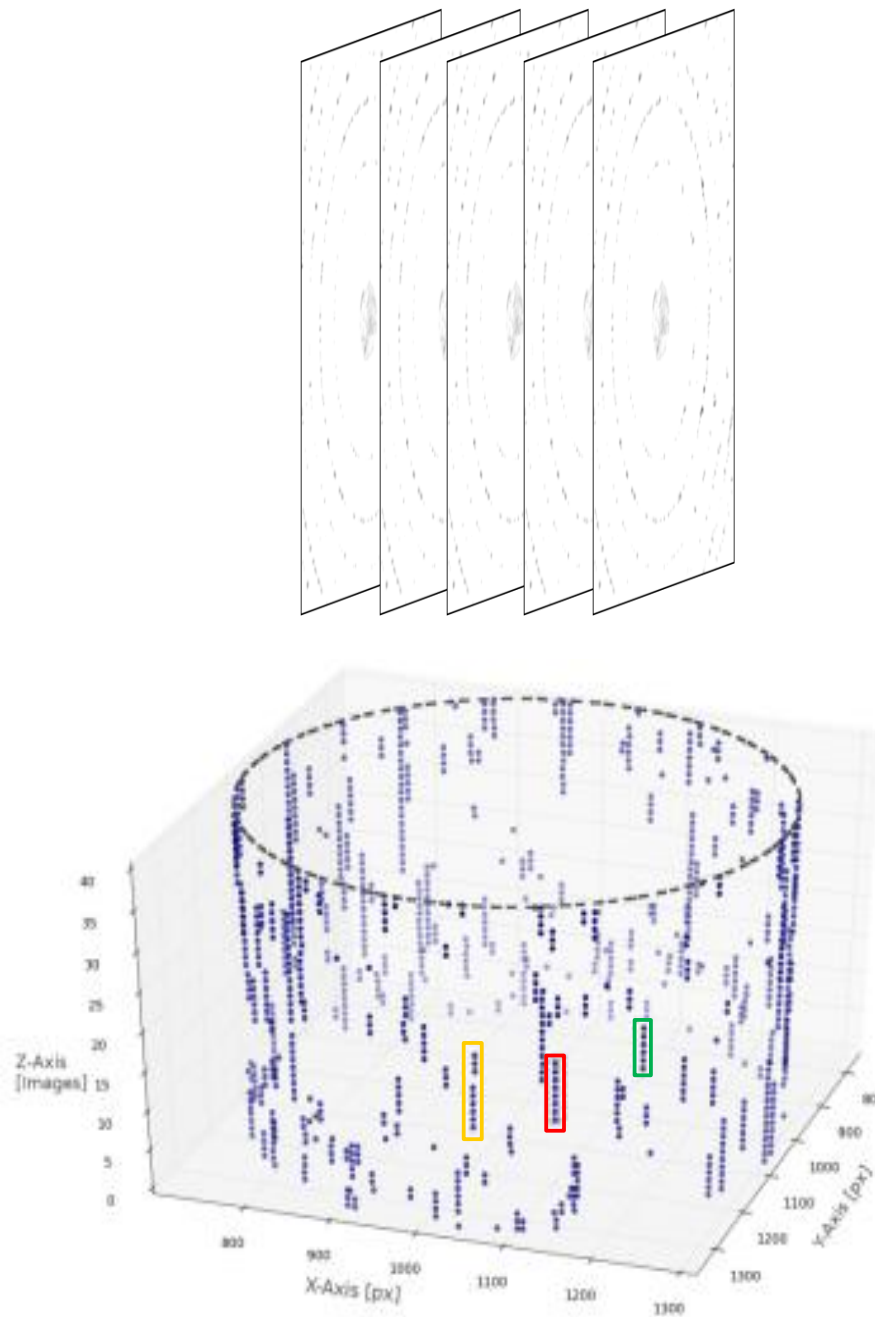


Figure 4-39. On the left hand side, a stack of 2D images analysed in order to extract intensity information of each peak from the different images which are shown on the right hand side images and marked by yellow, red and green boxes (image provided by Sigmund Neher).

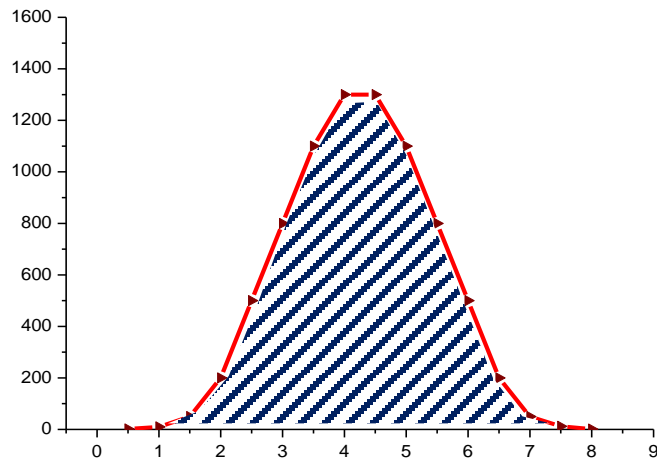


Figure 4-40. Example of a rocking curve of a crystal: intensity variation as a function of the rotation angle. The area under the curve (textured in blue) corresponds to the integrated intensity of the peak.

- (5) The output intensities are corrected for the Lorentz factor. The program calculates the Lorentz factor depending on the experimental setup and the velocity of the sample rotation (degree of steps/exposure time). The corrected intensities are obtained by dividing the raw intensities by the Lorentz factor.

5 | Observations of GH microstructures in sedimentary matrices

In the following chapter, the relevant results from the microstructural observations of GH-bearing sediments using SXRCT are presented and discussed. Our goal was to follow the nucleation and growth of Xe hydrate in sedimentary matrices and to study the effect of several parameters on the GH formation by taking several scans at different steps of GH formation. A complete sequence of GH formation (from the beginning till the end of the formation process at one spot) for all runs was difficult to get because of some inhomogeneity of the water distribution frequently observed over the scanned volume despite our effort to get a uniform distribution of water within the sediments. Thus, we consider only the local water saturation (W_s , the fraction of pore filling by water at the scan position) in the following discussion. Due to the big amount of data collected, only relevant results will be presented here. Table 5-1 shows the list of samples which will be presented in this Chapter. The recorded pressure curves of these samples are shown in Appendix B.

Table 5-1. List of samples presented and discussed in Chapter 5.

Sample N°	Formation procedure	Type of Sediment (wt.%)	Water sat. (Ws %)	Beamtime
Sample 1	I	Natural Qz Sand	22	2012
Sample 2	I	Natural Qz Sand	57	2012
Sample 3	II	Natural Qz Sand	49	2012
Sample 4	III	Natural Qz Sand	34	2013
Sample 5	I	Nat. Qz + 8% Kaolinite	77	2013
Sample 6	I	Nat. Qz + 8% Montmorillonite	72	2013
Sample 7	I	Natural Qz Sand	27	2013
Sample 8	I	Natural Qz Sand	41	2013
Sample 9	I	Natural Qz Sand	37	2013
Sample 10	I	Hydrophobic GB	54	2013
Sample 11	I	Natural Qz Sand	14.6	2013
Sample 12	I	Natural Qz Sand	49.5	2012
Sample 13	I	Natural Qz Sand	88.6	2013
Sample 14	I	Natural Qz Sand	32.4	2012
Sample 15	I	Natural Qz Sand	79.1	2012

5.1. Nucleation and growth processes

The nucleation and growth mechanisms of GH were studied in various sedimentary matrices and at different water saturation with a time resolution from seconds to several hours. Only the initial growth until depletion of one GH constituent was studied in our experiments. The coarsening process which takes place after the completion of GH formation continues to time-scales beyond our study.

The sub- μm resolution of the used tomographic setup and the “stop and go” approach to interrupt the reaction permitted to locate precisely the nucleation sites and to follow the growth process till the completion of GH formation.

The results from all runs performed using procedure I starting from juvenile water with the presence of a free-gas phase show that the nucleation of GH starts at the interface between Xe gas and liquid water. It appears that the gas-water interface, where the concentration of both constituents is the highest, is the most favorable site for GH nucleation. This might be due to the low solubility and slow diffusion rate of Xe gas in water. A Xe hydrate film covering the entire gas-water interface is first formed within few seconds (Figure 5-1). The initial GH film has a typical thickness of few μm (~ 2-5 μm). The thickness depends on various factors such as the stochastic nature of the nucleation process, local P/T variations and the heat transfer.

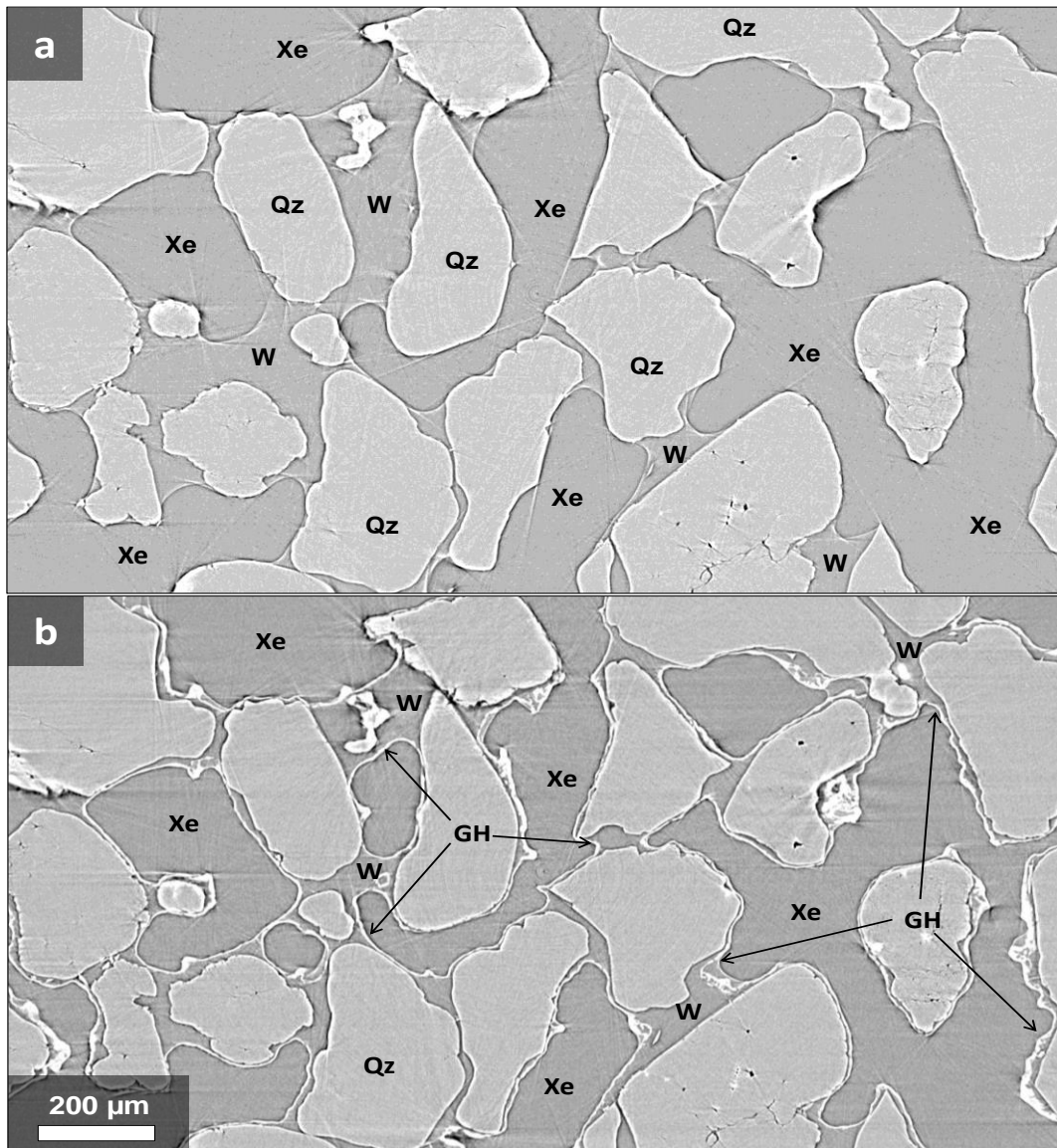


Figure 5-1. Nucleation of a thin GH film at the gas-water interface for GH formation using procedure I. (Sample 1, $W_s = 22\%$): a) CT image before starting GH formation, b) CT image taken after a reaction time of 70 seconds ($t_R = 70$ s). Gas hydrate (GH) in white, water (W) in gray, quartz sand (Qz) in light gray. Gas and juvenile water have the same contrast and can be distinguished only by the meniscus which separates the two phases.

After the formation of the initial GH film which intervenes between Xe gas and water, the formation process becomes diffusion controlled one. The further GH growth proceeds by thickening of the GH layer across the Xe-water interface over several minutes. This GH film may well be permeable; the hydrate film does not have a uniform density contrast which can be ascribed to porosity on a μm and sub- μm scale. This is in agreement with the optical observations at the gas-water interface by *Davies et al.* [2010] (see Figure 2-12). These pores could represent diffusion pathways for both gas and water molecules to allow further GH formation [*Staykova et al.*, 2003]. Whether the further hydrate growth is controlled by the transport of gas or water molecules through the hydrate film is not well known. There are some indications from our results that the thickening of GH occurs in both directions but preferentially towards the gas phase (see Figure 5-2). This may confirm the observation of *Davies*

et al. [2010] that water molecules are the most mobile species in the hydrate phase. The hydrate film growth controlled by permeation of water molecules through the GH film was also suggested by *Mori and Mochizuki* [1997].

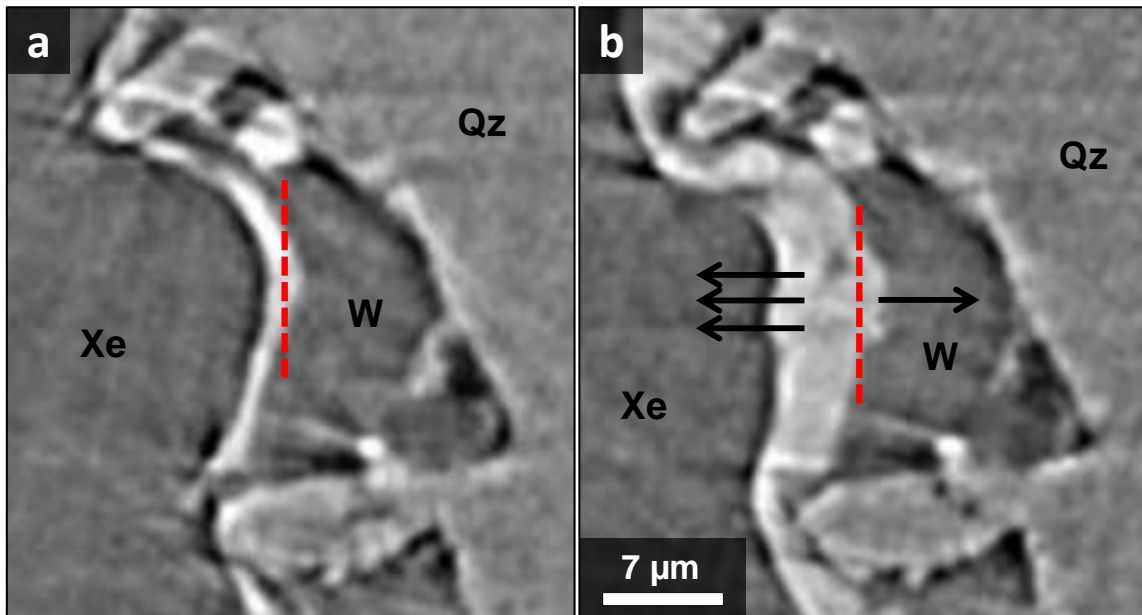


Figure 5-2. Initial growth of GH film preferentially towards the gas phase. a) Formation of an initial thin GH film at the gas-water interface ($t_R = 50$ s), b) thickening of the GH film across the GH water interface in both directions but preferentially towards the gas phase ($t_R = 130$ s). From the dashed red line representing the middle of GH film in (a), the hydrate film is more developed in the side of the gas phase in (b). (Sample 1, $W_s = 22\%$)

A growth sequence Figure 5-3 shows a sequence of Xe hydrate growth using procedure I. After few minutes, the hydrate film was observed to thicken. Some μm -sized single crystals as suggested by their emerging polyhedral shapes were observed to float on the hydrate film. These larger crystals also show an appreciable growth into the gas phase and lead to nearly isometric crystal shapes, consistent with a cubic crystal structure; their size at the point of the full conversion is 10-20 μm . With time the formation rate decreases which suggests a diffusion limited reaction. The pores are filled with hydrate leading to a more dense structure. The growth rate of GH is estimated to be between 2 and 4 $\mu\text{m min}^{-1}$. The GH film can reach a final thickness of 50 μm over a formation time of 15 to 20 min.

Infrequently the initial GH film grows as a layer composed of relatively big and less interconnected GH crystals. These GH crystals grow first laterally forming a denser GH layer. It might be that the thin hydrate film is composed of very fine crystals which cannot be solved by our resolution. The density of nucleation centers is roughly estimated from as $6.4\text{-}14.4 \times 10^7$ nuclei/ m^2

On the other hand, the nucleation process of GH from water-rich system studied by procedure II and III seems to be different from the usual formation process (gas-rich systems). For GH formation run using procedure II, the nucleation appeared to take place close to the gas-water interface leading to isometric often polyhedral crystals as shown in Figure 5-4. It is not clear whether the first nucleus grows preferentially at the gas-water interface or inside the water as the image below shows crystals

growing to appreciable sizes. Figure 5-4 shows that there are some crystals totally covered by water close to the gas-water interface and other crystals growing in the gas phase so it is difficult to predict where the nucleation started first. In comparison to the formation using procedure I, the nucleation density is lower for this case and it is roughly estimated as $1.6\text{-}3.6 \times 10^7$ nuclei/m².

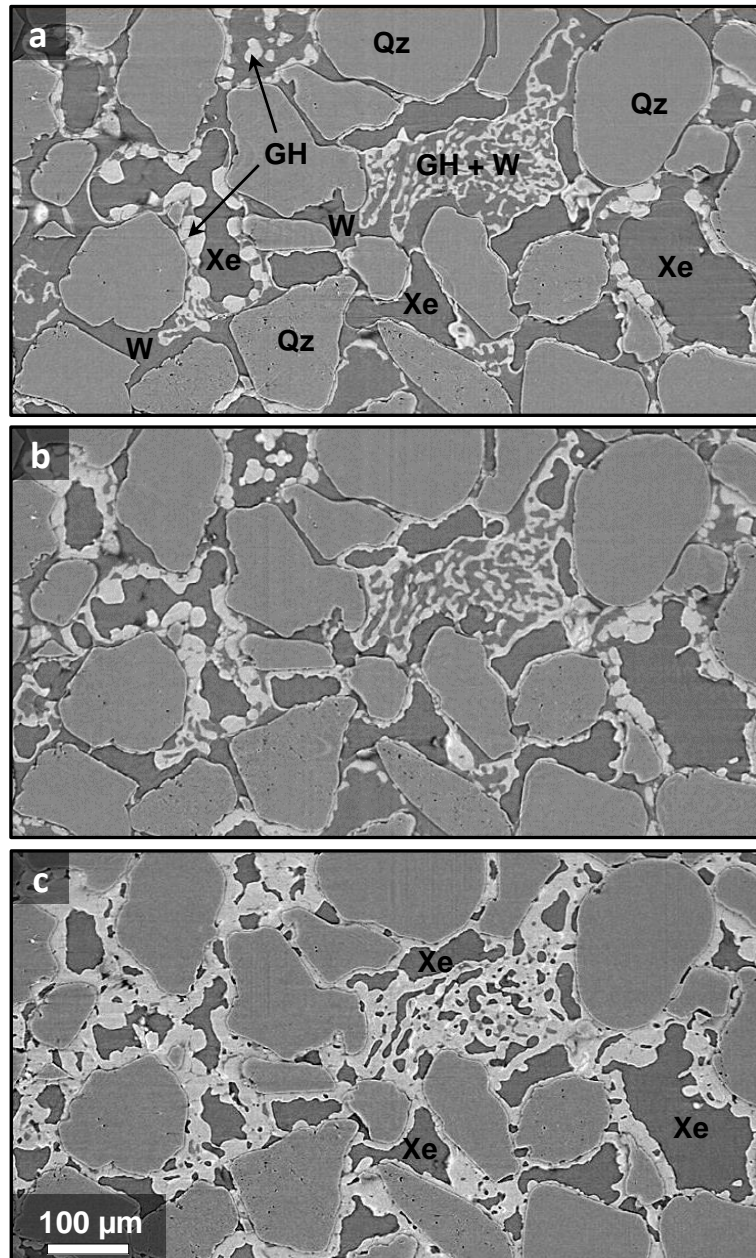


Figure 5-3. Sequence of GH film growth using procedure I (Sample 2, $W_s = 57\%$). a) initial ($t_R = 4.35$ min), b) intermediate ($t_R = 10.2$ min), and c) final ($t_R = 44.65$ min). Pockets of rest water trapped between GH crystals due to gas diffusion limitation can be seen in (c).

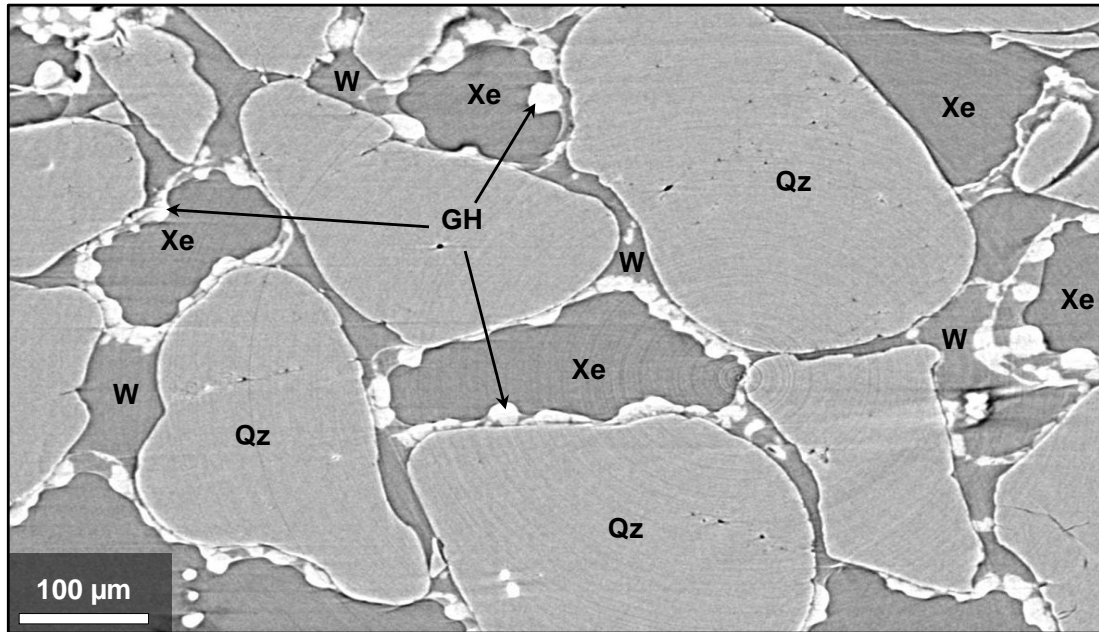


Figure 5-4. Nucleation of GH crystals inside the water close to the gas-water interface by formation using procedure II (Sample 3, $W_s = 49\%$). Before reformation, *in-situ* formed GH was decomposed at 275 K and atmospheric pressure. The sample was held at these conditions for ~ 1 h before the reformation. $t_R = 50$ s.

For procedure III, GH crystals grow preferentially inside the water phase; again with distinct polyhedral shapes (see Figure 5-5). For both runs, the formation of a GH film was not observed. Heterogeneous nucleation on the surface of Qz grains with subsequent growth into the pore space was also not evident using dissolved gas methods.

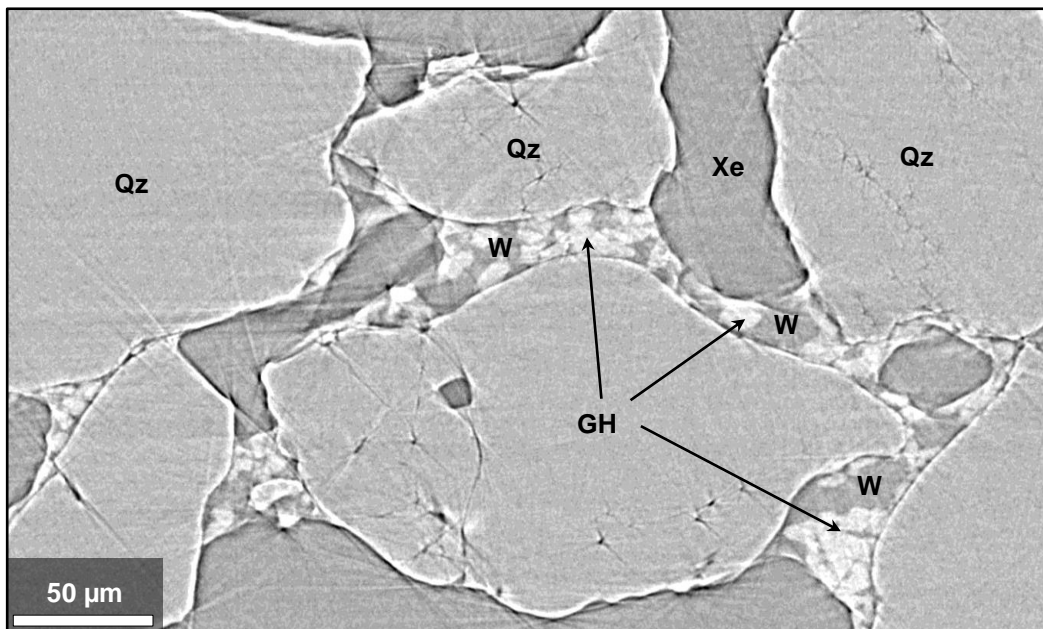


Figure 5-5. Nucleation of GH crystals inside the water phase by formation from Xe-enriched water using procedure III (Sample 4, $W_s = 34\%$). Before the formation the sample has been left for 1 h at 275 K and atmospheric pressure to completely decompose Xe-Hydrate powder. $t_R = 42$ s.

Figure 5-6 depicts the evolution of crystal habits for procedure II. The growth of polyhedral crystals is preferentially directed towards the Xe gas phase. The crystals are less interconnected and show clear isometric habits with indications for crystal facets. The resulting crystals again reach a size between 10 and 20 μm after several minutes. For procedure III, the nucleation of GH crystals inside the water phase is followed by isotropic growth which leads to the formation of rounded polyhedral crystals (Figure 5-7).

The volume growth of these crystals is distinctly slower than the one of the initial film suggesting a different transport mechanism of the crystals' constituents, no longer proceeding through pores in the GH. Whether the transport proceeds by solid state diffusion of water molecules through the crystals' molecular cages [Kirschgen *et al.*, 2003; Liang and Kusalik, 2011], along crystal defects like grain boundaries, dislocation cores or the crystal surface cannot be distinguished in our images.

The resulting crystals again reach a size between 10 and 20 μm after several minutes. The molecular rearrangements at the growth interface between liquid water and GH can be envisaged to be similar to what has been imagined in molecular dynamics simulations from metastably gas-enriched water e.g. [Walsh *et al.*, 2011; Walsh *et al.*, 2009].

A possible explanation for the differences of GH formation between method II and III is suggested in section 5.1.1.

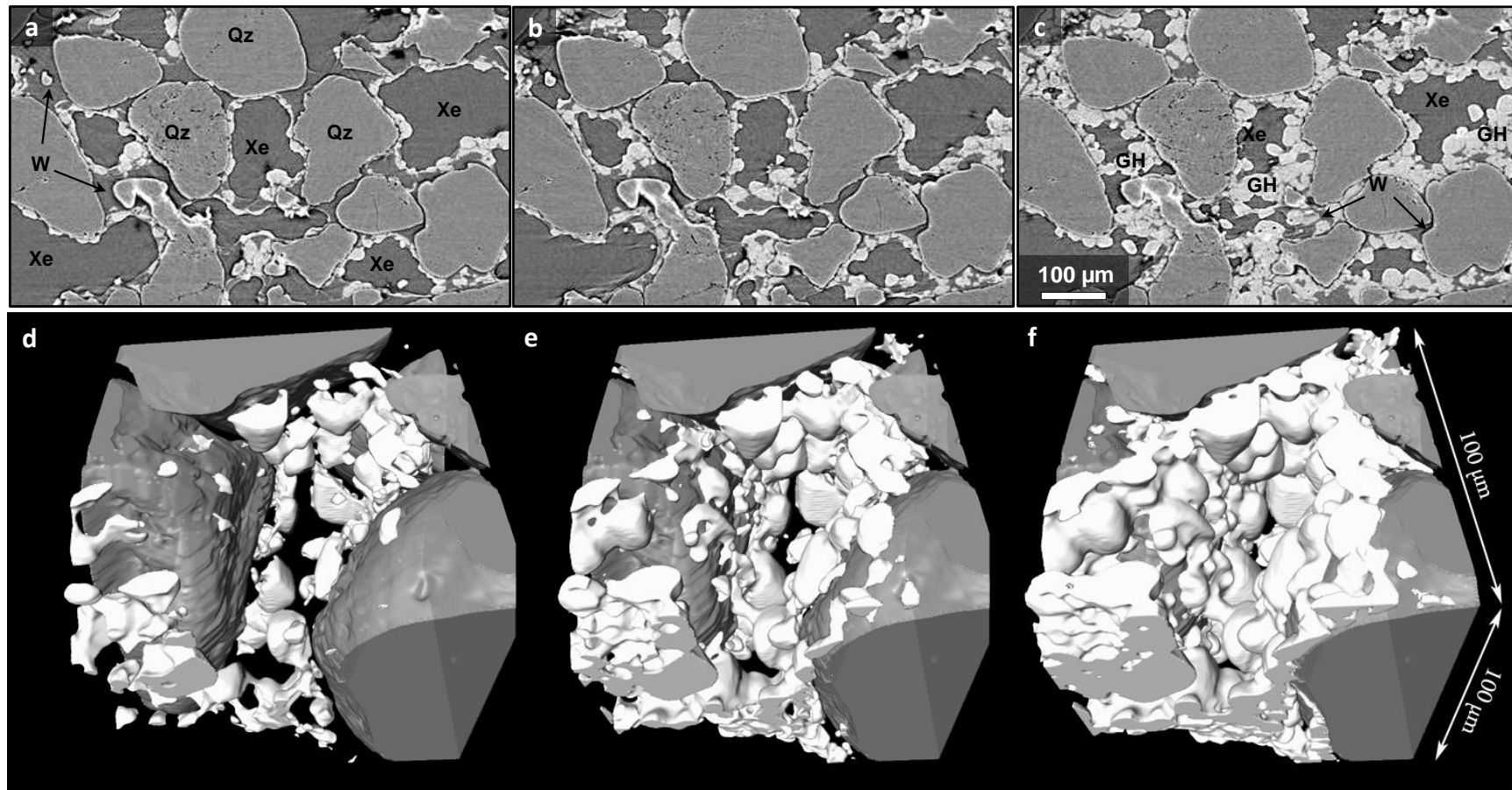


Figure 5-6. Evolution of GH growth from memory water using procedure II (Sample 3, $W_s = 49\%$). a) initial ($t_R = 40$ s), b) intermediate ($t_R = 4.2$ min), and c) final ($t_R = 11.3$ min). Large polyhedral crystals were initially formed inside the water near to the gas-water interface. The images d, e and f represent respectively the 3D rendered images of a, b and c (provided by Kathleen Sell). Rounded polyhedral crystals of GH (white) grow preferentially towards the center of the pore space; they do not adhere to the Qz (gray) surface, which is covered by a water layer of variable thickness. For clarity, the fluid phases have been removed from the rendered images

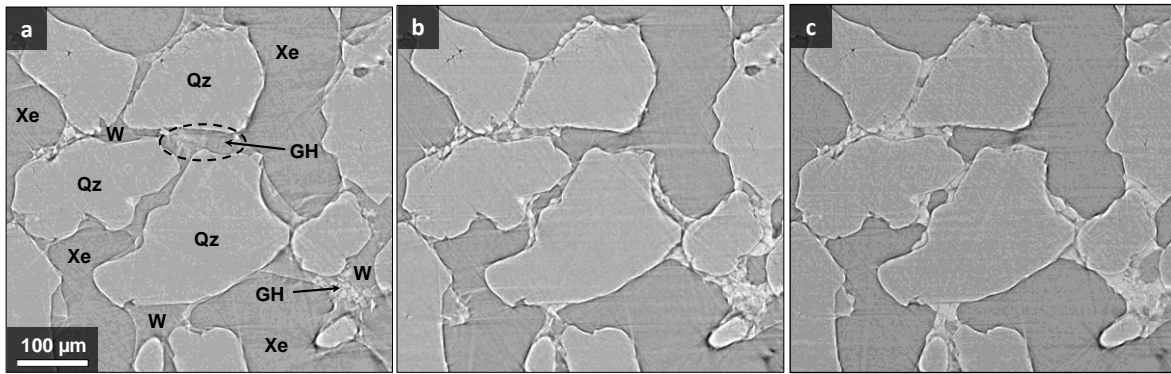


Figure 5-7. Evolution of GH growth from memory water, procedure III (Sample 4, $W_s = 34\%$). a) initial ($t_R = 32$ s), b) intermediate ($t_R = 3.6$ min), and c) final ($t_R = 11.7$ min). The nucleation starts inside the liquid water.

The growth mechanism of GH from juvenile water in gas-rich system using procedure I can be described in three steps as illustrated in Figure 5.8. The first stage consists in the formation of a porous thin-gas hydrate film at the gas-water interface. In the second stage the porous film gets thicker and propagates across the gas-water interface. Finally, the pores are filled over time and the GH structure becomes denser.

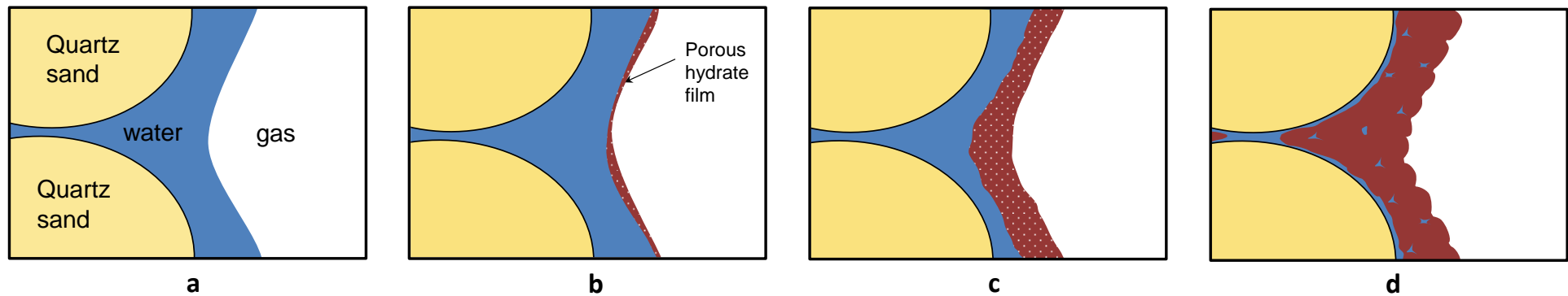


Figure 5-8. Conceptual model of GH formation from juvenile water using procedure I. a) Nucleation of a porous GH film at the gas-water interface, b) thickening of the GH film across the gas-water interface preferentially toward the gas phase, and c) final microstructure of GH after completion of the formation process: a water layer remains between GH and Qz grains. The structure of GH becomes more dense but characterized by the presence of water pockets

5.1.1. The memory effect

Our experimental findings clearly indicate that the GH nucleation and growth patterns observed in water obtained from GH decomposition (procedure II and III) is markedly different from the one observed in juvenile water (procedure I), thus lending further strong support to the existence of a so-called “memory effect”. We believe that the reformation process of GH after dissociation is enhanced by the presence of gas molecules in water in an unknown state rather than a remaining hydrate structure.

While there is clear evidence from reflectometry that gases can be enriched in water at the molecular-scale gas-water interface [Boewer *et al.*, 2012; Lehmkuhler *et al.*, 2008], unequivocal experimental evidence for a metastable enrichment of gases in thicker interfaces or bulk water is still not available. Molecular computer simulations often used an enrichment procedure of gases in bulk water by decomposing hydrates prior to reformation [Demurov *et al.*, 2002; Hawtin *et al.*, 2008; Jacobson *et al.*, 2010; Liang and Kusalik, 2010; Vatamanu and Kusalik, 2010; Walsh *et al.*, 2011; Walsh *et al.*, 2009] with a resulting metastable enrichment of gases in the liquid. Occasionally, the formation of nano-bubbles was observed in a gas-enriched liquid within the ns to μ s time-scale of the simulations [Bagherzadeh *et al.*, 2012; Koishi *et al.*, 2005; Walsh *et al.*, 2009].

For the first time, we have indications that indeed liquid water can become metastably enriched in Xe gas as suggested from the higher absorption coefficient observed for small water pockets in the pore space of Xe-hydrate (Figure 5-9); unfortunately the electron-density contrast cannot easily be quantified from the tomograms to obtain values for the gas enrichment. The observed Xe enrichment may well be the result of a dynamic equilibrium of gas and water at a nearby GH-water interface, where cage destruction with gas release and reformation with gas uptake must take place in a dynamic fashion on a μ s to s time scale; these enrichments (over the bulk solubility) are only temporarily maintained in μ m-sized water pockets or water layers as Xenon will steadily be diluted into the bulk water towards equilibrium solubility.

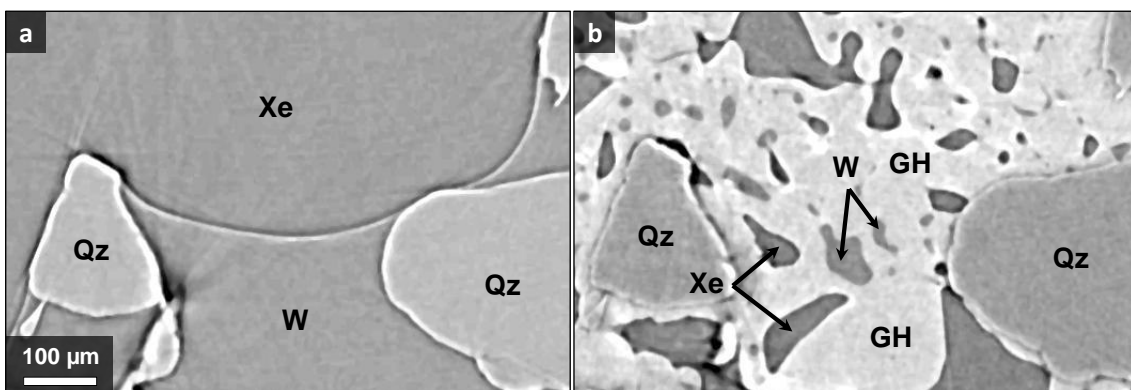


Figure 5-9. Enrichment of water with Xe gas with time (Sample 2, $W_s = 57\%$). a) CT image before GH formation ($t_R = 0$ min, $P = 0.22$ MPa, $T = 276$ K), b) CT image at the end of GH formation ($t_R = 14.65$ min, $P = 0.22$ MPa, $T = 276$ K). Water and xenon have almost the same gray value at the beginning of the reaction but water becomes brighter at the end of GH formation which may indicates an enrichment in xenon gas. The relative gray value of water taking xenon as reference increases from 102 % to 107 %.

In procedure II and III, the formation started inside the water phase. It appears that after GH dissociation, the dissolved Xe gas molecules or micro bubbles act as new preferential nucleation sites for GH. For procedure II, the crystallization occurs inside the water close to the gas-water interface which may indicate that the concentration of Xe gas in water is higher at the interface. While for procedure III, the nucleation occurred preferentially inside the bulk water. This could be due to the difference of the dissociation mechanism and the time allowed for GH decomposition between procedure II and III; after GH decomposition, the water is at its maximum concentration of gas. At low pressure, the solubility of gas in water decreases; hence gas molecules tend to exist in the gas phase rather than in water. Therefore the memory effect decreases with time. Subsequently, the process of GH formation after a short time of GH decomposition could be different of the one after long time of GH decomposition. As xenon is more soluble in water than methane, the memory effect is expected to be more prominent for xenon than for methane.

In our case, GH in procedure II was dissociated by depressurization and in procedure III, *ex-situ* formed GH was decomposed by warming up the sample. Thus, the differences in the GH formation processes could be attributed to differences in equilibration; fast for pressure changes and slow for temperature changes. In the following, we consider the formation procedure II and III as the same formation method from memory water for simplicity (Figure 5-10).

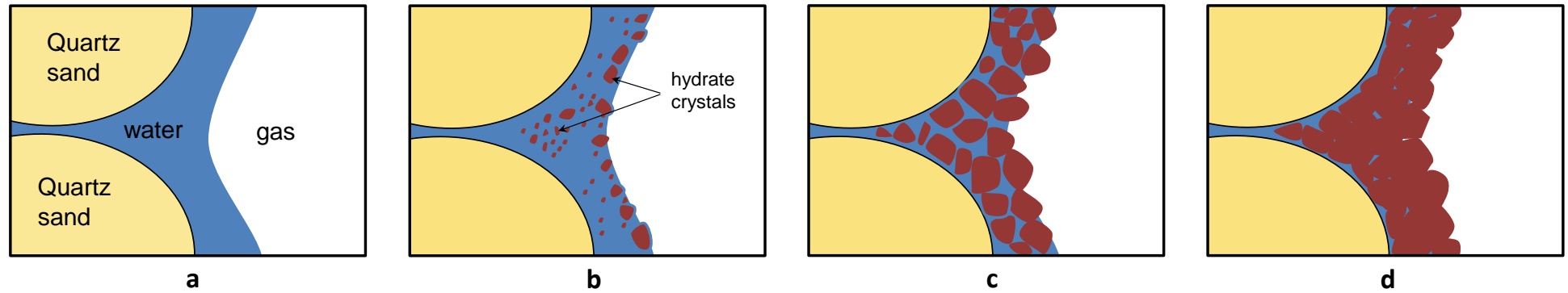


Figure 5-10. Conceptual model of GH formation from memory water using procedure II or III. a) Nucleation of isometric polyhedral GH crystals inside the liquid water, b) growth of GH crystals preferentially toward the pore space, and c) the final microstructure of GH show relatively large GH crystals less interconnected with liquid water remaining at their grain boundary. A liquid water layer remained also between GH and sediment grains as observed in procedure I.

5.1.2. Role of Qz surface

The role of the surface of sediment grains in the formation process of GH in porous media was the subject of a widespread controversy. It was suggested in the past that the nucleation of GH is induced by the surface of sediment grains [Song *et al.*, 2013]. Our observations from a large number

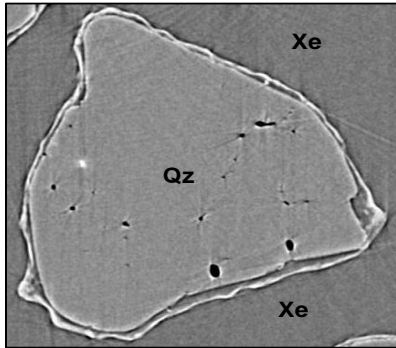


Figure 5-11. GH nucleation at the gas-water interface few μm away from the Qz surface (Sample 1).

of experiments do not show any compelling evidence for a nucleation of GH on the surface of Qz grains. At low water saturation, the liquid water is preferentially accumulated at the Qz surface and at grain contacts by capillary forces. The sub- μm pixel size resolution of the set-up allows locating the onset of nucleation at the gas-water interface, which sometimes appears to be only a few μm away from the Qz surface (Figure 5-11). However, it is very difficult to spot such fine details with low resolution imaging methods which may mislead the uncritical observer to conclude that GH is in direct contact with sediments grains.

5.1.3. Role of clay minerals

The role of montmorillonite and kaolinite clay minerals as enhancing factors in the hydrate nucleation and growth was also investigated in this study. After melting of ice, montmorillonite and kaolinite particles formed intimate mixtures with liquid water before starting the hydrate formation. Figure 5-12 shows the distribution of clay particles in the liquid phase before the beginning of GH formation.

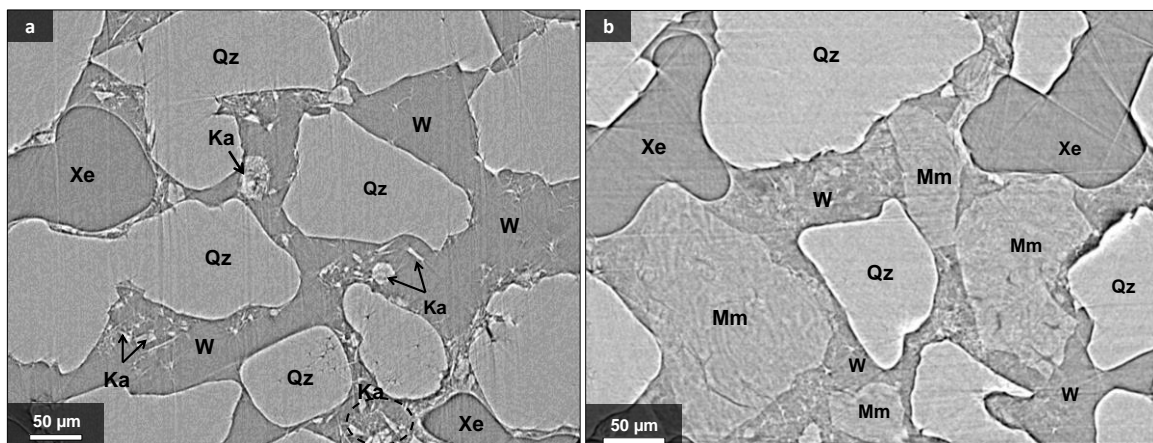


Figure 5-12. Distribution of (a) kaolinite (Sample 5, $W_s = 77\%$) and (b) montmorillonite (Sample 6, $W_s = 72\%$) particles in the water phase before the start of GH formation.

The particles of montmorillonite are observed to form larger agglomerates ranging between 50 and 100 μm in size which can be considered as a part of the matrix, whereas kaolinite clay has smaller particles inhomogeneously dispersed in water. The experiments with kaolinite did not show clear observations as the kaolinite particles are too small and can be distinguished so we will be

limited to the case of montmorillonite to analyse the effect of clay minerals on the formation process of GH in porous media.

The images do not show a clear indication of a preference GH nucleation on the surface of clay particles in the presence of a free-gas phase in contact with water. Figure 5.9 shows the formation of a GH film on the surface of montmorillonite but also at the gas-water interface. It is difficult from the images to figure out where GH started first to nucleate. It is also not clear if the GH film on the montmorillonite particle was formed at the gas-water interface and then proceeded toward the montmorillonite situated close to this interface or if it was formed from the water adsorbed between the layers of montmorillonite into the gas phase. In all cases, it appears that montmorillonite forms an intimate contact with GH due to the absence of a visible gap or a water interface as it can be seen in Figure 5-13.

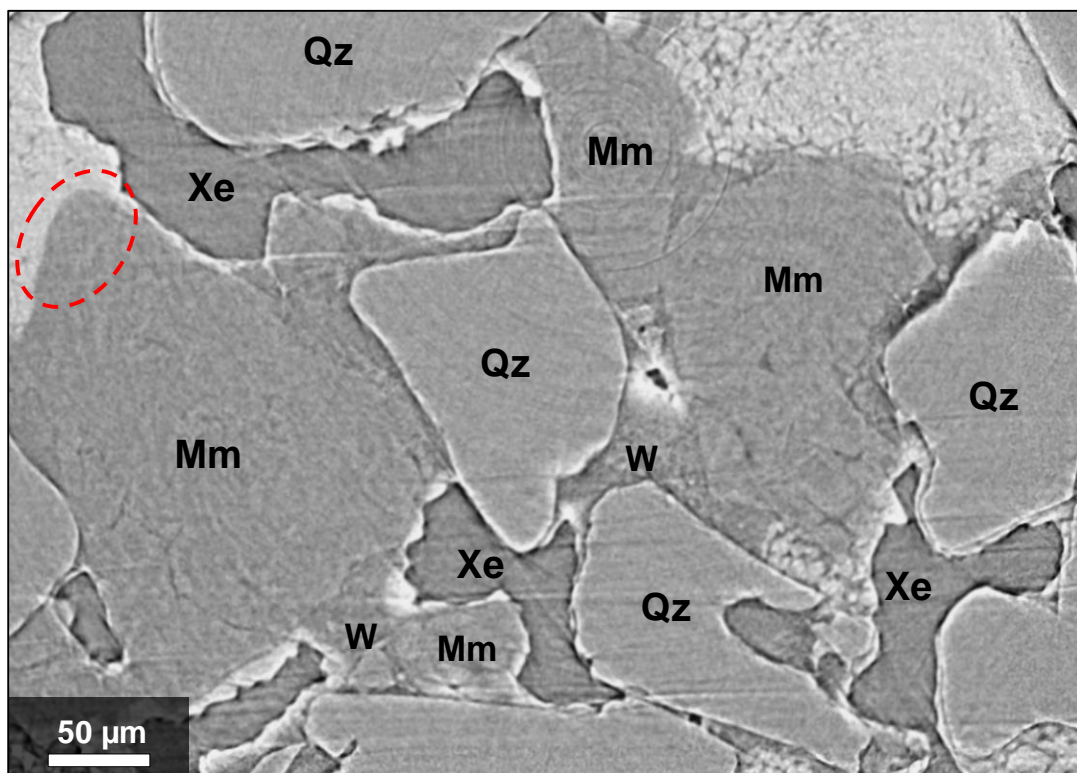


Figure 5-13. GH formation in natural Qz with 8 wt % montmorillonite (Sample 6, $W_s = 72\%$, $t_R = 6.2$ min). The nucleation of GH (white) takes place at the gas-water interface close to the Mm particles. An intimate contact between montmorillonite and GH is observed (red circle).

This could confirm a previous observation of intimate GH-clay mineral contacts made for sample from the JAPEX/JNOC/GSC Mallik 5L-38 research well [Techmer *et al.*, 2005]. There is also compelling evidence that under certain conditions GH can even form intercalates with a certain type of montmorillonite [Guggenheim and Koster van Groos, 2003; Yeon *et al.*, 2011]. Intercalates cannot be resolved by the applied tomographic method and would need to be confirmed using diffraction methods.

The role of clay minerals in promoting the formation process of GH-bearing sediments has to be clarified by further studies.

5.2. Liquid interface between GH and Qz grains

One of the main goals of this study consisted to investigate the nature of the contact between GH and sediments grains which might be the key to understand the origin of the seismic anomalies observed in natural GH-bearing sediments.

Our observations show that GH did not adhere to the surface of Qz grains and tended always to concentrate in the pore spaces. There is strong evidence that after completion of GH formation, a water layer of sub- μm to μm thickness remains between GH and Qz sand grains. The water layer is characterized by an inhomogeneous thickness. It reaches its maximum thickness at the boundary between GH crystals which can be identified by their often well-visible polyhedral shapes. The water layer was observed in a systematic manner for samples for all water saturations and using various formation methods (see Figure 5-14). The low affinity between GH and Qz grains presents as well evidence that the Qz surface does not act as a nucleation surface in sedimentary matrices.

The existence of a water layer between GH and the Qz grains was suggested in the past by *Tohidi et al.* [2001] even in case of high GH saturation and was also emerging from several molecular computer simulations indicative of the preference of a water layer at the GH-(hydroxylated) Qz interface [*Bagherzadeh et al.*, 2012; *Bai et al.*, 2011; *Liang et al.*, 2011]. Most recently, *Kerker et al.* [2014] used a common approach to enhance the contrast between water and GH which is to spike the water with a heavy element salt solution (5 % BaCl_2) and provided evidence that the host (glass spheres) and the GH formed in a pressurized aluminum cell were separated by an aqueous layer. However, as BaCl_2 is excluded from the hydrate structure the salinity of water increases which inhibits the GH formation. Thus, the existence of a water layer is self-evident in this case due to the salting-out effect of the BaCl_2 brine in a system which is not open to a large reservoir of sea-water and consequently diluted after an initial brine formation.

In contrast, our results show for the first time the presence of a liquid layer of pure water between GH and natural Qz sand in a systematic way in all experiments.

The existence of a water layer between GH and hydrophilic Qz surfaces could be attributed to chemical interactions between GH and Qz by means of electrostatic and Van der Waals forces.

Bonnefoy et al. [2005] used a Hamaker microscopic approach to quantify the Van der Waals interactions in different systems involving GH. The Hamaker constant calculations were made for methane hydrate but a change due to the host gas nature is not expected. They reported that the Hamaker constant of the system "Qz-hydrate-water" ($6.509 \cdot 10^{-21}$ J) is bigger than the one of the system "Qz-water-hydrate" ($2.890 \cdot 10^{-21}$ J) which means that Qz surfaces have more affinities to water than to hydrate which confirms the preference of a water layer at the Qz-GH interface [*Bonnefoy*, 2005]. Nonetheless, the Hamaker approach may explain the existence of the water layer but not the layer thickness of sub- μm to μm . A nanolayer of water could be sufficient to reduce the interfacial energy between Qz and GH. The thick water layer may play a role as well in the equilibrium state between gas molecules and hydrate.

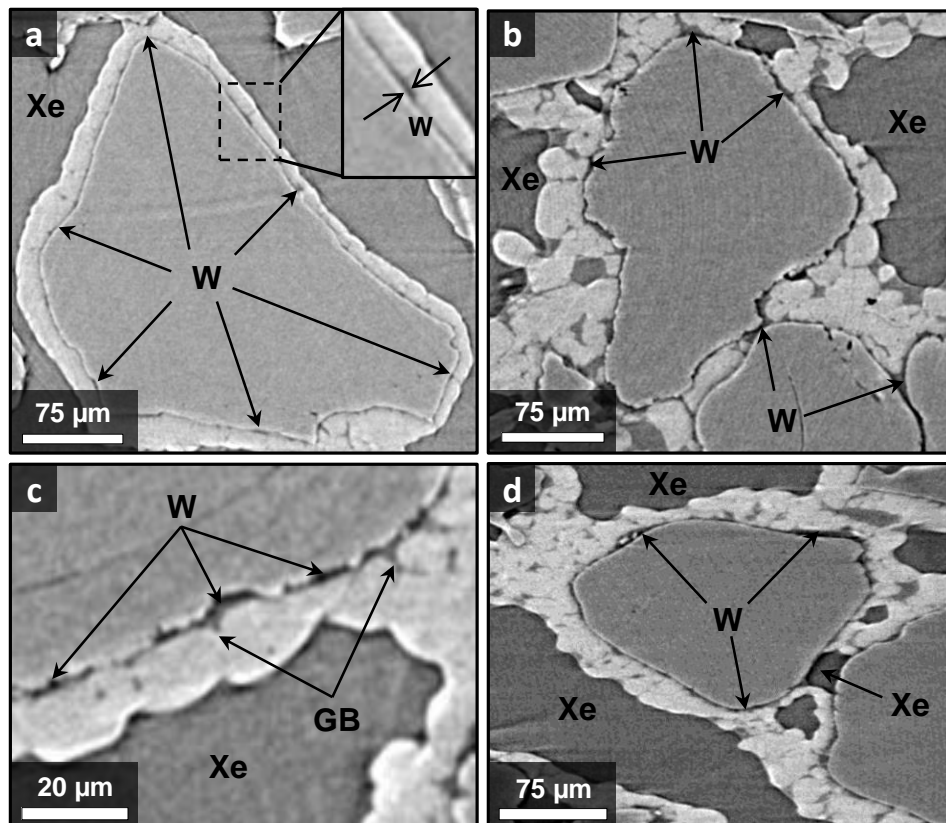


Figure 5-14. CT images showing a thin water layer remaining between GH (white) and Qz grains (Grey) in a systematic manner at the end of the GH formation process. a: using procedure I (Sample 7, $W_s = 27\%$). b: procedure II (Sample 3, $W_s = 57\%$). c: The water layer has an inhomogeneous thickness; it is thicker at the grain boundary (GrB) of GH crystals (Sample 8, $W_s = 41\%$). d: A remaining gas phase near grain contacts was also observed (Sample 9, $W_s = 37\%$).

The presence of the water film has important consequences for the distribution of GH in the sedimentary matrix and the corresponding seismic as well as electromagnetic responses [Dai *et al.*, 2012; Spangenberg and Kulenkampff, 2006; Waite *et al.*, 2009].

5.3. The role of hydrophilic and hydrophobic surfaces

In order to study the effect of the surface of sediments on the process of GH formation, both Qz sand and GB went through a hydrophilic and hydrophobic treatment and were used in GH formation experiments.

In the case of hydrophilic Qz (or GB), the results show no significant difference between the microstructure of GH formed in hydrophilic Qz and in natural Qz sand which are considered as well as hydrophilic [Tschapek *et al.*, 1983]. The microstructure of GH in sediments was characterized always by the presence of a liquid interface between hydrophilic Qz and GH, at grain contacts and the grain boundary of polyhedral GH crystals.

On the other hand, GH formed in hydrophobic matrices tended as well to concentrate in the pore space and did not adhere to the hydrophobic Qz however the liquid water layer was replaced by gas pockets that separate the hydrophobic Qz or GB and GH (see Figure 5-15). No remaining liquid water in the structure of GH was observed.

This observation suggests that the surface of GH, despite its predominantly hydrophilic character [Hirata and Mori, 1998], prefers to form low-energy interfaces with the guest gas, and not with quartz surfaces. It is noteworthy, however, that the stability of GH in hydrophobic matrices is lower than for hydrophilic ones [Hachikubo *et al.*, 2011]; further studies are needed to quantify microstructural differences as well as differences in the formation and decomposition kinetics.

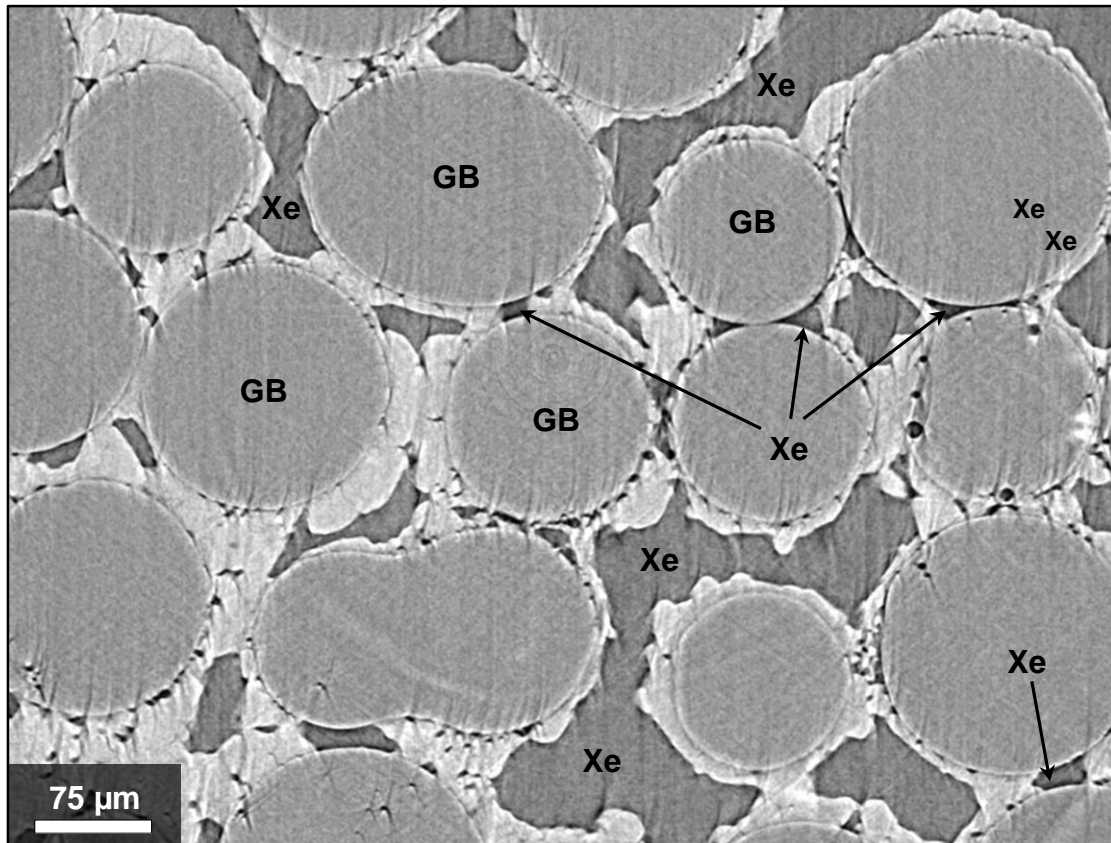


Figure 5-15. GH formation in hydrophobic GB (GB) (Sample 10, $W_s = 54\%$, $t_R = 16$ min). All water has been transformed into hydrate. Free Xe gas fills spaces between GH and GB grains.

5.4. Microstructural aspects of GH dissociation

The decomposition of GH is of central interest for all *in-situ* gas extraction processes. Its microstructural details are crucial for the evolution of mechanical stability upon extraction, in particular for the vicinity of the extraction site. Although not of central interest for this study, we have obtained first microstructural insight into the GH decomposition process.

The mechanism of GH decomposition was studied only for one sample before the reformation (procedure II). The procedure consisted in reducing the pressure below the stability limit for a short time (several seconds to minutes) and then restoring the pressure to the stability limit value. This operation was repeated several times till a full decomposition of the sample. Several scans were taken at these intervals. Figure 5-16 shows a sequence of GH decomposition.

The CT images show that GH starts to decompose preferentially at the interface with Xe gas towards the bulk water by eroding larger crystals sticking out, while the interface towards the Qz grain remains largely unchanged (albeit with the water layer as discussed in section 5.2) until the GHs

completely disappear in the inter-granular space. Subsequently, a water layer is formed which intervenes between GH and the gas phase. This water layer gets thicker as the GH decomposition proceeds. As for the formation process there are patches in which the decomposition is faster than in others. The rate of decomposition of GH in the inter-granular space is slower than the rate of decomposition of GH close to the pore space. This is probably due to the slow diffusion of gas molecules through the bulk water to the gas phase. If the concentration of Xe remains high at grain contacts then this will slow down the process of GH dissociation.

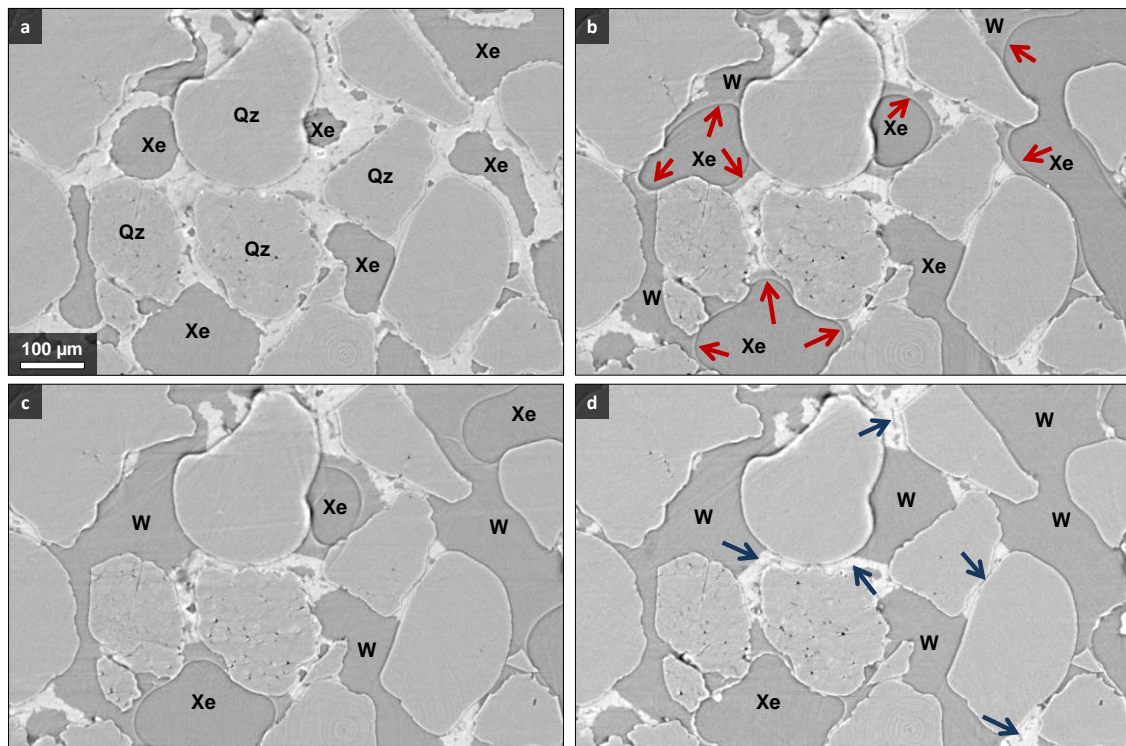


Figure 5-16. Sequence of GH dissociation by depressurization (Sample 3, $W_s = 41\%$). a) Sample fully transformed, b) initial decomposition, c) partial decomposition, d) GH remains at the grain contacts. Image b shows the beginning of GH decomposition at the interface of GH with Xe gas (red arrows). Image d shows the remaining GH at grain contacts as indicated by the blue arrows. After GH dissociation, water is redistributed in the sample.

5.5. Microstructure of GH on the pore scale

The goal of this PhD work was to study the effect of the microstructure of GH on the physical properties of the resulting aggregates and subsequently the wave velocities and attenuation of unconsolidated sediments. The physical properties of GH-bearing sediments depend on the spatial distribution of GH which itself depends on the formation method and growth mechanism. The microstructure of GH aggregates in a sedimentary matrix is frequently categorized into (a) contact-cementing, (b) grain-coating/cementing, (c) pore-filling, and (d) load-bearing based on the hydrate distribution models by *Dvorkin et al.* [2000] and *Helgerud et al.* [1999] as illustrated in Figure 5-17.

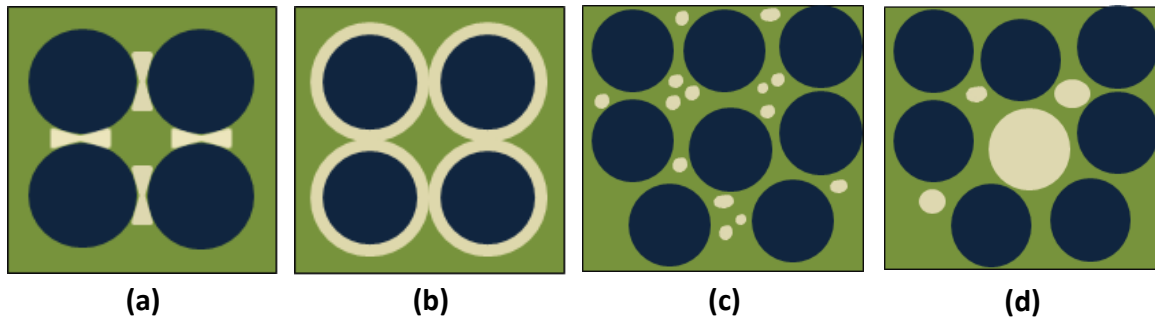


Figure 5-17. The four different microstructural models redrawn after Dvorkin et al. (2000) GH (khaki), sediment grains (dark blue), and fluid phase (green). (a) Hydrate as cement at grain contacts, (b) hydrate surrounding and cementing grains, (c) hydrate as part of the pore fluid, and (d) hydrate as part of load-bearing granular frame.

The classification of GH microstructures on the pore scale is done with respect to their elastic properties. In the case of GH formed from a free-gas phase in low water-saturated sediments, a cementing model (a, b) assuming a full transformation of water into GH is favored, while the gas-dissolved and ice-seeding methods leads preferentially to pore-filling or load bearing model (c, d) [Waite et al., 2009]. The measured wave velocities did not match perfectly any of the predicted seismic velocities from the four the microstructural models. This discrepancy can be explained by the lack of accurate information on the GH microstructure as the methods used did not reveal details of the sediment-GH contacts due to their limited resolution. Moreover, the seismic velocities measured in the field were also different from the laboratory data. This difference can be attributed to a difference of time scales of GH formation as it is difficult to reproduce natural conditions in the lab and the coarsening process which takes place after completion of GH formation may take years.

Until now these microstructural models were considered as distinct cases and researchers attempted in many cases to describe the experimental or field data using one unique model. However, these attempts were not successful and it appeared that none of the suggested models can describe alone the distribution of GH in the pore space and the evolution of GH saturation (see Figure 2-26) [Zhang et al., 2011].

Our experimental observations showed that the change in the microstructural regime with the increase of GH saturation is continuous and related to the initial water saturation:

At low water contents ($\sim W_s < 30\%$), gas was the continuous phase and liquid water tended to accumulate at the Qz sediment surface or near contacts forming "capillary bridges" between grains

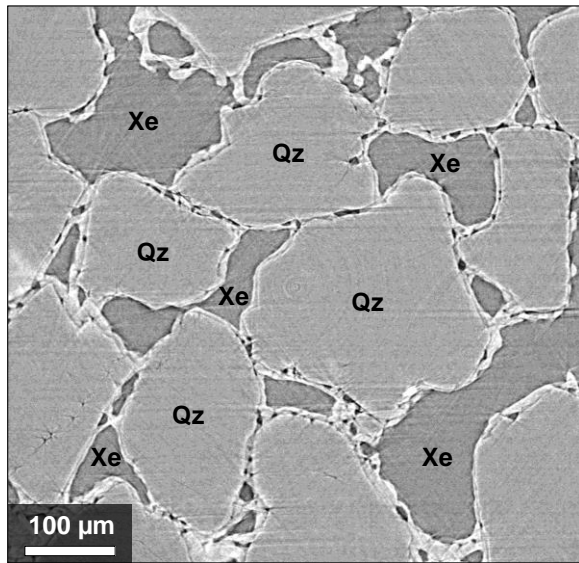


Figure 5-18. Microstructure of GH at low water saturation (Sample 11, $W_s = 14.6\%$). GH forms around Qz grains and forms bridges between Qz grains without cementing. A fluid phase remained between GH and Qz grains and at grain contacts.

due to capillary and adhesive forces which prevent the collection of water in one zone of the sample. The distribution of water appeared to be homogenous in the sample. Subsequently, GH formed around the Qz grains or formed bridges linking neighboring Qz grains (see Figure 5-18).

Due to the low affinity of GH with Qz surfaces, a water layer remained between GH and Qz surfaces but also at grain contacts. Hence, the hypothesis of cementation models at low water/GH saturation is not supported by our results. Our observations show that GH holds the sediments structure in place but do not cement in a strict sense. Nevertheless, it is assumed that GH increases the stiffening of the resulting aggregates but not dramatically as for a cementing model.

As the water saturation increases to the degree that water becomes continuous, water tends to form bigger agglomerations and to occur as patches; water occurred in some locations of the sample with small pores as the continuous phase,

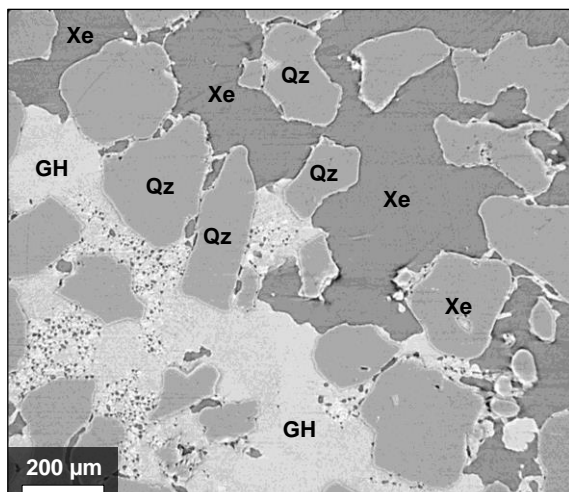


Figure 5-19. Microstructure of GH at intermediate concentration (Sample 12, $W_s = 49.5\%$). GH (white) fills completely some part of the sample while the rest is empty.

whereas Xe was the continuous phase in other parts. Hence, GH formed as patches in the pore spaces; while some parts of the sample were fully saturated with GH, others were void (Figure 5-19). Our results show that GH filled the center of pore spaces between sediment grains. Again a water layer remained between GH and Qz surfaces. The hydrate structure appeared to be porous with a pore sizes reaching few μm . The Qz grains of the void part of the sample appear sometimes to be covered by a non-cementing hydrate layer resulting from residual water and sometimes are free of GH. The distribution of GH is inhomogeneous. It is difficult to predict without measurements the stiffening effect of GH if it is higher or lower than the low water saturation

scenario.

As the water saturation increases more and more, water becomes the continuous phase in the sample and saturates a large part of pore spaces. Xe gas was observed to occur as bubbles or to form patches. Consequently, GH formed from such system gives highly GH saturated sediments. GH tended to concentrate in the pore spaces and did not adhere to the Qz surfaces with the presence of a water layer at the GH-Qz interface. The hydrate structure in the pore spaces appears fractured and it is characterized by water pockets and small-gas bubbles (Figure 5-20). A dense GH structure was not observed. The GH filling the pores increases the stiffening the host sediments which is expected to be more significant at the end of GH formation.

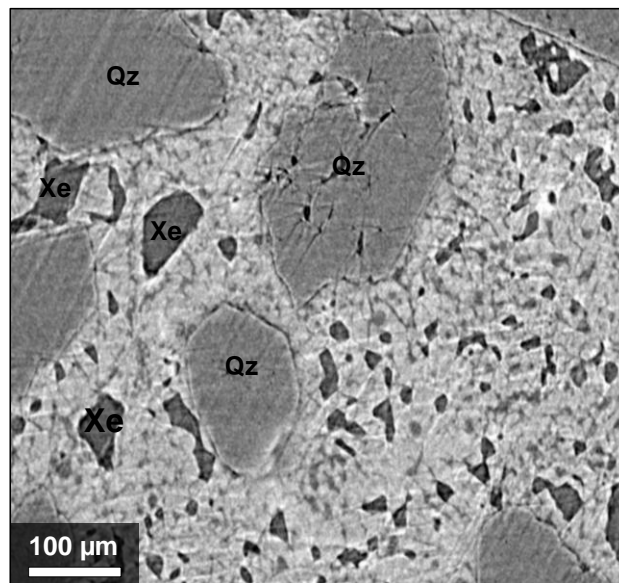


Figure 5-20. Microstructure of GH at high initial Ws (Sample 13, Ws = 88.6 %). GH (white) occurs as the continuous phase while the Xe gas forms bubbles in the hydrate structure with some water pockets as well.

Natural GH-bearing sediments systems are not eternally stable but last days, weeks, months, or years close to the seafloor and the water column, up to many hundred or many thousands of years deeper in the sediment. Some estimates on the GH formation times at a venting site are given by [Chen and Cathles, 2003; Chen and Cathles, 2005]. Figure 5-21 shows a sequence of CT images illustrating the evolution of the GH microstructure with the initial GH saturation. These images represent end-members of a continuous spectrum.

Increase of initial Ws / Decrease of porosity

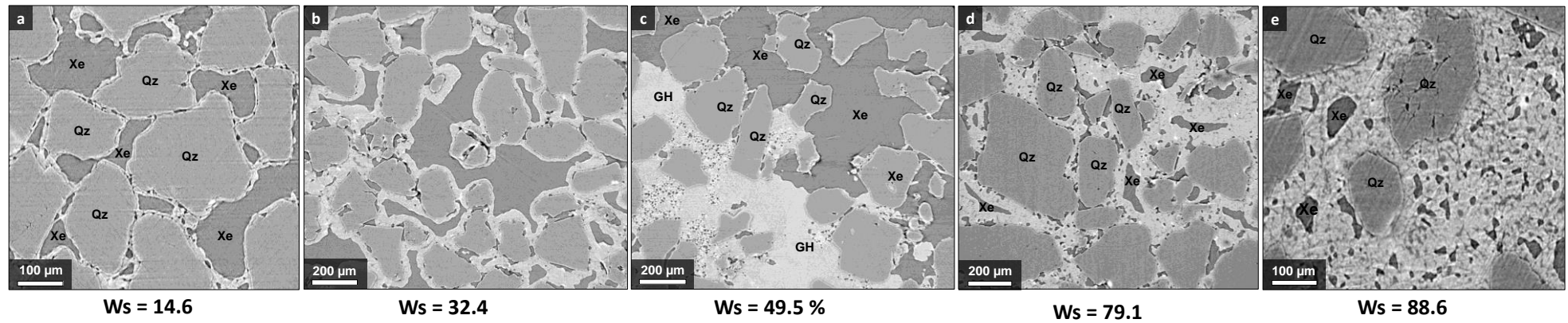


Figure 5-21. Evolution of GH microstructure as a function of initial water saturation (a: Sample 11, b: Sample 14, c: Sample 12, d: Sample 15, e: Sample 13). From the left to right the Ws increases. Images b and d represent transition stages between low and intermediate Ws and between intermediate and high Ws.

Additionally, the initial distribution of GH depended as well on the formation method.

Figure 5-22 illustrates a comparison of the GH microstructure from juvenile and memory water formation methods. At low water saturation (Figure 5.21a and 5.21b), GH is accumulated around quartz grains and at grain contacts without cementing the Qz grains, while at high water saturation, GHs tend to concentrate in the pore spaces without adhering the Qz surfaces. The differences observed consist in the formation of an intimately GH aggregates with small GH crystals for procedure I and less interconnected relatively large GH crystals for procedure II and III. The various GH crystal morphology observed could be attributed to a variation of nucleation densities due to a local variation of the driving forces as the number of nuclei depends on the driving force.

The spatial distribution of GH after complete formation from the two different formation methods (image c and d) appears to be similar even if the nucleation and growth mechanisms were different. The growth morphologies of method I-III tend to move towards more similar arrangements towards the end of the formation process. What remains unchanged in all formation scenarios and for all water saturations is the preference of GH to maintain a μm -sized water layer at the interface with quartz or GB; this is established as an intrinsic feature of GH in contact with quartz and must also be expected to occur in natural settings.

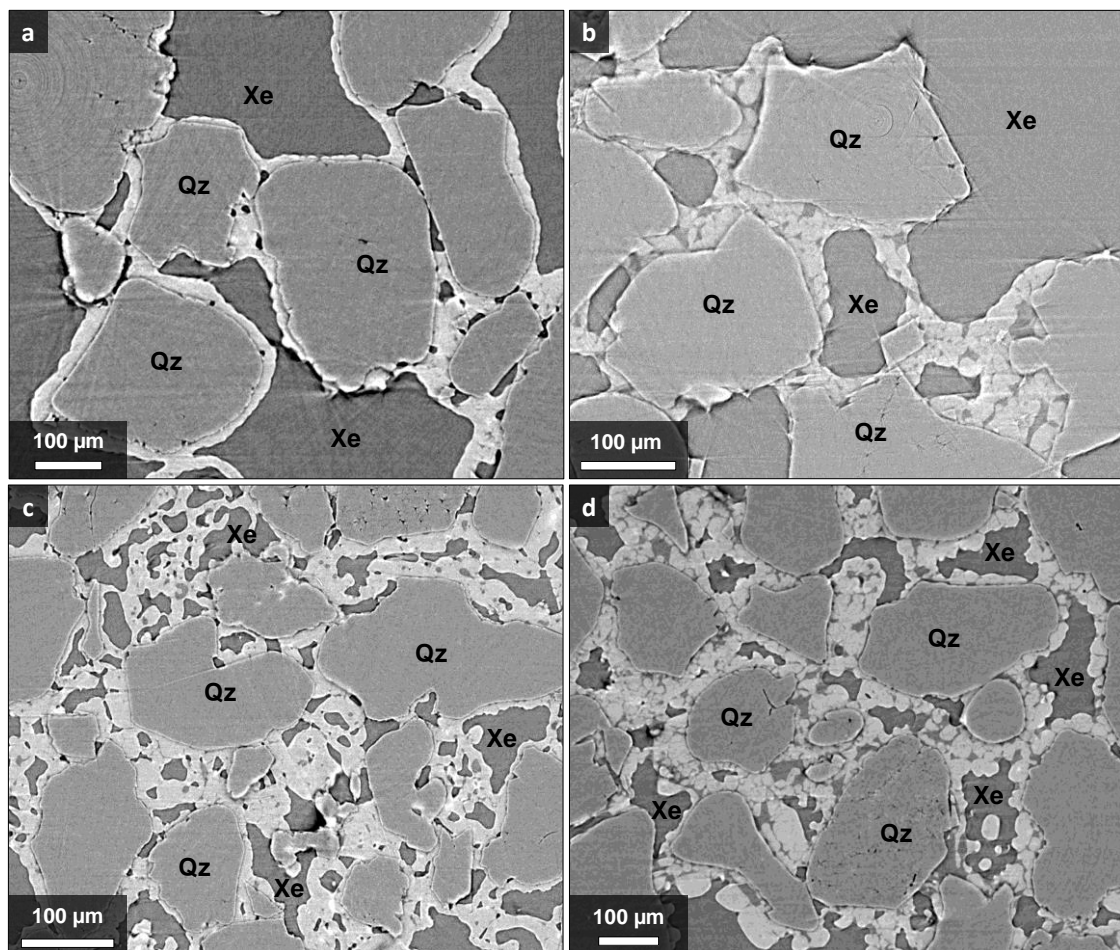


Figure 5-22. Comparison of GH microstructures using juvenile and memory water. GH formed using procedure I (a: Sample 1, Ws = 22 %; b: Sample 4, Ws = 34 %; c: Sample 2, Ws = 57 %; Sample 3, Ws = 41 %)

5.6. Review of the existing models

Our results revealed for the first time very important details of the microstructure of GH-bearing sediments on the pore scale which can have a significant impact on the physical and acoustic properties of the host sediments. Here we review the existing microstructural models as our observations do not support all of them.

A cementation of the sedimentary matrix in a strict sense, i.e. a direct attachment of GH to Qz grains, does not take place due to the presence of fluid phase most likely water at the GH-Qz grains interface and at grain contacts. Thus, we suggest a new "non-cementing" model for low water saturated sediments as illustrated in Figure 5-23.

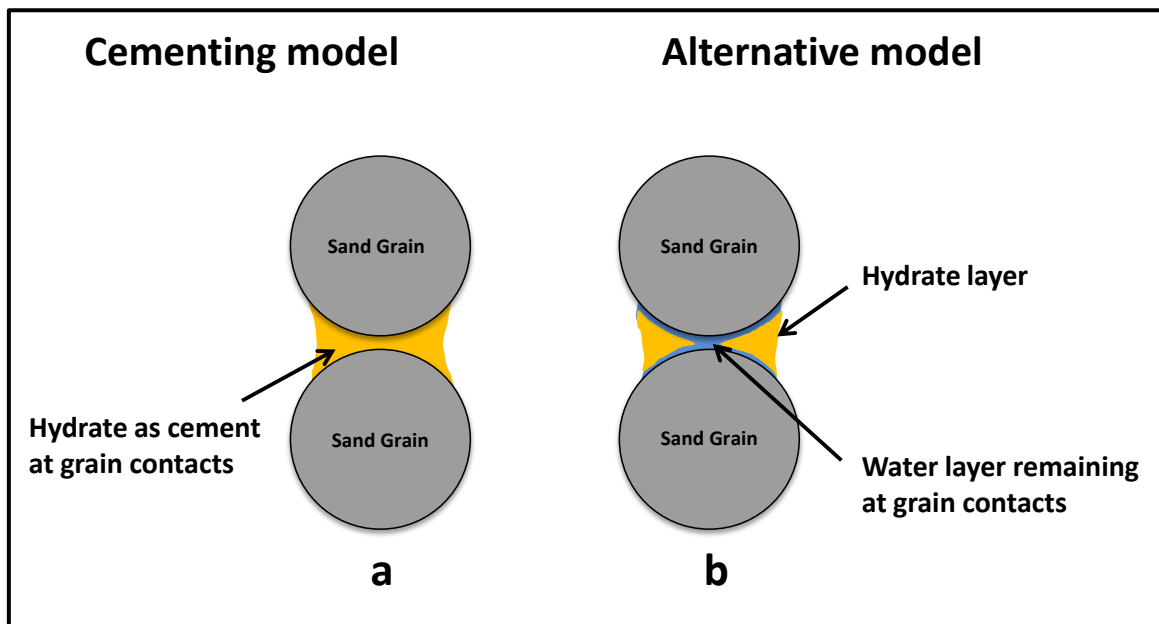


Figure 5-23. A new suggested non-cementing microstructural model for low-GH saturation.

As the GH saturation increases, more grains are held together by GH without any direct contact. The GH content is higher but not enough to fill the pore spaces which remain free of GH as shown in Figure 5-24.

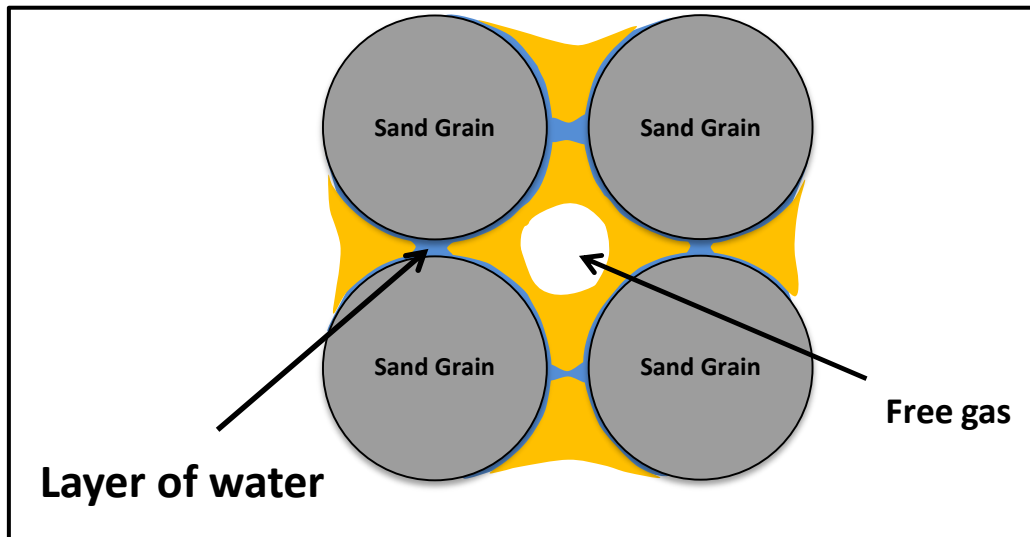


Figure 5-24. Microstructural model of higher GH content in undersaturated sediments

Our results do not also support the heterogeneous nucleation of GH occurring on the grain sediment surface (model "A" in Figure 2-16) as GHs was observed to nucleate either at the gas-water interface or inside the water phase.

In highly water-saturated samples (> 80 %), the GH microstructure changes from a more pore-filling situation towards a more load-bearing case. The pore spaces between Qz grains are filled with sometimes intimately, sometimes loosely connected aggregates of mostly polyhedral crystals. The solid GH holds the sedimentary particles in place via a cushion of liquid water again without a cementation of the matrix in a strict, i.e. direct attachment of GH to Qz does not take place. This also means that even in sediments with high GH saturation there are fluid pathways to and between every sedimentary grain in contrast to frozen sediments in permafrost. Figure 5-25 depicts the new suggested model for load-bearing GH.

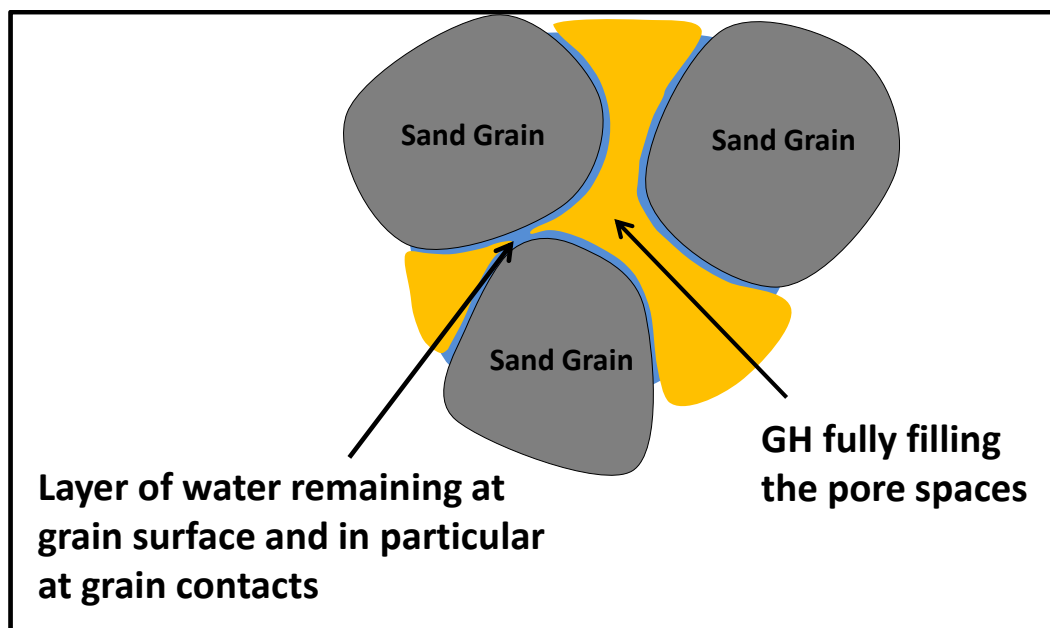


Figure 5-25. New suggested microstructural models for load-bearing GH.

These new microstructural findings are highly to affect the seismic velocities, the and attenuation of unconsolidated sediments and may explain some of the discrepancy observed between the experimental and predicted data.

5.7. Relationship between hydrate saturations and wave velocity and attenuation

The detection, quantification and control of GHs distributed in natural sediments are required. In order to use seismic techniques to detect and quantify the amount of GH distributed in sediments, it is important to understand the relationship between GHs content in sediments and their acoustic properties. Hence, a predictive model which relates the hydrate saturation and its microstructure on the pore scale to the wave velocities is required.

The P and S wave velocities increase with the increase of GH saturation. Meanwhile the hydrate content in sediments also affects the wave attenuation [*Chand and Minshull, 2004; Dvorkin and Uden, 2004; Guerin and Goldberg, 2005*]. As the GH saturation increases, the wave attenuation increases. The increase of the seismic attenuation is linked as well to the microstructure and spatial distribution of GH in pore spaces. The increase of the wave velocity and attenuation with GH content known as seismic anomalies [*Chand, 2008*] of GH-bearing sediments is still poorly understood. A better understanding of seismic wave velocity and attenuation in GH-bearing sediments is required to improve the geophysical detection and quantification of seafloor methane hydrate. The understanding and explanation of this puzzling phenomenon remains also one of the main goals of this project. In this section, we provide a possible qualitative explanation based on our microstructural observations and new findings for the increase of wave velocities and attenuation with the increase of GH saturation. A quantitative analysis carried out by Kathleen Sell (University of Mainz) to model the P-wave velocity from the 3D tomographic data may complement our observations.

5.7.1. Wave velocity

The general behavior of the increase of acoustic/seismic wave velocities with the increase of GH content is well understood by the GH research community; however the rate at which the wave velocities increase with the increase of hydrate saturation and the discrepancies in results observed remains puzzling.

GH has a higher elastic modulus than the pore fluid; hence the formation of GH in sediments increases the wave velocities. The rates at which the wave velocities increase depend strongly on where GH starts to form and grow in the pore spaces. Therefore, modelling GHs as a part of the pore fluid or as a part of the skeleton produces different results.

Our results do not support a GH microstructural cementing model due to the presence of a water layer at the GH-sediment grains interface and near grain contacts. Hence, we do not expect a dramatic increase of the seismic velocity at low-GH saturation. The stiffness effect by GH of the skeleton is reduced. In this case, the effective medium theory of *Ecker et al. [1998]* for gas, sediment and hydrate phases assuming a full transformation of water into hydrate is not anymore suitable due to the presence of the interfacial water layer revealed by our observations.

The water layer has a thickness of few microns which cannot be observed with low-resolution methods. Therefore it was always considered systematically that GH formation in low-water saturated sediments lead to a cementation of the matrix. Yet, the measurements of wave velocities in low-water saturated sediments did not much the predicted wave velocities from the cementing microstructural model of *Dvorkin et al.* [2000] as it is the case for the study of *Priest et al.* [2005] (see Figure 2-24). The measured wave velocities did not increase dramatically as for the predicted velocities which indicate that the cementing effect was reduced because of the remaining water layer at the sediment grain-GH interface.

At high water saturation, the formation of GH starts to form either at the gas-water interfaces or inside the water phase farther away from the sediment grains, GH does not affect the stiffness of the sediment frame. Consequently, wave velocities remain unchanged or increase slowly at low GH saturation. When GH saturation exceeds 70 %, GH starts to fully infill the small pore spaces and to hold the sediment grains in place leading to a significant increase of the stiffness and of the wave velocities. We expect that the further increase of the velocity at a rate similar to that of low water saturation as GH becomes closer to the sediment grains but this would need more elaboration. It appears that it is probably more adequate to use more than one microstructural model to describe the variation of the wave velocity with GH saturation for a load-bearing GH microstructure.

5.7.2. Wave attenuation

In addition to the increase of seismic wave velocities, the presence of GH in sediments causes an increase of the wave attenuation (see section 2.4). Here we provide a qualitative explanation for this strange phenomenon based on the new developed models consistent with our results and inspired from the work of *Priest et al.* [2006] but extended to high water saturation.

The conceptual model of *Priest et al.* [2006] used the inter-crack squirt flow model advanced by *Mavko and Nur* [1979] to interpret acoustic wave signal attenuation which suggests that the contact area and water content of the particles were key factors in determining the attenuation; the smaller the contact area and water content of the particles, the smaller the attenuation. In contrary, the increase of contact area and water content increases the attenuation. During GH formation, the contact area of particles increased but the water content changed little leading to an increase of the wave attenuation. This hypothesis is very well supported by our new findings.

Due to capillary forces, liquid water tends to accumulate near contacts and around sediment grains. As a seismic wave passes through the sediments, frictional losses occur due to squirt flow phenomena caused by the liquid water at grain contacts (Figure 5-26). As the attenuation is proportional to the water content, the attenuation is minimal in this case due to the low-water saturation.

When GH starts to form at the gas-water interface without cementing the grains, new contact areas appear. Subsequently, the water layer at sediment grain-Gh interface and between two GH layers will represent additional sites for squirt flow causing a further increase of the seismic wave attenuation (Figure 5-27).

As the water/GH saturation increases more and more, the number of sites for squirt flow increases further leading to an increase in the wave attenuation. When GHs coat (without cementing) all grains, the attenuation reaches a maximum (Figure 5-28). This stage may represent a transition stage.

For high water/hydrate saturation, our results showed that GH filled the center of pore spaces. The observations of seismic attenuation in sediments containing GH have demonstrated that the attenuation increase with the increase of GH saturation. The increase of wave attenuation at high GH saturation can be explained by the porous structure of GH in the pore spaces or by the water pockets/layers at the grain boundary of GH crystals. As the number of GH crystals increases with GH formation, more contact areas with interfacial water layer are created leading to an increase of the number of sites for squirt flow and consequently an increase of attenuation (Figure 5-29).

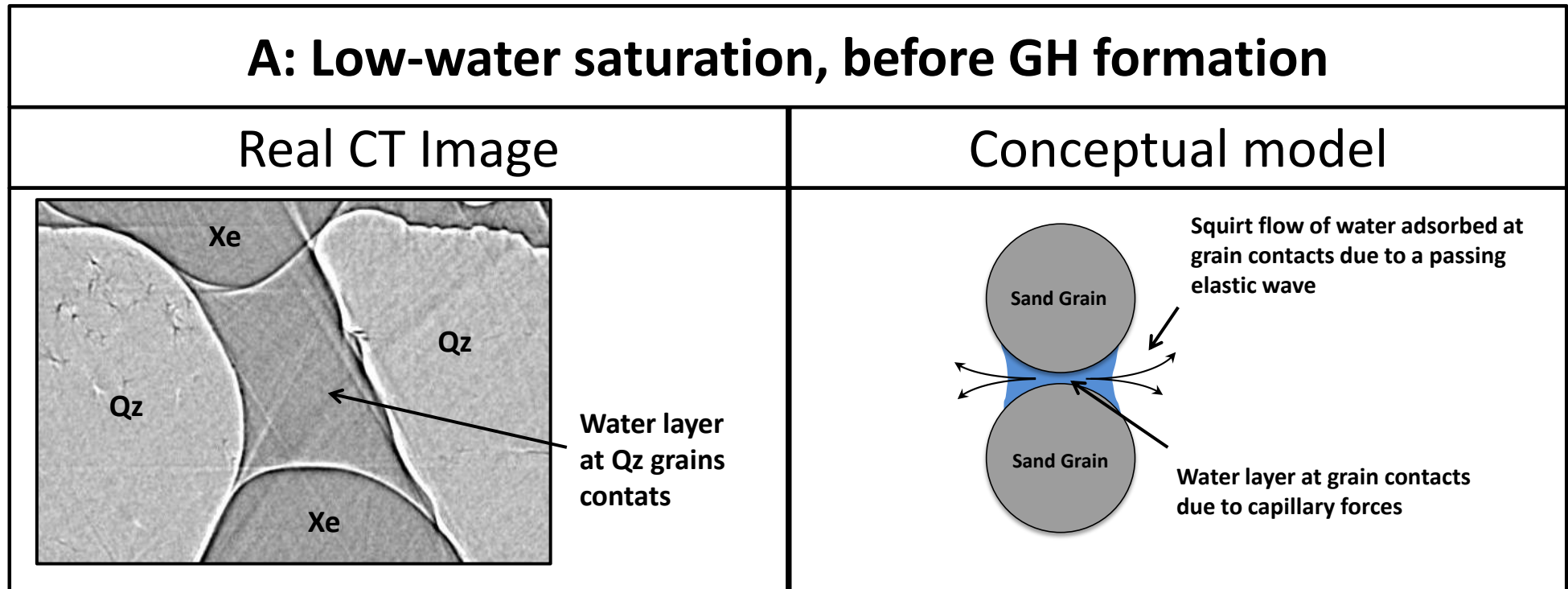


Figure 5-26. CT image (left) and conceptual model (right) for seismic wave attenuation in sediments free of GH. The water accumulated at grain contacts attenuates the passing elastic wave due to squirt flow phenomenon.

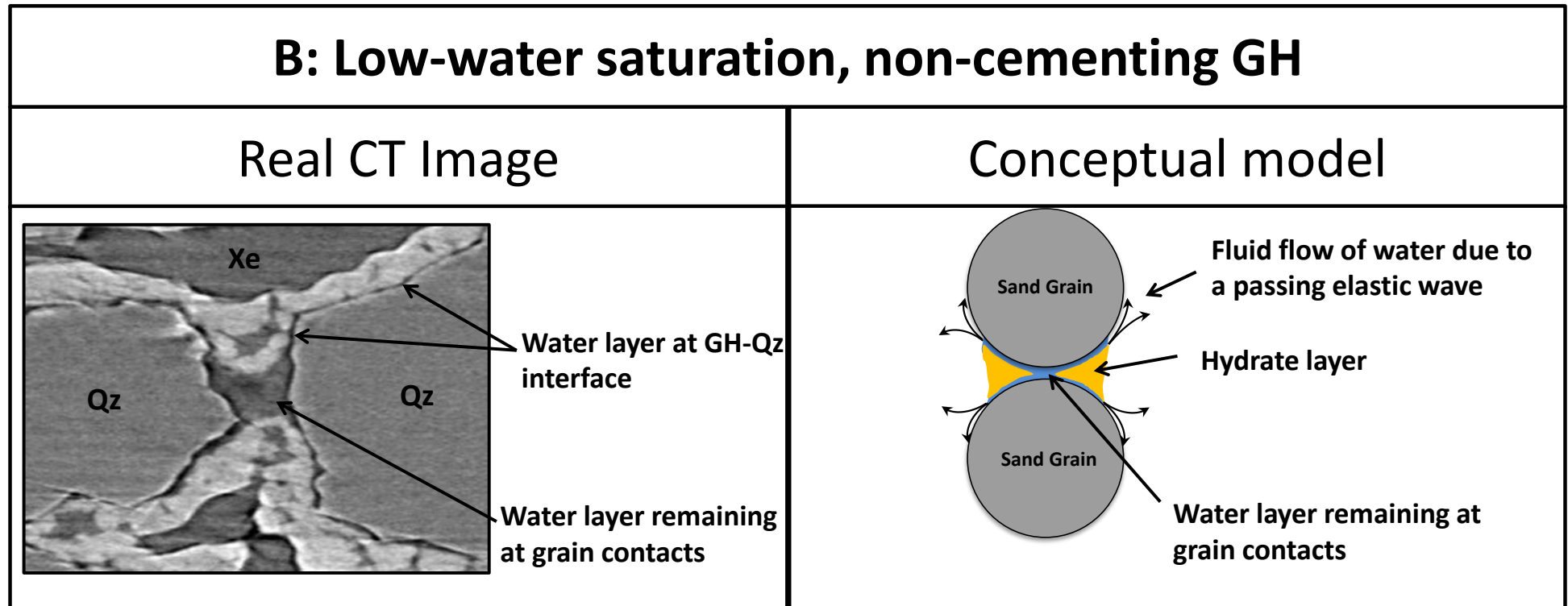


Figure 5-27. CT image (left) and conceptual model (right) for seismic wave attenuation in sediments with low-hydrate saturation. The hydrate layer formed at the gas-water interface increases the contact area leading to an increase of the wave attenuation

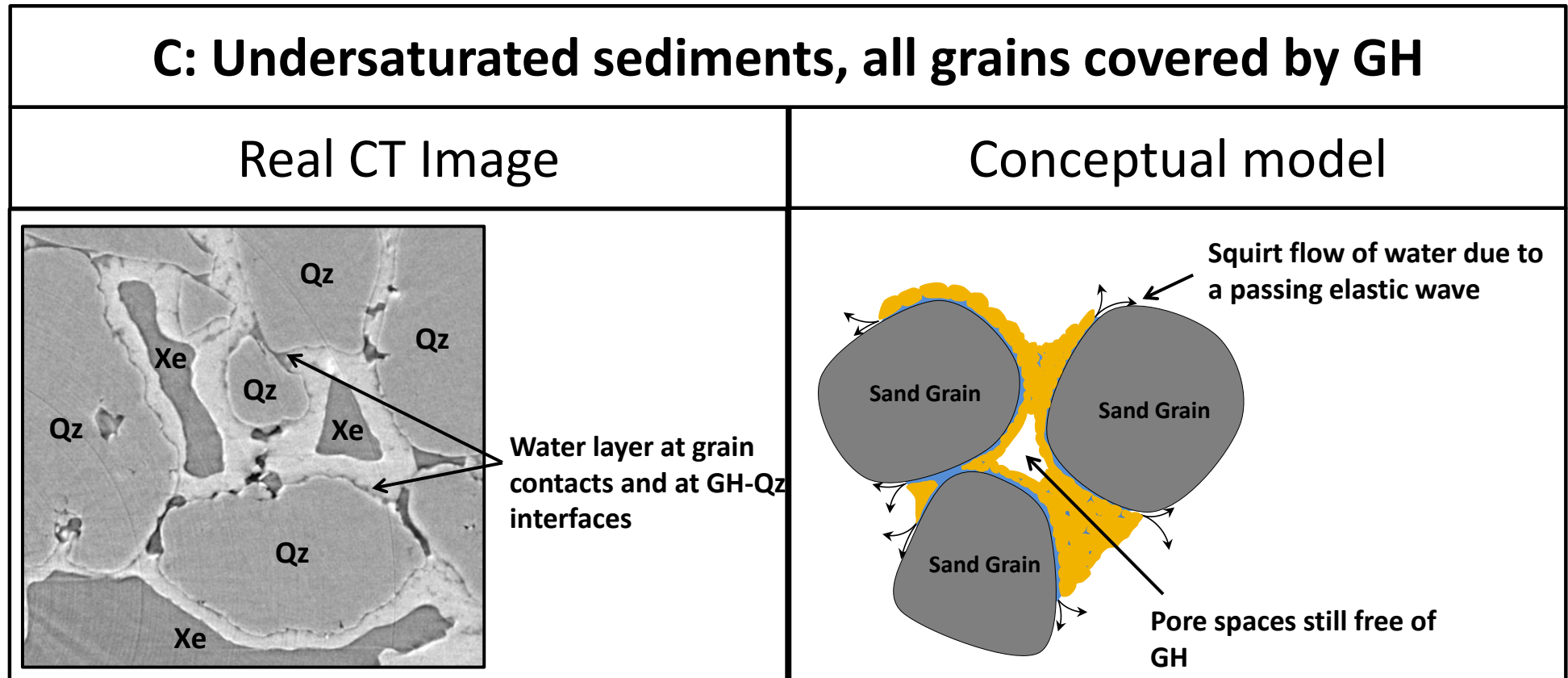


Figure 5-28. CT image (left) and conceptual model (right) for seismic wave attenuation in undersaturated sediments when all grains are covered by GH with the presence of an interfacial water layer. Hydrate starts to infill the pore spaces and to become the continuous phase.

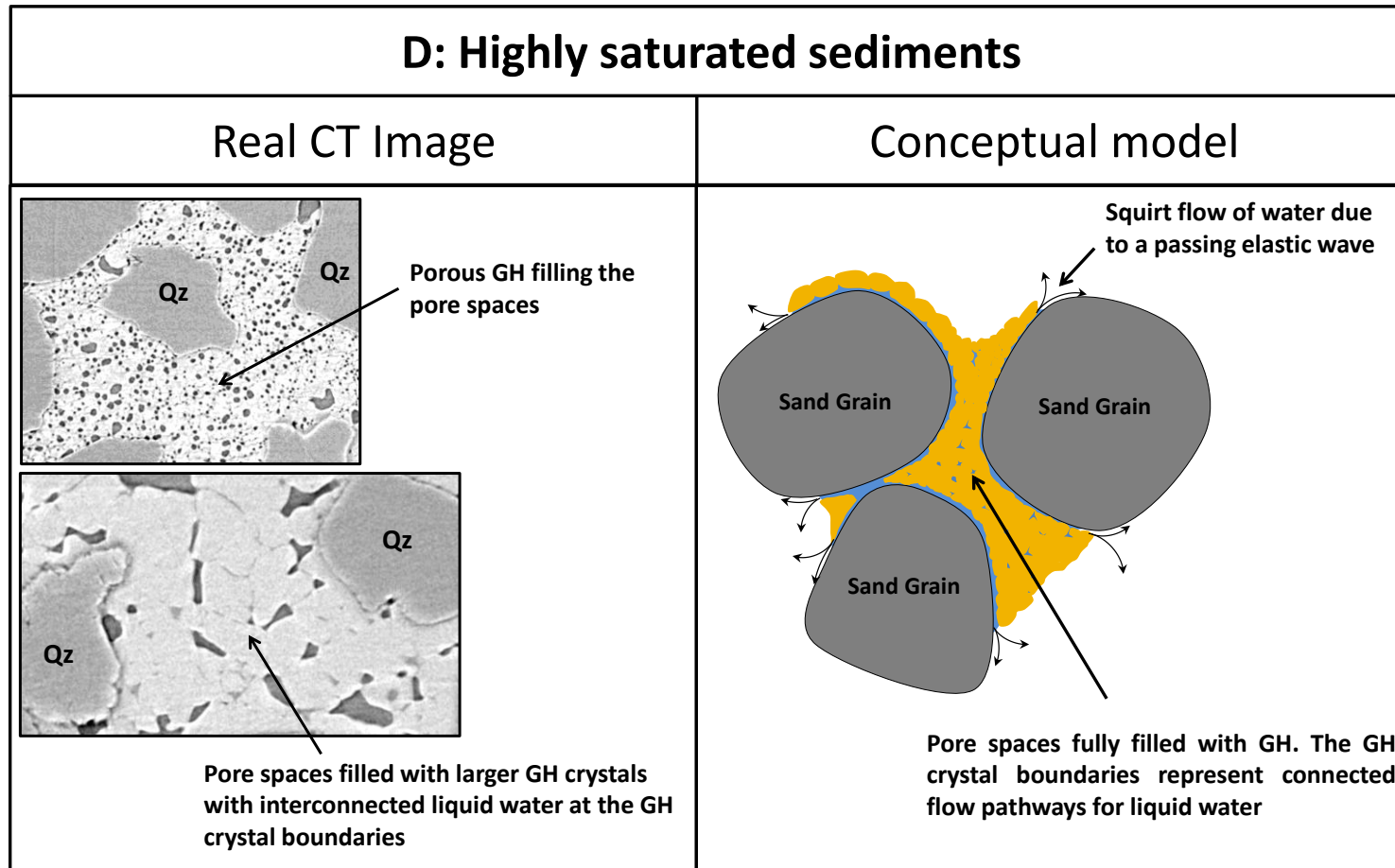


Figure 5-29. CT image (left) and conceptual model (right) for seismic wave attenuation at highly GH saturated sediments. The further increase of the attenuation with the increase of hydrate saturation is due to the microscopic structure of GH. The connected pores or GH grain boundaries represent flow pathways for gas or water causing an attenuation of the wave velocities by squirt flow.

6 | Crystallites Size Distributions of GHs

The visualization of the microstructure of GH-bearing sediments using μ -CT is complemented by a quantitative analysis of the crystallites size distributions (CSDs) of Xe hydrate-bearing sediments. The CSDs are important because they carry information about the formation process (e.g. coarsening or recrystallization process). The CSDs were established using our newly developed CSD method described in Chapter 3, section 3.4.5. The method has permitted to get access for the first time to the evolution of GH-bearing sediments CSDs.

6.1. Previous attempts

Crystallite sizes and CSDs of polycrystalline materials are of primary importance for their physical properties. Particularly important are the CSDs for the mechanical behaviour, e.g. the dependency of yield strength on the grain diameter via the Hall-Petch equation. Moreover, many transport properties depend on the grain-boundary network (GBN) which is determined also by the CSDs. As the manufacturing process strongly influences the CSDs (and GBNs) it is often necessary to control these quantities in fields reaching from metallurgy over ceramics to pharmaceutical products. Likewise, in natural samples much can be learned from CSDs about the formation process. Hence, the knowledge of the average crystallite size and CSDs of GHs is important.

Despite their importance, the sizes of GH crystals are largely unknown due to experimental difficulties to maintain GHs stable under high pressure/low temperature. Conventional optical methods were used to determine the crystal sizes of laboratory formed GHs: *Monfort and Nzihou* [1993] used light scattering technique to measure the CSD of cyclopropane clathrate and reported that it varies between 5.6 and 564 μm . *Bylov* [1997] used laser light method to measure the crystal sizes of methane, ethane and NGH and reported that the mean diameter was in the order of 7 to 12 μm . The mean size of crystals of methane hydrate measured by *Herri et al.* [1999] was between 10 and 22 μm . More recently, *Klapproth* [2002] used cryo-SEM to measure the crystal sizes of synthetic methane hydrate by looking at grains which were most likely single crystals. They reported that the mean size of crystals was in the range of 10-20 μm . Optical methods are not suitable for the determination of GH crystals as only the size of crystals which grow freely or polycrystals with a clear crystal boundaries can be determined which give poor visual observations.

Our group attempted in the last years to measure the CSDs of several NGH samples and synthetic samples using methods based on X-ray diffraction. Synchrotron X-ray diffraction is a non-destructive technique which is more suitable for GH studies under low temperature or high pressure and gives better statistics. *Klapp et al.* [2007] used the moving area detector method [*Bunge et al.*, 2003] to measure the CSD of different NGH samples retrieved from the Gulf of Mexico and from

Hydrate Ridge offshore Oregon from varying depths and one synthetic methane hydrate sample formed from ice spheres. They reported that the crystal sizes of NGH samples are much larger in the range of 300-600 μm with a tendency for bigger grains to occur in greater depth, possibly indicating a difference in the formation age. While the crystal sizes of synthetic methane hydrate aged of three weeks had a mean size of 40 μm or smaller because of the detection limit of the method (see Figure 6-1).

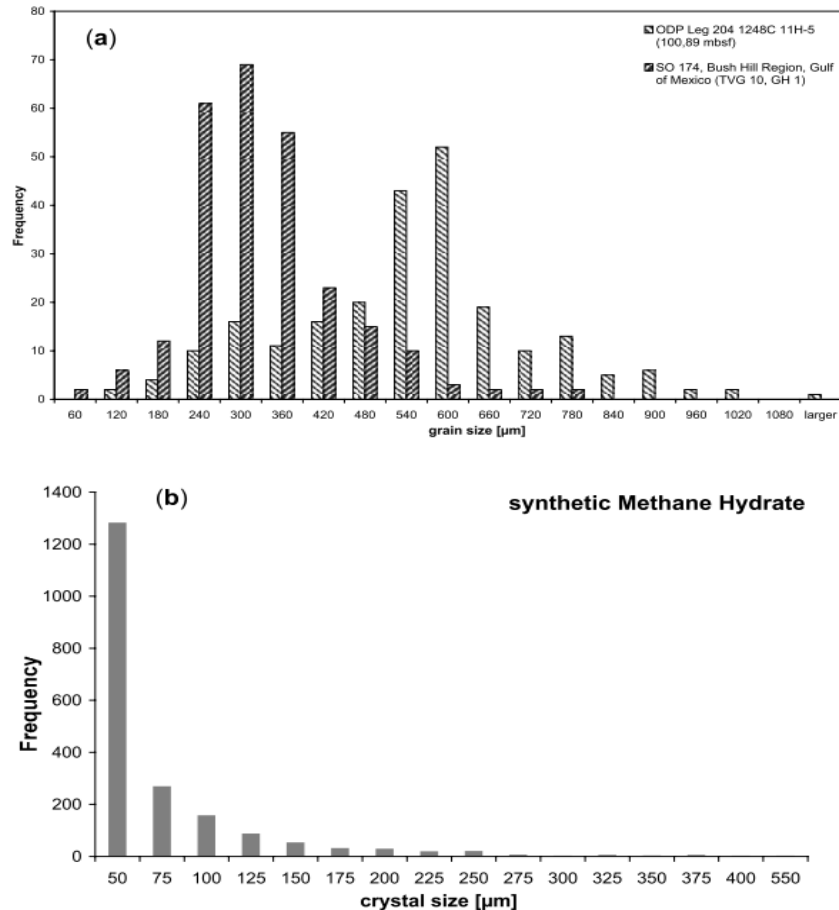


Figure 6-1. Examples of grain size distributions. (a) Sample ODP 204 1248C 11H-5 (100,89 mbsf). The crystallite sizes appear to be normally distributed with a mean size of 517 μm ; sample Gulf of Mexico, Bush Hill, TVG 10 GH 1 (sea floor). The crystallite sizes appear to be normally distributed with a mean size of 301 μm . (b) Synthetic methane hydrate sample. The size distribution is shaped like half a normal distribution, the mean grain size was given as 43 μm assuming a log-normal distribution ([*Klapp et al.*, 2007]).

[*Klapp et al.*, 2010a] used the same method to determine the crystallites size distributions of several NGH samples and synthetic methane hydrate sample. Again it was reported that the crystal sizes of NGHs were an order of magnitude bigger than the synthetic methane hydrate crystals as shown in Figure 6-2.

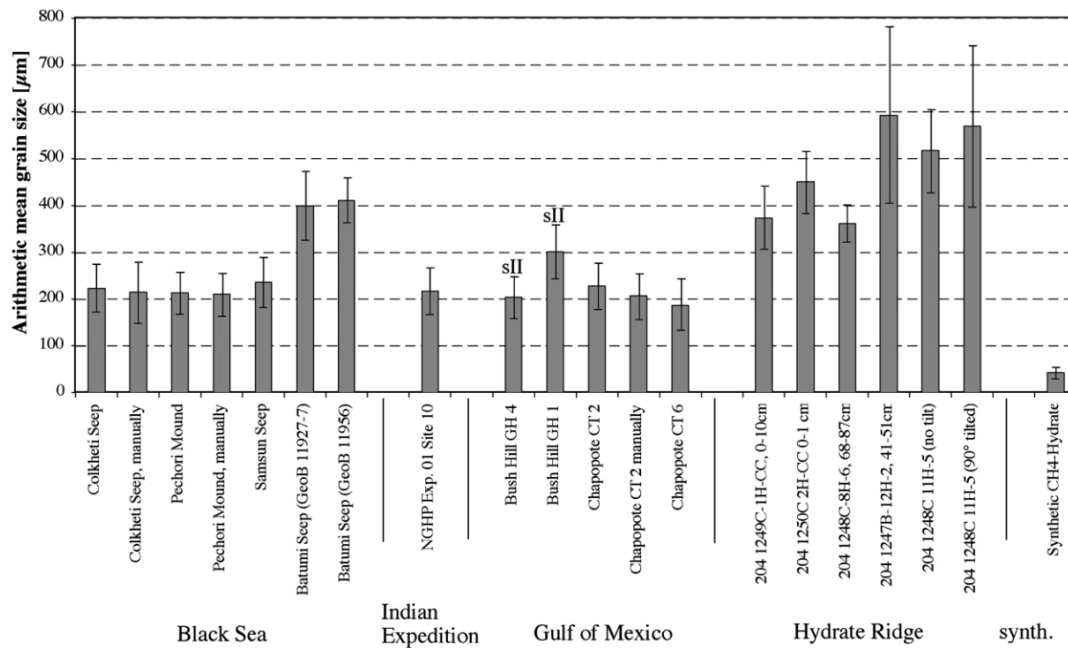


Figure 6-2. Bar diagram of the arithmetic mean crystal sizes given in Table 1. Geological locations are grouped. The two samples from Bush Hill/Gulf of Mexico are sII gas hydrates. Error bars indicate the standard deviation (from [Klapp *et al.*, 2010a]).

These results are very important and suggest that the microstructure of GH probably changes with time. The experiments realized in the lab permit to improve the understanding of GH systems but must be carefully applied to natural field data where the conditions are different and difficult to reproduce in the laboratory experiments.

The determination of the crystal sizes of GHs using the moving area detector method gave for the first time access to the crystal sizes of NGH samples. However this method has low sensitivity; only crystals bigger than 35 μm were detected in the case of synthetic GH due the low intensity to background ratio. This may lead to an over estimation of the size of GH crystals.

In the last years, we were working on the development of a new method for the determination of GH CSDs. The newly developed method called “Fast quantitative CSD method” permits a fast determination of the CSDs of polycrystalline materials and has detection limit below 0.5 μm using synchrotron X-ray source. Using this method we were able to have access for the first time to the CSDs of GH-bearing sediment samples and to follow *in-situ* the evolution of GH CSDs with time.

6.2. Calibration using LaB₆

The calibration was done using LaB₆ NIST standard powder in order to establish a scale factor between the size (volume) and intensity distribution of LaB₆. Figure 6-3 shows the diffraction pattern and a 2D spotty diffraction pattern of LaB₆.

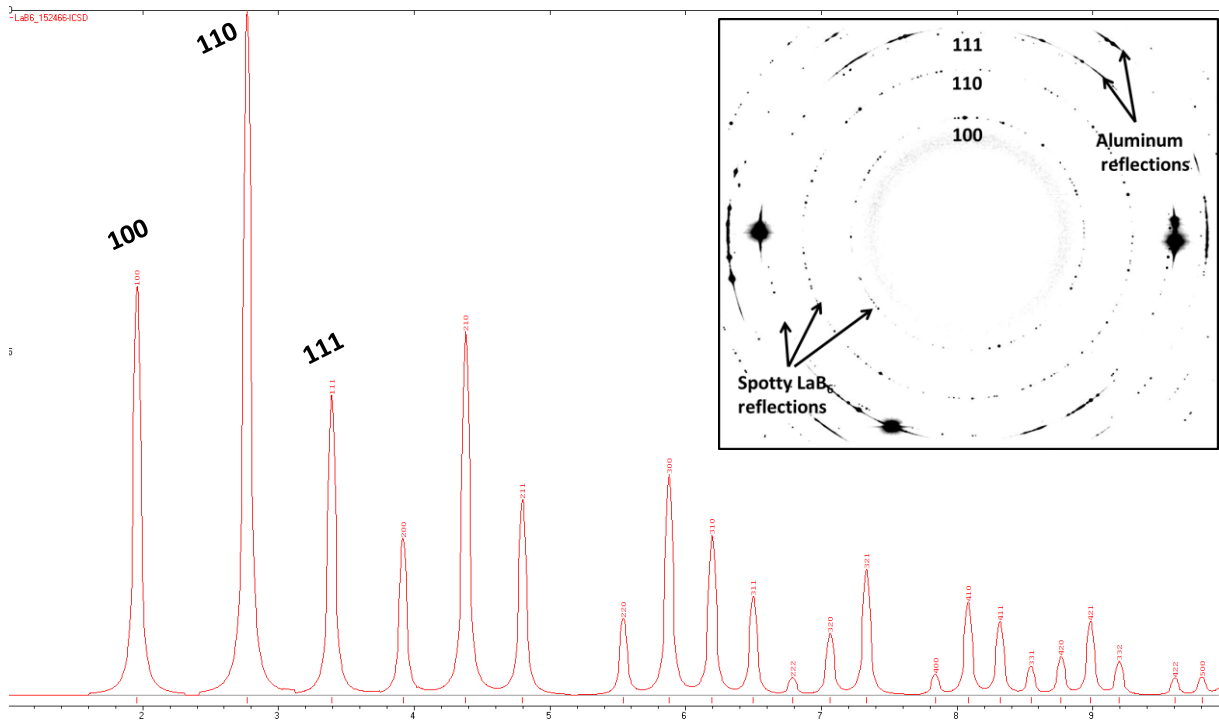


Figure 6-3. Diffraction pattern of LaB_6 powder calculated using Powder cell software. The insert image is a measured spotty diffraction pattern of LaB_6 .

It is recommended to use the intensity distribution from the strongest reflection because it has a better detection limit. In our case, the 110 reflection is the strongest reflection and was used for calibration. The size distribution of LaB_6 extracted from SEM images is plotted in Figure 6-4. For simplicity, the logarithm of the volume and intensity of LaB_6 crystals are plotted. The intensities distributions from both *in-situ* and *ex-situ* measurements are plotted in Figure 6-5. All distributions are better described by a log-normal distribution and were fitted with a Gaussian function using Origin Lab 8.5 program. The scale factor S_1 was calculated using the mode obtained from the fitting parameters (see Table 6-1).

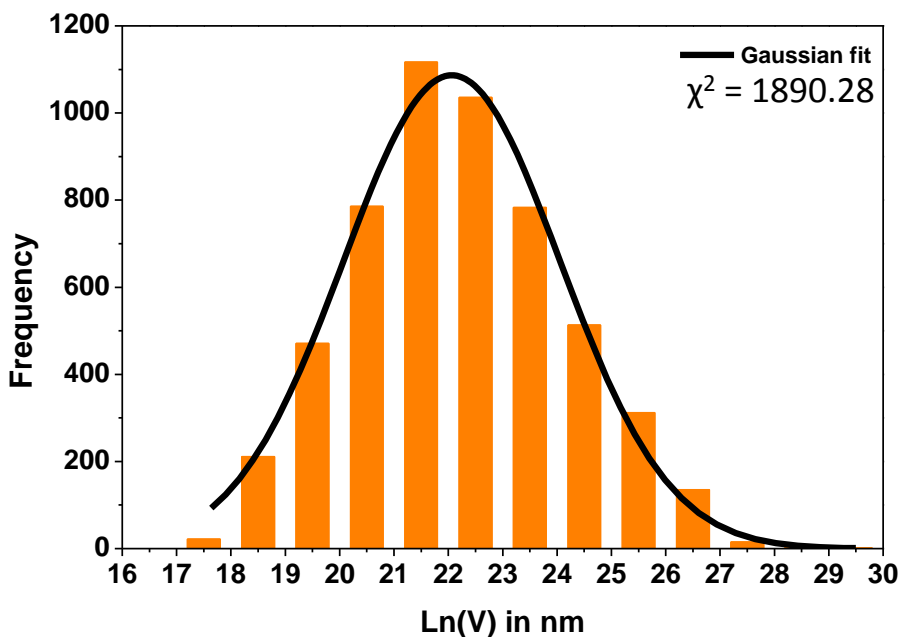


Figure 6-4. Distribution of the logarithm of size (volume (V)) distribution of LaB₆

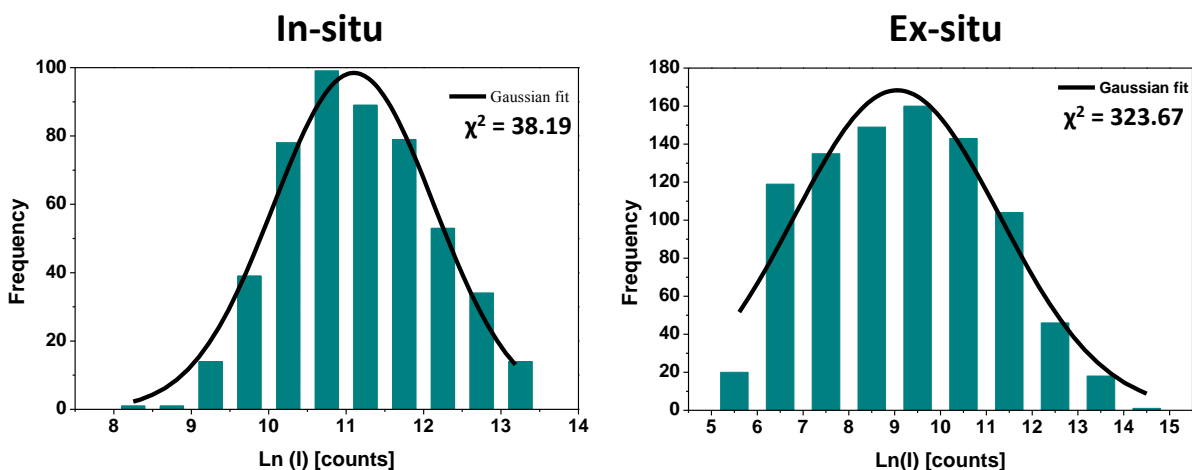


Figure 6-5. Distributions of the logarithm of measured intensities² of LaB₆ 110 reflection. Left hand side: *in-situ* measured LaB₆ inside the pressure cell. Right hand side: *ex-situ* measured LaB₆ in Kapton capillary.

² All CSD results presented in this chapter were reanalyzed using an updated version of the 00peak software. In the updated version, new selection process of peak intensities was added. Peak intensities with second moment, third moment (skewness) and the fourth moment (kurtosis) of the omega scan profiles bigger than the average $\pm 2\sigma$ (where σ is the standard deviation of the corresponding calculated statistical moment) are discarded. This selection process is important to remove outliers and overlapped peak profiles producing unexpected larger intensities. The moments are listed in Appendix D.

Table 6-1. Scale factor S_1

hkl	Mode	S_1
Size distribution	22.06	-
Intensity distribution (<i>Ex-situ</i>)	9.05	2.44
Intensity distribution (<i>In-situ</i>)	11.09	1.99

6.3. Results and discussions

The formation process of Xe hydrate in sediments was followed *in-situ* by measuring the evolution of crystallite sizes with time. Several scans were performed after a formation time of 2 min, 30 min, 2 days and 4 days. It was not possible to continue the measurements longer because of the limited duration of the beam time (~5 days). The measurements were systematically done at the same spot of the sample and using the same settings. Figure 6-6 shows a calculated pattern of xenon hydrate using Mercury software. A typical spotty diffraction pattern of Xe hydrate is also illustrated in Figure 6-7.

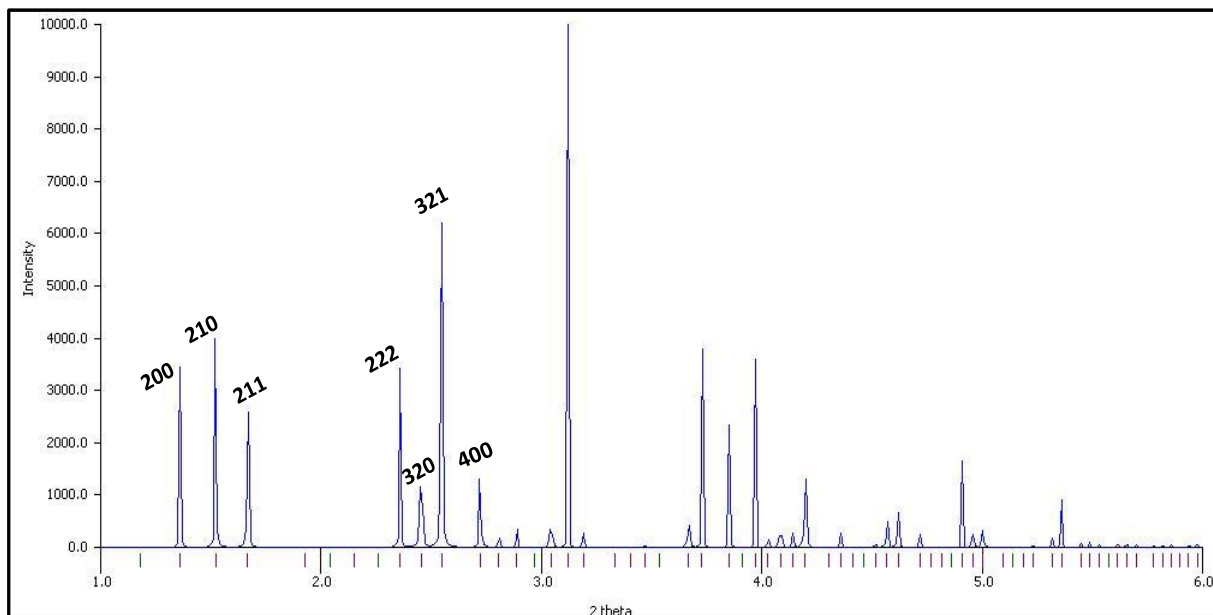


Figure 6-6. Calculated diffraction pattern of Xe hydrate using Mercury software

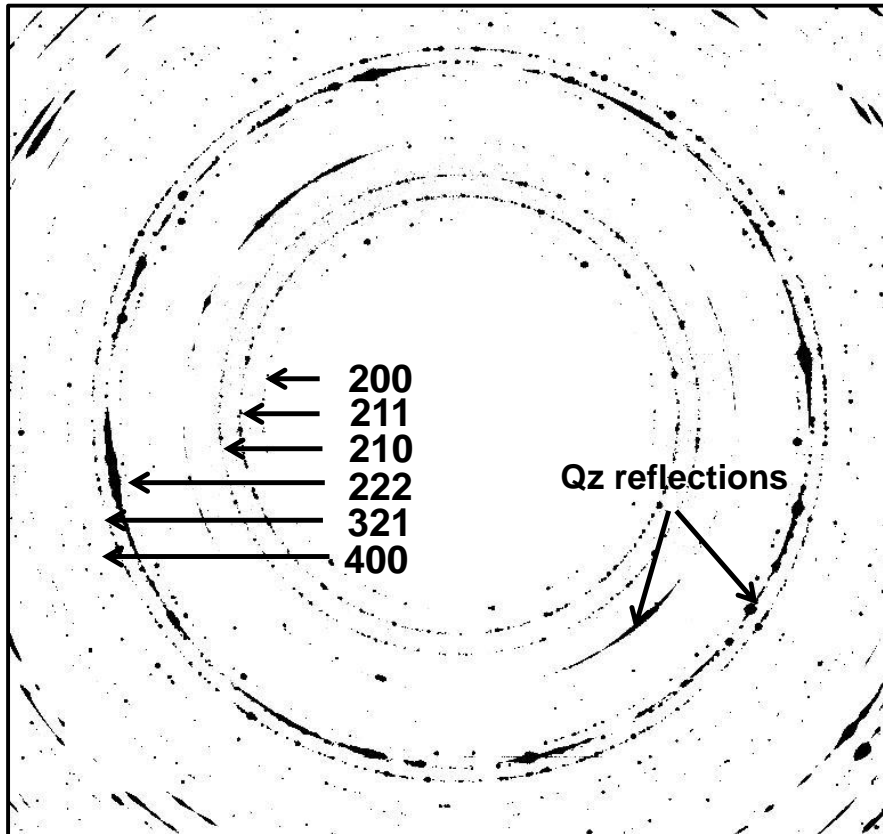


Figure 6-7. A measured 2D spotty diffraction pattern of Xe hydrate (run 4days).

Several GH hkl reflections are of interest and can be separated and analyzed by the software. These reflections are the 200, 210, 211, 222, 321 and 400.

The calculations of the second scale factor S_2 for the 6 reflections using the Equation 3.24 is given in Table 6-2. The cell files used to calculate the structure factors are presented in Appendix C.

Table 6-2. Scale factor S_2 for different Xe hydrate reflections

LaB6 ($V_c = 71.82 \text{ \AA}$)			Xe hydrate ($V_c = 1710.8 \text{ \AA}$)				S_2	
hkl	$ F^2 $	$ F^2 /V_c$	hkl	Multiplicity	$ F^2 $	$ F^2 /V_c$	100/hkl	110/hkl
100	1407.75	19.60	200	6	16162.04	9.44	2.07	3.47
110	2355.16	32.79	210	24	14986.66	8.76	2.24	3.74
111	2330.96	32.46	211	24	13317.16	7.78	2.51	4.21
			222	8	61757.22	36.09	0.54	0.91
			321	48	42530.81	24.86	0.50	1.32
			400	6	98520.65	57.58	0.34	0.57

* V_c : volume of the crystal lattice

An example of CSD calculation is shown in Table 6-3

The overall formula for calculating the crystal diameter d from the intensity is:

$$d = \sqrt[3]{\frac{6 \cdot \exp(S_1 \times \ln((I/Lz) \times S_2))}{\pi}} \quad (6.1)$$

where d is the crystal diameter, I is the raw intensity, Lz the factor for Lorentz correction and S_1 and S_2 are scaling factors.

Table 6-3. Exemplary CSD calculation with some random intensities values of Xe hydrate (sample at 2 days, reflection 211)

Int. (counts)	Ic x S₂	Ln (Ic x S₂)	Ln x S₁	Exp (V) (nm³)	R (nm)	D (μm)
60222.23	253535.57	12.44	24.76	5.7E+10	2383.95	4.77
6946.20	29243.52	10.28	20.46	7.7E+08	568.96	1.14
262677.82	1105873.62	13.92	27.69	1.1E+12	6332.99	12.67
74351.96	313021.75	12.65	25.18	8.6E+10	2741.67	5.48
18329.89	77168.83	11.25	22.39	5.3E+09	1082.98	2.17
380181.50	1600564.10	14.29	28.43	2.2E+12	8093.17	16.19
76246.10	320996.08	12.68	25.23	9.1E+10	2787.80	5.58
a	b	c	d	e	f	g

- a** Raw intensities generated by the program
b Correction of the intensities using S₂ scale factor (in this case it is 3.27 for 211 of Xe hydrate using 110 reflection of LaB₆): (Ic x S₂).
c Logarithmic function of the obtained intensities: Ln (Ic x S₂)
d Calibration of the intensities using the s₁ scale factor: Ln (Ic x S₂) x S₁
e Exp (Ln (Ic x S₂) x S₁) represents the volume of crystal in nm³
f Radius of crystals in nm
g Diameter of crystals in μm

During the analysis of GH crystal sizes produced from several hkl reflections, we encountered some problems as described below so we were forced every time to repeat the analysis and change some parameters until we obtained consistent results. Nevertheless, this exercise was beneficial as well to develop the method further.

The first analysis of GH CSDs showed discrepancies between the results obtained from different hkl reflections. In addition, the number of crystals detected within each hkl was not in agreement with the multiplicity factor. The difference between the expected and experimental number was sometimes exceeding 50 % (see Table in Appendix D).

In general, strong reflections have a better detection limit than weak reflections. In the case of GHs characterized by small crystal sizes in the range of 1-5 μm , this represents a problem because small crystals will not be detected in case of weak hkl reflections. The preliminary results of Xe hydrate-bearing sediments showed that the first three reflections with low structure factor values (200, 210 and 211) gave larger crystal sizes than the reflections with high structure factors (222, 321 and 400). Hence, we can conclude that there is a cut-off for the weak reflections. This means that the missing fraction of small crystals will lead to an increase of the average crystal size and unexpected low number of crystals not matching the multiplicity factor.

Furthermore, for weak reflections it is not possible to determine the right threshold multiplier as there is always a cut-off. Figure 6-8 shows the variation of the number of peaks detected per reflection as a function of the threshold multiplier. For the 222 and 400 reflections, we observe a plateau which represents a safe region for positioning a threshold. However for the 211, whatever threshold will be chosen, weak peaks will be cut off and thus missing in the CSDs.

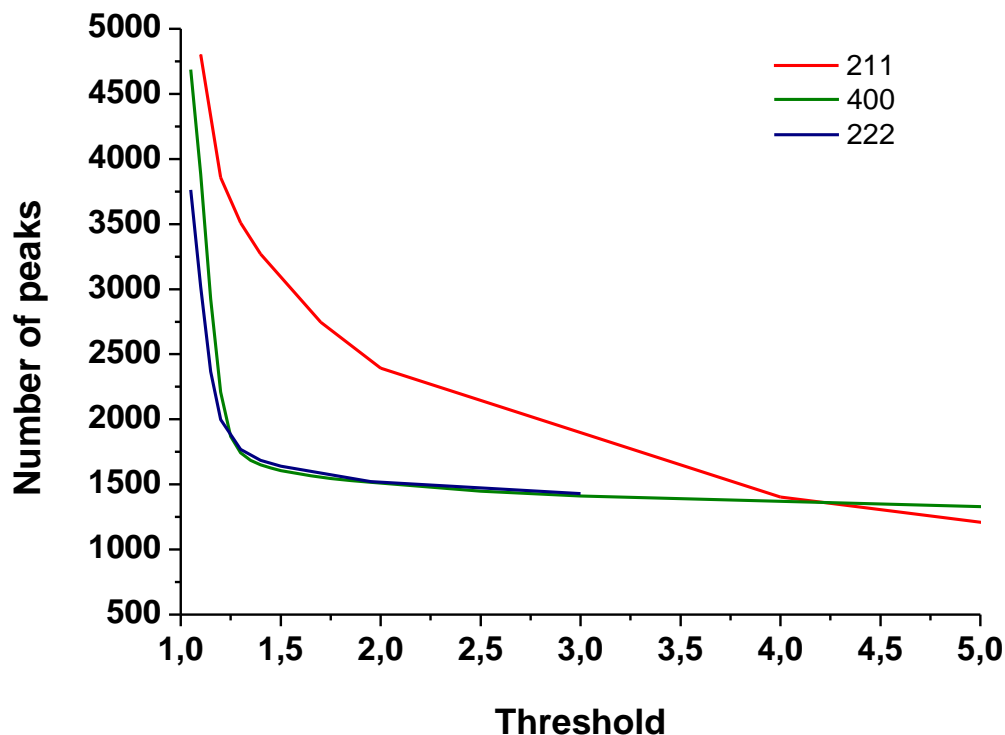


Figure 6-8. Variation of the total number of peaks as a function of the threshold multiplier of the hkl 211, 222 and 400

Therefore for the above mentioned reasons, the three weak reflections 200, 210 and 211 were discarded and not taken into account in order to not bias the final CSD results.

For the strongest reflections (222, 321 and 400), we know that we may miss some small crystals but by far not as much as in the case of the weak hkl. The other GH reflections have the strongest structure factor and even if GHs have small crystal sizes, the cut-off is not so critical in this case.

In addition to the cut-off problem, we discovered that the CSD data analysis program has a limit in handling overlapped peaks. The number of peaks in the 321 hkl which has a multiplicity of 48 was lower than expected (see Table in Appendix D). The 321 reflection is too crowded and overlapped peaks can be separated so we decided to discard as well this reflection from the final presentation of the CSD results.

Xe hydrate CSDs from 222 and 400

The final CSD results of Xe hydrate-bearing sediments are collected from the 222 and 400 reflections which are the most reliable hkl because they have a low multiplicity and strong structure factor. Indeed, the number occurrence of the observed 222 and 400 reflections correspond largely to the expected multiplicity ratio (see Table 6-4). The crystallites size measurements are collected into histograms. Meaningful statistics of several thousand counts are obtained from the two reflections considered. Figure 6-9 shows Xe hydrate CSDs calculated from the 222 and 400 reflections.

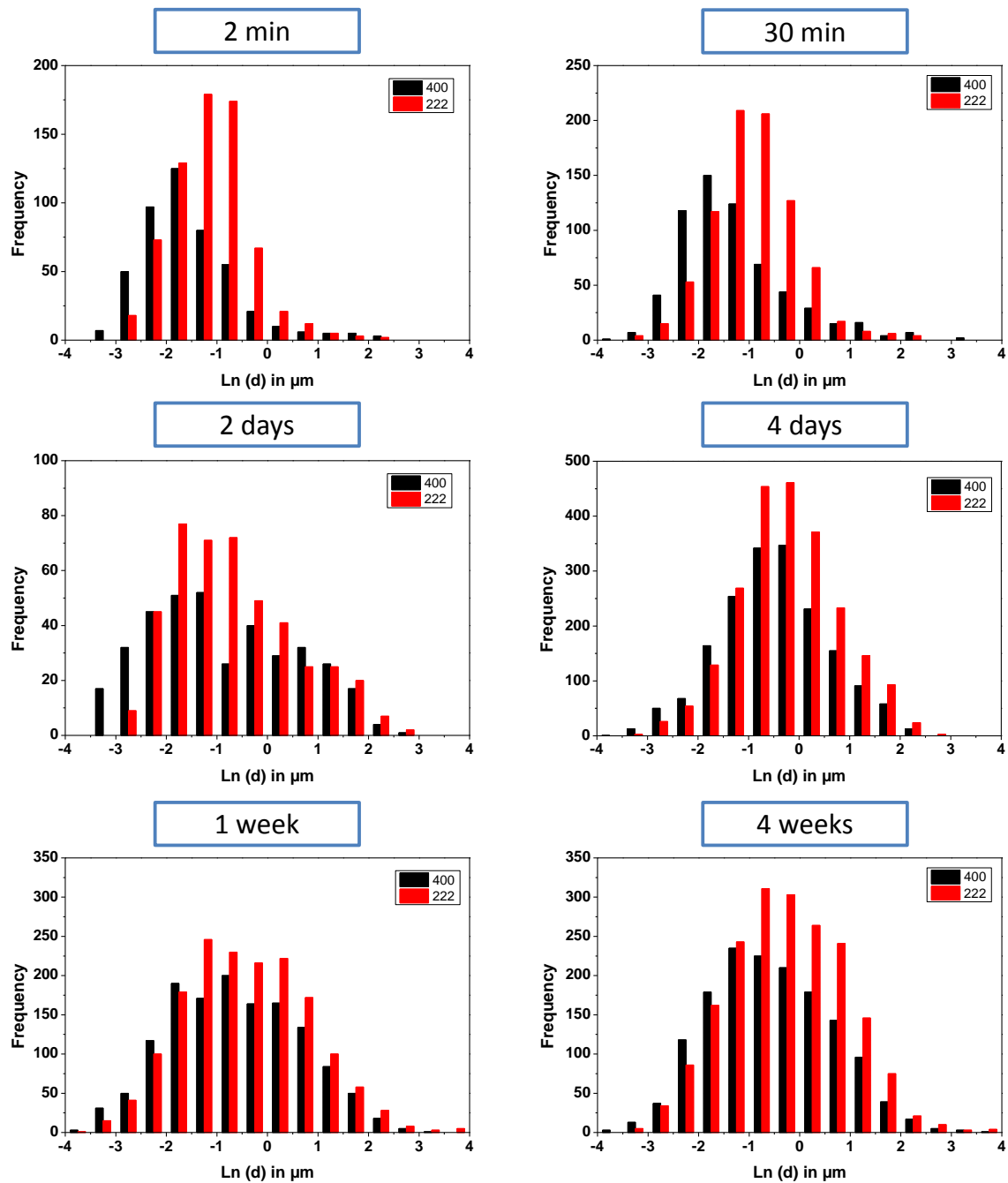


Figure 6-9. CSDs of Xe hydrates at different formation time collected from the 222 and 400 hkl reflections

As the sample was rotated only for few degrees, the peak reflections in each ring are statistically independent and result from the diffraction of different crystallites. Hence we can sum the results of the 222 and 400 hkl and produce one CSD plot for each data set. The evolution of Xe hydrate CSDs with time is illustrated in Figure 6-10.

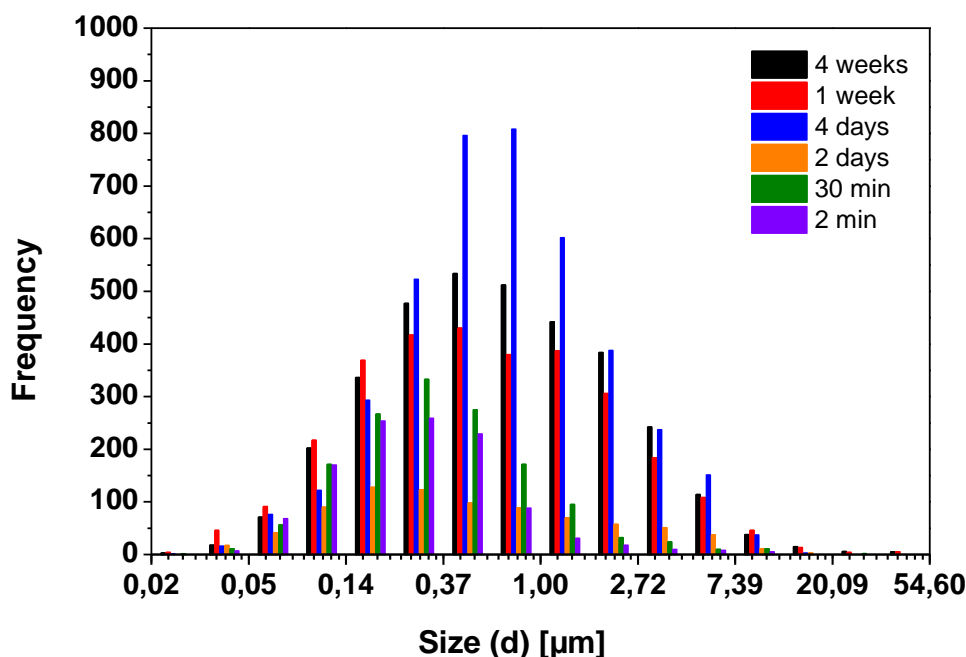


Figure 6-10. Evolution of GH CSDs with time

A summary of the results obtained from the 222, 400 reflection and their sum is shown in Table 6-4.

Table 6-4. Summary of statistical parameters

	hkl	Threshold	N initial	Ratio	N final	Ratio	Mean	SE of Mean
2 min	222	1.25	5059	1.08	683	1.47	0.466	0.029
	400	1.3	4703		464		0.423	0.043
	Sum	n.a	9762	n.a	1147	n.a	0.449	0.025
30 min	222	1.3	3781	1.32	832	1.33	0.597	0.028
	400	1.3	2859		627		0.631	0.042
	Sum	n.a	6640	n.a	1459	n.a	0.612	0.025
2 days	222	1.3	2045	0.60	443	1.19	1.163	0.057
	400	1.3	3387		372		1.115	0.073
	Sum	n.a	5432	n.a	815	n.a	1.141	0.046
4 days	222	1.25	6530	1.20	2266	1.27	1.307	0.020
	400	1.3	5441		1787		1.070	0.025
	Sum	n.a	11971	n.a	4053	n.a	1.203	0.016
1 week	222	3.5	8856	1.23	1626	1.18	1.457	0.030
	400	4	7200		1383		1.191	0.034
	Sum	n.a	16056	n.a	3009	n.a	1.334	0.022
4 weeks	222	3.5	8001	1.24	1908	1.27	1.496	0.030
	400	4	6467		1504		1.239	0.026
	Sum	n.a	14468	n.a	3412	n.a	1.384	0.020

The threshold multiplier was chosen from the safe region as illustrated in Figure 6-8.

Ninitial = the total number of peaks detected in each ring before any selection process.

Nfinal = number of peaks remained after application of all selection rules mentioned above.

Ratio = Multiplicity of 222 / Multiplicity of 400 = 1.33

The results obtained from the analysis of the 222 and 400 reflections are consistent. The number of crystals found per reflection before and after elimination of defect peaks respects the ratio of the multiplicity factor. One exception is the data set at 2 days of formation which shows a factor of 0.6. The reason for that is unknown but the ratio was adjusted after removing bad peaks.

On the other hand, the average crystal size determined from the 222 is relatively higher than the one of 400 in the most cases. This is because the 222 reflection has a structure factor lower than the 400 and some missing weak reflections leads to a slight increase of the average crystal sizes. The average diameter size determined from the sum of all peaks collected from the 222 and 400 hkl shows a continuous increase with time as it is illustrated in Figure 6-11.

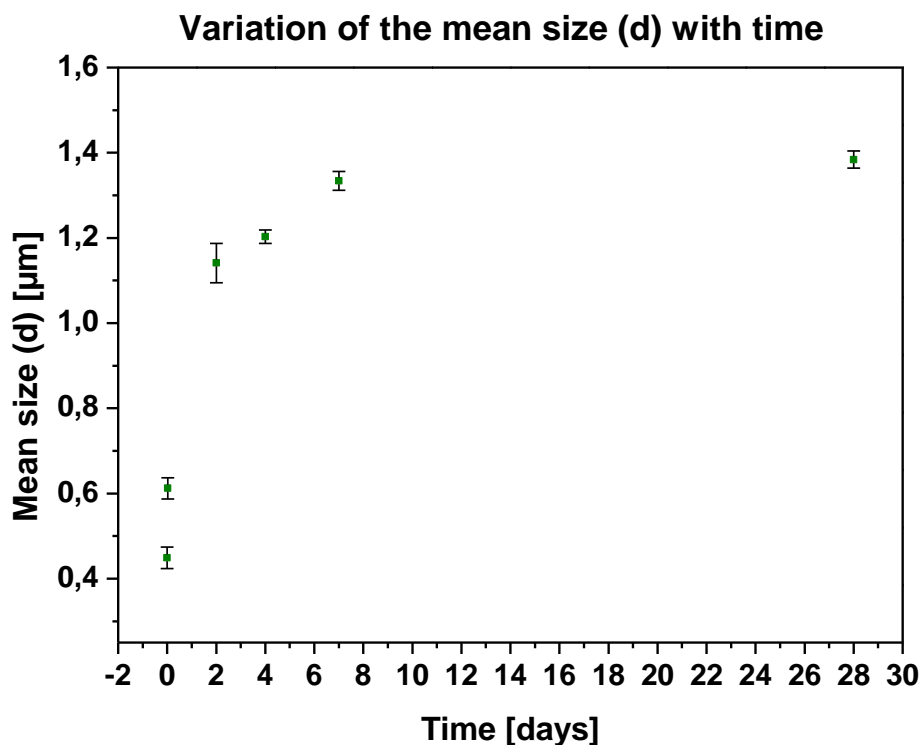


Figure 6-11. Evolution of the mean diameter size of GH with time

. The graph shows a fast initial increase of the size of crystals during the nucleation and growth processes. After completion of the formation process (after 2 days), GHs are expected to undergo a coarsening process where small crystals disappear in the expense of larger masses in order to reduce the total free energy of the system.

6.3.1. Summary

The determination of the crystal sizes of gas hydrate-bearing sediments is not an easy task and cannot be achieved using conventional optical method. In the last 4 years we were working on the development of a new fast method based on two-dimensional X-ray diffraction. The method was applied for the first time to investigate *in-situ* the evolution of Xe hydrate CSDs with time in order to complement our qualitative analysis of the GH microstructure using X-ray tomography. This work is a first step to better understand the physical/sonic properties of GH-bearing sediments and for a possible determination of the age of natural GH system.

GH-bearing sediments are characterized by a small crystal sizes in the range of 1-2 μm . This has influenced the analysis of the crystal sizes. Because of the small sizes of GH, weak reflections with low structure factors cannot give reliable results because of the cut-off of small crystals which may bias the final results. Hence, weak reflections were discarded from the final analysis. To overcome this problem, one could increase the exposure time during the experiments in order to improve the intensity to background ratio.

The second challenge was that overloaded hkl reflection with high multiplicity factor such as the 321 cannot be resolved by the Python analysis problem so the reflection was also discarded. Again to solve this problem, one could reduce the sample volume or the beam size during the collection of data.

GH-bearing sediments that are characterized by small crystal sizes have some inherent problems and limitations of the CSD method. Yet, the results obtained are very promising to develop the method further into a robust way to determine CSDs

7 | Conclusions and Outlook

The research presented in this thesis was focused on the study of the microstructure of GH-bearing sediments. The detection and quantification of GH in natural sediments require the knowledge of physical properties of GHs which depend on the microstructure. For this purpose, experimental devices and methods were specially developed as a part of this study. The nucleation and growth mechanisms of xenon hydrate in various sedimentary matrices and at different water saturations were followed *in-situ* inside a custom designed pressure cell using synchrotron X-ray micro-computed tomography. The observation of the evolution of the microstructure with time was complemented by a quantitative analysis of the evolution of GH crystallite size distributions. In the following, a summary of the key observations is given.

Xenon as hydrate former to replace methane: Xenon gas can be a good substitute of methane gas rather than THF as it doesn't require high formation pressures and it has more similar properties to methane gas. Xenon and methane are both rather insoluble in water and have small diffusion constants in water. Their hydrates form structure I and have similar physical properties.

Nucleation in sediments: The sub- μm pixel size resolution of the $\mu\text{-CT}$ setup used permitted to determine precisely the nucleation sites of GH in porous media. For GH formation, the most favorable site of GH formation is the gas-water interface. From the analysis of several hundred CT images, no nucleation on the surface of sediment grains was observed. For GH formation from "memory" water obtained from GH dissociation, the nucleation of GH starts inside the water phase. It appeared that the gas which remains in water in an unknown state acts as nucleation site for GH.

Growth pattern: The growth of GH depends on where the hydrate starts to nucleate. Different growth mechanisms were observed for the different formation scenarios using juvenile and "memory" water. However, the growth morphologies tend to move towards similar arrangements to the end of the formation process. The differences in the microstructure are expected to disappear more and more with time.

Water layer: The existence of the water layer between GH and sediment grains was one of the main key questions of this study which has never been observed at sub- μm resolution. The CT images showed clearly the existence of a μm water layer with variable thickness at the GH-Qz interface. The presence of the water film has important consequences for the distribution of GH in the sedimentary matrix and the corresponding seismic as well as electromagnetic responses. In particular, frictional losses due to squirt flow phenomena in the interfacial water were responsible for the anomalous attenuation of high frequency elastic waves in GH-bearing sediments.

Microstructural models: The existent microstructural models in literature were reviewed in this PhD based on the new findings. Our results do not support any of the cementing models of *Dvorkin et*

al. [2000] due to the presence of the water layer which reduces the effect of GH stiffness on the matrix. Therefore, a dramatic increase of the velocity with the hydrate saturation does not take place. This may explain discrepancies between the modeled and experimental data. At high water saturation, GH exhibits a pore-filling which changes to a load-bearing model as the GH saturation increases. GH fills the pore spaces and holds the sedimentary particles in place via a cushion of liquid water again without a cementation of the matrix in a strict sense.

Memory effect: The differences in the growth patterns observed in GH formation using juvenile and memory water support the existence of the so-called "memory effect". Furthermore, and for the first time, we have indications that indeed liquid water can become metastably enriched in Xe gas as suggested from the higher absorption coefficient observed for small water pockets in the pore space of Xe-hydrate.

Evolution of the microstructure with time: The evolution of the GH microstructure with time was studied by means of a quantitative analysis of GH crystallites size distributions. The results shows a continuous increase of the crystal sizes even after completion of the formation process due to the called Ostwald-ripening or normal grain growth processes in order to reduce the free energy of the system. The change of GH CSDs with time may also alter the physical/sonic properties of the resulting aggregates.

This study has permitted to reveal very important details of the microstructure of GH-bearing sediments. However, it cannot be taken for granted that the microstructural arrangements obtained in laboratory experiments are closely similar to what is observed under similar p - T conditions in natural environments. Nevertheless, there are some intrinsic features which remain unchanged such as the existence of μm -sized water layer at the interface with quartz or glass beads which is expected to occur as well in natural settings.

Although several research questions established for this study have been answered, further studies are needed to corroborate the remaining open questions. One concerns the role of clay minerals on the formation mechanism of GH-bearing sediments which was not clear in our results and may be clarified using additional characterization techniques.

Additional studies on the evolution of the microstructure over periods of several weeks to months using FXRCSD and SRXCT will permit to better understand the coarsening process and the equilibration of the microstructure with time. From modeling and extrapolating such studies using e.g. the Landau-Slyovitz-Wagner theory of coarsening, one may even gain access to the formation time, i.e. the age of GH in sedimentary matrices.

FXRCSD and SRXCT experiments carried out on natural GH-bearing sediments samples will also help to better understand the microstructural characteristics of natural systems and their physical properties.

Xenon is indeed a very good substitute of methane gas in terms of chemical and physical properties. Nevertheless, working with naturally occurring methane gas is desirable

The second part of this DFG project consisted to model the elastic wave velocities using the 3D tomographic data as direct input by our collaborators: Dr Eric Sänger and Kathleen Sell (PhD student).

Their contribution is summarized in a recently published paper cited below:

Sell, K., Saenger, E.-H., Falenty, A., Chaouachi, M., Haberthür, D., Enzmann, F., Kuhs, W. F., and Kersten, M.: On the path to the digital rock physics of gas hydrate bearing sediments – processing of in-situ synchrotron-tomography data, *Solid Earth Discuss.*, doi:10.5194/se-2016-54, in review, 2016.

8 | References

Agron, P. A., and H. A. Levy (1972), Thermoelectric cooling device for a single-crystal neutron diffractometer, *Journal of Applied Crystallography*, 5, 432.

Als-Nielsen, J., and D. McMorrow (2001), *Elements of Modern X-Ray Physics*, 318 pp., John Wiley & Sons Ltd, West Sussex, England.

Attwood, D. (2000), *Soft X-Rays and Extreme Ultraviolet Radiation: Principles and Applications*, 470 pp., The Press Syndicate of the University of Cambridge, Cambridge, United Kingdom

Attwood, D. (2007), Synchrotron Radiation for Materials Science Applications, University of California, Berkeley, PowerPoint slides, retrieved from <http://www.eecs.berkeley.edu/~attwood/srms/>.

Babu, P., D. Yee, P. Linga, A. Palmer, B. C. Khoo, T. S. Tan, and P. Rangsunvigit (2013), Morphology of Methane Hydrate Formation in Porous Media, *American Chemical Society*, 27, 3364-3372.

Bagherzadeh, S. A., I. L. Moudrakovski, J. A. Ripmeester, and P. Englezos (2011), Magnetic Resonance Imaging of Gas Hydrate Formation in a Bed of Silica Sand Particles, *Energy Fuels*, 25(7), 3083-3092, doi: 10.1021/ef200399a.

Bagherzadeh, S. A., P. Englezos, S. Alavi, and J. A. Ripmeester (2012), Molecular modeling of the dissociation of methane hydrate in contact with a silica surface, *J. Phys. Chem. B*, 116, 3188–3197, doi: 10.1021/jp2086544.

Bai, D., G. Chen, X. Zhang, and W. Wang (2011), Microsecond molecular dynamics simulations of the kinetic pathways of gas hydrate formation from solid surfaces, *Langmuir*, 27, 5961-5967, doi: 10.1021/la105088b.

Baldwin, B. A., A. Moradi-Araghi, and J. C. Stevens (2003), Monitoring hydrate formation and dissociation in sandstone and bulk with magnetic resonance imaging, *Magnetic Resonance Imaging*, 21(9), 1061-1069, doi: <http://dx.doi.org/10.1016/j.mri.2003.05.001>.

Barrer, R. M., and D. J. Ruzicka (1962), Non-stoichiometric clathrate compounds of water. 4. Kinetics of the formation of clathrate phases., *Transactions of the Faraday Society*, 58(479), 2262-2271, doi: 10.1039/tf9625802262.

Baruchel, J. (2004), Synchrotron radiation X-ray imaging: a tool for crystal growth, in: *Crystal Growth - from Fundamentals to Technology*, edited pp. 345-367.

Baruchel, J. (2012), Imaging with hard synchrotron radiation and neutrons "unpublished lectures notes (HERCULES)".

Baruchel, J. H., J. L., M. S. Lehmann, J. R. Regnard, and C. Schlenker (1993), *Neutron and Synchrotron Radiation for Condensed Matter Studies, Volume 1: Theory, Instruments and Methods*, Springer-Verlag Berlin Heidelberg and Les Editions de Physique Les Ulis, France.

Bech, M. (2009), *X-ray imaging with a grating interferometer*, PhD Thesis, University of Copenhagen.

Berge, L. I., K. A. Jacobsen, and A. Solstad (1999), Measured acoustic wave velocities of R11 (CCl₃F) hydrate samples with and without sand as a function of hydrate concentration, *J. Geophys. Res.-Solid Earth*, 104(B7), 15415-15424, doi: 10.1029/1999jb900098.

Best, A., J. Priest, and C. Clayton (2010), A resonant column study of the seismic properties of methane-hydrate-bearing sand, in: *Geophysical Characterization of Gas Hydrates*, edited by M. Riedel pp. 337-347.

Best, A. I., J. A. Priest, C. R. I. Clayton, and E. V. L. Rees (2013), The effect of methane hydrate morphology and water saturation on seismic wave attenuation in sand under shallow sub-seafloor conditions, *Earth Planet. Sci. Lett.*, 368, 78-87, doi: 10.1016/j.epsl.2013.02.033.

Boas, E. F., Fleischmann, D. (2012), CT artifacts: Causes and reduction techniques, *Imaging in Medicine*, 4(2), 229-240, <http://www.edboas.com/science/CT/0012.pdf>.

Boewer, L., J. Nase, M. Paulus, F. Lehmkuhler, S. Tiemeyer, S. Holz, D. Pontoni, and M. Tolan (2012), On the spontaneous formation of clathrate hydrates at water-guest interfaces, *J. Phys. Chem. C*, 116(15), 8548-8553, doi: 10.1021/jp211784w.

Bonnefoy, O. (2005), *Influence de cristaux d'hydrates de gaz ou de glace sur la permeabilite d'un milieu poreux*, PhD Thesis, Ecole Nationale Superieure Des Mines De Saint-Etienne.

Bonnefoy, O., F. Gruy, and J. M. Herri (2005), Van der Waals interactions in systems involving gas hydrates, *Fluid Phase Equilib.*, 231(2), 176-187, doi: 10.1016/j.fluid.2005.02.004.

Bonse, U., and M. Hart (1965), An X-ray interferometer, *Appl. Phys. Lett.*, 6(8), 155-156, doi: <http://dx.doi.org/10.1063/1.1754212>.

Buchanan, P., A. K. Soper, H. Thompson, R. E. Westacott, J. L. Creek, G. Hobson, and C. A. Koh (2005), Search for memory effects in methane hydrate: Structure of water before hydrate formation and after hydrate decomposition *J. Chem. Phys.*, 123, 89-93, doi: 10.1063/1.2074927.

Buerger, M. J. (1940), The correction of X-ray diffraction intensities for Lorentz and polarization factors, *Proceedings of the National Academy of Sciences*, 26, 637-642.

Bunge, H. J., L. Wcislak, H. Klein, U. Garbe, and J. R. Schneider (2003), Texture and microstructure imaging in six dimensions with high-energy synchrotron radiation, *Journal of Applied Crystallography*, 36(5), 1240-1255, doi: doi:10.1107/S0021889803014924.

Bylov, M. (1997), *An experimental study of the nucleation and growth of gas hydrates* PhD Thesis, Technical University of Denmark

Cao, Y., Z. Su, and D. Chen (2013), Influence of water flow on gas hydrate accumulation at cold vents, *Sci. China Earth Sci.*, 56(4), 568-578, doi: 10.1007/s11430-012-4553-6.

Carcione, J. M., and D. Gei (2004), Gas-hydrate concentration estimated from P- and S-wave velocities at the Mallik 2L-38 research well, Mackenzie Delta, Canada, *J. Appl. Geophys.*, 56(1), 73-78, doi: 10.1016/j.jappgeo.2004.04.001.

Cha, S. B., H. Ouar, T. R. Wildeman, and E. D. Sloan (1988), A third-surface effect on hydrate formation, *The Journal of Physical Chemistry*, 92(23), 6492-6494, doi: 10.1021/j100334a006.

Chand, S. (2008), Gas hydrate anomalies in seismic velocities, amplitudes and attenuation: What do they imply?, paper presented at Proceedings of the 6th International Conference on Gas Hydrates (ICGH 2008), Vancouver, British Columbia, Canada.

Chand, S., and T. A. Minshull (2004), The effect of hydrate content on seismic attenuation: A case study for Mallik 2L-38 well data, Mackenzie delta, Canada, *Geophys. Res. Lett.*, 31(14), 4 pp, doi: 10.1029/2004gl020292.

Chand, S., T. A. Minshull, J. A. Priest, A. I. Best, C. R. I. Clayton, and W. F. Waite (2006), An effective medium inversion algorithm for gas hydrate quantification and its application to laboratory and borehole measurements of gas hydrate-bearing sediments, *Geophys. J. Int.*, 166(2), 543-552, doi: 10.1111/j.1365-246X.2006.03038.x.

Chaplin, M. (2008), Interfacial water and water-gas interfaces, http://www1.lsbu.ac.uk/water/interfacial_water.html.

Chen, D. F., and L. M. Cathles (2003), A kinetic model for the pattern and amounts of hydrate precipitated from a gas steam: Application to the Bush Hill vent site, Green Canyon Block 185, Gulf of Mexico, *Journal of Geophysical Research: Solid Earth*, 108(B1), 2058, doi: 10.1029/2001JB001597.

Chen, D. F., and L. M. Cathles (2005), On the thermal impact of gas venting and hydrate crystallization, *Journal of Geophysical Research: Solid Earth*, 110(B11), B11204, doi: 10.1029/2004JB003533.

Christiansen, R. L., and E. D. Sloan (1995), A compact model for hydrate formation, in *74th Annual Convention of the Gas Processors Association*, edited, San Antonio, USA.

Chuvilin, E. M., and V. A. Istomin (2012), Temperature dependence of the equilibrium pore water content in gas hydrate contained sediments paper presented at Tenth International Conference on Permafrost Salekhard (Russia), 2, 57-60.

Chuvilin, E. M., V. A. Istomin, and S. S. Safonov (2011), Residual nonclathrated water in sediments in equilibrium with gas hydrate Comparison with unfrozen water, *Cold Reg. Sci. Technol.*, 68, 68-73, doi: 10.1016/j.coldregions.2011.05.006.

Cierniak, R. (2011), X-ray Computed Tomography in Biomedical Engineering, p. 319, Springer-Verlag, London.

Circone, S., L. A. Stern, and S. H. Kirby (2004), The role of water in gas hydrate dissociation, *Journal of Physical Chemistry B*, 108(18), 5747-5755.

Clennell, M. B., M. Hovland, J. S. Booth, P. Henry, and W. J. Winters (1999), Formation of natural gas hydrates in marine sediments: 1. Conceptual model of gas hydrate growth conditioned by host sediment properties, *Journal of Geophysical Research: Solid Earth*, 104(B10), 22985-23003, doi: 10.1029/1999JB900175.

Cloetens, P., M. Pateyron-Salomé, J. Y. Buffière, G. Peix, J. Baruchel, F. Peyrin, and M. Schlenker (1997), Observation of microstructure and damage in materials by phase sensitive radiography and tomography, *Journal of Applied Physics*, 81(9), 5878-5886, doi: doi:http://dx.doi.org/10.1063/1.364374.

Collett, T. S., and V. A. Kuuskraa (1998), Emerging U.S. gas resources; 4, Hydrates contain vast store of world gas resources *Oil and Gas Journal*, 96(19), 90-95.

Cormack, A. M. (1973), Reconstruction of densities from their projections, with applications in radiological physics, *Physics in Medicine and Biology*, 18(195-207).

Dai, J., H. Xu, F. Snyder, and N. Dutta (2004), Detection and estimation of gas hydrates using rock physics and seismic inversion: Examples from the northern deepwater Gulf of Mexico, *The Leading Edge*, 23(1), 60-66, doi: 10.1190/1.1645456.

Dai, S., J. C. Santamarina, W. F. Waite, and T. J. Kneafsey (2012), Hydrate morphology: Physical properties of sands with patchy hydrate saturation, *J. Geophys. Res.-Solid Earth*, 117, 12 pp, doi: 10.1029/2012jb009667.

Daniels, J. E., and M. Drakopoulos (2009), High-energy X-ray diffraction using the Pixium 4700 flat-panel detector, *J. Synchrot. Radiat.*, 16(4), 463-468, doi: doi:10.1107/S0909049509015519.

Davie, M. K., O. Y. Zatsepina, and B. A. Buffet (2004), Methane solubility in marine hydrate environments, *Marine Geology*, 203, 177-184.

Davies, S. R., E. D. Sloan, A. K. Sum, and C. A. Koh (2010), In situ studies of the mass transfer mechanism across a methane hydrate film using high-resolution Confocal raman spectroscopy, *J. Phys. Chem. C*, 114, 1173-1180, doi: 10.1021/jp909416y.

Davy, H. (1810), The bakterian Lecture: On some of the combinations of oxymuriatic gas and oxygen and on the chemical relations of these principles to inflammable bodies, *Phil. Trans. R. Soc. Lond.*, 101, 1-35.

De Roo, J. L., C. J. Peters, R. N. Lichtenthaler, and G. A. M. Diepen (1983), Occurrence of methane hydrate in saturated and unsaturated solutions of sodium chloride and water in dependence of temperature and pressure, *AIChE Journal*, 29(4), 651-657, doi: 10.1002/aic.690290420.

Demurov, A., R. Radhakrishnan, and B. L. Trout (2002), Computations of diffusivities in ice and CO₂ clathrate hydrates via molecular dynamics and Monte Carlo simulations, *J. Chem. Phys.*, 116(2), 702-709, doi: 10.1063/1.1425821.

Duchateau, C., P. Glénat, T.-E. Pou, M. Hidalgo, and C. Dicharry (2010), Hydrate precursor test method for the laboratory evaluation of kinetic hydrate inhibitors, *Energy & Fuels*, 24(1), 616-623, doi: 10.1021/ef900797e.

-
- Dvorkin, J., and R. Uden (2004), Seismic wave attenuation in a methane hydrate reservoir, *The Leading Edge*, 23(8), 730-732, doi: 10.1190/1.1786892.
- Dvorkin, J., A. Nur, R. Uden, and T. Taner (2003), Rock physics of a gas hydrate reservoir, *The Leading Edge*, 22(9), 842-847, doi: 10.1190/1.1614153.
- Dvorkin, J., M. B. Helgerud, W. F. Waite, S. H. Kirby, A. Nur, and M. D. Mas (2000), Introduction to physical properties and elasticity models in: *Natural gas hydrate in oceanic and permafrost environments* edited by M. D. Max pp. 245-260, Kluwer Academic Publishers, Dordrecht, Netherlands.
- Ecker, C., J. Dvorkin, and A. Nur (1998), Sediments with gas hydrates: Internal structure from seismic AVO, *GEOPHYSICS*, 63(5), 1659-1669, doi: doi:10.1190/1.1444462.
- Englezos, P., and S. Hall (1994), Phase equilibrium data on carbon dioxide hydrate in the presence of electrolytes, water soluble polymers and montmorillonite, *The Canadian Journal of Chemical Engineering*, 72(5), 887-893, doi: 10.1002/cjce.5450720516.
- Englezos, P., N. Kalogerakis, P. D. Dholabhai, and P. R. Bishnoi (1987), Kinetics of formation of methane and ethane gas hydrates, *Chemical Engineering Science*, 42(11), 2647-2658.
- Freer, E. M., M. Sami Selim, and E. D. Sloan (2001), Methane hydrate film growth kinetics, *Fluid Phase Equilib.*, 185(1-2), 65-75, doi: [http://dx.doi.org/10.1016/S0378-3812\(01\)00457-5](http://dx.doi.org/10.1016/S0378-3812(01)00457-5).
- Fultz, B., and J. Howe (2013), *Transmission Electron Microscopy and Diffractometry of Materials*, Graduate Texts in Physics, edited by C. Ascheron, Springer Heidelberg New York Dordrecht London.
- Genov, G., W. F. Kuhs, D. K. Staykova, E. Goreshnik, and A. N. Salamatin (2004), Experimental studies on the formation of porous gas hydrates, *American Mineralogist*, 89(8-9), 1228-1239.
- Gevantman, L. H. (2005), Solubility of selected gases in water, in *CRC Handbook of Chemistry and Physics*, edited by D. R. Lide, CRC Press, Boca Raton, FL
- Goetz, K., M. P. Kalashnikov, and Y. A. S. Mikhailov, G. V. defotov, S. I. Foerster, E. Zaumseil, P. (1979), Measurements of the parameters of shell targets for laser thermonuclear fusion using an X-ray schlieren method, *Soviet Journal of Quantum Electronics*, 9(5), 607-610.
- Guerin, G., and D. Goldberg (2005), Modeling of acoustic wave dissipation in gas hydrate-bearing sediments, *Geochem. Geophys. Geosyst.*, 6, 16 pp, doi: 10.1029/2005gc000918.
- Guggenheim, S., and A. F. Koster van Groos (2003), New gas-hydrate phase: Synthesis and stability of clay-methane hydrate intercalate, *Geol. Soc. of Am.*, 31, 653-656, doi: 10.1130/0091-7613.
- Hachikubo, A., S. Takeya, E. Chuvilin, and V. Istomin (2011), Preservation phenomena of methane hydrate in pore spaces, *Phys. Chem. Chem. Phys.*, 13(39), 17449-17452, doi: 10.1039/C1CP22353D.

Hall, E. O. (1951), The deformation and ageing of mild steel: III Discussion of results *Proceedings of the Physical Society*, 64(9), 747-753.

Hammerschmidt, E. G. (1934), *Ind. Eng. Chem.*, 26, 851.

Hammond, C. (2009), *The Basics of Crystallography and Diffraction*, Third Edition ed., Oxford University Press Inc., New York, USA.

Handa, Y. P., and J. G. Cook (1987), Thermal conductivity of xenon hydrate *J. Phys. Chem.*, 91, 6327–6328.

Hansen, T. C., A. Falenty, M. M. Murshed, and W. F. Kuhs (2015), Lattice constants and expansivities of gas hydrates from 10K up to the stability limit, in *Proceedings of the 8th International Conference on Gas Hydrates (ICGH-8)*, edited, Arxiv (arXiv:1510.06901), Beijing, China.

Hansen, T. C., P. F. Henry, H. E. Fischer, J. Torregrossa, and P. Convert (2008), The D20 instrument at the ILL: a versatile high-intensity two-axis neutron diffractometer, *Meas. Sci. Technol.*, 19(3), doi: 03400110.1088/0957-0233/19/3/034001.

Harrison, S. E. (2010), Natural gas hydrates, <http://large.stanford.edu/courses/2010/ph240/harrison1/>.

Hatzikiriakos, S. G., and P. Englezos (1994), Gas storage through impermeation of porous media by hydrate formation, paper presented at Proceedings of the fourth international offshore and polar engineering conference, Osaka (Japan), 337-344.

Hawtin, R. W., D. Quigleya, and P. M. Rodger (2008), Gas hydrate nucleation and cage formation at a water/methane interface, *Phys. Chem. Chem. Phys.*, 10, 4853-4864, doi: 10.1039/B807455K

He, B. (2011), Method for measuring crystallite size with a two-dimensional X-ray diffractometer, edited by U. S. Patent, Bruker AXS, Inc, Madison, WI United States.

He, B. B. (2009), *Two-Dimensional X-Ray Diffraction*, John Wiley & Sons, Inc., Hoboken, New Jersey, USA.

Helgerud, M. B., J. Dvorkin, A. Nur, A. Sakai, and T. Collett (1999), Elastic-wave velocity in marine sediments with gas hydrates: Effective medium modeling, *Geophysical Research Letters*, 26(13), 2021-2024, doi: 10.1029/1999GL900421.

Henry, D. (2012), Electron-Sample Interactions, http://serc.carleton.edu/research_education/geochemsheets/bse.html.

Henry, P., M. Thomas, and M. Ben Clennell (1999), Formation of natural gas hydrates in marine sediments 2. Thermodynamic calculations of stability conditions in porous sediments, *J. Geophys. Res.-Solid Earth*, 104(B10), 23005-23022, doi: 10.1029/1999jb900167.

Herri, J. M., J. S. Pic, F. Gruy, and M. Cournil (1999), Methane hydrate crystallization mechanism from in-situ particle sizing, *AIChE Journal*, 45(3), 590-602, doi: 10.1002/aic.690450316.

Hintermüller, C., F. Marone, A. Isenegger, and M. Stampanoni (2010), Image processing pipeline for synchrotron-radiation-based tomographic microscopy, *J. Synchrot. Radiat.*, 17(4), 550-559, doi: doi:10.1107/S0909049510011830.

Hirata, A., and Y. H. Mori (1998), How liquids wet clathrate hydrates - some macroscopic observations *Chem. Eng. Sci.*, 53(14), 2641-2643, doi: 10.1016/s0009-2509(98)00078-5.

Holbrook, W. S., H. Hoskins, W. T. Wood, R. A. Stephen, and D. Lizarralde (1996), Methane hydrate and free gas on the Blake ridge from vertical seismic profiling, *Science*, 273, 1840-1843.

Hounsfield, G. N. (1973), Computerized transverse axial scanning (tomography). Part I: Description of the system. part II: Clinical applications, *British Journal of Radiology*, 46, 1016-1022.

Hu, G. W., Y. G. Ye, J. Zhang, C. L. Liu, S. B. Diao, and J. S. Wang (2010), Acoustic properties of gas hydrate-bearing consolidated sediments and experimental testing of elastic velocity models, *J. Geophys. Res.-Solid Earth*, 115, 11, doi: 10.1029/2008jb006160.

Ida, T., and L. Jiang (2011), Crystallite size analysis method and apparatus using powder X-ray diffraction, edited by U. S. P. A. Publication, RIGAKU CORPORATION, United States.

Ingal, V. B., E. (1995), X-ray plane-wave topography observation of the phase contrast from a non-crystalline object, *Journal of Physics D: Applied Physics*, 28(11), 2314-2317.

Issonov, P., T. Gebrenegus, and M. Tuller (2009), Segmentation of X-ray computed tomography images of porous materials: A crucial step for characterization and quantitative analysis of pore structures, *Water Resources Research*, 45.

Jacobson, L. C., W. Hujo, and V. Molinero (2010), Amorphous precursors in the nucleation of clathrate hydrates, *Am. Chem. Soc.*, 132(33), 11806-11811, doi: 10.1021/ja1051445.

Jin, S., S. Takeya, J. Hayashi, J. Nagao, Y. Kamata, T. Ebinuma, and H. Narita (2004), Structure Analyses of Artificial Methane Hydrate Sediments by Microfocus X-ray Computed Tomography, *Japanese Journal of Applied Physics*, 43(8A), 5673-5675, doi: 10.1143/JJAP.43.5673.

Jin, S., J. Nagao, S. Takeya, Y. Jin, J. Hayashi, Y. Kamata, T. Ebinuma, and H. Narita (2006), Structural investigation of methane hydrate sediments by microfocus X-ray computed tomography technique under high-pressure conditions, *Jpn. J. Appl. Phys.*, 45(27), L714-L716, doi: 10.1143/JJAP.45.L714.

Jin, Y., Y. Konno, and J. Nagao (2012), Growth of Methane Clathrate Hydrates in Porous Media, *Energy & Fuels*, 26(4), 2242-2247, doi: 10.1021/ef3001357.

Jradi, K., C. Daneault, and B. Chabot (2011), Chemical surface modification of glass beads for the treatment of paper machine process waters, *Thin Solid Films*, 519, 4239-4245, doi: 10.1016/j.tsf.2011.02.080.

Kashchiev, D., and A. Firoozabadi (2002), Driving force for crystallization of gas hydrates, *Journal of Crystal Growth*, 241(1-2), 220-230, doi: [http://dx.doi.org/10.1016/S0022-0248\(02\)01134-X](http://dx.doi.org/10.1016/S0022-0248(02)01134-X).

-
- Kashchiev, D., and A. Firoozabadi (2003), Induction time in crystallization of gas hydrates, *Journal of Crystal Growth*, 250(3–4), 499-515, doi: [http://dx.doi.org/10.1016/S0022-0248\(02\)02461-2](http://dx.doi.org/10.1016/S0022-0248(02)02461-2).
- Kashchiev, D., and G. M. van Rosmalen (2003), Review: Nucleation in solutions revisited, *Crystal Research and Technology*, 38(7-8), 555-574, doi: 10.1002/crat.200310070.
- Katsuki, D., R. Ohmura, T. Ebinuma, and H. Narita (2006), Formation, growth and ageing of clathrate hydrate crystals in a porous medium, *Philosophical Magazine*, 86(12), 1753-1761, doi: 10.1080/14786430500509062.
- Katsuki, D., R. Ohmura, T. Ebinuma, and H. Narita (2007), Methane hydrate crystal growth in a porous medium filled with methane-saturated liquid water, *Philosophical Magazine*, 87(7), 1057-1069, doi: 10.1080/14786430601021652.
- Kerkar, P., K. W. Jones, R. Kleinberg, W. B. Lindquist, S. Tomov, H. Feng, and D. Mahajan (2009), Direct observations of three dimensional growth of hydrates hosted in porous media, *App. Phys. Lett.*, 95(2), -, doi: [doi:http://dx.doi.org/10.1063/1.3120544](http://dx.doi.org/10.1063/1.3120544).
- Kerkar, P. B., K. Horvat, K. W. Jones, and D. Mahajan (2014), Imaging methane hydrates growth dynamics in porous media using synchrotron X-ray computed microtomography, *Geochem. Geophys. Geosyst.*, 15(12), 4759-4768, doi: 10.1002/2014GC005373.
- Ketcham, A. R. (2012), X-ray Computed Tomography (CT), http://serc.carleton.edu/research_education/geochemsheets/techniques/CT.html.
- Ketcham, A. R. C., D. William (2001), Acquisition, optimization and interpretation of X-ray computed tomographic imagery: applications to the geosciences, *Computers & Geosciences*, 27, 381-400.
- Kirschgen, T. M., M. D. Zeidler, B. Geil, and F. Fujara (2003), A deuteron NMR study of the tetrahydrofuran clathrate hydrate - Part II: Coupling of rotational and translational dynamics of water, *Phys. Chem. Chem. Phys.*, 5(23), 5247-5252, doi: 10.1039/b212472f.
- Klapp, S. A., H. Klein, and W. F. Kuhs (2007), First determination of gas hydrate crystallite size distributions using high-energy synchrotron radiation, *Geophys. Res. Lett.*, 34(13), 5 pp, doi: 10.1029/2006gl029134.
- Klapp, S. A., S. Hemes, H. Klein, G. Bohrmann, I. MacDonald, and W. F. Kuhs (2010a), Grain size measurements of natural gas hydrates, *Mar. Geo.*, 274(1-4), 85-94, doi: 10.1016/j.margeo.2010.03.007.
- Klapp, S. A., M. M. Murshed, T. Pape, H. Klein, G. Bohrmann, P. G. Brewer, and W. F. Kuhs (2010b), Mixed gas hydrate structures at the Chapopote Knoll, southern Gulf of Mexico, *Earth Planet. Sci. Lett.*, 299(1-2), 207-217, doi: 10.1016/j.epsl.2010.09.001.
- Klapproth, A. (2002), *Strukturuntersuchungen an Methan- und Kohlenstoffdioxid-Clathrat-Hydraten*, Dissertation, Georg-August-Universität Göttingen.
- Klapproth, A. (2006), Investigations of microstructures of hydrates in porous media "Private Communication".
-

Klapproth, A., K. S. Techmer, S. A. Klapp, M. M. Murshed, and W. F. Kuhs (2007), Microstructure of gas hydrates in porous media, in: *Physics and Chemistry of Ice*, edited by W. F. Kuhs, Special Publication No 311, pp. 321-328, RSC Publishing, Cambridge.

Kneafsey, T. J., L. Tomutsa, G. J. Moridis, Y. Seol, B. M. Freifeld, C. E. Taylor, and A. Gupta (2007), Methane hydrate formation and dissociation in a partially saturated core-scale sand sample, *J. Pet. Sci. Eng.*, 56(1-3), 108-126, doi: 10.1016/j.petrol.2006.02.002.

Kobayashi, I., Y. Ito, and Y. H. Mori (2001), Microscopic observations of clathrate-hydrate films formed at liquid/liquid interfaces. I. Morphology of hydrate films, *Chem. Eng. Sci.*, 56, 4331-4338.

Koishi, T., K. Yasuoka, T. Ebisuzaki, S. Yoo, and X. C. Zeng (2005), Large-scale molecular-dynamics simulation of nanoscale hydrophobic interaction and nanobubble formation, *J. Chem. Phys.*, 123(20), 6 pp, doi: doi:http://dx.doi.org/10.1063/1.2102906.

Kossel, E., C. Deusner, N. Bigalke, and M. Haeckel (2013), Magnetic resonance imaging of gas hydrate formation and conversion at sub-seafloor conditions, *Diffusion Fundamentals*, 18, 1-4.

Kuhs, W. F., D. K. Staykova, and A. N. Salamatin (2006), Formation of methane hydrate from polydisperse ice powders, *Journal of Physical Chemistry B*, 110(26), 13283-13295, doi: 10.1021/jp061060f.

Kuhs, W. F., C. Sippel, A. Falenty, and T. C. Hansen (2012), Extent and relevance of stacking disorder in "ice Ic", *Proceedings of the National Academy of Sciences*, 109(52), 21259-21264, doi: 10.1073/pnas.1210331110.

Kvenvolden, K. A. (1993), GAS HYDRATES - GEOLOGICAL PERSPECTIVE AND GLOBAL CHANGE, *Reviews of Geophysics* 173-187.

Lee, J. Y., T. S. Yun, J. C. Santamarina, and C. Ruppel (2007), Observations related to tetrahydrofuran and methane hydrates for laboratory studies of hydrate-bearing sediments, *Geochemistry, Geophysics, Geosystems*, 8(6), Q06003, doi: 10.1029/2006GC001531.

Lee, J. Y., F. M. Francisca, J. C. Santamarina, and C. Ruppel (2010), Parametric study of the physical properties of hydrate-bearing sand, silt, and clay sediments: 2. Small-strain mechanical properties, *J. Geophys. Res.-Solid Earth*, 115, 11 pp, doi: 10.1029/2009jb006670.

Lehmkuhler, F., M. Paulus, C. Sternemann, D. Lietz, F. Venturini, C. Gutt, and M. Tolan (2008), The carbon dioxide-water interface at conditions of gas hydrate formation, *J. Am. Chem. Soc.*, 131(2), 585-589, doi: 10.1021/ja806211r.

Li, C., and X. Liu (2014), Analysis of P-wave attenuation in hydrate-bearing sediments based on BISQ model: a case study in shenhu area, south china sea, paper presented at 8th International Conference on Gas Hydrates Beijing, China.

Li, S.-L., C.-Y. Sun, B. Liu, Z.-Y. Li, G.-J. Chen, and A. K. Sum (2014), New Observations and Insights into the Morphology and Growth Kinetics of Hydrate Films, *Sci. Rep.*, 4, doi: 10.1038/srep04129
<http://www.nature.com/srep/2014/140219/srep04129/abs/srep04129.html#supplementary-information>.

-
- Liang, S., and P. G. Kusalik (2010), Crystal Growth Simulations of H₂S Hydrate, *J. Phys. Chem. B*, 114(29), 9563-9571, doi: 10.1021/jp102584d.
- Liang, S., and P. G. Kusalik (2011), The mobility of water molecules through gas hydrates, *J. Am. Chem. Soc.*, 133(6), 1870-1876, doi: 10.1021/ja108434h.
- Liang, S., D. Rozmanov, and P. G. Kusalik (2011), Crystal growth simulations of methane hydrates in the presence of silica surfaces, *Phys. Chem. Chem. Phys.*, 13(44), 19856-19864, doi: 10.1039/C1CP21810G.
- Lide, D. R. (2005), CRC Handbook of Chemistry and Physics, edited, CRC Press, Boca Raton, FL
- Lu, W., I. M. Chou, and R. C. Burruss (2008), Determination of methane concentrations in water in equilibrium with sl methane hydrate in the absence of a vapor phase by in situ Raman spectroscopy, *Geochemica et Cosmochimica Acta*, 72, 412-422.
- Machin, K. J., G. S. Begg, and N. W. Isaacs (1984), A low-temperature cooler for protein crystallography, *Journal of Applied Crystallography*, 17, 358-359.
- Makogon, Y. F. (1997), *Hydrates of Hydrocarbons*, PennWell Publishing Company, Tulsa, Oklahoma.
- Marone, F., and M. Stampanoni (2012), Regridding reconstruction algorithm for real-time tomographic imaging, *J. Synchrot. Radiat.*, 19(6), 1029-1037, doi: doi:10.1107/S0909049512032864.
- Massa, W. (2004), *Crystal Structure Determination*, Second Edition ed., Springer, Heidelberg Germany.
- Mavko, G. M., and A. Nur (1979), Wave attenuation in partially saturated rocks, *Geophysics*, 44(2), 161-178, doi: 10.1190/1.1440958.
- Max, M. D., A. H. Johnson, and W. P. Dillon (2006), *Economic Geology of Natural Gas Hydrate*, 341 pp., Springer, Dordrecht, Netherlands.
- Momose, A. (1995), Demonstration of phase-contrast X-ray computed tomography using an X-ray interferometer, *Nuclear Instruments and Methods in Physics Research Section A: Accelerators, Spectrometers, Detectors and Associated Equipment*, 352(3), 622-628.
- Monfort, J. P., and A. Nzihou (1993), Light scattering kinetics study of cyclopropane hydrate growth, *Journal of Crystal Growth*, 128(1-4, Part 2), 1182-1186, doi: [http://dx.doi.org/10.1016/S0022-0248\(07\)80120-5](http://dx.doi.org/10.1016/S0022-0248(07)80120-5).
- Mori, Y. H. (2001), Estimating the thickness of hydrate films from their lateral growth rates: application of a simplified heat transfer model, *Journal of Crystal Growth*, 223(1-2), 206-212, doi: [http://dx.doi.org/10.1016/S0022-0248\(01\)00614-5](http://dx.doi.org/10.1016/S0022-0248(01)00614-5).
- Mori, Y. H., and T. Mochizuki (1997), Mass transport across clathrate hydrate films — a capillary permeation model, *Chemical Engineering Science*, 52(20), 3613-3616, doi: [http://dx.doi.org/10.1016/S0009-2509\(97\)00169-3](http://dx.doi.org/10.1016/S0009-2509(97)00169-3).
-

-
- Mork, M., G. Schei, and R. Larsen (2000), NMR imaging study of hydrates in sediments, in: *Gas Hydrates: Challenges for the Future*, edited by G. D. Holder and P. R. Bishnoi pp. 897-905, New York Acad Sciences, New York.
- Müller, T., B. Gurevich, and M. Lebedev (2010), Seismic wave attenuation and dispersion resulting from wave-induced flow in porous rocks — A review, *Geophysics*, 75(5), 75A147-175A164, doi: doi:10.1190/1.3463417.
- Mullin, J. W. (2001), *Crystallization*, 4th ed., 600 pp., Butterworth-Heinemann, Oxford.
- Natarajan, V. (1993), *Thermodynamics and Nucleation Kinetics of Gas Hydrates* PhD, University of Calgary, Alberta.
- Ohmura, R., S. Matsuda, T. Ebinuma, and H. Narita (2005), Clathrate hydrate crystal growth in liquid water saturated with a guest substance: Observations in methane + water system, *Crystal Growth & Design*, 5(3), 953-957.
- Oksanen, E., F. Dauvergne, A. Goldman, and S. Budayova-Spano (2010), Design of a novel Peltier-based cooling device and its use in neutron diffraction data collection of perdeuterated yeast pyrophosphatase, *Journal of Applied Crystallography*, 43, 113-1120.
- Ouar, H. (1992), The formation of natural gas hydrates in water-based drilling fluids, *Chem. Eng. Res. Des.*, 70, 48-54.
- P. J. Soille, M. M. A. (1990), *Signal Processing*, 20, 171-182.
- Paulus, M. J., S. S. Gleason, S. J. Kennel, P. R. Hunsicker, and D. K. Johnson (2000), High Resolution X-ray Computed Tomography: An Emerging Tool for Small Animal Cancer Research, *Neoplasia (New York, N.Y.)*, 2(1-2), 62-70.
- Petch, N. J. (1953), The cleavage strength of polycrystals, *Journal of Iron and Steel Institute*, 174, 25-28.
- Priest, J. A., A. I. Best, and C. R. I. Clayton (2005), A laboratory investigation into the seismic velocities of methane gas hydrate-bearing sand, *Journal of Geophysical Research-Solid Earth*, 110(B4), 13, doi: 10.1029/2004jb003259.
- Priest, J. A., A. I. Best, and C. R. I. Clayton (2006), Attenuation of seismic waves in methane gas hydrate-bearing sand, *Geophys. J. Int.*, 164(1), 149-159, doi: 10.1111/j.1365-246X.2005.02831.X.
- Priest, J. A., E. V. L. Rees, and C. R. I. Clayton (2009), Influence of gas hydrate morphology on the seismic velocities of sands, *J. Geophys. Res.-Solid Earth*, 114, 13 pp, doi: 10.1029/2009jb006284.
- Rodger, P. M. (2000), Methane Hydrate: Melting and Memory, *Annals of the New York Academy of Sciences*, 912(1), 474-482, doi: 10.1111/j.1749-6632.2000.tb06802.x.
- Rodriguez Navarro, A. B., P. O.-H. Alvarez-Lloret, M., and M. Rodriguez-Gallego (2006), Automatic Crystal Size Determination in the Micrometer Range from Spotty X-Ray Diffraction Rings of Powder Samples, *Journal of American Ceramic Society*, 89(7), 2232-2238.

Roehlsberger, R. (2005), Synchrotron Radiation—Generation, Properties and Applications (Lecture-1), http://photonscience.desy.de/sites/site_photonscience/content/e62/e187741/e187759/e188006/e188007/infoboxContent188011/RR-Lecture-1_eng.pdf.

Rogers, R. E., G. Zhang, C. Kothapalli, and W. T. French (2004), Laboratory evidence of microbial-sediment-gas hydrate synergistic interactions in ocean sediments, paper presented at Proceedings of The Fourteenth International Offshore and Polar Engineering Conference, Toulon, France, May 23-28, 41-47.

Röntgen, W. C. (1895), On a New Kind of Rays, *Nature*, 53, 274-276.

Ruppel, C., and D. Noserale (2012), Gas hydrates and climate warming - Why a methane catastrophe is unlikely <http://soundwaves.usgs.gov/2012/06/>.

Saito, K., M. Kishimoto, R. Tanaka, and R. Ohmura (2010), Crystal Growth of Clathrate Hydrate at the Interface between Hydrocarbon Gas Mixture and Liquid Water, *Crystal Growth & Design*, 11(1), 295-301, doi: 10.1021/cg101310z.

Salamatin, A. N., and W. F. Kuhs (2002), Formation of porous gas hydrates, in *Proceedings of the 4th International Conference on Gas Hydrates (ICGH-4)*, edited by Y.H.Mori, pp. 766-770, Arxiv (2015arXiv151100248S), Yokohama.

Sato, M. T., Satoshi, J. Nagao, S. Jin, Y. Kamata, H. Minagawa, T. Ebinuma, and H. Narita (2005), Distribution of Hydrate Saturation Ratios in Artificial Methane Hydrate Sediments Measured by High-Speed X-Ray Computerized Tomography, *Japanese Journal of Applied Physics*, 44(1A), 473-475, doi: 10.1143/JJAP.44.473.

Scherrer, P. (1918), Bestimmung der Größe und der inneren Struktur von Kolloidteilchen mittels Röntgenstrahlen, *Nach. Ges. Wiss. Göttingen*, 98-100.

Sefidroodi, H., E. Abrahamsen, and M. A. Kelland (2013), Investigation into the strength and source of the memory effect for cyclopentane hydrate, *Chem. Eng. Sc.*, 87, 133-140, doi: 10.1016/j.ces.2012.10.018.

Seltzer, S. M., and J. H. Hubbell (1996), Tables of X-ray Mass attenuation coefficients and mass energy-absorption coefficients from 1 keV to 20 MeV for elements $Z = 1$ to 92 and 48 additional substances of dosimetric interest, <http://www.nist.gov/pml/data/xraycoef/>.

Servio, P., and P. Englezos (2001), Measurement of Dissolved Methane in Water in Equilibrium with Its Hydrate, *Journal of Chemical & Engineering Data*, 47(1), 87-90, doi: 10.1021/je0102255.

Servio, P., and P. Englezos (2003), Morphology of Methane and Carbon Dioxide Hydrates Formed from Water Droplets, *AIChE J.*, 49(1), 269-276.

Skovborg, P., H. J. Ng, P. Rasmussen, and U. Mohn (1993), Measurement of induction times for the formation of methane and ethane gas hydrates, *Chemical Engineering Science*, 48(3), 445-453, doi: 10.1016/0009-2509(93)80299-6.

Sloan, E. D., and C. A. Koh (2008), *Clathrate hydrates of natural gases*, 3rd ed., CRC Press, Taylor & Francis Group, Boca Raton, FL.

Smelik, E. A., and H. E. King (1997), Crystal-growth studies of natural gas clathrate hydrates using a pressurized optical cell, *American Mineralogist*, *82*, 88-98.

Smilgies, D.-M. (2002), Geometry-independent intensity correction factors for grazing-incidence diffraction, *Review of scientific instruments*, *73*(4), 1706-1710, doi: 10.1063/1.1461876.

Snigirev, A., I. Snigireva, V. Kohn, S. Kuznetsov, and I. Schelokov (1995), On the possibilities of x-ray phase contrast microimaging by coherent high-energy synchrotron radiation, *Review of Scientific Instruments*, *66*(12), 5486-5492, doi: <http://dx.doi.org/10.1063/1.1146073>.

Song, Y., K. Xue, J. Zhao, W. Lam, C. Cheng, M. Yang, Y. Zhang, D. Wang, W. Liu, and Y. Liu (2013), In situ observation of hydrate growth habit in porous media using magnetic resonance imaging, *EPL (Europhysics Letters)*, *101*(3), 36004.

Souza, A., J. K. Udupa, and P. K. Saha (2005), Volume rendering in the presence of partial volume effects, *Medical Imaging, IEEE Transactions on*, *24*(2), 223-235, doi: 10.1109/TMI.2004.840295.

Spangenberg, E., and J. Kulenkampff (2006), Influence of methane hydrate content on electrical sediment properties, *Geophys. Res. Lett.*, *33*(24), 5 pp, doi: 10.1029/2006gl028188.

Stampanoni, M., et al. (2006), Trends in synchrotron-based tomographic imaging: the SLS experience, paper presented at SPIE Proceedings, 6318.

Staykova, D. K., W. F. Kuhs, A. N. Salamatin, and T. Hansen (2003), Formation of porous gas hydrates from ice powders: Diffraction experiments and multistage model, *Journal of Physical Chemistry B*, *107*(37), 10299-10311, doi: 10.1021/jp027787v.

Stern, L. A., S. H. Kirby, and W. B. Durham (1996), Peculiarities of Methane Clathrate Hydrate Formation and Solid-State Deformation, Including Possible Superheating of Water Ice, *Science*, *273*(5283), 1843-1848, doi: 10.1126/science.273.5283.1843.

Stern, L. A., S. H. Kirby, and W. B. Durham (1998), Polycrystalline Methane Hydrate: Synthesis from Superheated Ice, and Low-Temperature Mechanical Properties, *Energy & Fuels*, *12*(2), 201-211, doi: 10.1021/ef970167m.

Stern, L. A., S. Circone, S. H. Kirby, and W. B. Durham (2005), SEM imaging of gas hydrate formation processes and growth textures, and comparison to natural hydrates of marine and permafrost origin, paper presented at 5th International Conference on Gas Hydrates, Trondheim, Norway, 300-310.

Stewart, K. R., and R. E. Westacott (2008), The interface between water and hydrophobic gas, *Physical Chemistry Chemical Physics*, *10*, 4614-4622.

Sugaya, M., and Y. H. Mori (1996a), Behavior of clathrate hydrate formation at the boundary of liquid water and a fluorocarbon in liquid or vapor state, *Chemical Engineering Science*, *51*, 3505-3517.

-
- Sun, C. Y., B. Z. Peng, A. Dandekar, Q. L. Ma, and G. J. Chen (2010), Studies on hydrate film growth, *Annual Reports Section "C" (Physical Chemistry)*, 106(0), 77-100, doi: 10.1039/B811053K.
- Susan, S. (2013), http://serc.carleton.edu/research_education/geochemsheets/techniques/SEM.html.
- Takeda, Y., W. Yashiro, Y. Suzuki, S. Aoki, T. Hattori, and A. Momose (2007), X-Ray Phase Imaging with Single Phase Grating, *Japanese Journal of Applied Physics*, 46(1L), L89.
- Takeya, S., W. Shimada, Y. Kamata, T. Ebinuma, T. Uchida, J. Nagao, and H. Narita (2001), In situ X-ray diffraction measurements of the self-preservation effect of CH₄ hydrate, *Journal of Physical Chemistry A*, 105(42), 9756-9759, doi: 10.1021/jp011435r.
- Talbot, H. F. (1836), LXXVI. Facts relating to optical science. No. IV, *Philosophical Magazine Series 3*, 9(56), 401-407, doi: 10.1080/14786443608649032.
- Tanaka, R., R. Sakemoto, and R. Ohmura (2009), Crystal growth of clathrate hydrates formed at the interface of liquid water and gaseous methane, ethane, or propane: variations in crystal morphology, *Cryst. Growth Des.*, 9(5), 2529-2536.
- Taylor, C. J., K. T. Miller, C. A. Koh, and E. D. Sloan (2007), Macroscopic investigation of hydrate film growth at the hydrocarbon/water interface, *Chemical Engineering Science*, 62, 6524-6533.
- Techmer, K. S., T. Heinrichs, and W. F. Kuhs (2005), Cryo-electron microscopic studies of structures and compositions of Mallik gas-hydrate-bearing samples, in: *Scientific Results from the Mallik 2002 Gas Hydrate Production Research Well Program, Mackenzie Delta, Northwest Territories, Canada*, edited by S. R. Dallimore and T. S. Collett, Geological Survey of Canada, Bulletin 585 (12 p.).
- Thompson, H., A. K. Soper, P. Buchanan, N. Aldiwan, J. L. Creek, and C. A. Koh (2006), Methane hydrate formation and decomposition: Structural studies via neutron diffraction and empirical potential structure refinement *J. Chem. Phys.*, 124, 5 pp, doi: 10.1063/1.2191056.
- Tishchenko, P., P. Hensen, and K. Wallmann (2005), Calculation of the stability and solubility of methane hydrate in seawater, *Chem. Geol.*, 219, 37-52.
- Tohidi, B., R. Anderson, M. B. Clennell, R. W. Burgass, and A. B. Biderkab (2001), Visual observation of gas-hydrate formation and dissociation in synthetic porous media by means of glass micromodels, *Geology*, 29(9), 867-870, doi: 10.1130/0091-7613(2001)029<0867:vooghf>2.0.co;2.
- Topham, D. R. (1978), Observations of the formation of hydrocarbon gas hydrates at depth in seawater "UNPUBLISHED MANUSCRIPT", <http://www.dfo-mpo.gc.ca/Library/52634.pdf>, edited by P. Bay, Institute of Ocean Sciences Sidney, British Columbia.
- Tschapek, M., C. Wasowski, and S. Falasca (1983), Character and change in the hydrophilic properties of quartz sand, *Z. Pflanz. und Bodenk.*, 146(3), 295-301, doi: 10.1002/jpln.19831460305.
- Uchida, T., T. Ebinuma, and H. Narita (2000), Observations of CO₂-hydrate decomposition and reformation processes, *Journal of Crystal Growth*, 217, 189-200.

Vatamanu, J., and P. G. Kusalik (2010), Observation of two-step nucleation in methane hydrates, *Phys. Chem. Chem. Phys.*, 12(45), 15065-15072, doi: 10.1039/c0cp00551g.

Vysniauskas, A., and P. R. Bishnoi (1983), A kinetic study of methane hydrate formation, *Chemical Engineering Science*, 38(7), 1061-1072, doi: 10.1016/0009-2509(83)80027-X.

Waite, W. F., W. J. Winters, and D. H. Mason (2004), Methane hydrate formation in partially water-saturated Ottawa sand, *Am. Min.*, 89(8-9), 1202-1207.

Waite, W. F., et al. (2009), Physical properties of hydrate-bearing sediments, *Rev. Geophys.*, 47, 38 pp, doi: 10.1029/2008rg000279.

Walsh, M. R., G. T. Beckham, C. A. Koh, E. D. Sloan, D. T. Wu, and A. K. Sum (2011), Methane hydrate nucleation rates from molecular dynamics simulations: Effects of aqueous methane concentration, interfacial curvature, and system size, *J. Phys. Chem. C*, 115(43), 21241-21248, doi: 10.1021/jp206483q.

Walsh, M. R., S. H. Hancock, S. J. Wilson, S. L. Patil, G. J. Moridis, R. Boswell, T. S. Collett, C. A. Koh, and E. D. Sloan (2009), Preliminary report on the commercial viability of gas production from natural gas hydrates, *Energy Econ.*, 31(5), 815-823, doi: 10.1016/j.eneco.2009.03.006.

Watanabe, S., K. Saito, and R. Ohmura (2011), Crystal Growth of Clathrate Hydrate in Liquid Water Saturated with a Simulated Natural Gas, *Crystal Growth & Design*, 11(7), 3235-3242, doi: 10.1021/cg2005024.

Wei, Z., S. Wiebe, and D. Chapman (2013), Ring artifacts removal from synchrotron CT image slices, *Journal of Instrumentation*, 8(06), C06006.

Wernick, M. N., O. Wirjadi, D. Chapman, Z. Zhong, N. P. Galatsanos, Y. Yang, J. G. Brankov, O. Oltulu, M. A. Anastasio, and C. Muehleman (2003), Multiple-image radiography, *Physics in Medicine and Biology*, 48(23), 3875.

Wilkins, S. W., T. E. Gureyev, D. Gao, A. Pogany, and A. W. Stevenson (1996), Phase-contrast imaging using polychromatic hard X-rays, *Nature*, 384(6607), 335-338.

Wilson, P. W., and A. D. J. Haymet (2010), Hydrate formation and re-formation in nucleating THF/water mixtures show no evidence to support a "memory" effect, *Chem. Eng. J.*, 161, 146-150, doi: 10.1016/j.cej.2010.04.047.

Wood, I. G., N. J. Hughes, F. Browning, and A. D. Fortes (2012), A compact, transportable, thermoelectrically cooled cold stage for reflection geometry X-ray powder diffraction, *Journal of Applied Crystallography*, 45, 608-610.

Wu, Q., and B. Zhang (2010), Memory effect on the pressure-temperature condition and induction time of gas hydrate nucleation, *Natural Gas Chemistry*, 19, 446-451, doi: 10.1016/S1003-9953(09)60086-4.

Yeon, S.-H., J. Seol, D.-Y. Koh, Y.-j. Seo, K.-P. Park, D.-G. Huh, J. Lee, and H. Lee (2011), Abnormal methane occupancy of natural gas hydrates in deep sea floor sediments, *Energy Environ. Sci.*, 4(2), 421-424, doi: 10.1039/c0ee00355g.

Yun, T. S., F. M. Francisca, J. C. Santamarina, and C. Ruppel (2005), Compressional and shear wave velocities in uncemented sediment containing gas hydrate, *Geophys. Res. Lett.*, 32(10), 5 pp, doi: 10.1029/2005gl022607.

Zatsepina, O. Y., and B. A. Buffett (1997), *Geophys. Res. Lett.*, 24, 1567.

Zatsepina, O. Y., D. Riestenberg, S. D. McCallum, M. Gborigi, C. Brandt, B. A. Buffett, and T. J. Phelps (2004), Influence of water thermal history and overpressure on CO₂-hydrate nucleation and morphology, *Am. Mineral.*, 89, 1254-1259.

Zehbe, R., A. Haibel, F. Schmidt, H. Riesemeier, K. C. J., H. Schubert, and C. Brochhausen (2010), High Resolution X-Ray Tomography - 3D Imaging for Tissue Engineering Applications, in *Tissue-engineering*, edited, InTech.

Zhang, Q., F. G. Li, C. Y. Sun, Q. P. Li, X. Y. Wu, B. Liu, and G. J. Chen (2011), Compressional wave velocity measurements through sandy sediments containing methane hydrate, *Am. Mineral.*, 96(10), 1425-1432, doi: 10.2138/am.2011.3681.

Zhang, Z., D. McConnell, and Q. Yao (2014), Seismic Amplitudes and attenuations of gas hydrate-bearing sediments in fractured and sand reservoirs, paper presented at 8th International Conference on Gas Hydrates Beijing, China.

Zhao, J., L. Yao, Y. Song, K. Xue, C. Cheng, Y. Liu, and Y. Zhang (2011), In situ observations by magnetic resonance imaging for formation and dissociation of tetrahydrofuran hydrate in porous media, *Magnetic Resonance Imaging*, 29(2), 281-288, doi: <http://dx.doi.org/10.1016/j.mri.2010.08.012>.

9 | Appendices

Appendix A: Absorption calculations for individual media using the Beer-Lambert law: $I = I_0 e^{-D(\mu/\rho)}$

Appendix B: Recorded pressure curves

Appendix C: Calculations of the S_2 scale factor using structure factors determined using Powder cell program for each compound.

Appendix D: Exemplary CSD determination of Xe hydrate

Appendix E: Accepted Publication (Author Proof)

Appendix A: Absorption calculations for individual media using the Beer-Lambert law: $I = I_0 e^{-\rho(\mu/\rho) t}$

1) Polyethylenimine - single wall	weight fraction (M_i/M_{total})	μ/ρ (cm ² /g)	ρ (g/cm ³)	t: thickness (cm)	Absorption
Hydrogen	0.116	0.367	0.089		
Nitrogen	0.326	0.555	1.33		
Carbon	0.558	0.402	2.267		
Total (C ₂ H ₅ N) _n	1.000	0.448	1.03	0.3	0.129

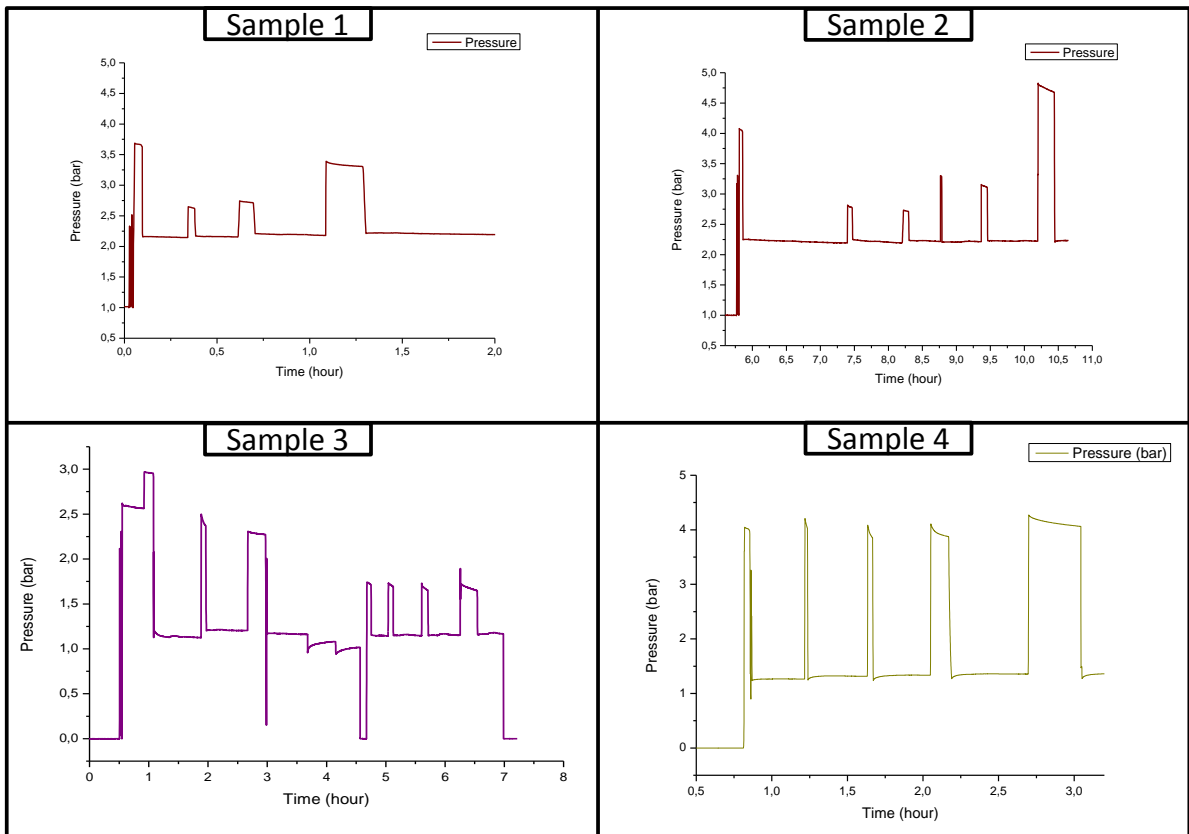
2) Xenon gas - single wall	Pressure (bar)	μ/ρ (cm ² /g)	ρ (g/cm ³)	t (cm)	Absorption
	2	23.002	0.011	0.08	0.021

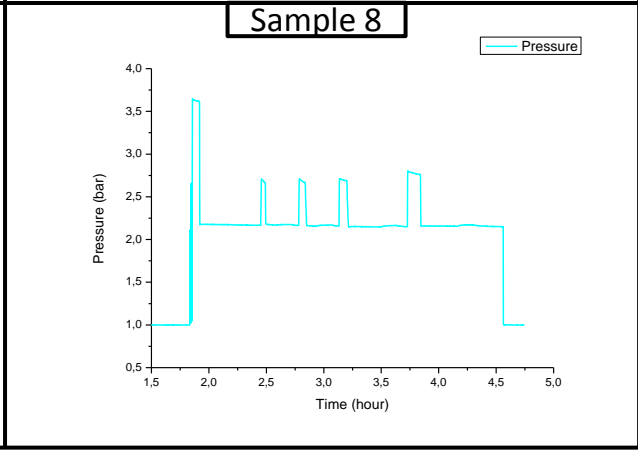
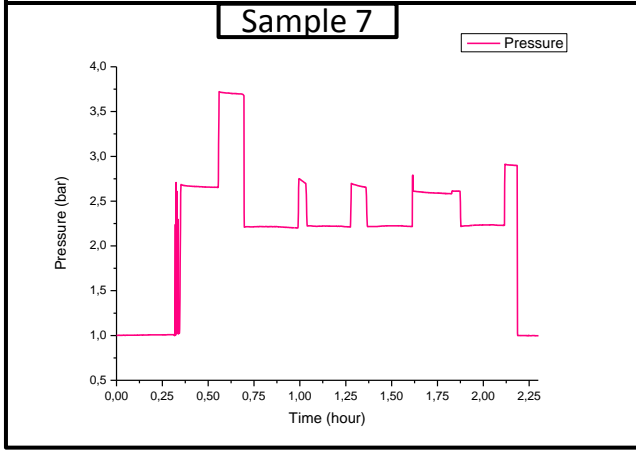
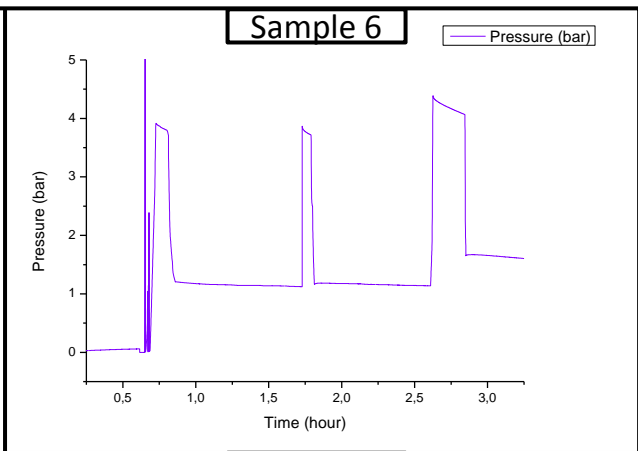
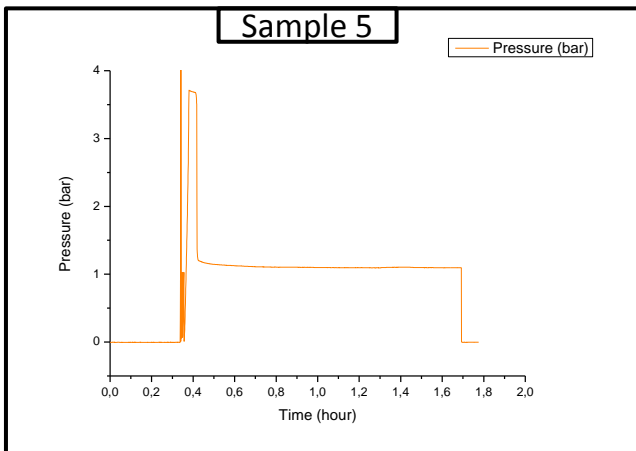
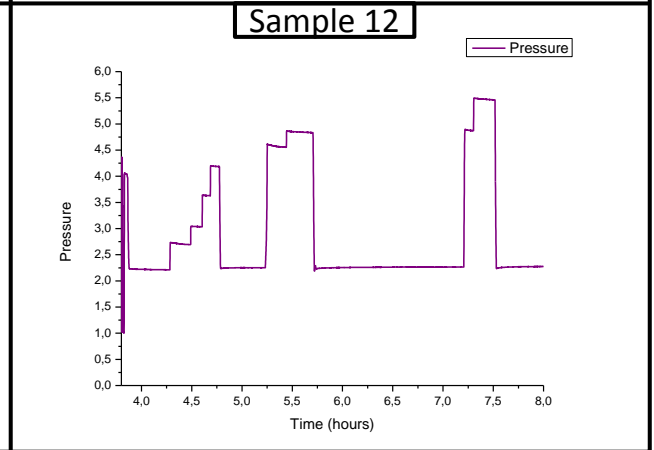
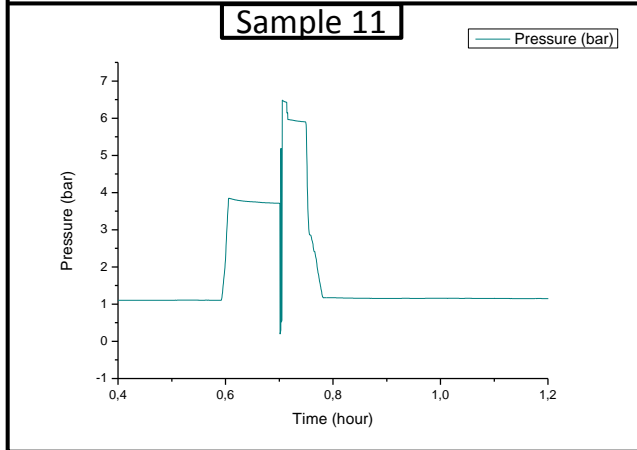
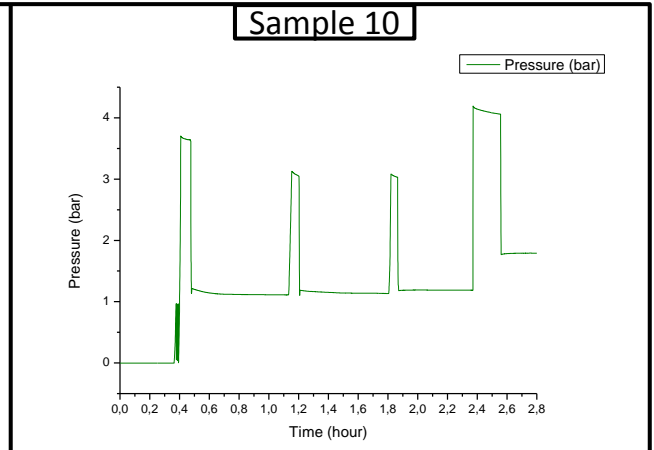
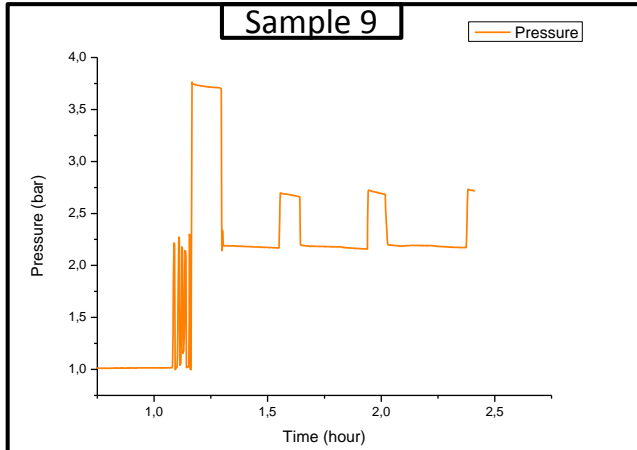
3) Aluminium - single wall	μ/ρ (cm ² /g)	ρ (g/cm ³)	t (cm)	Absorption
	3.441	2.7	0.03	0.1951

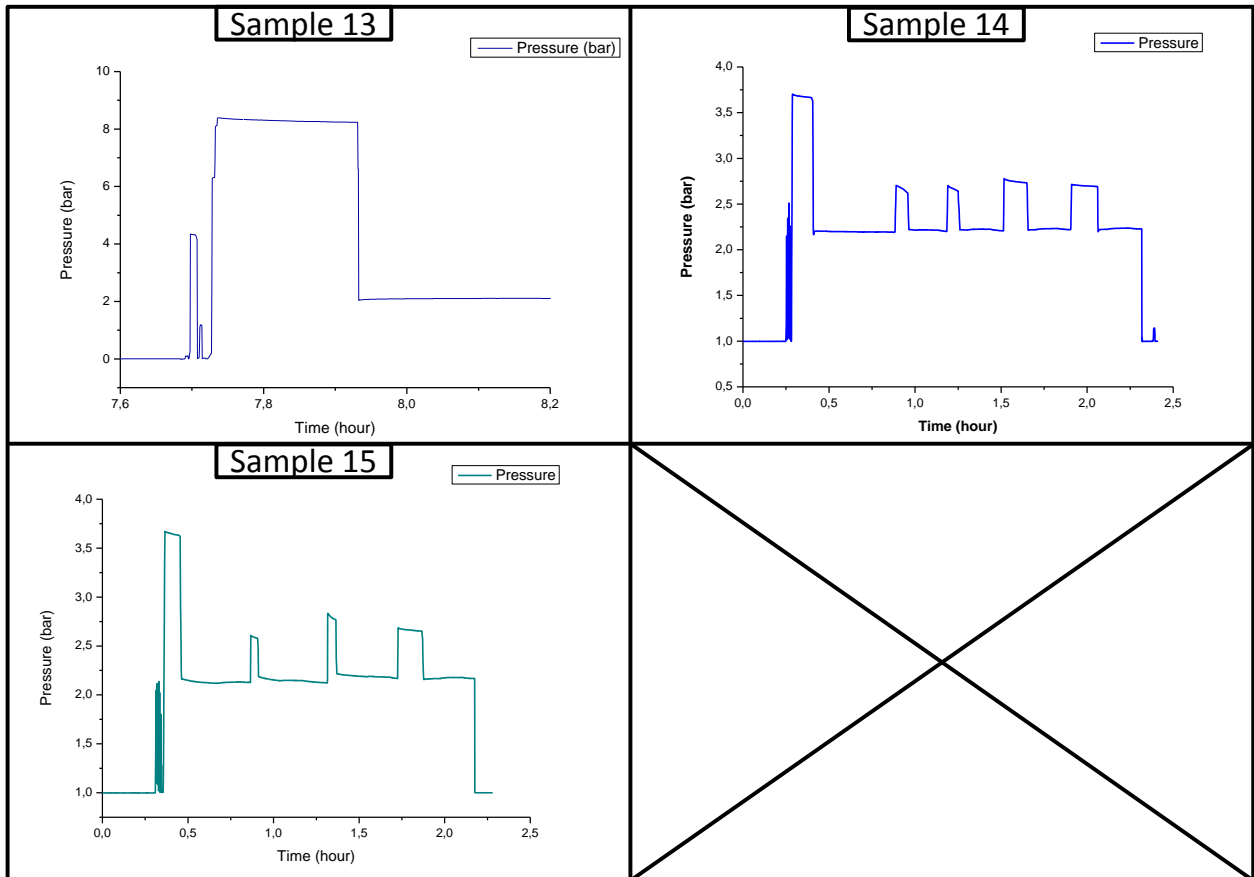
4) Sample - thickness: 0.2 cm	filling	μ/ρ (cm ² /g)	ρ (g/cm ³)	t (cm)	Absorption
Quartz sand	60%	2.544	1.2	0.120	0.411
water	10%	0.81	1	0.020	0.014
Xenon gas (at 3 bar)	30%	23.002	0.011	0.060	0.023

Xenon hydrate	weight fraction (M_i/M_{total})	μ/ρ (cm ² /g)	ρ (g/cm ³)	t (cm)	Absorption
Hydrogen	0.052	0.370			
Oxygen	0.415	0.865			
Xenon	0.533	23.002			
Total (46(H ₂ O)8Xe)	1.000	12.640	1.712	0.020	0.351

Appendix B: Recorded pressure curves







Appendix C: calculations of the S_2 scale factor using structure factors determined using Powder cell program for each compound.

- LaB₆:**

CELL	4.1566	4.1566	4.1566	90.000	90.000
90.000					
La	57	0.0000	0.0000	0.0000	1.0000
1.0000					
B	5	0.1996	0.5000	0.5000	0.9720
1.0000					
RGNR 221					

- Xenon Hydrate:**

The xenon-clathrate (type I) fractional coordinates, isotropic thermal factors (U_{iso}), fractional occupancies (Occ) and crystallographic site for the data set collected on D2B @ILL at 7 bar and 273 K. e.s.d.s are quoted in parentheses.

Atoms	x	y	z	U_{iso} (\AA^2)	Occ	Site
O(1)	0.1837(2)	0.1837(2)	0.1837(2)	0.042	1.0000	16i
O(2)	0.0000	0.3098(2)	0.1158(2)	0.047	1.0000	24k
O(3)	0.0000	0.5000	0.2500	0.043	1.0000	6c
D(4)	0.2326	0.2326	0.2326	0.053	0.5000	16i
D(5)	0.0000	0.4337	0.2027	0.061	0.5000	24k
D(6)	0.0000	0.3798	0.1589	0.055	0.5000	24k
D(7)	0.0000	0.3132	0.0356	0.055	0.5000	24k
D(8)	0.0659	0.2660	0.1402	0.049	0.5000	48l
D(9)	0.1196	0.2279	0.1596	0.052	0.5000	48l
XE(10)	0.0000	0.0000	0.0000	0.056	0.85(1)	2a
XE(11)	0.5000	0.0000	0.2500	0.101	0.9700	6c

Appendix D:

This Appendix shows the results of the reanalysis including the rejection criteria based on the moments of the omega scan profiles. These rejection criteria were introduced to eliminate odd-shaped reflections e.g. as a consequence of accidental overlap. Still, the crystal sizes calculated from different hkl reflections were not consistent and the number of peaks found did not much the multiplicity number because of (1) the cut-off for the case of small crystallites for the weaker reflections and (2) a remaining problem of overlap for the case of the 321 hkl with its highest multiplicity.

The CSDs plotted below show a systematic shift of the CSD of the 200, 210 and 211 to higher values because of the cut-off of small crystals.

The table illustrates these discrepancies between the individual results, in particular how the numbers of peaks found in each reflection do not match the expected ratios of multiplicities.

The list of the moments used is given below (source: Origin Lab software):

- Second moment:

$$s = \sqrt{\sum_{i=1}^n w_i (x_i - u)^2 / d}$$

- Third moment (skewness):

$$\gamma_1 = \frac{n}{(n-1)(n-2)} \sum_{i=1}^n w_i^{\frac{3}{2}} \left(\frac{x_i - \bar{x}}{s} \right)^3$$

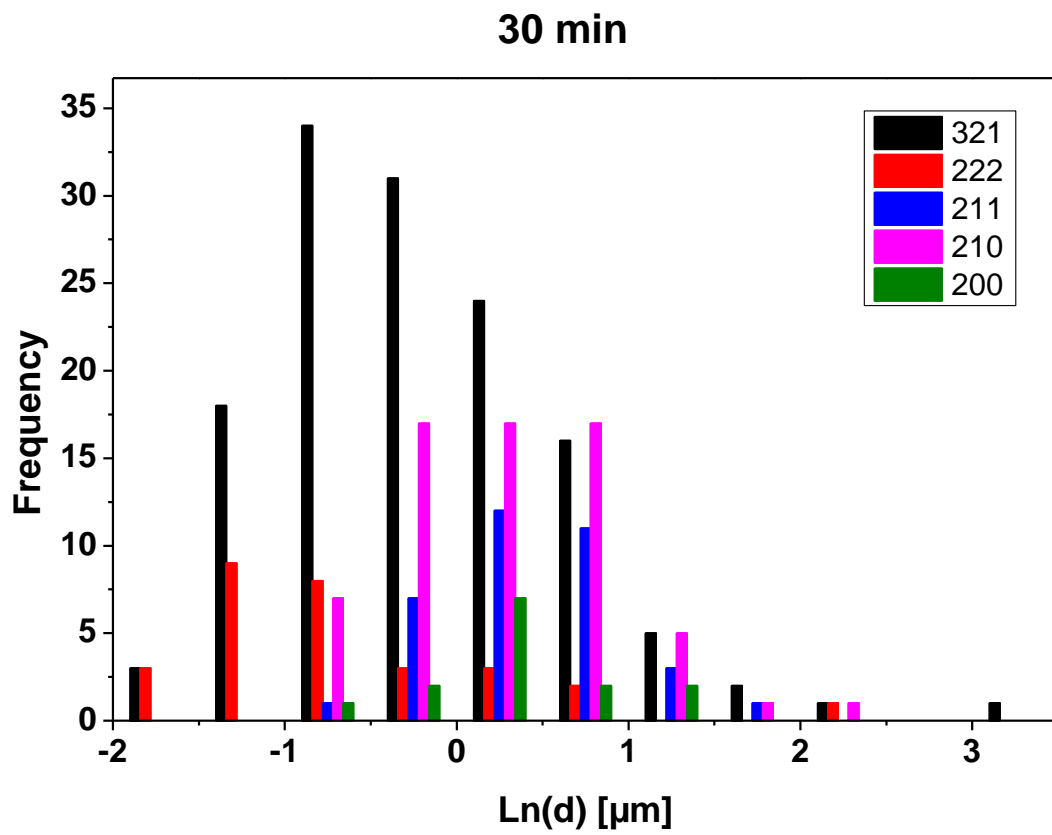
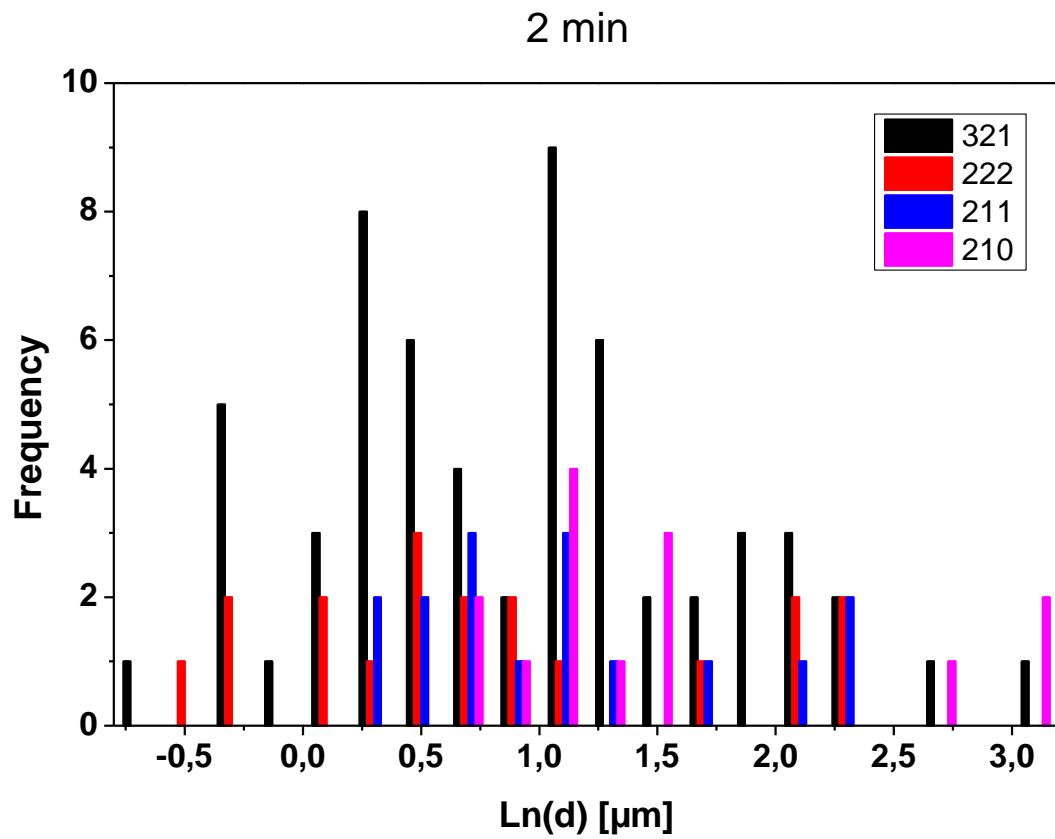
- Fourth moment (kurtosis):

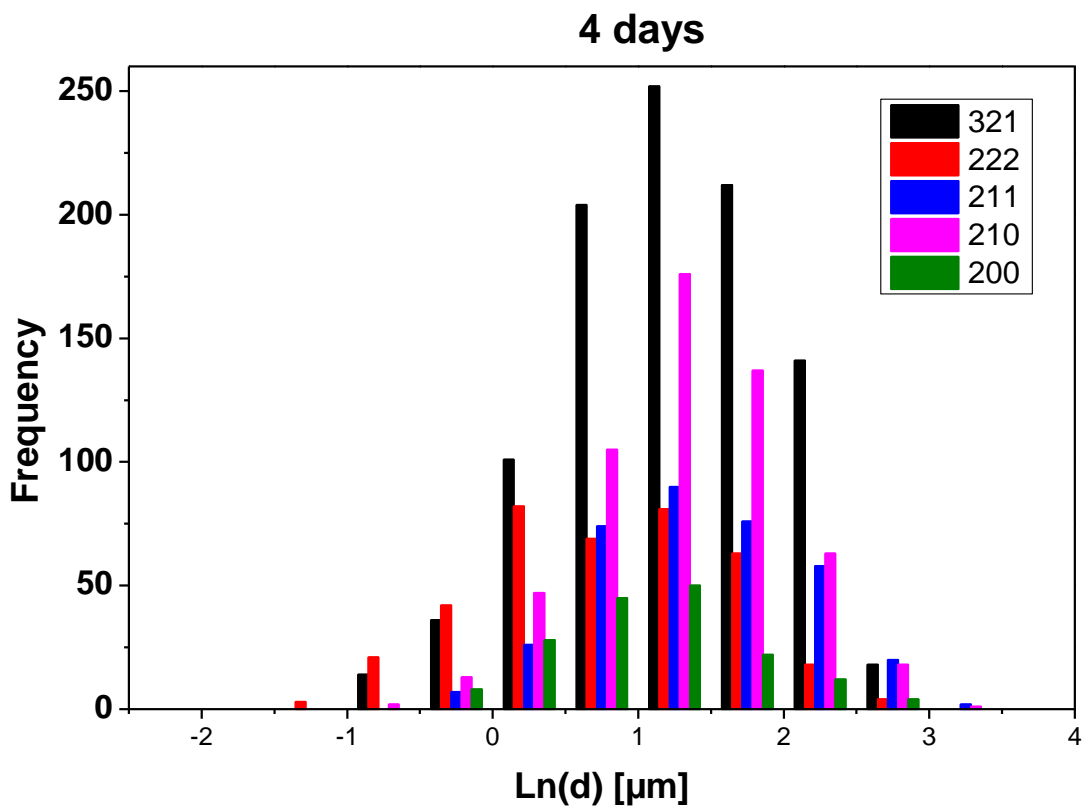
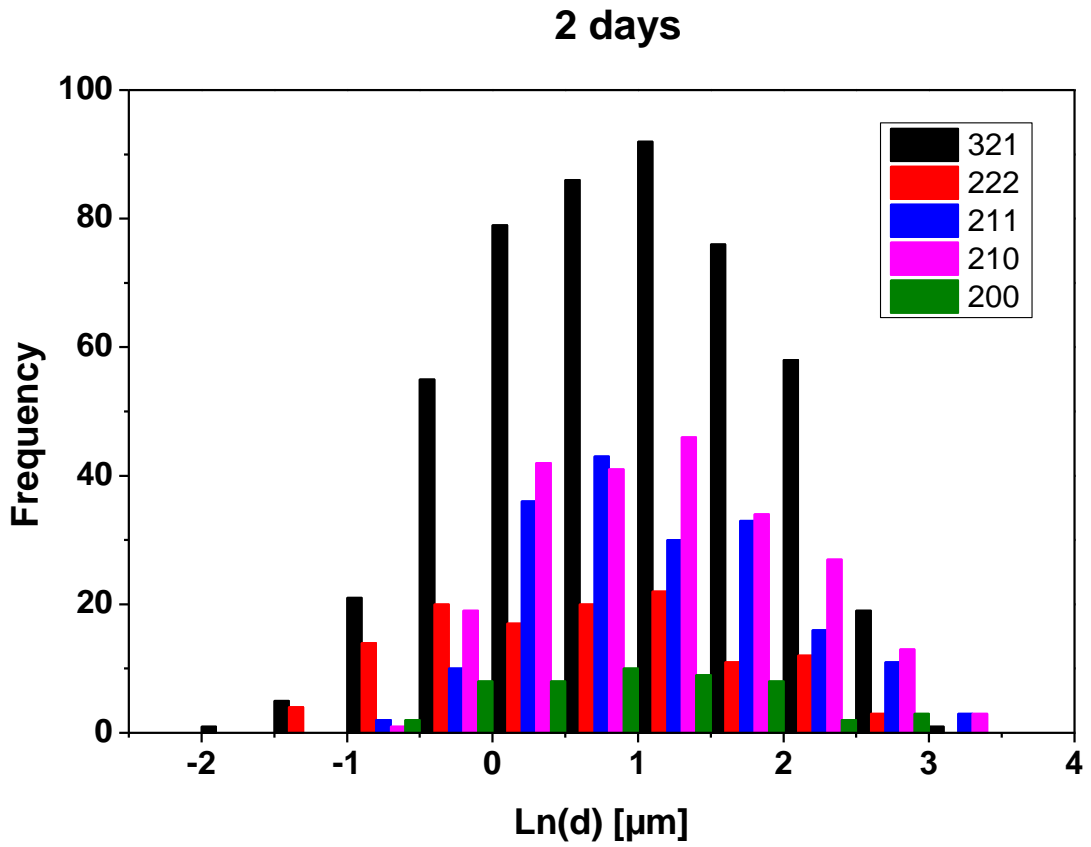
$$\gamma_2 = \frac{n(n+1)}{(n-1)(n-2)(n-3)} \sum_{i=1}^n w_i^2 \left(\frac{x_i - \bar{x}}{s} \right)^4 - \frac{3(n-1)^2}{(n-2)(n-3)}$$

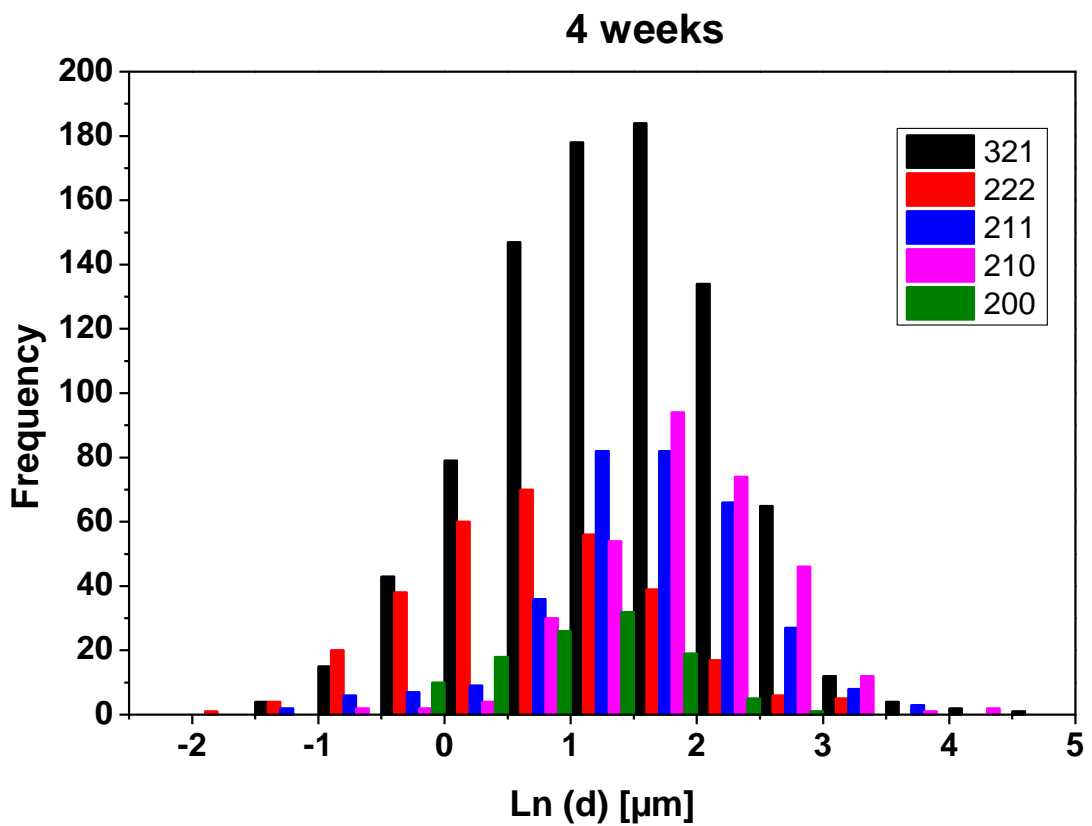
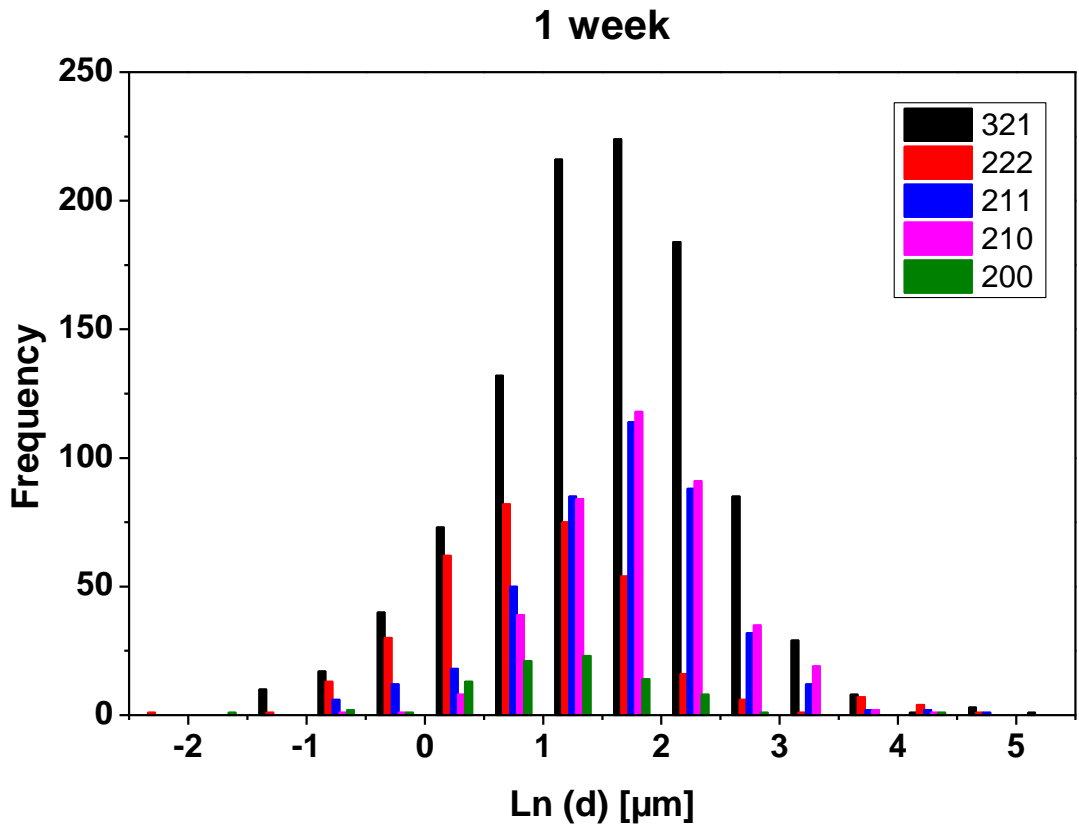
n: number of observations

d = n-1

wi: weighted fraction







Summary of the first analyzed CSDs which were done not with the appropriate thresholding as in Table 6-4. Due to the cut off, the average size of weak reflections is shifted to higher values. The number of peaks found per reflection does not match the multiplicity factor.

		N		Mean	Std. Dev.	mean Ln(d)	Std. Dev	Median
		N total	N final					
2 min	321	110	59	3,58	3,74	0,92	0,83	0,84
	222	26	19	3,24	2,94	0,82	0,86	0,72
	211	152	16	3,75	2,92	1,09	0,67	0,96
	210	25	14	6,78	7,27	1,53	0,82	1,22
30 min		N		Mean	Std. Dev.	mean Ln(d)	Std. Dev	Median
		N total	filtered					
	321	354	135	1,22	2,08	-0,21	0,78	-0,32
	222	92	29	0,94	1,87	-0,67	0,90	-0,93
	211	97	35	1,66	1,02	0,36	0,55	0,40
	210	107	65	1,68	1,37	0,30	0,64	0,24
2 days		N		Mean	Std. Dev.	mean Ln(d)	Std. Dev	Median
		N total	filtered					
	321	807	493	4,01	3,75	0,98	0,93	0,99
	222	185	123	3,25	3,61	0,66	1,02	0,64
	211	331	184	4,90	4,60	1,14	0,83	1,05
	210	377	226	4,66	4,64	1,14	0,89	1,09
4 days		N		Mean	Std. Dev.	mean Ln(d)	Std. Dev	Median
		N total	filtered					
	321	2281	978	4,37	3,00	1,24	0,72	1,26
	222	915	383	3,04	2,49	0,80	0,81	0,81
	211	1008	353	5,12	3,74	1,40	0,69	1,40
	210	1174	562	4,53	2,98	1,31	0,65	1,31
1 week		N		Mean	Std. Dev.	mean Ln(d)	Std. Dev	Median
		N total	filtered					
	321	2172	1023	6,93	9,68	1,50	0,93	1,55
	222	685	353	5,12	10,75	1,00	0,96	0,91
	211	888	422	7,25	8,28	1,63	0,84	1,69
	210	828	399	7,74	6,54	1,80	0,69	1,77
4 weeks		N		Mean	Std. Dev.	mean Ln(d)	Std. Dev	Median
		N total	filtered					
	321	1593	868	5,86	6,77	1,38	0,89	1,43
	222	528	316	3,29	3,85	0,76	0,91	0,75
	211	640	329	7,62	15,90	1,62	0,85	1,65
	210	589	321	8,17	6,67	1,85	0,73	1,85
200	183	111	3,31	2,23	0,99	0,65	1,02	

Appendix E: Published work

AGU PUBLICATIONS



Geochemistry, Geophysics, Geosystems

RESEARCH ARTICLE

10.1002/2015GC005811

Key Points:

- In situ gas hydrate growth in sediments observed with submicron tomography
- A water layer is commonly observed between quartz grains and gas hydrates
- Growth patterns starting from gas-enriched and juvenile water are different

Supporting Information:

- Supporting Information S1

Correspondence to:

W. F. Kuhs,
wkuhs1@gwdg.de

Citation:

Chaouachi, M., A. Falenty, K. Sell, F. Enzmann, M. Kersten, D. Haberthür, and W. F. Kuhs (2015), Microstructural evolution of gas hydrates in sedimentary matrices observed with synchrotron X-ray computed tomographic microscopy, *Geochem. Geophys. Geosyst.*, 16, 1711–1722, doi:10.1002/2015GC005811.

Received 12 MAR 2015

Accepted 8 MAY 2015

Accepted article online 15 MAY 2015

Published online 12 JUN 2015

© 2015. American Geophysical Union.
All Rights Reserved.

Microstructural evolution of gas hydrates in sedimentary matrices observed with synchrotron X-ray computed tomographic microscopy

Marwen Chaouachi¹, Andrzej Falenty¹, Kathleen Sell², Frieder Enzmann², Michael Kersten², David Haberthür³, and Werner F. Kuhs¹

¹GZG Abt. Kristallographie, Georg-August-Universität Göttingen, Göttingen, Germany, ²Geosciences Institute, Johannes Gutenberg-University, Mainz, Germany, ³X-Ray Tomography Group, Swiss Light Source, Paul Scherrer Institute, Villigen, Switzerland

Abstract The formation process of gas hydrates in sedimentary matrices is of crucial importance for the physical and transport properties of the resulting aggregates. This process has never been observed in situ at submicron resolution. Here we report on synchrotron-based microtomographic studies by which the nucleation and growth processes of gas hydrate were observed at 276 K in various sedimentary matrices such as natural quartz (with and without admixtures of montmorillonite type clay) or glass beads with different surface properties, at varying water saturation. Both juvenile water and metastably gas-enriched water obtained from gas hydrate decomposition was used. Xenon gas was employed to enhance the density contrast between gas hydrate and the fluid phases involved. The nucleation sites can be easily identified and the various growth patterns are clearly established. In sediments under-saturated with juvenile water, nucleation starts at the water-gas interface resulting in an initially several micrometer thick gas hydrate film; further growth proceeds to form isometric single crystals of 10–20 μm size. The growth of gas hydrate from gas-enriched water follows a different pattern, via the nucleation in the bulk of liquid producing polyhedral single crystals. A striking feature in both cases is the systematic appearance of a fluid phase film of up to several micron thickness between gas hydrates and the surface of the quartz grains. These microstructural findings are relevant for future efforts of quantitative rock physics modeling of gas hydrates in sedimentary matrices and explain the anomalous attenuation of seismic/sonic waves.

1. Introduction

The microstructure of natural gas hydrates (GH) dispersed in sedimentary matrices is largely unknown. In only a few occasions have samples been retrieved from sea-floor or subpermafrost occurrences without major alterations due to partial decomposition. A notable exception is the JAPEX/JNOC/GSC Mallik 5L-38 research well from which largely intact sediment-GH-aggregates were successfully recovered [Techmer *et al.*, 2005]. Even then, insight into the microstructure might be hampered by the fact that the recovered samples were usually stored in liquid nitrogen which freezes liquid water present in the sample – possibly altering the microstructure and obscuring details of the GH-sediment interface. Largely unperturbed samples can be expected from pressure-cored samples [Abegg *et al.*, 2008; Konno *et al.*, 2015; Santamarina *et al.*, 2012, 2015; Yoneda *et al.*, 2013] but access to microstructural information on a submicron scale has not been obtained so far. A number of researchers have attempted to emulate the nucleation and growth of gas hydrate in sedimentary matrices via laboratory experiments to obtain the material properties as a function of the saturation of GH in order to support geophysical exploration methods [Berge *et al.*, 1999; Best *et al.*, 2010, 2013; Dai *et al.*, 2012; Dvorkin *et al.*, 2003; Ecker *et al.*, 2000; Hu *et al.*, 2010; Li *et al.*, 2011; Priest *et al.*, 2006, 2009; Spangenberg and Kulenkampff, 2006; Yun *et al.*, 2005; Zhang *et al.*, 2011]. Other studies were devoted to better understanding the origin of the unexpected seismic attenuation [Best *et al.*, 2010; Guerin and Goldberg, 2005; Matsushima *et al.*, 2015; Priest *et al.*, 2006]. Providing a complete list of references is beyond the scope of the current paper; for reviews of these works see Hu *et al.* [2013] and Waite *et al.* [2009]. It appears that both GH saturation and distribution in the sediment affect seismic and electric responses, as well as other material properties and cannot be fully disentangled without detailed

knowledge of the microstructure at submicron scale. The abovementioned studies have also revealed that the chosen growth procedure is likely to affect the microstructural arrangement of GH in sediments [Priest *et al.*, 2009; Waite and Spangenberg, 2013] and thus the physical properties, yet details of the microstructures were unknown.

Studies at the pore-scale can help to reveal mechanisms of GH formation/dissociation and guide efforts to incorporate experimental observations to the continuum scale simulations after performing an appropriate upscaling of the parameters involved. Experimental works examining GH at the pore scale were reported by a number of researchers. Some insight into gross features of the microstructure has been gained in particular by modern imaging methods. Nuclear Magnetic Resonance Imaging (MRI) has been used to study the growth and distribution of GH in sedimentary matrices produced in the laboratory [Bagherzadeh *et al.*, 2011; Kossel *et al.*, 2013; Mork *et al.*, 2000]. These studies do not find any support for a nucleation of GHs on the surface of quartz grains, yet the limited resolution does not allow a more detailed access of microstructural details. Notable work to study GH nucleation, growth and dissociation by using optical microscopy on glass micromodels was conducted by Tohidi *et al.* [2001]; similar work is presented in Katsuki *et al.* [2007]. They were the first to provide time-lapse information on GH formation mechanisms suggesting GH formation in the water and not at the hydrophilic glass surface. However, both studies were limited by an essentially 2D configuration due to the micromodel experimental approach. Also, natural and laboratory grown GHs have been studied with *ex situ* cryo-scanning-electron-microscopy [e.g., Bohmann *et al.*, 2007; Kuhs *et al.*, 2000; Stern *et al.*, 2011], a well-established method with submicron resolution. However, a possible risk of alterations during recovery and the difficulty to distinguish frozen water from methane GH hampered an unequivocal characterization of the sediment-GH contact. Similar issues have been encountered in studies of cryopreserved natural gas hydrates in their sedimentary matrix with the *ex situ* high resolution synchrotron radiation X-ray tomography (SRXCT) used [Klapp *et al.*, 2012; Murshed *et al.*, 2008]. Other attempts to gain 3-D information on microstructures of natural [Abegg *et al.*, 2007; Rees *et al.*, 2011] and laboratory grown GH [Jin *et al.*, 2006; Kneafsey *et al.*, 2007; Sato *et al.*, 2005; Seol and Kneafsey, 2011] by means of conventional computed X-ray tomography typically suffered from the insufficient resolution of the sediment-GH contact and low X-ray contrast between methane-bearing GH and water. Recent microtomographic observations circumvent the latter issue by spiking the water with a heavy element salt solution (5 % BaCl₂) [Kerker *et al.*, 2014]. The authors provided evidence that the host medium (glass spheres) and the GH that was formed in a pressurized aluminum cell were separated by an aqueous layer. However, this is largely self-evident due to the salting-out effect of the BaCl₂ brine in a closed laboratory system; in marine environments the brine resulting from GH formation may eventually become diluted by contacts with sea water. In the following, we report on the first *in situ* time-lapse SRXCT study of the nucleation and growth of xenon-bearing GH in a sedimentary matrix (quartz grains) with a pixel resolution down to a few 100 nm. The heavy xenon gas was used to enhance the contrast between the GH and the aqueous phase without loading the latter with any salt.

2. Experimental

The formation of gas hydrates was investigated *in situ* at the TOMCAT beamline, Swiss Light Source (SLS), Paul Scherrer Institute (PSI) in Villigen (Switzerland) [Stampanoni *et al.*, 2006]. For each tomogram, 3201 (or 1501) projections at an integration time of 150 ms (or 350 ms) each were acquired over a sample rotation of 180° with a monochromatic X-ray beam energy of 21.9 keV. Two different objectives (UPLAPO10× or UPLAPO20×) with an optical 10× or 20× magnification were used, respectively. After penetrating the sample, X-rays were converted into visible light by a 20 μm thick scintillator LuAG:Ce and captured by a high-resolution CCD camera (2048×2048 pixels). The data were reconstructed by a gridded Fourier transform-based algorithm [Marone and Stampanoni, 2012]. This results in data sets with an isometric voxel size of 740 and 380 nm for the 10× and 20× magnifications, respectively, which enables the distinction between gas, water, sediment grains and hydrate in particular for interfacial areas of the sample. In order to enhance the absorption contrast, methane was substituted by xenon gas. As shown in Table S1, methane and xenon have similar properties, in particular concerning the aqueous gas solubility.

The experimental series have been performed with three sedimentary matrices composed of (a) pure natural quartz sand (Qz), (b) natural quartz sand with a small quantity of montmorillonite clay particles

(Qz+Mm), and (c) glass beads (GB) of 150–212 μm in diameter (Sigma-Aldrich, Germany). Quartz sand with a uniform grain size of 200–300 μm originating from Lyubertsy (Moscow region, Russia), and montmorillonite from Dzhebel (Turkmenistan); further sedimentological details are given in *Chuvilin et al.* [2011]. Moreover, in separate experiments, surfaces of quartz and glass beads have been modified to study the effects of hydrophobic and hydrophilic surfaces on the GH microstructures. The hydrophilic treatment consists of cleaning the porous media for 1 h using a freshly prepared Piranha solution (3:1 H_2SO_4 (98 %)/ H_2O_2 (30%)) at 90°C, rinsing with deionized water and drying in a clean oven at 120°C for 1 h. The hydrophobic properties have been obtained via a salinization process using a solution of trimethylethoxysilane at 90°C for 1 h, rinsing with deionized water and drying at 120°C [*Jradi et al.*, 2011].

Sediments have been mixed with ice (10–20 wt.-%) or Xe-hydrate powder (20 wt.-%) in a mortar under liquid nitrogen to a predefined degree of water saturation. A homogenous distribution of water in pore spaces has been obtained by (a) admixing fine particles of frost prepared by a condensation of water vapor on a precooled rotating copper disk [*Falenty et al.*, 2011; *Klapproth et al.*, 2007] or (b) admixing water-containing Xe-hydrate powder that was formed from ice spheres and ground under liq.N_2 following the procedure in [*Kuhs et al.*, 2006].

Water frost and Xe-hydrate bearing sediments were used to explore three specific scenarios of hydrate formation:

- I. Formation from deionized, juvenile water;
- II. Formation from Xe-enriched water obtained from in situ formed (scenario I) and subsequently decomposed Xe-hydrate ("memory water");
- III. Formation from Xe-enriched water obtained from the in situ dissociation of Xe-hydrate powder admixed to the sediment.

In scenario II the GH formed was dissociated by reducing the pressure. This was done in steps to follow the process by tomography; for each tomographic scan the sample was brought back up to the stability limit (0.22 MPa) to maintain a stable configuration. In the first step the pressure was dropped to 0.1 MPa for a minute, in the following two steps the pressure was reduced to ~ 0.195 MPa and left there for about 30 min; the final dissociation step at 0.1 MPa lasted 7 min. For scenario III, the initial GH and sediment mixture was dissociated at 0.1 MPa while the temperature was slowly approaching 276 K. Thus, the main difference between procedure II and III is that in the former decomposition was done at constant temperature by dropping the pressure, while in the latter the sample was dissociated by heating at constant pressure.

For all runs, a portion of the homogenized starting material (sediment + ice/hydrate) was filled under liq.N_2 into a pure aluminum sample holder with an inner diameter of 2 mm and a length of 10 mm and subsequently manually compacted. The holder is mounted onto a central aluminum cylinder and sealed with a transparent polyethylenimide dome. The ambient atmosphere in the closed volume is replaced via several compression and decompression cycles with pure Xe gas while staying below the thermodynamic stability boundary of Xe-hydrate. Thermal equilibration is reached within a few minutes. Cooling is achieved by a Peltier element mounted with its cold side to the base of the cell and its hot side in contact with a rectangular water jacket. The temperature of the sample is actively controlled via a PID controller with long term stability within $\pm 0.1^\circ\text{C}$. In order to avoid potential mechanical vibrations of the setup, water flows gravitationally through the cooling block. The pressure inside the cell is measured with an ASHCROFT KXD pressure sensor and the data were recorded every 5 s on a computer. A schematic drawing of the pressure cell is shown in supporting information Figure S1.

After thermal equilibration was reached at a constant temperature of 276 K, the first tomographic scan was recorded to verify the homogeneity of the mineral matrix and initial water distribution for each sample. As some inhomogeneity was frequently observed over the scanned volume we consider only the local water saturation in the following discussion (W_s , fraction of pore filling by water at the scan position). The reaction is started by elevating the pressure in the cell to 0.35–0.60 MPa. The pressure is controlled by the amount/volume of Xe gas injected. There was no confining pressure applied to the sediment matrix. A rapid drop of pressure marks the beginning of the nucleation and growth of Xe-hydrate crystals (supporting information Figure S2). In case of juvenile water (scenario I), this stage is preceded by an incubation period of typically 3–4 min. The formation with Xe-enriched water (scenarios II and III) was nearly instantaneous. Prior to each

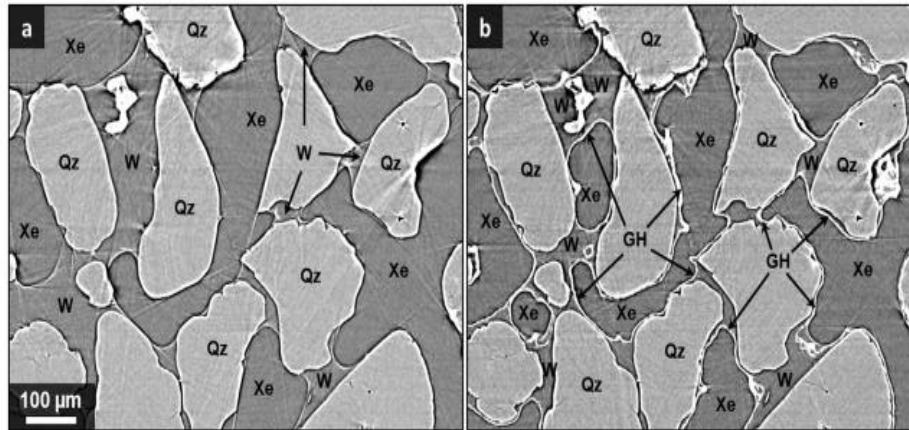


Figure 1. Nucleation of a thin GH film at the gas-water interface for GH formation using procedure I. (Sample 1, $W_s = 20\%$): (a) CT image before starting GH formation, (b) CT image taken after a reaction time of 70 s ($t_R = 70$ s). Gas hydrate (GH) in white, water (W) and xenon (Xe) in gray, quartz, sand (Qz) in light gray. Gas and juvenile water have almost the same contrast and can be distinguished only by the meniscus which separates the two phases.

tomographic scan the reaction was paused by a fast depressurization to an equilibrium pressure of 0.22 MPa at 276 K (established experimentally). After the scan, the pressure was raised again to continue the transformation as shown in supporting information Figure S3. The start-pause approach allows for capturing the very early stages of hydrate formation in terms of full three-dimensional tomographic information. This procedure can be repeated as many times as desired; typically between 3 and 7 scans were taken for one growth/nucleation event following the initial state (no hydrate) to the full-transformed state.

3. Nucleation and Growth

Our time-resolved investigations leave very little doubt that the most favorable site for GH nucleation in juvenile water (scenario I) is the interface between water and xenon gas; a typical example (out of very many) is shown in Figure 1. Our time resolution together with a submicron spatial resolution allows us to even state this in the case of low water saturations where water is concentrated on the surface of quartz grains. The resulting GH film appears to have a different gray-scale compared to dense GH but it is difficult to quantify this due to reconstruction artifacts of the rather thin films. Absorption differences might be expected due to a porosity of the film on a micron and submicron scale as observed in GH at the gas-water interface [Davies *et al.*, 2010]; this is in line with a suggestion that gas and water transport occurs *via* those pores from the gas phase toward liquid water [Mori and Mochizuki, 1997]. The thickening of the film is observed predominantly in the direction of the water phase, which suggest that the gas transport through the pores is the dominant process. After a few minutes the film consists of micron-sized single crystals as suggested by the emerging polyhedral shapes (Figure 2). Some of these accumulated crystals appear to grow faster than others. These larger crystals also show an appreciable growth into the gas phase and lead to nearly isometric crystal shapes, consistent with a cubic crystal structure; their size at the point of the full conversion is 10–20 μm . The volume growth of these crystals is distinctly slower than the one of the initial film suggesting a different transport mechanism of the crystals' constituents, no longer proceeding through pores in the GH. Whether the transport proceeds by solid state diffusion of water molecules through the crystals' molecular cages [Kirschgen *et al.*, 2003; Liang and Kusalik, 2011], along crystal defects like grain boundaries, dislocation cores or the crystal surface cannot be distinguished in our images.

The nucleation and growth patterns from gas-enriched water (scenarios II and III) are distinctly different from scenario I. With gas-enriched water the nucleation frequently occurs inside the water phase followed by isotropic growth; after several minutes of growth, rounded polyhedral crystals are formed. In scenario II the nucleation often takes place inside the liquid close to the gas-water interface (supporting information Figure S4), crystals are less interconnected than in procedure I and show clear isometric habits with indications for crystal facets (Figure 3). In scenario III nucleation and growth occur typically in the bulk liquid, not necessarily close to the water-gas interface (supporting information Figure S5). It is remarkable that the

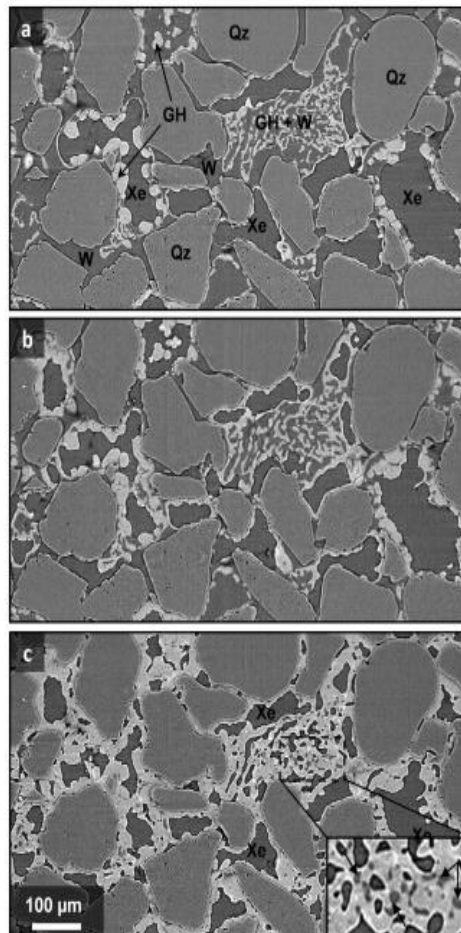


Figure 2. Sequence of GH film growth (scenario I): (a) initial ($t_n = 4.35$ min), (b) intermediate ($t_n = 10.2$ min), and (c) final ($t_n = 14.65$ min). The enlarged image in Figure 2c shows pockets of rest water trapped between GH crystals probably due to a gas diffusion limitation.

appearance of crystals inside the water phase occurs in certain parts of the pore space but not in others (Figure 4). Similar observations have been reported by e.g., *Bagherzadeh et al.* [2011], *Dai et al.* [2012], *Kerker et al.* [2014], and *Kossel et al.* [2013]. While in natural settings patchy growth can be ascribed to lithological control, spatially varying hydraulic conditions affecting methane transport or locally varying stress states [*Bagherzadeh et al.*, 2011], the reason for a small-scale GH inhomogeneity in our mineralogically homogeneous matrix is less obvious. The nucleation is not necessarily of homogeneous nature but may occur on nanometer-sized impurities inside the water, those remain invisible at the resolution of our chosen method. The initial growth patterns in scenario I and II (or III) are different, yet after several minutes the emerging polyhedral crystals reach a size between 10 and 20 μm for all scenarios. The molecular rearrangements at the growth interface between liquid water and GH can be envisaged to be similar to what has been found in molecular dynamics simulations from metastably gas-enriched water [e.g., *Walsh et al.*, 2011].

4. Liquid Interface Between Qz and GH

Our experimental results give strong evidence of a submicron to micron thick water layer at the Qz-GH and GB-GH interfaces (Figure 5). This observation is in accordance with the pioneering work of *Tohidi et al.* [2001] and several molecular computer simulations indicating the preference of a water layer at the GH (hydroxylated)-Qz interface [*Bagherzadeh et al.*, 2012; *Bai et al.*, 2011; *Liang et al.*, 2011]. Likewise, in a Hamaker approach the estimation of van der Waals related interactions between Qz, water and GH surfaces also indicate the preference of a water layer at the Qz-GH interface [*Bonnefoy et al.*, 2005]. Natural Qz surfaces are considered hydrophilic; as then expected no significant differences between untreated quartz (or GB) and additionally hydrophilized quartz were found. At low water saturation the liquid is frequently located at this Qz surface by capillary forces; in this case the submicron pixel size resolution of the setup allows locating the onset of nucleation at the gas-water interface, sometimes appearing only a few microns away from the Qz surface. The thickness of the layer varies and has its maximum at the grain boundaries between individual GH crystals which can be easily identified by their often obvious polyhedral shapes. Undoubtedly, Qz does not usually act as a nucleation surface in sedimentary matrices.

In case of a hydrophobic Qz the water layer is replaced by gas pockets that separate the mineral matrix from GH accumulations (Figure 6); similar observations were also made for hydrophobic GB. These observations suggests that the surface of GH, despite its predominantly hydrophilic character [*Hirata and*

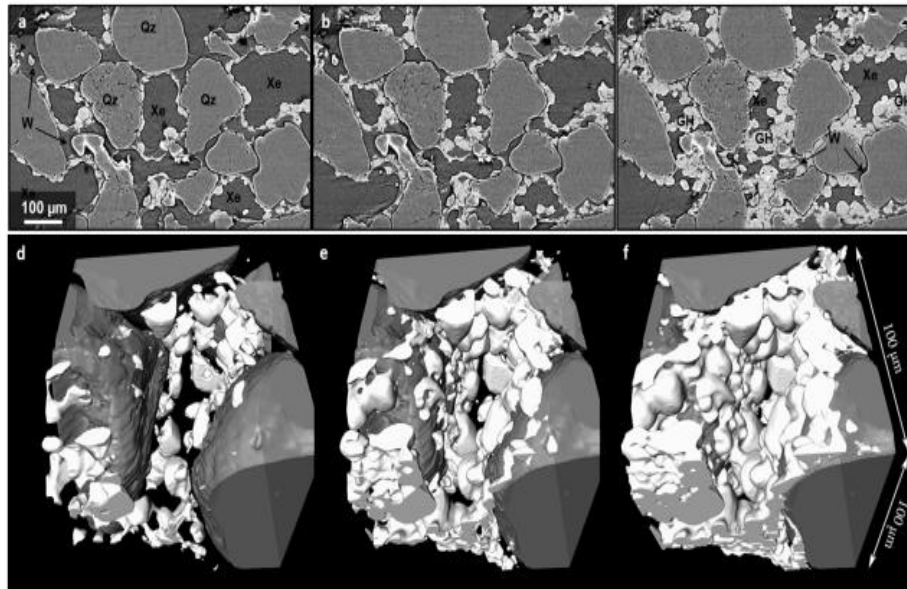


Figure 3. Evolution of GH growth from memory water (scenario II): (a) initial ($t_0 = 5.05$ min), (b) intermediate ($t_0 = 11.65$ min), and (c) final ($t_0 = 19.77$ min). Large polyhedral crystals were initially formed inside the water near the gas-water interface. (d–f) The 3-D rendered images of Figures 3a–3c. Rounded polyhedral crystals of GH (white) grow preferentially toward the center of the pore space; they do not adhere to the quartz (gray) surface, which is covered by a water layer of variable thickness. For clarity, the fluid phases have been removed from the rendered images.

Mori, 1998], prefers to form low-energy interfaces with the guest gas, and not with quartz surfaces. It is noteworthy in this context that the stability of GH in hydrophobic matrices is lower than for hydrophilic ones [Hachikubo *et al.*, 2011].

The presence of the water film has important consequences for the distribution of GH in the sedimentary matrix and the corresponding seismic as well as electromagnetic responses [Dai *et al.*, 2012; Spangenberg and Kulenkampff, 2006; Waite *et al.*, 2009]. In particular, frictional losses due to squirt flow phenomena in the interfacial water were responsible [Chand *et al.*, 2006; Priest *et al.*, 2006] (Figure 7) for the anomalous attenuation of high frequency elastic waves in GH-bearing sediments [e.g., Best *et al.*, 2010; Chand and Minshall, 2004; Guerin and Goldberg, 2005; Matsushima, 2006]. Broadband and waveform analysis of the response can help to distinguish other possible sources of attenuation [Suzuki and Matsushima, 2013]. More investigations are needed to corroborate the results in order to make attenuation studies useful for GH quantification.

5. The Role of Clay Minerals

The presence of bentonite and montmorillonite has been found beneficial for GH formation in laboratory experiments [Cha *et al.*, 1988] and will also alter the effective elastic properties [e.g., Lee *et al.*, 2010a, 2010b]. There is compelling evidence that under certain conditions, GH can even form intercalates with a certain type of montmorillonite [Guggenheim and Koster van Groos, 2003; Yeon *et al.*, 2011]. Another supporting argument for such scenario has been provided by a cryo-SEM study of samples from the JAPEX/JNOC/GSC Mallik 5L-38 research well [Techmer *et al.*, 2005]. Intercalates cannot be resolved by the applied tomographic method and would need to be confirmed using diffraction methods. Yet it is evident from our results that intimate contacts between montmorillonite and GH are frequently observed (Figure 8), even if the nucleation does not necessarily start at the surface of clay particles. Further work is needed to clarify the role of clay minerals in GH-bearing sediments.

6. Metastable Enrichment of Gases in Liquid Water

Enhanced formation rates of GH from water obtained by a decomposition of crystalline hydrates ("memory water") were repeatedly reported [Duchateau *et al.*, 2010; Sefidroodi *et al.*, 2013; Wu and Baoyong, 2010;

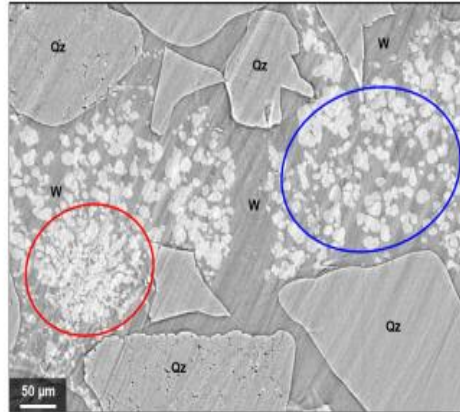


Figure 4. Image depicting a patchy growth of GH crystals (white) inside the water phase by formation using scenario II). ($W_s = 80\%$, $t_e = 5.7$ min). The region delimited by the red circle show a high density of GH crystals than the one in blue.

Zatsepina *et al.*, 2004], yet the issue is still controversial [Buchanan *et al.*, 2005; Thompson *et al.*, 2006; Wilson and Haymet, 2010]. The enhancement of growth may well be due to the enrichment of gases in the liquid beyond the equilibrium solubility, either in a hydrophobically hydrated state or as nanometer-sized gas aggregates embedded into the liquid; the "memory effect" therefore does not imply the presence of a relic structure of water itself facilitating GH formation. It rather implies an enrichment of guest molecules in the water phase. While there is clear evidence from reflectometry that gases can be enriched in water at the molecular-scale gas-water interface [Boewer

et al., 2012; Lehmkuhler *et al.*, 2008], unequivocal experimental evidence for a metastable enrichment of gases in thicker interfaces or bulk water was not available.

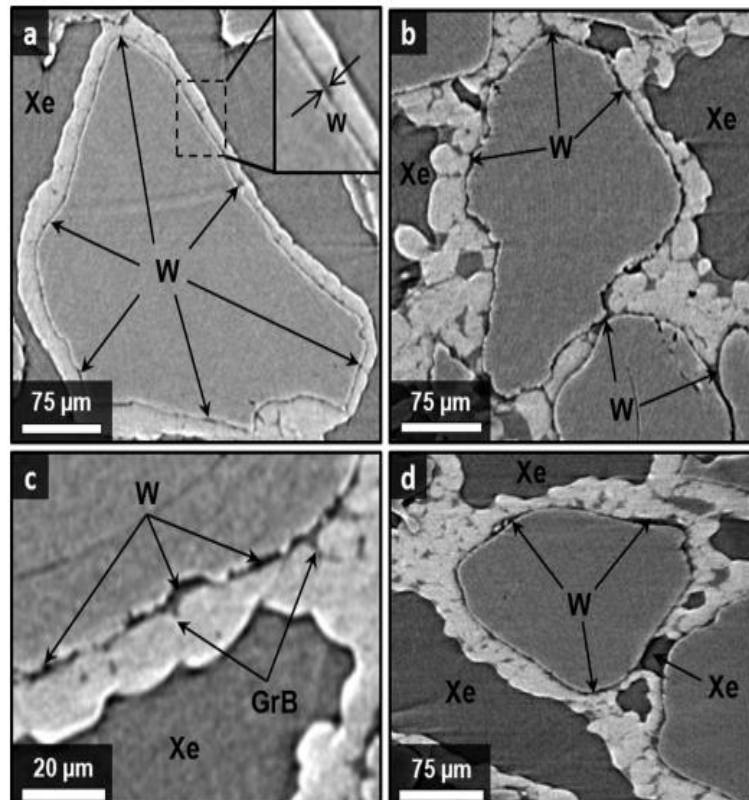


Figure 5. CT images showing a thin water layer remaining between GH (white) and sediment grains in a systematic manner at the end of the GH formation process using procedure (a) I or (b) II. The water layer is inhomogeneous; it is thicker at the grain boundary (GrB) of GH crystals. A remaining fluid phase ((c) water or (d) gas) near grain contacts was systematically observed.

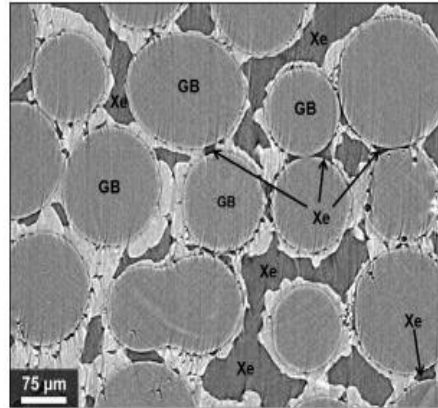


Figure 6. GH formation in hydrophobic glass beads (GB) ($t_0 = 16$ min). Almost all water has been transformed into hydrate; only a few water pockets remain inside the GH aggregates, probably linked to grain boundaries or triple junctions. Free xenon gas fills spaces between GH and GB grains.

Molecular computer simulations often use an enrichment procedure of gases in bulk water by decomposing hydrates prior to reformation [e.g., *Hawtin et al., 2008; Jacobson et al., 2010; Vatamanu and Kusalik, 2010; Walsh et al., 2011*] with a resulting metastable enrichment of gases in the liquid. Occasionally, the formation of nano-bubbles was observed in a gas-enriched liquid within the ns to μ s time scale of the simulations [e.g., *Bagherzadeh et al., 2012; Koishi et al., 2005*].

Our experimental findings now clearly indicate that the GH nucleation and growth pattern observed in water obtained from juvenile water (scenario I) is markedly different from the one observed from GH decomposition (scenario II and III) lending further strong

support to the existence of a so-called "memory effect." Furthermore, and for the first time, we have indications that indeed liquid water can become metastably enriched in Xe gas as suggested from the higher absorption coefficient observed for small water pockets in the pore space of Xe-hydrate (supporting information Figure S6); unfortunately the electron-density contrast cannot easily be quantified from the tomograms to obtain values for the gas enrichment. The observed Xe enrichment may well be the result of a dynamic equilibrium of gas and water at a nearby GH-water interface, where cage destruction with gas release and reformation with gas uptake must take place in a dynamic fashion on a μ s to s time scale; these enrichments (over the bulk solubility) are only temporarily maintained in micron-sized water pockets or water layers as Xenon will steadily be diluted into the bulk water toward equilibrium solubility.

7. Microstructural Aspects of GH Decomposition

The decomposition of GH is of central interest for all in situ gas extraction processes. Its microstructural details are crucial for the evolution of mechanical stability upon extraction, in particular for the vicinity of

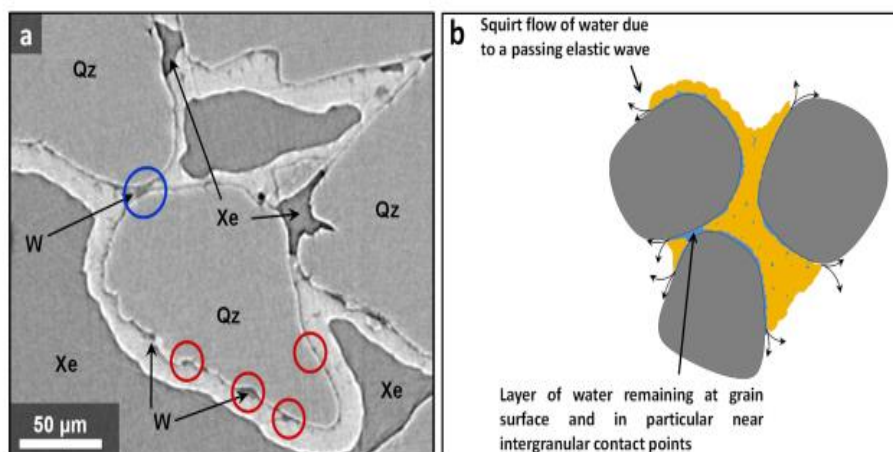


Figure 7. (a) Tomographic image illustrating a remaining fluid phase (most likely water) between the sediment grain and GH; the blue encircled area shows a water bridge close to an intergranular contact, the red encircled areas show larger water pockets on the grain's surface. (b) Conceptual model of squirt flow modified after [Priest et al., 2006] with quartz in gray, water in blue and GH in yellow, showing a water bridge as well as water pockets, the latter likely located at grain boundaries between GH crystals.

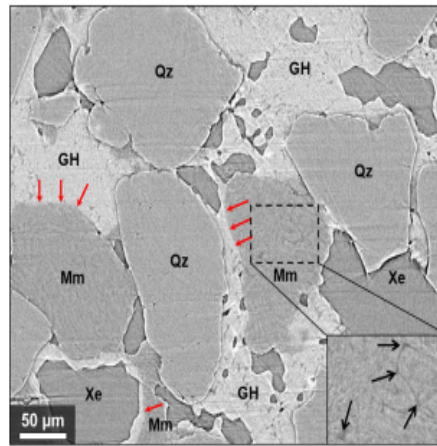


Figure 8. GH formation in natural quartz with 8 % Montmorillonite ($W_s = 40\%$, $t_a = 6.2$ min). Montmorillonite (Mm) particles (several microns) form aggregates of $100\ \mu\text{m}$ which are dispersed in the water phase. The enlarged image shows water channels in the structure of montmorillonite (black arrows). It is not clear where GH starts first to nucleate. An intimate contact between montmorillonite and GH is observed (red arrows).

interfacial water film. We emphasize that the microstructural situation may be different in case of thermal destabilization as in contrast to the depressurization case the heat transfer is limited by conductivity and may locally vary. As observed for the formation process, there are also patches in which the decomposition is faster than in others. Occasionally GH reformation can be observed locally, mainly by a growth at the gas liquid interface; this may indicate some micron-millimeter scale fluctuations of chemical activity and temperature.

8. Microstructure and Physical Properties

The microstructure of GH aggregates in a sedimentary matrix is frequently categorized into (a) contact-cementing, (b) grain-coating/cementing, (c) pore-filling, (d) load-bearing and (e) patchy pore-filling [Dai *et al.*, 2012]. For the same GH saturation, the predicted material properties, (in particular the seismic and electrical response and the permeation behavior) vary considerably with the chosen microstructural model. Experimentally observed seismic velocities suggest that the actually adopted microstructure in a fully water-saturated regime changes with GH saturation [Dai *et al.*, 2012; Konno *et al.*, 2015; Zhang *et al.*, 2011] ranging from a more pore-filling situation toward a more load-bearing case. While this general trend certainly is also observed in our tomographic experiments, some further details emerge. Larger formerly water-filled pores between Qz grains are filled with sometimes intimately, sometime loosely connected aggregates of mostly polyhedral crystals. In the former case the crystals are smaller compared to the latter case, thus the difference may simply be due to a variation in nucleation densities (see section 3). A cementation of the sedimentary matrix in a strict sense, i.e., a direct attachment of GH to Qz, does not take place. Rather the solid GH holds the sedimentary particles in place *via* a cushion of liquid water as discussed above. This also means that even in sediments with high GH saturation there are fluid pathways to and between every sedimentary grain in contrast to frozen sediments in permafrost. Moreover, it is noteworthy that the measured wave velocities increase with GH saturation in a way which cannot be reconciled with only one microstructural model. Our tomographically observed change of the microstructural regime at higher GH saturation provides the key for understanding these seismic observations.

To advance our understanding it would be very helpful to combine future petrophysical investigations with microstructural studies. This is an experimental challenge as the optimal samples sizes for petrophysics and high-resolution tomography do not match. The development of subsampling tools may provide a solution and will allow in the future also the microstructural investigation of pressure-cored samples from natural settings.

the extraction site. Although not of central interest for this study, we have obtained the first microstructural insight into the GH decomposition process (see supporting information Figure S7). When the pressure is lowered below stability, decomposition starts at the GH surface toward the gas phase and then proceeds at the interface with the formed bulk water, while the interface toward the Qz grain remains largely unchanged (albeit with the water layer as discussed in section 4.2) until the GHs completely disappear in the intergranular space. The fact that dissociation is much slower at the water interface toward the quartz surface might be related to a metastable xenon enrichment in this water interface; the small water volume involved and the long pathways to larger water pockets slow down diffusional mixing in the

9. Conclusion

High-resolution X-ray tomographic in situ studies of the formation and decomposition of GH are able to reveal unprecedented details of the changing microstructure; the microstructure in turn affects the petrophysical properties of the aggregates, in particular the seismic/sonic response. The initial distribution of GH for three formation methods studied is different as is the microstructural evolution. The distribution of GH in the sedimentary matrix depends not only on the formation scenario but also on the water saturation of the matrix. Yet the initially different growth morphologies of method I–III for a given water saturation appear to move toward more similar arrangements toward the end of the formation process. What remains unchanged in all scenarios and for all water saturations is the preference of GH to maintain a micron-sized water layer at the interface with quartz or glass beads; this is established as an intrinsic feature of GH in contact with quartz and must also be expected to occur in natural settings. However, it cannot be taken for granted that the microstructural arrangements obtained in laboratory experiments are closely similar to what is observed under similar p - T conditions in natural environments. After full conversion, either by consuming all locally available water or gas, coarsening processes are expected to reduce the total interfacial or grain boundary energies, which might in turn change some of the petrophysical properties of the sediment-GH aggregates.

There is good evidence that natural GH crystals can grow into much larger crystallites of several hundreds of microns [Klapp *et al.*, 2007, 2010]; unfortunately the characteristic time constants of this normal grain growth and/or Ostwald ripening processes are not yet known. Likewise, an extensive centimeter-decimeter scale redistribution of GH in layered sedimentary matrices is predicted as a consequence of local variations of surface energies/solubilities [Rempel, 2011]. Experiments over longer periods of time are needed to get further insight; from modeling and extrapolating such studies using e.g., the Landau-Slyovitz-Wagner theory of coarsening, one may even gain access to the formation time, i.e., the age of GH in sedimentary matrices as suggested by [Klapp *et al.*, 2007].

Acknowledgments

We acknowledge the Paul Scherrer Institut, Villigen, Switzerland for provision of synchrotron radiation beamtime at the TOMCAT beamline of the SLS and would like to thank Bernd Pinzer for assistance. We are grateful to Jens-Oliver Schwarz, Martin Wolf and Faisal Khan (all University of Mainz) for their valuable help during these experiments. The pressure cell was designed and constructed by Ulf Kahmann and Heiner Bartels (both Göttingen). The financial support from the Deutsche Forschungsgemeinschaft (DFG grants Ku 920/18 and Ke 508/20) is gratefully acknowledged. Support came also from the BMBF in the framework of the SUGAR-II program (grant 03G08198).

References

- Abegg, F., G. Bohrmann, J. Freitag, and W. Kuhs (2007), Fabric of gas hydrate in sediments from Hydrate Ridge—Results from ODP Leg 204 samples, *Geo Mar. Lett.*, 27(2–4), 269–277, doi:10.1007/s00367-007-0080-4.
- Abegg, F., H. J. Hohnberg, T. Pape, G. Bohrmann, and J. Freitag (2008), Development and application of pressure-core-sampling systems for the investigation of gas- and gas-hydrate-bearing sediments, *Deep Sea Res., Part I*, 55(11), 1590–1599, doi:10.1016/j.dsr.2008.06.006.
- Bagherzadeh, S. A., I. L. Moudrakovski, J. A. Ripmeester, and P. Englezos (2011), Magnetic resonance imaging of gas hydrate formation in a bed of silica sand particles, *Energy Fuels*, 25(7), 3083–3092, doi:10.1021/ef200399a.
- Bagherzadeh, S. A., P. Englezos, S. Alavi, and J. A. Ripmeester (2012), Molecular modeling of the dissociation of methane hydrate in contact with a silica surface, *J. Phys. Chem. B*, 116, 3188–3197, doi:10.1021/jp2086544.
- Bai, D., G. Chen, X. Zhang, and W. Wang (2011), Microsecond molecular dynamics simulations of the kinetic pathways of gas hydrate formation from solid surfaces, *Langmuir*, 27, 5961–5967, doi:10.1021/la105088b.
- Berge, L. I., K. A. Jacobsen, and A. Solstad (1999), Measured acoustic wave velocities of R11 (CC13F) hydrate samples with and without sand as a function of hydrate concentration, *J. Geophys. Res.*, 104(B7), 15,415–15,424, doi:10.1029/1999JB900098.
- Best, A. I., J. A. Priest, and C. R. I. Clayton (2010), A resonant column study of the seismic properties of methane-hydrate-bearing sand, *Geophysical Characterization of Gas Hydrates, Society of Exploration Geophysicists*, edited by Riedel, et al., 337–347, (SEG Geophysical Developments Series, 14), Tulsa, U. S.
- Best, A. I., J. A. Priest, C. R. I. Clayton, and E. V. L. Rees (2013), The effect of methane hydrate morphology and water saturation on seismic wave attenuation in sand under shallow sub-seafloor conditions, *Earth Planet. Sci. Lett.*, 368, 78–87, doi:10.1016/j.epsl.2013.02.033.
- Boewer, L., J. Nase, M. Paulus, F. Lehmkuhler, S. Tiemeyer, S. Holz, D. Pontoni, and M. Tolan (2012), On the spontaneous formation of clathrate hydrates at water–guest interfaces, *J. Phys. Chem. C*, 116(15), 8548–8553, doi:10.1021/jp211784w.
- Bohrmann, G., W. F. Kuhs, S. A. Klapp, K. S. Techmer, H. Klein, M. M. Murshed, and F. Abegg (2007), Appearance and preservation of natural gas hydrate from Hydrate Ridge sampled during ODP Leg 204 drilling, *Mar. Geol.*, 244(1–4), 1–14, doi:10.1016/j.margeo.2007.05.003.
- Bonnefoy, O., F. Gruy, and J. M. Herri (2005), Van der Waals interactions in systems involving gas hydrates, *Fluid Phase Equilibria*, 231(2), 176–187, doi:10.1016/j.fluid.2005.02.004.
- Buchanan, P., A. K. Soper, H. Thompson, R. E. Westcott, J. L. Creek, G. Hobson, and C. A. Koh (2005), Search for memory effects in methane hydrate: Structure of water before hydrate formation and after hydrate decomposition, *J. Chem. Phys.*, 123, 89–93, doi:10.1063/1.2074927.
- Cha, S. B., H. Ouar, T. R. Wildeman, and E. D. Sloan (1988), A third-surface effect on hydrate formation, *J. Phys. Chem.*, 92(23), 6492–6494, doi:10.1021/j100334a006.
- Chand, S., and T. A. Minshull (2004), The effect of hydrate content on seismic attenuation: A case study for Mallik 2L-38 well data, Mackenzie delta, Canada, *Geophys. Res. Lett.*, 31, L14609, doi:10.1029/2004GL020292.
- Chand, S., T. A. Minshull, J. A. Priest, A. I. Best, C. R. I. Clayton, and W. F. Waite (2006), An effective medium inversion algorithm for gas hydrate quantification and its application to laboratory and borehole measurements of gas hydrate-bearing sediments, *Geophys. J. Int.*, 166(2), 543–552, doi:10.1111/j.1365-246X.2006.03038.x.

- Chuvilin, E. M., V. A. Istomin, and S. S. Safonov (2011), Residual nonclathrated water in sediments in equilibrium with gas hydrate Comparison with unfrozen water, *Cold Reg. Sci. Technol.*, *68*, 68–73, doi:10.1016/j.coldregions.2011.05.006.
- Dai, S., J. C. Santamarina, W. F. Waite, and T. J. Kneafsey (2012), Hydrate morphology: Physical properties of sands with patchy hydrate saturation, *J. Geophys. Res.*, *117*, B11205, doi:10.1029/2012JB009667.
- Davies, S. R., E. D. Sloan, A. K. Sum, and C. A. Koh (2010), In situ studies of the mass transfer mechanism across a methane hydrate film using high-resolution Confocal Raman spectroscopy, *J. Phys. Chem. C*, *114*, 1173–1180, doi:10.1021/jp909416y.
- Duchateau, C., P. Glehat, T.-E. Pou, M. Hidalgo, and C. Dicharry (2010), Hydrate precursor test method for the laboratory evaluation of kinetic hydrate inhibitors, *Energy Fuels*, *24*(1), 616–623, doi:10.1021/ef900797e.
- Dvorkin, J., A. Nur, R. Uden, and T. Taner (2003), Rock physics of a gas hydrate reservoir, *Leading Edge*, *22*(9), 842–847, doi:10.1190/1.1614153.
- Ecker, C., J. Dvorkin, and A. M. Nur (2000), Estimating the amount of gas hydrate and free gas from marine seismic data, *Geophysics*, *65*(2), 565–573, doi:10.1190/1.1444752.
- Falenty, A., G. Genov, T. C. Hansen, W. F. Kuhs, and A. N. Salamatina (2011), Kinetics of CO₂ hydrate formation from water frost at low temperatures: Experimental results and theoretical model, *J. Phys. Chem. C*, *115*(10), 4022–4032, doi:10.1021/jp1084229.
- Guerin, G., and D. Goldberg (2005), Modeling of acoustic wave dissipation in gas hydrate-bearing sediments, *Geochem. Geophys. Geosyst.*, *6*, Q07010, doi:10.1029/2005GC000918.
- Guggenheim, S., and A. F. Koster van Groos (2003), New gas-hydrate phase: Synthesis and stability of clay-methane hydrate intercalate, *Geol. Soc. Am.*, *31*, 653–656, doi:10.1130/0091-7613.
- Hachikubo, A., S. Takeya, E. Chuvilin, and V. Istomin (2011), Preservation phenomena of methane hydrate in pore spaces, *Phys. Chem. Chem. Phys.*, *13*(39), 17,449–17,452, doi:10.1039/C1CP22353D.
- Hawtin, R. W., D. Quigley, and P. M. Rodger (2008), Gas hydrate nucleation and cage formation at a water/methane interface, *Phys. Chem. Chem. Phys.*, *10*, 4853–4864, doi:10.1039/B807455K.
- Hirata, A., and Y. H. Mori (1998), How liquids wet clathrate hydrates—Some macroscopic observations, *Chem. Eng. Sci.*, *53*(14), 2641–2643, doi:10.1016/S0009-2509(98)00078-5.
- Hu, G. W., Y. G. Ye, J. Zhang, C. L. Liu, S. B. Diao, and J. S. Wang (2010), Acoustic properties of gas hydrate-bearing consolidated sediments and experimental testing of elastic velocity models, *J. Geophys. Res.*, *115*, B02102, doi:10.1029/2008JB006160.
- Hu, G. W., Y. G. Ye, J. Zhang, and S. B. Diao (2013), Relationship between acoustic properties and hydrate saturation in *Natural Gas Hydrates: Experimental Techniques and Their Applications*, edited by Y. Ye and C. Liu pp. 89–126, Springer, Heidelberg.
- Jacobson, L. C., W. Hujo, and V. Molinero (2010), Amorphous precursors in the nucleation of clathrate hydrates, *Am. Chem. Soc.*, *132*(33), 11,806–11,811, doi:10.1021/ja1051445.
- Jin, S., J. Nagao, S. Takeya, Y. Jin, J. Hayashi, Y. Kamata, T. Ebinuma, and H. Narita (2006), Structural investigation of methane hydrate sediments by microfocus X-ray computed tomography technique under high-pressure conditions, *Jpn. J. Appl. Phys.*, *45*(2), L714–L716, doi:10.1143/JJAP.45.L714.
- Jradi, K., C. Daneault, and B. Chabot (2011), Chemical surface modification of glass beads for the treatment of paper machine process waters, *Thin Solid Films*, *519*, 4239–4245, doi:10.1016/j.tsf.2011.02.080.
- Katsuki, D., R. Ohmura, T. Ebinuma, and H. Narita (2007), Methane hydrate crystal growth in a porous medium filled with methane-saturated liquid water, *Philos. Mag.*, *87*(7), 1057–1069, doi:10.1080/14786430601021652.
- Kerker, P. B., K. Horvat, K. W. Jones, and D. Mahajan (2014), Imaging methane hydrates growth dynamics in porous media using synchrotron X-ray computed microtomography, *Geochem. Geophys. Geosyst.*, *15*, 4759–4768, doi:10.1002/2014GC005373.
- Kirschgen, T. M., M. D. Ziedler, B. Geil, and F. Fajana (2003), A deuteron NMR study of the tetrahydrofuran clathrate hydrate - Part II: Coupling of rotational and translational dynamics of water, *Phys. Chem. Chem. Phys.*, *5*(23), 5247–5252, doi:10.1039/b212472f.
- Klapp, S. A., H. Klein, and W. F. Kuhs (2007), First determination of gas hydrate crystallite size distributions using high-energy synchrotron radiation, *Geophys. Res. Lett.*, *34*, L13608, doi:10.1029/2006GL029134.
- Klapp, S. A., S. Hemes, H. Klein, G. Bohrmann, I. MacDonald, and W. F. Kuhs (2010), Grain size measurements of natural gas hydrates, *Mar. Geol.*, *274*(1–4), 85–94, doi:10.1016/j.margeo.2010.03.007.
- Klapp, S. A., et al. (2012), Microstructure characteristics during hydrate formation and dissociation revealed by X-ray tomographic microscopy, *Geo Mar. Lett.*, *32*(5–6), 555–562, doi:10.1007/s00367-012-0276-0.
- Klapproth, A., K. S. Techmer, S. A. Klapp, M. M. Murshed, and W. F. Kuhs (2007), Microstructure of gas hydrates in porous media, in *Physics and Chemistry of Ice*, Spec. Publ. 311, edited by W. F. Kuhs, pp. 321–328, RSC Publ., Cambridge, U. K.
- Kneafsey, T. J., L. Tomutsa, G. J. Moridis, Y. Seol, B. M. Freifeld, C. E. Taylor, and A. Gupta (2007), Methane hydrate formation and dissociation in a partially saturated core-scale sand sample, *J. Pet. Sci. Eng.*, *56*(1–3), 108–126, doi:10.1016/j.petrol.2006.02.002.
- Koishi, T., K. Yasuoka, T. Ebisuzaki, S. Yoo, and X. C. Zeng (2005), Large-scale molecular-dynamics simulation of nanoscale hydrophobic interaction and nanobubble formation, *J. Chem. Phys.*, *123*(20), 6, doi:10.1063/1.2102906.
- Konno, Y., Y. Jin, J. Yoneda, M. Kida, K. Egawa, T. Ito, K. Suzuki, and J. Nagao (2015), Effect of methane hydrate morphology on compressional wave velocity of sandy sediments: Analysis of pressure cores obtained in the Eastern Nankai Trough, *Mar. Pet. Geol.*, doi:10.1016/j.marpetgeo.2015.02.021, in press.
- Kossel, E., C. Deuser, N. Bigalke, and M. Haackel (2013), Magnetic resonance imaging of gas hydrate formation and conversion at sub-seafloor conditions, *Diffus. Fundam.*, *18*, 1–4.
- Kuhs, W. F., A. Klapproth, F. Gotthardt, K. Techmer, and T. Heinrichs (2000), The formation of meso- and macroporous gas hydrates, *Geophys. Res. Lett.*, *27*, 2929–2932, doi:10.1029/2000GL006112.
- Kuhs, W. F., D. K. Staykova, and A. N. Salamatina (2006), Formation of methane hydrate from polydisperse ice powders, *J. Phys. Chem. B*, *110*(26), 13,283–13,295, doi:10.1021/jp061060f.
- Lee, J. Y., J. C. Santamarina, and C. Ruppel (2010a), Parametric study of the physical properties of hydrate-bearing sand, silt, and clay sediments: 1. Electromagnetic properties, *J. Geophys. Res.*, *115*, B11104, doi:10.1029/2009JB006669.
- Lee, J. Y., F. M. Francisca, J. C. Santamarina, and C. Ruppel (2010b), Parametric study of the physical properties of hydrate-bearing sand, silt, and clay sediments: 2. Small-strain mechanical properties, *J. Geophys. Res.*, *115*, B11105, doi:10.1029/2009JB006670.
- Lehmkuhler, F., M. Paulus, C. Sternemann, D. Lietz, F. Venturini, C. Gutt, and M. Tolan (2008), The carbon dioxide–water interface at conditions of gas hydrate formation, *J. Am. Chem. Soc.*, *131*(2), 585–589, doi:10.1021/ja806211r.
- Li, F. G., C. Y. Sun, Q. Zhang, X. X. Liu, X. Q. Guo, and G. J. Chen (2011), Laboratory measurements of the effects of methane/tetrahydrofuran concentration and grain size on the P-wave velocity of hydrate-bearing sand, *Energy Fuels*, *25*(5), 2076–2082, doi:10.1021/ef101665v.
- Liang, S., and P. G. Kusalik (2011), The mobility of water molecules through gas hydrates, *J. Am. Chem. Soc.*, *133*(6), 1870–1876, doi:10.1021/ja108434h.

Marwen Chaouachi

Date of Birth: 08.08.1984

Place of Birth: Testour (Beja, Tunisia)

Nationality: Tunisian

EDUCATION

- 06/11 – 06/15 **Georg-August-Universitaet Goettingen** Göttingen (Germany)
• PhD – “Study of the Microstructure of Gas Hydrate-bearing Sediments” using X-ray Diffraction, Scanning Electron Microscopy and μ -X-ray Computed Tomography.
Advisor: Prof. Dr. Werner F. KUHS
- 09/10 **University of Paris VII Denis Diderot** Paris (France)
• Master's Degree in Materials Science & Engineering "Surface, Thin films, Nanomaterials"
- 03/09 **National Institute of Applied Sciences and Technology Tunis** (Tunisia)
• Engineer Degree in Industrial Chemistry

EXPERIENCE

- 03/12 – 04/12 **Higher European Research Course for Users of Large Experimental Systems**
ESRF/ILL (Grenoble, France) - PSI - SLS (Villigen, Switzerland) - SOLEIL (Paris, France)
• Lectures, practicals and tutorials, visits of large facilities
• Neutron and Synchrotron Radiation for condensed matter studies (Biology, Chemistry, Physics, Materials Science, Geosciences, Industrial applications)
- 04/10 – 10/10 **Research Assistant**
Siemens AG Corporate Technology, Munich (Germany)
Project: “Search for New LED Converter Phosphors using High Throughput Experimentation”
- 09/08 – 01/09 **Research Assistant**
Laboratory of Earth Materials and Environment (LGE), Paris (France)
Project: "Study of the Degradation of the Herbicide Sulcotrion in Aqueous Medium by Electrochemical Processes of Oxidation"

LANGUAGES

Arabic: Native
French: Native
English: Good level
German: Intermediate level

AWARDS

• "Outstanding Student Paper Award", American Geophysical Union, December 2013.

SERVICE/**LEADERSHIP**

- Vice President of Talent Management Team, AIESEC Goettingen, 2012-2013.
- Co-founder and team leader in Chemclub, INSAT (Tunisia), 2006 - 2009

CONFERENCES

- **21st Annual Conference of the German Crystallographic Society** – Freiberg (Germany), March 2013, *Fast quantitative determination of crystallite size distributions from 2D diffraction data*
Marwen Chaouachi, Sigmund Neher, Stefanie Stracke, Andrzej Falenty, Helmut Klein, and Werner F. Kuhs – Talk
- **AGU Fall Meeting** – San Francisco (USA), December 2013
Direct observation of gas-hydrate formation in natural porous media on the micro-scale
Marwen Chaouachi, Kathleen Sell, Andrzej Falenty, Frieder Enzmann, Michael Kersten, Bernd Pinzer, Erik H. Saenger and Werner F. Kuhs – Talk
- **The 29th European Crystallographic Meeting** – Rovinj (Croatia), August 2015
In-situ determination of the evolution of the crystallite size distributions of GH- bearing sediments using two-dimensional X-ray diffraction
Marwen Chaouachi, Sigmund H. Neher, Andrzej Falenty, Werner F. Kuhs

PUBLICATIONS

- Chaouachi, M., A. Falenty, K. Sell, F. Enzmann, M. Kersten, D. Haberthür, and W. F. Kuhs (2015), Microstructural evolution of gas hydrates in sedimentary matrices observed with synchrotron X-ray computed tomographic microscopy, *Geochem. Geophys. Geosyst.*, 16, doi:10.1002/2015GC005811.
- Sell, K., Saenger, E.-H., Falenty, A., Chaouachi, M., Haberthür, D., Enzmann, F., Kuhs, W. F., and Kersten, M.: On the path to the digital rock physics of gas hydrate bearing sediments – processing of in-situ synchrotron-tomography data, *Solid Earth Discuss.*, doi:10.5194/se-2016-54, in review, 2016.